Aggregation of Amyotrophic Lateral Sclerosis-Associated Cu/Zn Superoxide Dismutase

by

Young Mi Hwang

A thesis
presented to the University of Waterloo
in fulfillment of the
thesis requirement for the degree of
Doctor of Philosophy
in
Chemistry

Waterloo, Ontario, Canada, 2010

AUTHOR'S DECLARATION

I hereby declare that I am the sole author of this thesis. This is a true copy of the thesis, including any required final revisions, as accepted by my examiners.

I understand that my thesis may be made electronically available to the public.

Abstract

Amyotrophic lateral sclerosis (ALS) is a devastating, progressive, and fatal neurodegenerative disease. Despite the fact that ALS is the most common motor neuron disease in adulthood, there is no effective treatment for the disease. Although most ALS cases (90-95%) are sporadic (sALS), the remaining cases (5-10%) are dominantly inherited and referred to as familial ALS (fALS). Because sALS and fALS show indistinguishable disease symptoms, a common disease mechanism has been proposed. After the discovery of the link between fALS and mutants of cytosolic Cu/Zn superoxide dismutase (SOD1), over 140 mutations in SOD1 have been identified to account for ~20% of fALS. The location of these mutants are scattered throughout the primary and tertiary structures of the protein. It is widely accepted that fALS-linked mutations in SOD1 result in a gain of toxic function to cause the disease, rather than a loss of physiological function, although the nature of the toxic mechanism remains unclear.

SOD1 is a β-rich, homodimeric metalloenzyme that catalyzes the dismutation of superoxide radicals to O_2 and H_2O_2. The protein is ubiquitously expressed and the mature form of SOD1 (holo SOD1) contains one catalytic Cu ion, one structural Zn ion, one intra-molecular disulfide bond (between C57 and C146) and two free Cys residues (C6 and C111) per 153 residue subunit. Analogous to many different human diseases in which protein aggregation is a hallmark, aggregation of Cu/Zn superoxide dismutase (SOD1) is implicated in the pathogenesis of ALS. This thesis reports the first observation of aggregation of the most abundant form of SOD1 *in vivo*, the native, metallated (holo) dimer, under physiologically relevant conditions (37 °C and pH 7.8). The medical relevance of aggregates

is demonstrated by structural and tinctorial analyses as well as the novel observation of binding of an anti-SOD1 antibody that specifically recognizes pathological aggregates in ALS. Additionally, ALS-associated SOD1 mutations promote aggregation but are not required, supporting a common mechanism in familial and sporadic ALS. The aggregation is characterized by a lag phase, which is diminished by self- and cross-seeding where heterogeneous nucleation is the underlying mechanism. Moreover, multiple pathways of aggregation are elucidated including dimer dissociation and metal loss. It is shown that if holo SOD1 loses more Zn ions than Cu ions, the aggregation profiles have shorter duration and lower final intensity, whereas when holo SOD1 loses more Cu ions than Zn ions, the aggregation profiles have longer duration and higher intensity. Taken together, the data in this thesis establish a valuable system for understanding SOD1 aggregation and toxicity mechanisms which can be used for developing therapeutic strategies targeting protein aggregation.

Acknowledgements

I would like to thank the following people:

my supervisor Elizabeth Meiering, who has been supporting me in every circumstance and teaching me what is to be a true scientist.

all the members of the Meiering group past and present, especially Peter Stathopulos and Kristin Dimmick, who have been so patient, understanding, and so helpful.

my family and friends that I have met in Canada, who have made me realize what is most important in my life.

Dedication

For my parents Taewan Hwang and Taesoon Jang, my two nieces Heji and Gaul Han, and my fiancé Akira Isoda

Table of Contents

viii

List of Figures

xiv

List of Tables

List of Abbreviations

A...alanine

A...parameter for the hyperbolic cosine function

Å...angstrom

Aβ..amyloid β

ABTS.................................2-2'-azino-di-(3-ethylbenzthiazoline sulfonic acid

A_{free} ....concentration of non-aggregated proteins

AFM..atomic force microscopy

AGE..advanced glycation end product

ALS ....amyotrophic lateral sclerosis

ANS...anilinonaphthalene sulphonic acid

A_0 ....initial protein concentration

Apo SOD1...superoxide dismutase free of copper and zinc

APS...ammonium persulfate

Arg..arginine

A_s...concentration of soluble proteins at equilibrium

Asp..aspartic acid

Ast-...hyaline inclusions in astrocyte

ATR...attenuated total reflectance

B...parameter for the hyperbolic cosine function

BSA..bovine serum albumin

bSOD1..bovine SOD1

C...cysteine

CCS...copper chaperone for SOD1

CD..circular dichroism

C_j..concentration of solution phase j-mer

COX17...cytochrome c oxidase copper chaperone

C_P...total concentration of total aggregates

C_{P1}................................total concentration of aggregates formed by primary nucleation

xvi

H………………………………………………………..................................observed height

H^+………………………………………………………………...........proton

HEPES…………………………………4-(2-hydroxyethyl)-1-piperazineethanefulfonic acid

His…………………………………………………..………………………...histidine

Holo SOD1…superoxide dismutase coordinating the full complement of copper and Zinc

HRP…………………………………………..…………..horseradish peroxidease

hSOD1…………………………………………..…………………human SOD1

HSP…………………………………………..…………….heat shock protein

H_2O_2…………………………………………..…………….hydrogen peroxide

I………………………………………..……………………………….isoleucine

ICP-AES…………………………inductively coupled plasma- atomic emission spectroscopy

ITV…………………………………………..……………….in-torch vaporization

K…………………………………………………………………………..Kelvin

K…………………………………………..………………equilibrium constant

k …………………………………….................................Boltzmann's constant

$\tilde{K}_j$ ………………equilibrium constant for formation of a *j*-mer in solution from *j* monomers

k_+…………………….rate constant for addition of a monomer during formation of a nucleus

k.………………….rate constant for dissociation of a monomer during formation of a nucleus

kDa………………………………………..…………………………kilodaltons

LB……………………………………………………..………………luria broth

LBHI……………………………………………...Lewy body-like hyaline inclusion

LS…………………………………………..…………………light scattering

Lys……………………………………………..……………………........lysine

M…………………………………..……………..…………molar concentration

MCT…………………………………..……………...……mercury-cadmium-telluride

MeCN ………………………………………...……………acetonitrile

Mn SOD………………………………………manganese superoxide dismutase

MS………………………………………………………mass spectroscopy

MW…………………………………………………….molecular weight

N……………………………………………………...……………………………………..asparagine

NF…………………………………………………………...……………………………….neurofilament

Ni SOD……………………………………………...……………........nickel superoxide dismutase

NMR…………………………………………………...................nuclear magnetic resonance

NO……………………………………………………………………………….nitric oxide

O^{2-}………………………………….....……………………...…………………....superoxide anion

O_2………………………………………………...………………....................diatomic oxygen

$OONO^-$…………………………………………………...…………………peroxynitrite

P……………………………...……….aggregates formed by both primary and secondary nucleation

P1……………………………....……………………...aggregates formed by primary nucleation

P2……………………...…………………….aggregates formed by secondary nucleation

PBS……………………………………………………....................phosphate buffer saline

PBST………………………….....……phosphate buffer saline with 0.05 % (v/v) of Tween 20

pdb …………………………………………………...……………….protein data bank

P_j………………………………………………………...……………heterogeneous nucleus

P_{jt}……………...……total concentration of available sites for attaching a solution phase *j*-mer

PMCA ………………………………...…………………protein misfolding cyclic amplification

Pro……………………………………………………………………….....proline

pWT……………...……………………………………...………………pseudo wild type

Q……………………………………………………………………...…...glutamine

q…………………………………………………………………...scattering vector

R……………………………………………………………………...arginine

R_c……………………………...………radius of curvature of a tip for atomic force microscopy

RHI………………………...…………………………………...…………round hyaline inclusion

ROS…………………………………………...................reactive oxygen species

RT…………………………………………………………………….room temperature

S……………………………………………………………………...…serine

sALS …………………………………………………sporadic amyotrophic lateral sclerosis

s.d. …………………………...……………………...………………standard deviation

xix

[θ] …………………………..……………………………...……………mean residue ellipticity

θ …………………………………………………….……………………..scattering angle

τ.………………………………………………..……………………….............interval

λ.…………………………………………………………………………….wavelength

Chapter 1
General Introduction

1.1 Cu/Zn Superoxide Dismutase (SOD)

1.1.1 SODs

Reactive oxygen species (ROS), such as superoxide and hydroxyl radicals have been shown to be toxic due to their high reactivity due to the presence of unpaired electrons. Therefore, it is crucial for a living cell to regulate ROS homeostasis (Lenaz, 1998). Superoxide is formed mainly on the matrix side of the inner mitochondrial membrane as a byproduct of respiration (Fridovich, 1986). In addition, superoxide can be formed enzymatically by enzymes such as xanthine oxidase, aldehyde oxidase, dihydrorotic dehydrogenase, and flavoprotein dehydrogenases (for a review see (Fridovich, 1975)). To prevent cellular damage arising from superoxide reactivity, cells have evolved a number of defense mechanisms to limit the levels of superoxide. One such mechanism involves conversion of superoxide (O_2^-) into diatomic oxygen (O_2) and hydrogen peroxide (H_2O_2), a reaction that is catalyzed by superoxide dismutases (SODs).

SODs exist in both prokaryotic and eukaryotic cells where they perform the same function but possess different catalytic cofactors. These include: Cu/Zn SOD (Cu^{2+} is the metal involved in catalytic reactions), Mn SOD, Fe SOD, and Ni SOD. Mn SOD is found mostly in the matrix of mitochondria in eukaryotic cells and in bacteria (Barondeau *et al*, 2004). Although Mn SODs from bacteria and eukaryotic cells bind the same metal, the tertiary structure of the proteins are different; the former is dimeric with a molecular weight

of 40 kDa, while the latter is tetrameric with a molecular weight of 80 kDa. SOD2 refers to Mn SOD in the matrix of mitochondria from eukaryotic cells (Zelko *et al*, 2002). The theory that mitochondria developed from a prokaryote that entered into an eukaryotic cell is powerfully supported by this finding (Fridovic.I, 1974). Fe SOD is found in the cytosol of cyanobacteria, in the periplasmic space of bacteria, and in the chloroplast stomata of most eukaryotic algae (Grace, 1990). Cu/Zn SOD found in the cytosol of eukaryotic cells is called SOD1. Recently, Cu/Zn SOD has also been identified in the extracellular matrix of eukaryotic cells, and has been referred to as SOD3. The sequences of SOD1 and SOD3 are homologous but the structures differ in that SOD1 is a dimeric protein, whereas SOD3 is a tetramer (Zelko, Mariani & Folz, 2002). In addition, Cu/Zn SOD is also found in bacteria (Puget & Michelso.Am, 1974). However, the structure of Cu/Zn SOD from *Escherichia coli* (*E. coli)* is monomeric, resulting from the substitution of hydrophobic residues with charged residues at positions located in the dimer interface of the human enzyme (Battistoni, 2003). Most recently, a completely distinct third SOD class, hexameric Ni SOD was discovered in *Streptomyces* (Youn *et al*, 1996) and cyanobacteria (Plakoutsi *et al*, 2005). To summarize, humans have three different SODs: SOD1, SOD2, and SOD3 which vary in location but all act on superoxide (Zelko, Mariani & Folz, 2002). The focus of this thesis is SOD1, which will be described in further detail in the following sections.

1.1.2 SOD1 structure

SOD1 is a homodimeric metalloenzyme with a molecular weight of 32 kDa, in which each subunit contains 153 residues, one Cu ion, one Zn ion, two free cysteines (C6 and C111), and one intramolecular disulfide bond between C57 and C146. Human SOD1 (hSOD1) was crystallized in 1986, and the structure was determined at a resolution of 2.0 Å (Parge *et al*, 1986; Parge *et al*, 1992). In 2003, the structure was solved to a higher resolution of 1.78 Å (Strange *et al*, 2003). More recently, the crystal structures of various hSOD1 mutants, including A4V, I113T, G37R, H46R, S134N and G85R (Antonyuk *et al*, 2005; Cao *et al*, 2008; Hart *et al*, 1998; Hough *et al*, 2004b) and solution structures of S143N, G93A and G37R have also been determined (Banci *et al*, 2003; Banci *et al*, 2005; Banci *et al*, 2007a; Shipp *et al*, 2003).

Fig. 1.1 illustrates key structural features of SOD1. These features include: a Greek key domain, two long functional loops, the active site, and the dimer interface. Each subunit is composed of eight antiparallel β strands that form a Greek key motif (Fig. 1.1b) resembling a flattened cylinder. Seven loops connect the strands: Loop I, residues 12–15; loop II, residues 23-28; loop III, residues 38-40; loop IV, residues 47-82; loop V, residues 90-93; loop VI, residues 102-114; and loop VII, residues 121-143 (Parge, Hallewell & Tainer, 1992). Loop IV and VII play central roles in enzymatic function. Loop IV is composed of three different sections that are defined as follows: the dimer interface section (residues 49-54), the disulfide bond section (residues 55-61) and the Zn binding section (residues 62-82) (Hornberg *et al*, 2007). Loop VII is called the electrostatic loop and is involved in guiding the superoxide substrate into the active site (Getzoff *et al*, 1992a). These

loops (loop IV and VII) also contain residues that form salt bridges which help maintain the native structure. For example, salt bridges form between residues Asp 76 and Lys 128, Asp 101 and Arg 79, as well as Glu 132 and Lys 136 (Tainer *et al*, 1982).

a

loop IV
loop II
loop VI
N
loop II
loop VI
loop IV

β3
β5
β2
β1
β1
β2
β3
β6
β6
β4
C
loop VII
β7
β4
β7
β8
β8
loop VII
loop III
loop I
loop V
loop V
loop III
loop III
loop V
loop I

b

loop III
loop I
loop V
electrostatic loop
loop VII

11   16   37   94   89   41   120   144

β1   β2   β3   β6   β5   β4   β7   β8

3   22   29   101 83   46   115 151

N   loop II   loop VI   C

loop IV
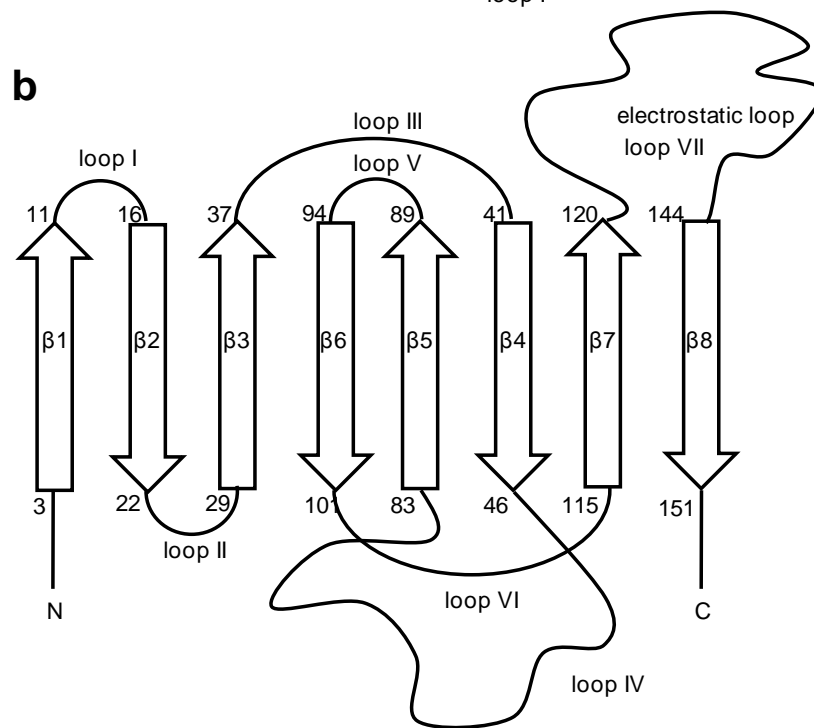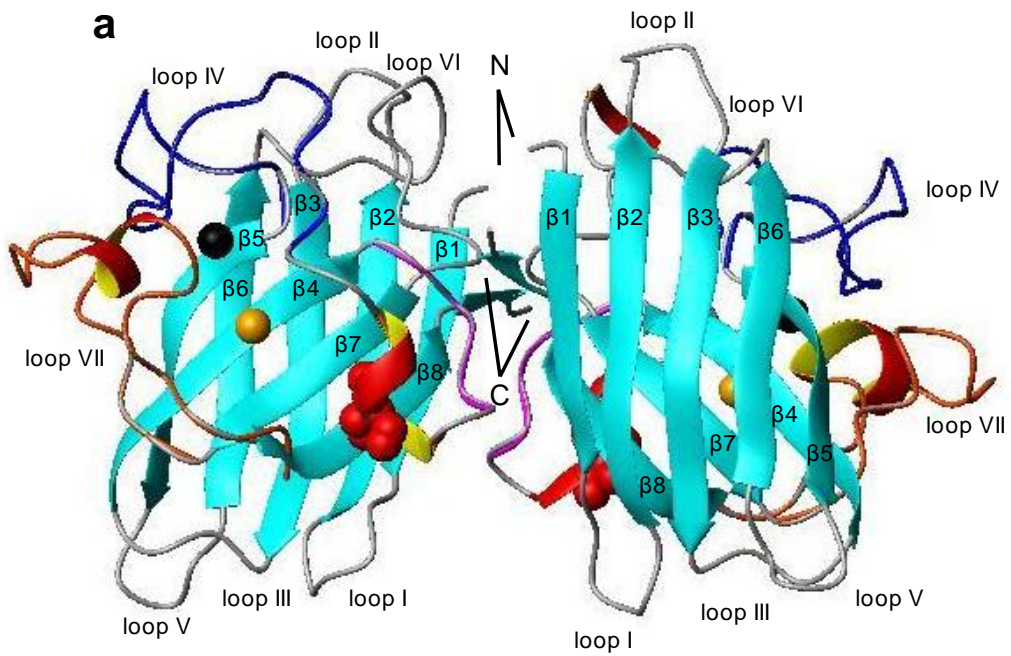
Figure 1.1 Structure of human Cu/Zn SOD1

(a) Ribbon representation of dimeric Cu/Zn SOD1 (pdb code 1SOS) was made using Molmol (Koradi *et al*, 1996). Eight β-stands are represented by cyan arrows and labeled β1 – β8, whereas short helical structures within loops are represented in red. 5 loops (loop I-III, V, and VI) connecting the β strands are colored gray and labeled in Roman numerals. Loop IV is composed of three different regions: the dimer interface region (residues 47-54); the disulfide bond region (residues 55-61); and the Zn binding region (residues 62-82). These regions are coloured magenta, red, and blue, respectively (Hornberg, Logan, Marklund & Oliveberg, 2007). The electrostatic loop, loop VII (residues 121-144) is coloured dark orange. The overall shape of each subunit resembles a flattened cylinder. Cu and Zn ions are shown as orange and black spheres, respectively. The intra-subunit disulfide bond between C57 and C146 is indicated by red spheres. The image is based on the crystal structure of the C6A/C111S recombinant hSOD1, which exhibits a very similar structure with the wild type of hSOD1 (Lepock *et al*, 1990; Parge, Hallewell & Tainer, 1992). (b) The Greek-key motif of a monomer SOD1 is shown using 8 arrows to represent the 8 β strands. The strands are labeled β1-β8 and the loops connecting the strands are labeled with Roman numerals (I-VII). The amino acid numbers are labeled to the left of each β strand.

The Cu and Zn binding sites in hSOD1 (Fig. 1.2) are close in space and share an imidazolate ligand (His 63). In addition to His 63, the Zn ion is coordinated in an approximately tetrahedral geometry by His 71, His 80, and the aspartyl side chain of Asp 83. The Cu ion is coordinated in an irregular five coordinate geometry by His 46, His 48, His 120, a water molecule, and the shared His 63 ligand. In addition, a secondary hydrogen bond network stabilizes and interconnects the metal binding regions of the electrostatic loop *via* the loop residue Asp 124, the copper ligand His 46, and the zinc ligand His 71 (Valentine *et al*, 2005)
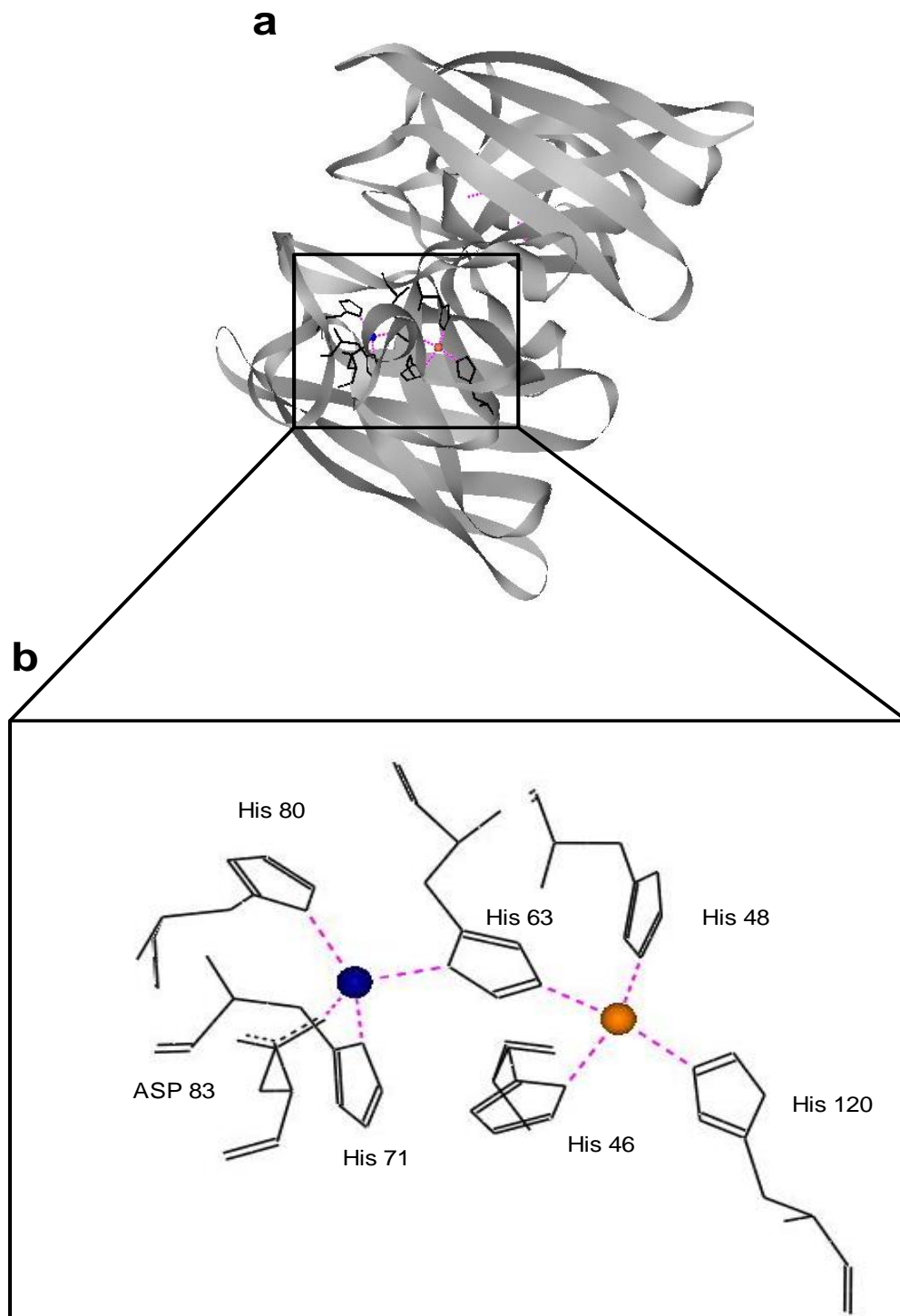
Figure 1.2 The active site of hSOD1

An illustration of the structure of hSOD1, made using pdb code 1SOS in Viewerlite 5.0, is shown with the active site (a). The box in (a) is expanded in (b). The residues (black) that are involved in the coordination of Cu (orange sphere) and Zn (blue sphere) ions are shown. The interaction between the metals and the various amino acids are represented in dots (magenta). 4 residues (His 80, His 71, His 63 and Asp 82) coordinate the Zn ion, whereas the Cu ion is coordinated by 4 residues (His 46, His 48, His 63, His 120) and a water molecule (not shown). His 63 acts as a bridge between Cu and Zn ions. The image is based on the crystal structure of the C6A/C111S recombinant hSOD1.

Within the dimer, the forces contributing to the strong dimer interface are hydrophobic interaction and hydrophilic interactions, which include hydrogen bonding between two subunits and a number of hydrophilic residues interacting through bridging water molecules (Getzoff *et al*, 1986; Getzoff *et al*, 1989). Overall the dimer interface is formed by 10 β strand residues and 12 loop residues, with the N and C termini of each monomer juxtaposed near the dimer interface (Getzoff, Tainer & Olson, 1986; Getzoff *et al*, 1989) (Fig.1.1). The highly conserved residues in the dimer interface, Cys 57 and Cys 146, form an intramolecular disulfide bond stabilizing the dimer interface section of loop IV by covalently joining it to the β barrel. Thus, one can expect that reduction of the disulfide bond would weaken the dimer interface, and this has been observed experimentally (Lindberg *et al*, 2004). Additionally, Gly 51 and Gly 114 stabilize the dimer interface through the

hydrogen bonding to Ile 151 in the opposite subunit, so that these three residues form all four of the hydrogen bonds across the dimer interface (Getzoff *et al*, 1989).

All of the elements described in this section: stable β domain, salt bridges, intramolecular disulfide bond, metal cofactors, and the strong dimer interface contribute to the stability of this protein. As a consequence, SOD1 is highly resistant to denaturants, extreme pH and high temperatures. For example, the enzyme is not denatured by even 8M urea or 1% of sodium dodecyle sulfate (SDS) (Lyons *et al*, 1999). SOD1 has been shown to be stable in the pH range of 6-11 (Senoo *et al*, 1988), and exhibits a high melting temperature that exceeds 80 °C (Lepock, Frey & Hallewell, 1990; Rodriguez *et al*, 2005). Stability analysis of bovine SOD1 (bSOD1) shows that the dimer remains intact in 8M urea or 4% SDS, and the functional activity remains normal in 4% SDS or 10 M urea (Forman & Fridovic.I, 1973; Malinowski & Fridovich, 1979). However, despite the stability of its native structure, aggregation of human SOD1 has been implicated in the pathogenesis of the neurodegenerative disease, amyotrophic lateral sclerosis (ALS) (see section 1.2).

1.1.3 SOD activity

As an antioxidant enzyme, SOD1 protects the cell by catalyzing the conversion of superoxide into oxygen and hydrogen peroxide in the active site, where Cu^{2+} is bound (Valentine, Doucette & Zittin Potter, 2005). The reactions include:

$$E Cu^{2+} \; + \; {}^{\bullet}O_2^{-} \quad \leftrightarrow \quad E Cu^{2+} {-} {}^{\bullet}O_2^{-} \qquad\qquad \text{Eq 1.1}$$

$$ECu^{2+}\!\!-\!{}^{\bullet}O_2{}^- \quad \rightarrow \quad ECu^+ \ + \ O_2 \qquad\qquad\qquad \text{Eq 1.2}$$

$$ECu^+ \ + \ {}^{\bullet}O_2{}^- \quad \leftrightarrow \quad ECu^+\!\!-\!{}^{\bullet}O_2{}^- \qquad\qquad\qquad \text{Eq 1.3}$$

$$ECu^+\!\!-\!{}^{\bullet}O_2{}^- \quad + \quad 2H^+ \rightarrow \quad ECu^{2+} \ + \ H_2O_2 \qquad\qquad \text{Eq 1.4}$$

$$\text{(Overall)} \ 2\,{}^{\bullet}O_2{}^- \ + 2H+ \quad \rightarrow \quad O_2 \ + \ H_2O_2 \qquad\qquad\qquad \text{Eq 1.5}$$
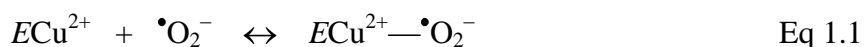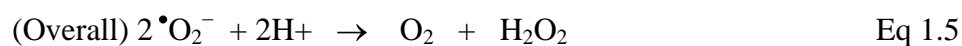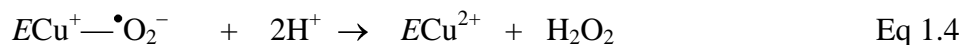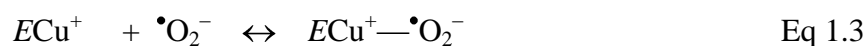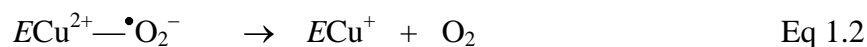
where E represents the enzyme with bound Zn^{2+}. First, the substrate is delivered to Cu^{2+} (Eq 1.1) then the Cu^{2+} becomes reduced to Cu^+ through transfer of one electron from superoxide (Eq 1.2). Reduction of the Cu ion changes the Cu binding site geometry from a distorted square pyramide to a nearly trigonal planar orientation. This involves protonation of His 63 which no longer coordinates Cu^+ (Banci *et al*, 2002), and release of the water molecule involved in copper binding from the active site (for reviews see (Miller, 2004; Valentine, Doucette & Zittin Potter, 2005)). In the other half of the reaction, the Cu^+ is reoxidized when a second superoxide molecule is reduced and takes up two protons to form hydrogen peroxide (Klug *et al*, 1972). Therefore overall O_2 and H_2O_2 are produced from two superoxide molecules reacting with two protons at the SOD1 active site. The hydrogen peroxide formed in this reaction can be disproportioned into water and oxygen by other enzymes including peroxiredoxins, catalase, and glutathione peroxidases (Rhee *et al*, 2005). The observed dismutation of superoxide is a first order reaction with respect to the concentration of superoxide. Therefore, the reactions shown in Eq 1.2 and 1.4 are effectively irreversible as written. The first reaction (Eq 1.1) is rate limiting and occurs with a rate constant of $\sim 2 \times 10^9 \ M^{-1}s^{-1}$. In other words, the dismutation of superoxide by SOD1 is

limited by the diffusion of superoxide into the SOD1 active site (Getzoff *et al*, 1992b; Getzoff *et al*, 1983; Klug, Fridovic.I & Rabani, 1972).

It has been proposed that the conserved, positively charged residues in the electrostatic loop (loop VII) promote enzyme-substrate interaction by attracting the negatively charged superoxide substrate to the highly positive catalytic binding site at the bottom of the active site channel (Getzoff *et al*, 1992b; Getzoff *et al*, 1983). These conserved residues include Lys 136, Glu 132, Glu 133, and Arg 143. Lys 136 and Glu 132 direct the long range approach of superoxide by forming a hydrogen bonding network while Glu 133, located close to the substrate binding pocket between Thr 137 and Arg 143, plays a role in positioning the substrate and preventing other anions from entering the binding pocket (Getzoff *et al*, 1992b; Getzoff *et al*, 1983).

1.1.4 SOD Metallation

The intracellular concentration of free copper has been proposed to be less than one free copper ion per cell (Rae *et al*, 1999), which suggests that copper is not inserted into metalloenzymes from an intracellular pool of free copper ions. This theory is further supported by the fact that free copper ions are cytotoxic (Rae *et al*, 1999). The involvement of a copper metallochaperone for the *in vivo* copper insertion into SOD1 was first discovered by Lyons *et al.* in 1998 (Lyons *et al*, 1998), in which the studying yeast mutants lacking LYS7 expressed a form of SOD1 that contained a single zinc ion per dimer of SOD1 . After this discovery, the human <u>c</u>opper <u>c</u>haperone for <u>S</u>OD1, CCS, was quickly cloned and

identified (Culotta *et al*, 1997). It is worth noting that additional copper chaperones have been identified, including COX17 for delivery of copper to mitochondrial proteins, and cytochrome oxidase, HAH, and ATOX1 for copper delivery to the Golgi (for a review see (O'Halloran & Culotta, 2000)).

The largest copper metallochaperone identified to date, CCS, folds into three domains (Lamb *et al*, 1999; Schmidt *et al*, 1999a) and delivers a single copper ion. The first domain (domain I) of CCS is near the N terminus and has a copper binding site, while the central domain (domain II) of CCS is homologous to its target protein, the SOD1 monomer, and facilitates interaction with SOD1 during copper insertion (Casareno *et al*, 1998; Hall *et al*, 2000; Schmidt *et al*, 1999b). The C terminal domain III of CCS is highly conserved among CCSs from different species and is positioned close to the N terminal domain I, such that these two domains can bind a copper ion together (Lamb *et al*, 1999).

A recent study proposed mechanistic details of CCS involvement in Cu insertion and intramolecular disulfide bond formation during SOD1 maturation (Furukawa *et al*, 2004). Upon copper binding, CCS undergoes a conformational change in order to bind SOD1 with a higher affinity (Lamb *et al*, 1999). The Cu-bound CCS and a disulfide reduced, Zn bound monomer of SOD1 form a heterodimer through interaction of domain II. In this state, Cu^+ is coordinated by two Cys residues in domain III and two Cys residues (C57 and C146) in SOD1, which replace the ligands from CCS domain I. In the next step, O_2 attacks the Cu^+ ion bound to the CCS-SOD1 complex, resulting in formation of an intermolecular disulfide bond between CCS and C57 of SOD1. Additionally, the oxidation of Cu^+ (*i.e.,* formation of Cu^{2+}) occurs and Cu^{2+} is transferred into the active site of the SOD1. Next, C57 in SOD1

13

forms an intramolecular disulfide bond with C146 and subsequently the oxidized monomer with bound Cu^{2+} and Zn^{2+}, which was bound at the outset of the reaction, is released from the CCS. Due to the proper positioning of the dimer interface residues as a result of disulfide bond formation and metallation, the monomers released from CCS will readily form dimers. The proposed mechanism for the Cu insertion of SOD1 has been widely accepted, but it should be noted that other mechanisms may also occur (*e.g.,* with no bound Zn (Furukawa, Torres & O'Halloran, 2004)). In addition, an alternative mechanism for activating SOD1 in the absence of CCS is also proposed, in which the reduced form of glutathione (GSH) plays a key role for the insertion of copper ions (Carroll *et al*, 2004). However, it remains unclear whether or not the copper-binding process requires zinc-bound SOD1 monomers.

1.2 Amyotrophic lateral sclerosis

Amyotrophic lateral sclerosis (ALS) is a term used to cover the spectrum of neurodegenerative syndromes characterized by fatal and progressive muscular paralysis resulting from the degeneration of motor neurons in the primary motor cortex, brainstem and spinal cord (Boillee *et al*, 2006a; Wijesekera & Leigh, 2009). The features of ALS were first described by French neurologist Dr. Jean Martin Charcot in 1869 (Charcot & Joffoary, 1869). Because of this, ALS is more commonly called Charcot's disease in Europe. In North America, it is more commonly known as Lou Gehrig's disease, after the American baseball player who developed the disease in the 1930's. Approximately two thirds of patients with typical ALS show symptoms related to muscle weakness in the upper and lower

14

limbs. Most patients go on to develop bulbar symptoms and eventually respiratory failure (Wijesekera & Leigh, 2009).

ALS occurs in sporadic (sALS) and familial (fALS) forms. The incidence of sALS in the 1990's was close to 1.9 per 100,000 people in North America. Typically, males are affected more than females, with a ratio about 1.5:1, suggesting that some hormones may affect ALS (Worms, 2001). The mean age of onset for sALS has been reported to be between 55-65 years. Most cases of ALS are sporadic while the remaining ~10% have a genetic component (fALS), which is characterized by high penetrance and an autosomal dominant pattern of inheritance (Wijesekera & Leigh, 2009) . Importantly, sALS and fALS are clinically indistinguishable, implicating similar disease mechanisms (Boillee, Vande Velde & Cleveland, 2006a). Geographically, Western Pacific countries have 50 − 100 times higher prevalence of ALS than the rest of the world. These countries include Guam and Marianas Islands (Steele & McGeer, 2008). A recent review suggests that smoking may be an exogenous risk factor associated with development of ALS, while other factors such as occupation are not related to prevalence of ALS (Sutedja *et al*, 2007).

1.2.1 Human ALS neuropathology

Generally, sALS and fALS share a common essential pathological feature, which is the loss of both upper and lower motor neurons. Analysis of the affected motor neurons shows that they contain inclusions in the perikarya, dendrites, and axons that are characteristic of sALS and fALS (see below). These inclusions are complex structures that contain a number

of different proteins (Kato, 2008). From this observation, one can expect the toxic mechanisms that give rise to ALS to also be complex. However, the reasons why differing inclusions (see below) arise and how they are related to disease development remain unclear. The following sections describe the differences and the components within each characteristic inclusion found in sALS and fALS patients.

1.2.1.1 sALS neuropathology

Bunina bodies, skein-like inclusions (SLIs) and round hyaline inclusions (RHIs) are characteristic inclusions of sALS. Bunina bodies are small inclusions (1-3 µm in diameter) and appear either as a single inclusion or arranged in small beaded chains. It is important to note that Bunina bodies are never reported in SOD1-associated fALS and transgenic mice models expressing SOD1 mutants (for a review see (Kato, 2008)). SLIs and RHIs are filamentous and granular structures, and it has been hypothesized that SLIs evolve to form RHIs. Both inclusions stain positively for ubiquitin, but negatively for phosphorylated neurofilaments (NFs) and SOD1s (Kato, 2008; Kato *et al*, 1996). It is important to note that there are some sALS cases where SOD1 was detected in inclusions that resembled Lewy body-like hyaline inclusions (Shibata *et al*, 1996; Shibata *et al*, 1994).

1.2.1.2 SOD1-associated fALS neuropathology

The inclusions in SOD1-associated fALS are characterized as Lewy body-like hyaline inclusions (LBHIs) in motor neurons and hyaline inclusions in astrocytes (Ast-HIs). Both

16

inclusions are highly immunoreactive to SOD1, NF and ubiquitin, (Kato, 2008; Kato *et al*, 1997; Kato *et al*, 2000; Kato *et al*, 1999; Kato *et al*, 2001; Shibata *et al*, 1994). Also, both WT and mutant SOD1 are detected in the inclusions of fALS patients (Bruijn *et al*, 1998). The structure of LBHIs and Ast-HIs are described as 15-25 nm granule-coated fibrils that are occasionally blended with NF. In addition to LBHIs, the NF conglomerate is another characteristic inclusion in SOD1-associated fALS, which is less common in patients with sALS (Ince *et al*, 1998). In a previous study, immunohistochemical analysis using various antibodies revealed that the LBHIs and Ast-HIs are composed of a mixture of different proteins, including synaptophysin, neuron-specific enolase, and astrocyte-specific proteins such as αβ-crystallin, metallothionein, glutamine synthetase, and S-100 protein. Furthermore, the modification of SOD1 with advanced glycation end product (AGE) is identified in inclusions. It is worth noting that AGE is considered as cytotoxic, owing to the fact that it prevents protein digestion systems such as ubiquitination and lysosomal degradation (Kato *et al*, 2001). These results suggest that cellular defense mechanisms are closely involved in fALS toxicity.

1.2.2 Pathogenesis in ALS

The exact molecular mechanism causing motor neuron degeneration in ALS is unknown; however, a number of factors, described in the following section, are likely to be involved in pathogenic pathway(s); these factors may not be mutually exclusive.

1.2.2.1 Genetic factors

Several mutations leading to ALS-like motor neuron diseases have been identified and the cases have been classified as ALS1 to ALS8 (Boillee, Vande Velde & Cleveland, 2006a). The primary known cause of ALS1, typically called ALS (from the next section onwards, ALS refers to ALS1), is mutation in the SOD1 gene located on chromosome 21, which accounts for ~ 20 % of all cases of fALS (Boillee, Vande Velde & Cleveland, 2006a). The effect of SOD1 mutants on ALS will be discussed further in section 1.3.

Genes responsible for other ALS cases have also been identified. These mutations are located on various chromosomes. Mutations in the genes responsible for ALS2, ALS4, and ALS5 cause severe juvenile ALS. Although mutations linked to ALS1 to ALS8 have been identified, only some of the encoded proteins and their functions have been characterized. Briefly, SOD1 for ALS1, Tau protein for ALS with frontotemporal dementia coupled with Parkinson's disease (ALS-FTDP) and vesicle-associated membrane proteins B (VAPB) for ALS8, are a few of the proteins that have been identified. Whether loss of function by mutation for ALS-associated proteins, except for SOD1 (see below for details), is the cause of toxicity is not clear at this time (for reviews see (Boillee, Vande Velde & Cleveland, 2006a; Bruijn *et al*, 2004)).

1.2.2.2 Mitochondrial dysfunction

Mitochondrial damage is a common feature of many neurodegenerative diseases, including ALS (Boillee, Vande Velde & Cleveland, 2006a). sALS patients show abnormalities in mitochondrial function (Siklos *et al*, 1996; Wiedemann *et al*, 1998) as well

as show an accumulation of mutations in mitochondrial DNA (Ro *et al*, 2003). Furthermore, SOD1 transgenic mice models of ALS show vacuolated mitochondria within spinal motor neurons very early in the disease development (Dalcanto & Gurney, 1994; Kong & Xu, 1998; Wong *et al*, 1995a). Moreover, vacuolated mitochondria have been proposed to result from expansion of the mitochondrial intermembrane space due to aggregation of SOD1 mutants (Higgins *et al*, 2003). Thus, mitochondrial damage may be an important component in the toxic mechanism of ALS. However, the idea that vacuolated mitochondria are a pathological feature in the disease development has been disputed because mice models expressing WT SOD1 do not develop the disease but show vacuolated mitochondria. Additionally, other mice models with SOD1 mutations develop the disease without vacuolated mitochondria (for a review see (Boillee, Vande Velde & Cleveland, 2006a)). However, there is further evidence suggesting that mitochondria are involved in disease development. Mitochondria play a key role for neuronal death because cytochrome *c*, which activates the cascade of apoptosis is released through the permeability transition pore. To support this notion, Caspase-3 was found to be responsible for the final apoptotic mechanism in mutant SOD mice models, implying a role of mitochondrial apoptosis activation (Li *et al*, 2000). Interestingly, a recent study found that caspase-3 activation inactivates the glutamate transporter EAAT2, which can lead to excitotoxicity (Boston-Howes *et al*, 2006) (excitotoxicity will be discussed as a disease mechanism in section 1.2.2.5). Taken together, mitochondrial damage may be an important factor in the progression of some ALS cases, but further studies are required before a clear connection between the damage of mitochondria and ALS can be made.

1.2.2.3 Impaired axonal transport

Motor neurons have a very distinctive shape that is different from other cell types: extreme asymmetry (up to one meter long) and large volume (up to 5000 times that of a typical cell) (Boillee, Vande Velde & Cleveland, 2006a). Impaired axon transport appears to be a common pathological features in ALS, supported by the observation of alterations in axonal structure in both sALS and fALS (Hirano *et al*, 1984) and in mice models (Bruijn *et al*, 1998). Importantly, SOD1 transgenic mice models of ALS show evidence of impaired axonal transport months prior to disease onset (Williamson & Cleveland, 1999), implying that impaired axonal transport is an early event in the disease process.

1.2.2.4 Astrocytes and excitotoxicity

Astrocytes have been suggested to play a significant role in the pathogenesis of the disease, since histopathological features of fALS include astrocyte inclusions ((Kato, 2008; Kato *et al*, 1997; Kato *et al*, 2000; Kato *et al*, 1999; Kato *et al*, 2001; Shibata *et al*, 1994) and references in (Kato, 2008)). There are many studies to support the involvement of astrocytes in ALS. When SOD1 mutants are expressed exclusively in either motor neurons (Lino *et al*, 2002) or in astrocytes (Gong *et al*, 2000) of ALS mice models, the mice do not show degeneration of motor neurons. Furthermore, when the mutant SOD1 is expressed in motor neurons which are surrounded by astrocytes expressing WT SOD1, the ALS-affected mice have an extended lifespan, whereas when motor neurons with WT SOD1 are surrounded by

astrocytes with mutants of SOD1, motor neuron damage is accelerated (Clement *et al*, 2003). Therefore, communication between motor neurons and astrocytes may be an important component of ALS toxicity, although the expression level of mutant SOD1 may affect the sensitivity of these results (Van Den Bosch & Robberecht, 2008). This hypothesis is supported by another study, which showed that the amount of mutant SOD1 in astrocytes is a critical factor in controlling disease duration (Boillee *et al*, 2006b). Another study proposed that astrocytes can be a source of extracellular mutant SOD1 to trigger microgliosis and eventually motor neuron death (Urushitani *et al*, 2006). This neural death is thought to result from the mutants of SOD1 co-localizing with components of neurosecretory vesicles from asctrocytes (Urushitani *et al*, 2006). These results reinforce the hypothesis that an interaction between motor neurons and astrocytes is a significant contributor to the disease.

Generally, a major role of astrocytes is to protect motor neurons by providing neurotrophic factors and maintaining extra-neural concentrations of glutamate by scavenging glutamate using a glutamate transporter such as EAAT2 (Van Den Bosch & Robberecht, 2008). High concentration of extra-neuronal glutamate may lead to motor neuron death by over-stimulating the glutamate receptor; this event is called excitotoxicity (Van Den Bosch *et al*, 2006). It is likely that excitotoxicity is involved in ALS because of the reduced density of EAAT2 detected in both sALS and fALS (Shaw *et al*, 1994). Taken together, there is strong evidence that non-cell autonomous processes and excitotoxicity contribute to ALS, even though a detailed mechanism describing ALS toxicity must still be elucidated.

1.3 SOD1 in ALS

Mutation in the gene for SOD1 is the most common known cause of ALS and is by far the most studied. Since 1993, when Rosen *et al*. discovered a link between SOD1 mutations and fALS (Rosen, 1993), over 140, mainly missense, mutations in the SOD1 gene have been reported to cause fALS (Turner & Talbot, 2008) (Fig.1.3). These disease-associated mutations are located throughout the protein structure including the dimer interface and metal binding sites (Valentine, Doucette & Zittin Potter, 2005). The structural diversity of fALS-associated mutations in SOD1 suggests that this disease occurs as a result of a general toxic mechanism, but not a site-specific mechanism. Most mutants exhibit a dominant pattern of inheritance, with the exception of N86S, D90A, and D96N. Furthermore, individuals with fALS-associated SOD1 mutations are heterozygous and exhibit a disease onset and duration that is characteristic of each mutation (Table 1.1) (Turner & Talbot, 2008). However, even affected families show variability in disease onset and severity.
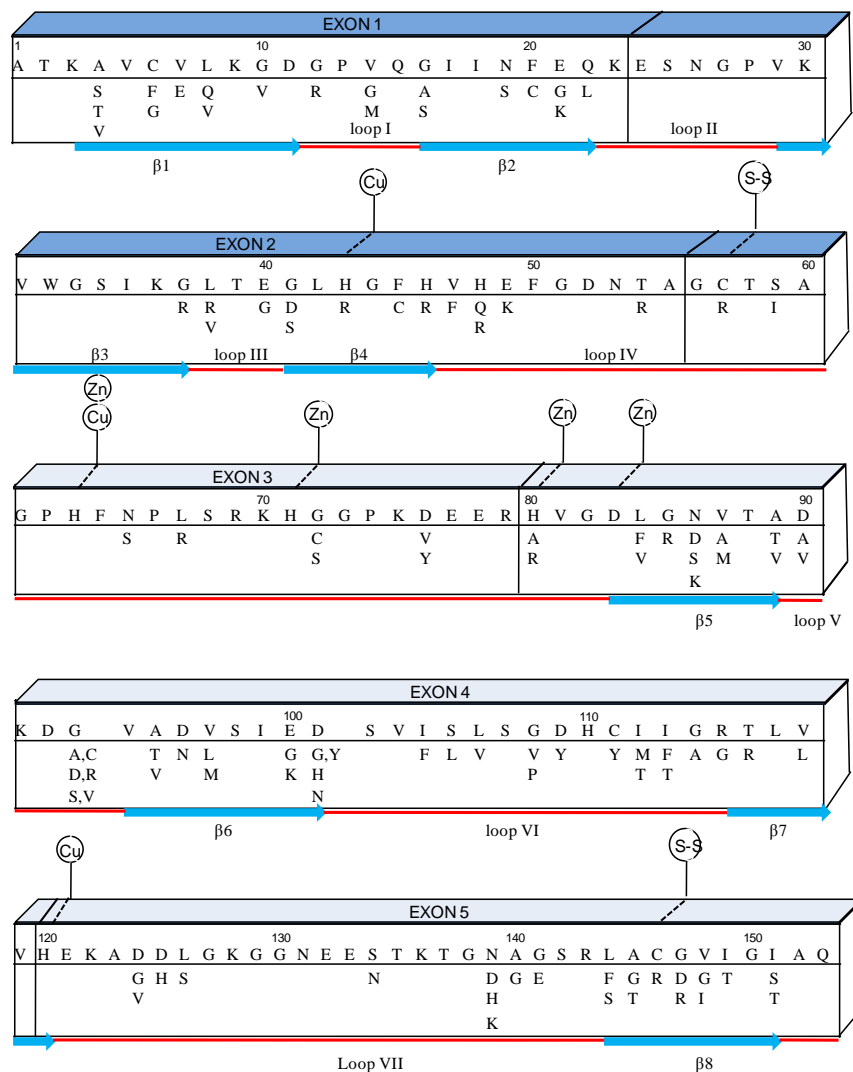
Figure 1.3 ALS-associated point mutations in hSOD1

Schematic diagram of the hSOD1 primary sequence with exons. The 8 β strands and 7 loops
are shown with Roman numerals. The metal binding residues (Cu and Zn), intramolecular
disulfide bond, and mutations linked to fALS are also indicated
(http://alsod.iop.kcl.ac.uk/misc/sod1MutationsDiagram.aspx). Insertion, deletion and silent

mutations represent a small fraction of ALS-associated mutations in SOD1, thus they are not shown here, but can be found at (http://alsod.iop.kcl.ac.uk/misc/sod1MutationsDiagram.aspx).

Table 1.1 Disease duration and age of onset for selected[a] fALS-associated SOD1 mutants and sALS patients[b]

mutant	average duration[c] (# of patients)	average onset[c] (# of patients)
A4S	< 3 (0)	34 (1)
A4T	0.5 (21)	45.3 (26)
A4V	1.2 (205)	47.7 (212)
H43R	1.8 (12)	49.3 (14)
H46R	17.6 (49)	45.6 (70)
H48Q	1.2 (4)	43.6 (4)
G85R	6.0 (11)	55.5 (11)
G93A	3.1 (16)	46 (15)
G93D	8.8 (7)	39.3 (10)
G93S	8.6 (11)	51.6 (15)
G93V	6.0 (2)	46.0 (3)
I113T	4.3 (38)	56.3 (43)
I149T	2.7 (15)	37.6 (14)
SALS	2.5 (269)	58.4 (359)

[a] The selected mutants are based on the ones characterized in this thesis, which are described in chapter 2 and 3.

[b] The information in Table 1.1 is from Wang et al. (Wang *et al*, 2008) as well as the references therein.

[c] Units for average duration and average disease onset are years.

1.3.1 Oxidative stress vs. Protein aggregation

The initially proposed pathogenic mechanism of fALS-associated SOD1 mutants was loss of the superoxide detoxifying activity. However, a number of studies have shown that the simple loss-of-function does not result in motor neuron death. Firstly, SOD1 knockout mice do not develop the disease (Reaume *et al*, 1996). In addition, the mice models expressing mutants of SOD1 with varying activity levels, including similar to wild-type, develop comparable disease pathologies to those seen in fALS patients (for a review see (Kato, 2008)). Taken together, a gain of toxic function by mutation, not a loss of function, is thought to be responsible for the disease. Two main hypotheses have been put forward to explain how fALS-associated SOD1 mutants may confer toxicity to the affected neural cells. The first suggests that aberrant copper-dependent oxidative damage occurs and causes motor neuron degeneration, while the second hypothesis proposes that SOD1 aggregation is the cause of toxicity. The following sections discuss each hypothesis in detail.

1.3.1.1 Aberrant copper-dependent oxidative chemistry

Extensive research indicates that oxidative stress plays an important role in ALS (Simpson *et al*, 2003). Transgenic mice expressing SOD1 disease mutation G93A show enhanced levels of free radicals in the spinal cord (Liu *et al*, 1998). Furthermore, the levels of oxidatively damaged proteins in G93A mice models are twice as high as the levels found in the age matched control (Andrus *et al*, 1998). The toxic reactions are proposed to be

mediated by Cu^{2+} bound to the mutants in which the active site is "loosened" and so can more easily catalyze aberrant reactions. In other words, abnormal substrates have easier access to the active site in mutants of SOD1 where they can react with Cu^{2+}. The products from the Cu-mediated aberrant chemistry can then damage amino acid residues near the Cu binding sites in SOD1 (see below for details).

Three harmful and abnormal substrates for SOD1 have been proposed: nitric oxide (NO), peroxynitrite (OONO$^-$) and hydrogen peroxide (H_2O_2). Nitric oxide (NO) is produced by nitric oxide synthase to help modulate synaptic plasticity by interneurons that surround motor neurons (Valtschanoff *et al*, 1992) and is also produced as a response to neuron injury (Wu *et al*, 1995). SOD1 mutants with disruptions in their active site pockets (*e.g.,* A4V) can allow greater access of nitric oxide (NO) to the active site (Beckman *et al*, 1993; Estevez *et al*, 1999). The nitric oxide (NO) can react with superoxide more rapidly than the Cu^{2+} bound to the active site (Huie & Padmaja, 1993). Peroxynitrite (OONO$^-$) is formed by the reaction between nitric oxide (NO) and superoxide in the active site or freely in cytosol. The peroxynitrite (OONO$^-$) formed in the SOD1 active site can react with the Cu^{2+} bound to the active site, resulting in nitration of tyrosine residues (Beckman, 1996; Beckman *et al*, 1992). This hypothesis is strongly supported by the identification of increased levels of *free* 3-nitrotyrosine in mice models as well as sALS and fALS patients, although there is no evidence of increased levels of nitrotyrosine bound to proteins in ALS (Abe *et al*, 1995; Bruijn *et al*, 1997a; Chou *et al*, 1996; Ferrante *et al*, 1997; Strong *et al*, 1998). Moreover, Zn-deficient SOD1s, including mutants as well as WT, show much faster reactions between peroxynitrite (OONO$^-$) and Cu^{2+}, resulting in apoptosis in cultured motor neuron cells

(Estevez *et al*, 1999). Therefore, Estevex *et al.* proposed Zn-deficient SOD1 (*i.e.,* aberrant copper-dependent oxidative chemistry) as the critical species in the disease. However, there is reason to question whether this mechanism describes the primary event in the neuron cell death pathway in all ALS, because survival of ALS-affected mice is independent of nitric oxide synthase expression, even though peroxynitrite related toxicity should be dependent on nitric oxide (NO) and therefore on nitric oxide synthase. This suggests that aberrant copper-dependent oxidative chemistry cannot be the only critical component of disease pathology (Son *et al*, 2001).

Hydrogen peroxide has been proposed as another harmful abnormal substrate for SOD1. The interaction of bovine SOD1 (bSOD1) with hydrogen peroxide can induce enzyme inactivation *in vitro via* rapid reduction of Cu^{2+} by hydrogen peroxide. Furthermore, the reduced Cu ion (Cu^+) and hydrogen peroxide can generate harmful hydroxyl radicals *via* a Fenton reaction mechanism (Hodgson & Fridovich, 1975). fALS-associated mutants also show a greater ability to produce hydroxyl radicals. (WiedauPazos *et al*, 1996). The hydroxyl radicals can react with copper ligands (His 46, His 48, and His 120 as well as Pro 62, which is adjacent to His 63) *in vitro*, resulting in oxidation of these amino acids at the active site of SOD1 (Kurahashi *et al*, 2001; Uchida & Kawakishi, 1994). There is, however, no evidence for enhanced production of hydroxyl radicals throughout the disease progression in fALS mice models.

Although aberrant copper-dependant oxidative chemistry has been extensively studied and proposed to be the underlying toxic mechanism through which fALS-associated mutants of SOD1 cause the disease, there is significant *in vivo* result that disputes this claim.

First of all, mutant SOD1 that lack all four copper coordinating His residues still cause progressive motor neuron degeneration, indicating that the disease is developed without the copper-mediated reaction discussed above (Wang *et al*, 2003). In addition, transgenic mice lacking CCS in motor neurons show no difference in onset and progression of the disease, even though the mice show a significant reduction in the amount of properly copper loaded mutant SOD1 (Subramaniam *et al*, 2002). These two observations suggest that an alternative mechanism must exist to give rise to the gain-of-toxic function seen in ALS, discussed next.

1.3.1.2 Protein aggregation

Protein aggregation has been implicated in the pathogenesis of many different neurodegenerative diseases including Alzheimer's, Parkinson's, Huntington's, and prion disease (Chiti & Dobson, 2006; Ross & Poirier, 2004). Similarly, SOD1-containing aggregates have been found in sALS and fALS patients (Kato *et al*, 2001; Okamoto *et al*, 1991; Shibata, Asayama, Hirano & Kobayashi, 1996; Shibata *et al*, 1994) and ALS-SOD1 transgenic mice models (for reviews see (Kato, 2008; Turner & Talbot, 2008)). However, whether protein aggregation itself is toxic or a harmless byproduct of oxidative damage has been debated. Several lines of evidence support the theory that a gain-of-toxic function arises as a result of a mutation in SOD1, which predisposes the protein to form toxic aggregates. In support of this theory, it has been found that high molecular weight complexes containing mutant SOD1 are detectable in spinal cord extracts from transgenic mice before motor neuron pathology is apparent (Johnston *et al*, 2000). Additionally, a recent study investigated the appearance and abundance of mutant SOD1 aggregates

throughout the disease course in SOD1 fALS mice models (G93A, G37R and H46R/H48Q) (Karch *et al*, 2009). This work reported that small aggregates (*e.g.,* soluble oligomers) form in the early stages of the disease but larger aggregates of mutant SOD1 form primarily in the later stages of the disease, concurrent with the appearance of rapidly progressing symptoms (Karch *et al*, 2009). Taken together, small aggregates of mutant SOD1, rather than large and mature aggregates, appear to be more toxic. However, the mechanisms that connect SOD1 aggregation to motor neuron toxicity still remain unknown. There are various hypotheses to explain the toxicity of aggregation including: aggregate-mediated inhibition of the proteasome machinery; impaired chaperone activity; and deregulation of organelle function such as mitochondria, and microglia (Boillee, Vande Velde & Cleveland, 2006a). Each hypothesis is discussed in detail.

Misfolded proteins are targeted for disposal *via* the proteasome. Therefore, the proteasome machinery can be adversely affected by accumulation of ubiquitinated and/or misfolded proteins. In the case of ALS, ubiquitinated proteins have been confirmed as part of the inclusions found in patients (see section 1.2.2), implicating that impaired proteasomal machinery is prominent in ALS. More specifically, the insoluble forms of mutant SOD1 in the spinal cords of G93A mice models clearly show both mono- and oligo-ubiquitinated proteins (Basso *et al*, 2006). Additionally, Dorfin, a RING finger type E3 ubiquitin ligase, is an abundant component in inclusions in both fALS and sALS (Niwa *et al*, 2002). Furthermore, Dorfin enhances degradation of mutant SOD1, but not WT, *in vitro*, and overexpression of Dorfin (Niwa *et al*, 2002) protects against motor neuron degeneration and reduces the levels of intracellular protein inclusions. While proteasome malfunction has

been implicated in motor neuron death, contradictory results have been reported; Shaw *et al.* found that the most abundant proteins recovered from aggregates in transgenic mice models were full length unmodified (*i.e.,* no ubiquitination) SOD1 polypeptides (Shaw *et al*, 2008). Misfolded and aggregates of SOD1 can also interact improperly with folding chaperones, abolishing their normal functions. In fact, inclusions from sALS and fALS patients, and transgenic mice models, have been shown to contain CCS (Watanabe *et al*, 2001), Hsp 70 (Watanabe *et al*, 2001) and Hsp 25 (Wang *et al*, 2003). Thus, it can be postulated that mutants of SOD1 may devastate the cells' defense mechanism through diminishing the protective effects of the proteasome and chaperone mechanisms, thereby causing the disease.

There is growing evidence that SOD1 mutants cause ALS by interfering with a different cell type and organelles, the mitochondria (Velde *et al*, 2008) and microglia (Urushitani *et al*, 2006). Misfolded SOD1 has been found to be associated with the cytoplasmic face of the outer mitochondrial membrane in spinal cord tissues, but not other tissues, of mice models (Sturtz *et al*, 2001). Velde *et al.* proposed that the mutant proteins bound to mitochondria might be responsible for the malfunction of protein import, ionic homeostasis, mitochondrial mobility, mitochondrial fission/fusion, or mitochondrial regulation of apoptosis (Sturtz *et al*, 2001). However, detecting misfolded SOD1 in mice models may have limited relevance to disease because the mice models have a higher possibility of containing mismetallated or misfolded proteins due to overexpression of SOD1 and insufficient amounts of CCS for full metallation, for example, G93A mice (either 25 copies (Gurney, 1997) or 8 copies (Chiu *et al*, 1995)), G37R (12 copies) (Wong *et al*, 1995b), and G85R (between 2 and 15 copies) (Bruijn *et al*, 1997b). Additionally, there is

significant experimental evidence to indicate that WT and mutant SOD1 can be secreted through secretory pathways in the transgenic mice models, even though SOD1 is a cytosolic protein without a specific translocation sequence (Turner *et al*, 2005; Urushitani *et al*, 2006). The extracellular SOD1 mutant may trigger microgliosis, which can lead eventually to motor neuron death (Urushitani *et al*, 2006).

There has been significant research on the topics of protein aggregation and oxidative damage in ALS. As seen above, neither mechanism can completely explain the toxic mechanism of SOD1 mutations. Current research indicates that the two hypotheses may not be mutually exclusive, because there is evidence to show that oxidative damage to SOD1 enhances aggregation of the protein (Rakhit *et al*, 2002), and that aggregates from patients contain oxidative modifications (Kato *et al*, 2000). Thus, further research should consider both possible toxic mechanisms.

1.4 Protein misfolding and aggregation

1.4.1 Protein folding

Following synthesis on the ribosome, each polypeptide must fold into its native conformation in order to enable properly function. Often *in vivo* the protein folding process is aided by a variety of chaperones (Hinault *et al*, 2006). However, a polypeptide can also reach its correctly folded structure *in vitro* in the absence of any chaperones under appropriate conditions, suggesting that the primary amino acid sequence contains the folding information (Anfinsen, 1973). In order to achieve the native state, a protein must find a

pathway to the correctly folded structure, rather than one of the countless alternatives, because it would take an infinite amount of time for even a small polypeptide to search all possible conformations, yet real proteins can fold into the native state within 1 sec (Karplus, 1997). The concept of an energy landscape has emerged in attempt to describe protein folding pathways (Bryngelson *et al*, 1995). In this approach, the unfolded state of a given peptide folds along an energy landscape towards the compact native state (Fig 1.4). As the size and complexity of the protein increases, so does the complexity of the folding process. Therefore, intermediates with partially formed structures can be populated and have significant life times. Additionally, during the search for the stable native conformation between residues, non-native interactions may take place, which is generalized by the term "misfolding". *In vivo*, molecular chaperones can provide some protection for these undesired events (Hinault, Ben-Zvi & Goloubinoff, 2006). Nevertheless, misfolded or partially folded species that arise in the cell can participate in further undesired events (*e.g.,* aggregation) that can cause diseases. Indeed, an increasing number of diseases are linked to protein misfolding and aggregation (see Table 1.2 for selected examples). Thus, in recent decades, many researchers have been making efforts to understand protein folding, misfolding, and aggregation *in vivo* and *in vitro*.
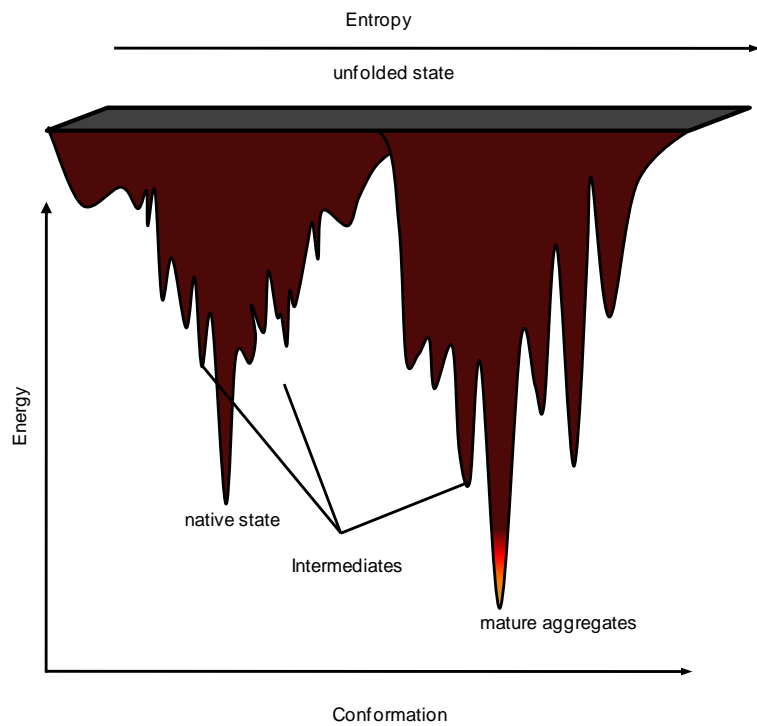
Figure 1.4 Schematic diagram of a folding and aggregation energy landscape

The surface represents a multitude of conformational states during folding of a polypeptide into its native conformation, or partially folded intermediates and soluble oligomers that lead to aggregate formation. The lowest energy states in the protein folding (left) and protein aggregation (right) pathways are the native state and mature aggregates (*e.g.,* amyloid), respectively.

Table 1.2 Protein misfolding diseases [a]

Human Disease	Protein Involved
Cystic fibrosis	cystic fibrosis transmembrane regulator
Sickle cell anemia	hemoglobin
Alzheimer's disease	β amyloid
Spongiform encephalopathies	prion protein
Familial amyloidoses	transthyretin or lysozyme
Parkinson's disease	α-synuclein
Huntington's disease	Huntingtin
Cataracts	crystallin
ALS	SOD1
Cancer	P53

[a] Table 1.2 is modified from Thomas *et al.*(Thomas *et al*, 1995) and Dobson (Dobson, 2001b) .

1.4.2 Amyloid and human diseases

A significant number of proteins readily fold into not only their native structures but also have the ability to fold into an alternative structure, known as amyloid (Jahn & Radford, 2008b). Thus, an energy landscape should also include the unfolding pathways that lead to aggregate formation, thereby connecting unfolding/aggregation pathways to the native protein folding pathways (Fig. 1.4). A given protein can maintain its native structure most of the time in a living cell because the kinetic barrier associated with partial unfolding provides

protection, even though the aggregated state may be thermodynamically more stable than the native state (Dobson, 2001a). Thermodynamic stability of protein aggregates is typically attributed to increased entropy. The entropy increase is a result of the water molecules that are initially bound to the unfolded protein being released upon aggregation (Oosawa, 1975). The aggregation component of an energy landscape may contain many different species, including amyloid, amorphous aggregates, and soluble oligomers. Their existence is supported by *in vitro* experiments, in which a multitude of aggregate morphologies have been identified simultaneously under the same solution conditions (Jahn & Radford, 2008b).

Many protein misfolding diseases are classified as amyloidoses (Sunde *et al*, 1997). Amyloidosis is defined as a disease involving the extracellular deposition of insoluble protein complexes, amyloid (Tan & Pepys, 1994) (see Table 1.3 for selected examples). Many neurodegenerative diseases are included in Table 1.3. Many of the amyloidoses occur both in sporadic and familial forms. One of the striking characteristics of the amyloid diseases is that protein aggregates possess very similar properties and appearance (Sunde *et al*, 1997). The fibrils are typically smooth and bind the dye, Congo red, and exhibit green-gold birefringence under polarized light. Also, they are composed of very extensive β-sheet structures, in which the β strands are oriented perpendicular to the fibril axis to generate what is described as a cross β structure (Fig. 1.5) (Sunde *et al*, 1997). This commonality of the aggregate structures is very surprising, because the precursor proteins in different diseases do not share sequence homologies or native structures (Jahn & Radford, 2008b). With regards to the toxicity of amyloid, precursor amyloid oligomeric species are found to be substantially more toxic than the mature amyloid (Ross & Poirier, 2004). Support for this is that soluble

35

oligomers of Aβ correlate better with the severity of Alzheimer's disease than insoluble fibrillar deposits (Kuo *et al*, 1996). Additionally, Kayed *et al.* found that an antibody that specifically recognized the oligomeric state of Aβ can neutralize the toxicity of soluble oligomers (Kayed *et al*, 2003). This antibody also recognized other soluble oligomers that formed from a wide variety of amyloidogenic proteins including α synuclein, islet amyloid polypeptide, polyglutamine, lysozyme, insulin and prion peptide (Kayed *et al*, 2003). This finding indicates that amyloid oligomers likely share common structural features regardless of their precursor protein sequences. Therefore, it is possible that amyloidoses can share a common mechanism of toxicity *via* the primary toxic species, the soluble oligomer (Kayed *et al*, 2003).
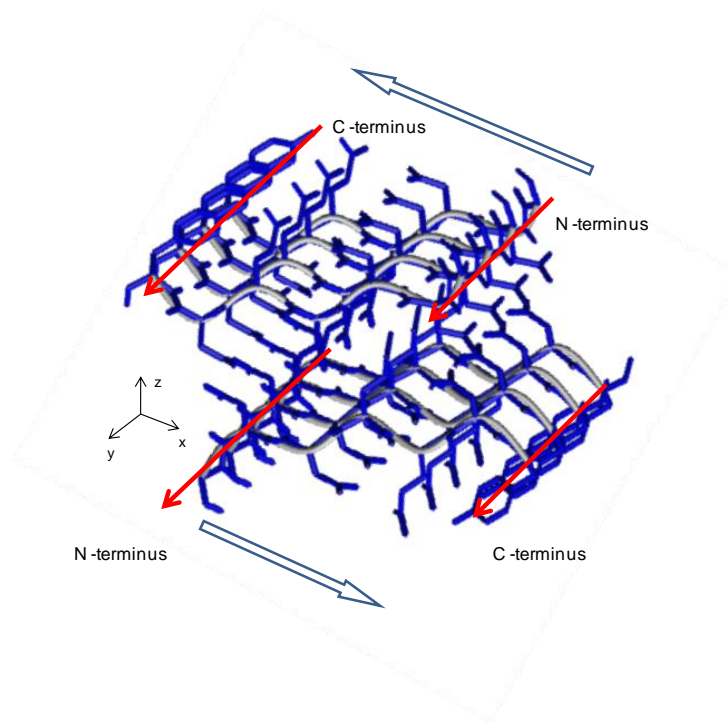
Figure 1.5 Cross-β structure of an amyloid fibril, modeled by the peptide GNNQQNY

A total of 8 peptide molecules in Fig.1.5 form 4 β-sheets. Amyloid fibril grows along the y-axis (red arrow). One peptide from the top layer and one from the bottom layer (stacked along the z axis) form an anti-parallel β sheet. Each β-strand is parallel to the x axis (*i.e.,* β strands run perpendicular to the long axis of the fibril). Side chains are colored blue, and two blue arrows represent the orientation of β strands in the top and bottom layer, respectively. The figure was made using pdb code 1YJP (Nelson *et al*, 2005) in Molmol (Koradi, Billeter & Wuthrich, 1996).

Table 1.3 Human amyloid diseases and their related fibril components [a]

Human Disease	Fibril Components
Alzheimer's disease	Aβ peptide, 1-42, 1-43
Spongiform encephalopathies	full length prion or fragments
Familial amyloidotic polyneuropathy I	transthyretin variants and fragments
Senile systemic amyloidosis	WT transthyretin and fragments
Familial amyloidotic polyneuropathy II	β2 microglobulin
Type II diabetes	fragments of islet-associated polypeptide
Lysozyme amyoidosis	full length lysozyme variants
Parkinson's disease [b]	α-synuclein
Huntington's disease [b]	huntingtin

[a] Table 1.3 is modified from in Sunde *et al.* (Sunde *et al*, 1997).

[b] amyloid formation is involved in the diseases but the deposit is intracellular instead of extracellular.

A great deal of research *in vitro* has been conducted to provide detailed insight into molecular mechanisms for amyloid formation. *In vitro,* amyloid has been generated from disease-related proteins under a range of solution conditions. Additionally, proteins with no known connection to disease, for example apo myoglobin (Fandrich *et al*, 2003a), are also found to be converted into amyloid under appropriate conditions. This finding suggests that amyloid formation can occur under appropriate conditions from any protein (for a review see (Dobson, 2001b)). Furthermore, amyloid formation *in vitro* is promoted by adding seeds (preformed aggregates). For example, mutant-specific cross seeding ability has been shown for prion propagation (Sparrer *et al*, 2000). Strain-specific behavior has been reported, in

which the morphology of final aggregates resemble that of the seeds (Sparrer, Santoso, Szoka & Weissman, 2000).

As for proposed SOD1 aggregate toxicity mechanisms, impaired cellular defense systems against protein aggregation are related to amyloid diseases. For example, prion protein oligomers and α-synuclein protofibrils inhibit the 26S proteasome (Kristiansen *et al*, 2007; Zhang *et al*, 2008). Thus, some research into possible treatment for amyloidoses has focused on decreasing the accumulation of amyloid in the affected tissue or enhancing its clearance using antibodies or small molecules. Using an antibody that recognizes toxic oligomers, a vaccination approach has also been investigated (Holtzman, 2008). Small molecules that can prevent protein unfolding or stabilize partially unfolded species against aggregation have strong potential for therapeutic strategies. Thus, understanding aggregation in more detail and developing ways of controlling aggregation has profound medical implications. Furthermore, understanding protein aggregation can further our knowledge of the physical properties of proteins that facilitate proper folding in normal cellular processes.

1.5 Thesis outline

1.5.1 hSOD1 pseudo wild-type (pWT)

Our lab has been investigating the thermodynamic stability and kinetic stability of SOD1. In all experiments from our lab, a well established pseudo wild-type (pWT) background was used in which the free cysteines at positions 6 and 111 are mutated to alanine and serine, respectively. Using pWT allows us to carry out an accurate

thermodynamic analysis of protein denaturation since it should be fully reversible. Moreover, the pWT has very similar structure, dynamics, stability and activity to wild-type SOD1, but aberrant disulfide bond formation by oxidation of the free cysteines is eliminated (Lepock, Frey & Hallewell, 1990; Parge, Hallewell & Tainer, 1992). All the experiments in this thesis were also performed using pWT in order to make use of accumulating thermodynamic and kinetic data from our lab. Furthermore, recently Borchelt, *et. al.* reported that intermolecular disulfide bond *via* the free cysteines have a minor effect on the disease (Karch *et al*, 2009). This supports the notion that pWT is a valid model to study the pathogenesis of ALS.

1.5.2 Outlines

Aggregation has been emerged as one of the leading hypotheses for the toxic gain of function associated with ALS (Valentine, Doucette & Zittin Potter, 2005). Thus, many research labs have studied the aggregation mechanism of SOD1 (Banci *et al*, 2007b; Chattopadhyay *et al*, 2008; DiDonato *et al*, 2003; Furukawa *et al*, 2008; Khare *et al*, 2004; Oztug Durer *et al*, 2009; Rakhit *et al*, 2002). Nevertheless, toxic aggregation mechanisms remain poorly understood at a molecular level and the diseases have very limited treatment options (Wijesekera & Leigh, 2009). In most studies of protein aggregation, the solution conditions used were quite extreme (*e.g.,* extreme pH or temperature, strongly oxidizing conditions). Aggregation is favoured in such scenarios, making it easier to characterize experimentally; however, the biological relevance is often questionable, or unclear. In

contrast, aggregation under mild, physiological conditions has received very little attention, although such conditions are frequently relevant to disease. All previous studies of aggregation for SOD1 have used either harsh, non-physiological solution conditions, or various immature or aberrant forms of the protein (Banci *et al*, 2007b; Chattopadhyay *et al*, 2008; DiDonato *et al*, 2003; Furukawa *et al*, 2008; Khare, Caplow & Dokholyan, 2004; Oztug Durer *et al*, 2009; Rakhit *et al*, 2002; Stathopulos *et al*, 2003), whereas the native, fully metallated (holo) state of SOD1 has been thought to be unaffected by aggregation due to its very high stability.

Based on preliminary experimental observation on aggregation of holo SOD1, our lab has developed the hypothesis that pathological aggregates of SOD1 do form in complex ways, such that multiple species (*e.g.,* the least stable form of SOD1, reduced apo SOD1 and the most stable form of SOD1, holo SOD1) form mixed aggregates during the disease process. In other words, no single form of SOD1 is responsible for aggregation and global stability is not the only factor of aggregation propensity. This thesis presents an in-depth analysis of holo SOD1 aggregation in pathologically relevant conditions. Structurally and chemically different mutants of SOD1 are used in order to characterize the effects of mutations on the aggregation and elucidate a possible aggregation mechanism.

Chapter 2 will report that SOD1 readily aggregates from the holo state under physiologically relevant conditions. General mechanisms (dimer dissociation and metal loss) of *in vitro* holo SOD1 aggregation and their relevance to *in vivo* aggregation have been elucidated, based on experimental evidence obtained using light scattering, atomic force microscopy (AFM), mass spectrometry, dye binding assay and an ALS specific antibody

assay. These findings have valuable implications for understanding disease mechanisms in ALS and other neurodegenerative diseases, as well as other diseases where aggregation may occur from the native state.

In chapter 3, the aggregation mechanism is further characterized in detail, using methods such as metal content analysis and various spectroscopy techniques including ultraviolet-visible spectroscopy (UV), Fourier transform infrared (FTIR) spectroscopy, circular dichroism (CD) spectroscopy, and fluorescence. Holo SOD1 can lose either more Cu or more Zn ions relative to the other metal during aggregation, resulting in different durations and final intensities of the aggregation profiles. However, the significance of these two aggregations mechanisms needs to be studied further.

Previously, our lab published the effect of sonication on the formation of amyloid, (Stathopulos *et al*, 2004). This finding has significant implications since protein aggregation and amyloid have been implicated in many human diseases, including Alzheimer's Huntington's, Parkinson's and prion disease. Chapter 4 will report further details on the effects of sonication as influenced by cycle settings, temperature, and free radical scavenger. Other types of protein damages (backbone cleavage and non-physiological dimer formation) were investigated using various proteins including bovine serum albumin (BSA), myoglobin, β-lactoglobulin, SOD1, hisactophilin, and lysozyme. These findings provide important evidence of necessity of proper controls when sonication is employed in various fields such as food processing and medical applications.

In chapter 5, general implications of the findings of this thesis, and avenues for future research are considered.

Chapter 2

Pathological aggregation from the holo state of Cu/Zn superoxide dismutase in ALS

2.1 Introduction

Amyotrophic lateral sclerosis (ALS) is a devastating, rapidly progressive, and invariably fatal neurodegenerative disease, characterized by motor neuron degeneration and paralysis (Boillee, Vande Velde & Cleveland, 2006a). Approximately 10% of ALS cases are familial, the remaining cases being sporadic. The familial and sporadic diseases are clinically indistinguishable and so have been proposed to share common disease mechanisms (Boillee, Vande Velde & Cleveland, 2006a). The main known cause of ALS is mutations in SOD1, which accounts for ~20% of familial disease (fALS). It is generally accepted that fALS-linked SOD1 mutations result in a gain of toxic function, rather than a loss of function (Boillee, Vande Velde & Cleveland, 2006a). Recently, much attention has focused on toxic protein aggregation as a cause for ALS, analogous to pathogenic protein aggregation in other neurodegenerative diseases, including Alzheimer's, Huntington's, Parkinson's, and prion diseases (Boillee, Vande Velde & Cleveland, 2006a; Chiti & Dobson, 2006; Kato *et al*, 2001; Shibata, Asayama, Hirano & Kobayashi, 1996; Shibata *et al*, 1994). SOD1 is present in aggregates in motor neurons of SOD1-linked fALS patients (Kato *et al*, 2001; Okamoto *et al*, 1991) and mice models (Johnston, Dalton, Gurney & Kopito, 2000; Karch *et al*, 2009; Kato *et al*, 2001; Rakhit *et al*, 2007; Urushitani *et al*, 2007), and in some sporadic ALS (sALS) patients (Shibata, Asayama, Hirano & Kobayashi, 1996; Shibata *et al*, 1994). In mice models,

mutant SOD1 oligomers/higher molecular weight complexes appear well before the onset of disease symptoms (Johnston, Dalton, Gurney & Kopito, 2000; Karch *et al*, 2009), implicating small aggregates of the protein as a cause of the disease; however, the molecular mechanisms for this are not clear. This chapter will discuss a possible aggregation mechanism that might be responsible for disease: aggregates formed from holo SOD1s under physiologically relevant conditions, pH 7.8 and 37 °C. The following sections will describe the background and rationale for the studies presented in this chapter.

2.1.1 Abundance of SOD1 in motor neurons

SOD1 is ubiquitously expressed in aerobic cells. Expression levels have been studied in many different tissues, including the liver, kidneys, stomach, muscles and cerebral cortex (Valentine, Doucette & Zittin Potter, 2005). Comparisons of the concentrations of SOD1 in different tissues suggest that SOD1 has a higher level of expression in the nervous system (Valentine, Doucette & Zittin Potter, 2005). The cellular distribution of SOD1 in motor neurons has been also studied using immunocytochemistry (Pardo *et al*, 1995). An abundance of SOD1 was identified in the perikarya, dendrites, axons, cytoplasm, and peroxisomes of the motor neurons. The concentration of SOD1 has been reported as 10 μM in erythrocytes (Rakhit *et al*, 2004), based on the normal values for the amount and volume of hemoglobin and the known ratio of SOD1 to hemoglobin in erythrocytes (0.95 ± 0.07 μg of SOD1/mg hemoglobin) (Kurobe *et al*, 1990). Since the brain contains approximately 4.5 times more SOD1 than erythrocytes (Kurobe, Suzuki, Okajima & Kato, 1990), the concentration of SOD1 in the brain has been estimated to be 45 μM (Rakhit *et al*, 2004). The

concentration of cytoplasmic SOD1 in motor neurons tends to be higher than the average concentration in the brain (Kurobe, Suzuki, Okajima & Kato, 1990). Thus, 100 µM is typically accepted as the concentration of SOD1 in motor neurons and this value has been used in previous *in vitro* experiments (Banci *et al*, 2008; Banci *et al*, 2007b; Rakhit *et al*, 2004) as well as the current study. It is worth noting that those parts of the nervous system that are affected by ALS are not always parts that are abundant in SOD1. Therefore, the apparent abundance of SOD1 in motor neurons is only partially related to motor neuron degeneration in ALS, rather than the primary toxic properties SOD1 in the disease (Pardo *et al*, 1995).

2.1.2 Rationale

This section provides an overview of previous studies of SOD1 aggregation related to ALS and shows how they relate to the research reported in this chapter. Many previous studies have attempted to correlate ALS disease characteristics (such as survival times and disease onset) with SOD1 biophysical properties (*e.g.,* aggregation propensity and/or protein stability); however, no universal trends have been identified (Wang, Johnson, Agar & Agar, 2008). Biophysical properties that have received particular attention include protein stability, charge and aggregation propensity. Owing to the very high stability of holo SOD1 (Stathopulos, 2005), many studies have focused on the stability of less mature and less stable forms of the protein (*e.g.,* those lacking bound metals or the intra-subunit disulfide bonds). An initial claim was that all mutations decrease the apparent melting temperatures of

unmetallated (apo) SOD1s (Lindberg *et al*, 2002). Later, this was refuted when it was discovered that the melting temperatures of various mutants that are located at the metal binding sites were similar or even slightly higher than wild-type (Rodriguez *et al*, 2005). The change in net charge of the protein has been investigated as a common trend between fALS associated mutants of SOD1. Based on analysis of 100 fALS-linked SOD1 mutants, a preference to reduce the net negative charge of the protein is observed; however, there are exceptions, V7E, G41D, N86D, G93D, R115G and G141D (Sandelin *et al*, 2007). Recently, there has been some success in correlating ALS disease duration with properties of SOD1 mutants by combining apo protein stability with predicted aggregation propensities of the mutant proteins (Wang, Johnson, Agar & Agar, 2008). More specifically, SOD1 aggregation propensities were calculated using an equation developed by Dobson and coworkers for prediction of aggregation propensity of the amyloid forming protein, acylphosphatase and its mutants (Chiti *et al*, 2003a). The equation was derived empirically by examining how three physicochemical properties, hydrophobicity, secondary structure (including loss of α helix and gain of β sheet) and protein net charge, contribute to aggregation propensity for the proteins. Wang *et al.* showed that combining calculated aggregation propensity with experimental data on apo SOD1 stability accounted for 69% of the varied disease duration of mutant-SOD1 associated fALS (Wang, Johnson, Agar & Agar, 2008). The remaining variation may be due in part to limitations in patient data and in mutant protein characterization. Consideration of additional data, such as stability of the native, fully metallated (holo) form of SOD1, which has received relatively little attention, may be

essential in giving more clarity to the roles of mutant SOD1 in disease (Meiering, 2008; Wang, Johnson, Agar & Agar, 2008)

The holo form of SOD1 has been thought to be incompatible with aggregation because of its high stability, although the majority of cellular SOD1 is in the holo form (Shaw & Valentine, 2007; Valentine, Doucette & Zittin Potter, 2005). Furthermore, aggregation has been reported mostly for immature or aberrant forms of the protein, often under highly destabilizing conditions which generally favor aggregation (DiDonato *et al*, 2003; Rakhit *et al*, 2004; Stathopulos *et al*, 2003). However, the relevance of these aggregation studies to human disease is not clear. It is not known which forms of SOD1 may give rise to or be present in aggregates in patients to date (Hayward *et al*, 2002). There is some nuclear magnetic resonance (NMR) evidence for increased association of holo S134N (Banci *et al*, 2005), and partially metallated forms have been found to form fibrillar assemblies in crystals (Hough *et al*, 2004a; Shipp *et al*, 2003). Recently, evidence has been accumulating for pathological aggregation of various other disease-associated proteins under mild solution conditions *via* states that are close to the native (Chiti & Dobson, 2009). For example, β2-microglobulin in dialysis-related amyloidosis (Chiti & Dobson, 2009) and serpins in serpinopathies, early-onset dementia, emphysema, and thrombosis (Yamasaki *et al*, 2008) have been shown to aggregate from the native protein. Thus, it may be necessary to look beyond the immature forms of SOD1 to determine how SOD1 may be involved in disease pathology.

2.1.3 Chapter overview

This chapter shows that aggregates can form from the native, holo form of SOD1, with or without ALS-associated mutations, under physiologically relevant solution conditions. The similarity of the aggregates to those observed *in vivo* is demonstrated by structural and tinctorial analyses as well as the novel observation of binding of an anti-SOD1 antibody that specifically recognizes pathological aggregates in ALS. ALS-associated SOD1 mutations can promote aggregation but are not required, suggesting that SOD1 aggregation may be a common mechanism in familial and sporadic ALS. The SOD1 aggregation is characterized by a lag phase, which is diminished by self- and cross-seeding, and heterogeneous nucleation. Metal loss and/or dimer dissociation promote aggregation. This establishes a valuable system for understanding SOD1 aggregation and toxicity mechanisms, and ultimately developing urgently needed therapeutic strategies targeting protein aggregation.

2.1.4 Acknowledgements

aggregation profiles of holo A4S and holo A4T; Hong Yang, for help with the AFM measurements in Pu Chen's lab; Hamid R. Badiei and Vassili Karanassios for help with metal analysis experiments; and Janice Robertson and Hsueh-Ning (Shirley) Liu from the University of Toronto who provided the SEDI antibody and suggestions for performing enzyme-linked immunosorbent assay (ELISA).

2.2 Materials and Methods

2.2.1 Expression and purification of pWT and mutant SOD1 and SEDI antibody

The plasmid, pHSOD1Lac1^q, was used for expression of human cytosolic Cu/Zn SOD1 in *E. coli* cells. The plasmid contains a human SOD1 gene joined to the leader sequence of *Photobacterium leiognathi* Cu/Zn SOD (Getzoff *et al*, 1992b), the ampicillin resistance gene, and the *lacI^q* gene in a pBR322 derivative containing the *tac1* promoter. The leader sequence directs the translated protein to the periplasm (Getzoff *et al*, 1992b). The synthetic SOD1 gene contains the mutations, C6A and C111S, and the resulting protein is referred to as pWT. The strain employed in this study (derived from QC779) is deficient in bacterial SODs, Mn SOD and Fe SOD by mutation (SOD (-/-)) and resistant to kanamycin and chloramphenicol (Farr *et al*, 1986; Natvig *et al*, 1987).

SOD (-/-) *E. coli* were transformed with pHSOD1Lac1^q by electroporation. 1 μg of the vector DNA was added to 40 μL of electrocompetent cells in 10 % (v/v) glycerol and then placed into an electroporation cuvette (0.1 cm gap, BioRad Laboratories, Inc.). A high electric field, 1.80 kV for 1 sec, was applied to the cell/DNA mixture (*E.coli* Pulser, BioRad

Laboratories, Inc.). The electroporated cells were grown for 1 hr at 37 °C in 1 mL of a

medium (containing 0.4 % (w/v) glucose, 20.0 g tryptone, 5.0 g yeast extract, 0.5 g NaCl,

and 0.01 M $MgSO_4$ per liter). The cells were then plated on Luria Bertani (LB)-agar plates

containing ampicillin (100 µg/mL), kanamycin (30 µg/mL) and chloramphenicol (30 µg/mL)

and then incubated overnight at 37 °C. A single colony was selected and grown overnight in

50 mL of LB medium. Next, 10 mL of the LB culture was used to inoculate 1 L of 2TY rich

medium (containing 16.0 g tryptone, 10.0 g yeast extract, and 5.0 g NaCl per liter) at 37 °C

with constant shaking at 200 rpm. In addition, the medium contained three antibiotics: 0.1

mg/mL ampicillin, 0.03 mg/mL kanamycin, and 0.03 mg/mL chloramphenicol. When the

cultures reached an optical density between 0.6 and 0.8 at 600 nm, isopropylthiogalactoside

(0.25 mM, final concentration) was added to induce expression of human SOD1. At the time

of induction, $CuSO_4$ and $ZnSO_4$ were also added to final concentrations of 0.5 mM and 0.01

mM, respectively. The growth medium was further incubated at 37 °C for 8 hrs from the

time of induction. Cells were harvested by centrifugation (4500g for 15 min) and if

necessary, stored at – 80 °C.

Human SOD1 was obtained from the periplasm of cells by osmotic shock. The

following procedures apply to a cell pellet obtained from 1 L flask of culture. Cells were

resuspended in 50 mL of sucrose solution (20 % (w/v)) containing 15 mM

ethylenediaminetetraacetic acid (EDTA) and 10 mM tri(hydroxymethyl)aminomethane

hydrochloride (Tris-HCl), pH 7.5. The resuspended cells were gently agitated on ice for 20

minutes and then centrifuged to collect pellets (4000 g for 30 min). The cell pellets were

lysed by osmotic shock with the addition of 20 mL of ice-cold deionized water obtained from

a milliQ water system (Millipore Ltd.). Centrifugation was performed (4500 g for 45 min) and the soluble fraction from the periplasm was collected. The solution from osmotic shock was stored in – 80 °C if needed.

Heat treatments were performed to remove unwanted proteins after osmotic shock. The final solution from osmotic shock was diluted to 0.8 mg/mL using 20 mM Tris-HCl, pH 7.8 and milliQ water. The used volume of Tris buffer is twice more than the volume of water. The diluted solution was heat-treated at 70 °C for 20 min in the presence of 1.4 mM $CuSO_4$ as the final concentration. The pH of this solution was adjusted to 6.7. This step helps Cu ions bind to human SOD1 and removes thermally unstable proteins. The soluble fraction was obtained by centrifugation (4000 g for 10 min).

Purification of human SOD1 was carried out by hydrophobic interaction chromatography. $(NH_4)_2SO_4$ was added to the supernatant from heat treatments to a final concentration of 3 M. All the solutions to be used in the chromatography column: the highly saturated protein solution, 3 M $(NH_4)_2SO_4$, and 20 mM Tris-HCl, all at pH 7.8, were filtered through 0.45 micron low protein binding filter. Then, the solutions were degassed for at least 20 min. Appropriate aliquots of the protein solution were subsequently loaded onto a Waters column (2.2 cm diameter x 10 cm length, Waters), packed with Poros 20 micron HP2 (polystyrene-divinylbenzene). The typical gradient used was 65 % (v/v) of 3 M $(NH_4)_2SO_4$ against 20 mM Tris-HCl, pH 7.8 and decreased to 40 % (v/v) of 3 M $(NH_4)_2SO_4$ against 20 mM Tris-HCl, pH 7.8 over 4 column volumes. It is worth noting that the gradient was very subjective to the mutant of interest and the concentration of the prepared $(NH_4)_2SO_4$. When the column purification was complete, the holo form of SOD1 was collected and pooled

52

together. The final solution was extensively dialyzed with milliQ water at 4 °C using a dialysis membrane to remove salt. The reservoir water was changed at least three times after at a minimum of 8 hrs incubation each time using 10000 Da cutoff cellulose membranes, (Spectrum Laboratories, Inc.). The protein was concentrated using an Amicon ultrafiltration device with a regenerated cellulose membrane (YM10 Amicon untrafiltration, Millipore Ltd.). The purified and concentrated protein was examined for purity, metal status and concentration using differential scanning calorimetry (DSC), enzymatic activity assays, inductively coupled plasma- atomic emission spectroscopy (ICP-AES), mass spectroscopy (MS), and Lowry assays (Lowry *et al*, 1951). The concentrated solution was once again filtered using a 0.45 micron low protein binding filter and then aliquoted into various volumes and stored in -80 °C until it was used.

Mutant genes were prepared and were provided from Kristin Dimmick for current work. SOD1 Exposed Dimer Interface (SEDI) antibody was generously provided by Dr. Janice Robertson from University of Toronto and its preparation is described in reference (Rakhit *et al*, 2007).

2.2.2 Holo SOD1 aggregation

Samples for aggregation experiments were prepared by concentrating by ultrafiltration (Nanosep 3K Omega, PALL Corporation) and then diluted to the desired final protein concentration, which was generally 10 mg/mL (317 µM) unless otherwise stated, in 20 mM 4-(2-hydroxyethyl)-1-piperazineethanefulfonic acid (HEPES), pH 7.8. Except for the experiment to determine the effect of filtration, samples were then filtered using 20 nm filters

(Anotop 10 Plus, Whatman) to remove any dust particles and preformed aggregates. Samples were incubated without agitation at 37 °C in 4 mL glass vials (VWR) sealed with parafilm to minimize evaporation. Samples were measured 2 times per day during the lag time, 3 times per day during rapid growth phase, and 1 time per day at the plateau phase.

2.2.3 Light scattering measurements

Time average light scattering was measured using a 90Plus particle sizer (Brookhaven Instruments, Inc.) or a Zetasizer Nano-ZS (Malvern) and the two instruments gave comparable results. However, since the detectors of the two instruments are located at different angles (90° and 173° for the 90Plus and Nano-SZ, respectively), the total counts are higher for Nano-SZ (van Holde Kensal E. *et al*, 1998). The reported light scattering values are the averages of 3 measurements, each consisting of 10 (5) consecutive 30 (10) second data accumulations by the 90Plus (Nano-SZ) instrument. For restart experiments, samples were monitored until they reached the plateau phase, aggregates were removed by centrifugation (2000 *g*, 10 min) and filtration (20 nm filters, Anotop 10 Plus, Whatman). Then, samples were then incubated at 37 °C and monitored by light scattering.

2.2.4 Activity of soluble SOD1 during aggregation

Activity of remaining soluble SOD1 during aggregation time courses was determined by removing a sample aliquot, diluting this to a suitable concentration for activity measurement, centrifuging (14,000 *g* for 8 min) to remove aggregates, and determining the

activity of SOD1 samples by the inhibition of pyrogallol autooxidation activity assay (Marklund & Marklund, 1974). The protein concentration after centrifugation was determined by the Lowry assay (Lowry, Rosebrough, Farr & Randall, 1951), and used to calculate specific activity. To minimize activity assay variability, a specific activity was also determined in parallel for control unaggregated pWT, and sample activity determined as the ratio of aggregated sample to unaggregated pWT specific activity.

2.2.5 Data fitting for protein aggregation profiles

Aggregation profiles were fit using an empirical equation for a sigmoidal curve:

$$Y = Y_f + \frac{Y_i - Y_f}{1 + \exp(\frac{x - x_0}{d_x})} \qquad \text{Eq. 2.1}$$

where Y_i and Y_f are the initial and average plateau light scattering intensity, respectively, x_0 is the time of half completion, and d_x is the time constant (Nielsen *et al*, 2001). The lag time for aggregation was calculated from the fitted parameters as:

$$\text{lag time} = x_0 - 2d_x \qquad \text{Eq. 2.2}$$

To gain insight into the aggregation mechanism, the initial 10-20 % of the light scattering aggregation time course data was fit as described by Ferrone *et al.* (Ferrone, 1999) for primary nucleation, described by a cosine function:

$$\text{fractional completion} = |A| \{1\text{-}\cos(|Bt|)\} \qquad \text{Eq. 2.3}$$

and secondary nucleation, described by a hyperbolic cosine function:

$$\text{fractional completion} = |A| \{\cosh(|Bt|)\text{-}1\} \qquad \text{Eq. 2.4}$$

where A is the fitted amplitude, B is an effective rate, and t is time (Ferrone, 1999). All the fits were performed in Origin 7.5, and reported R^2 values are from the fitting. The two tailed Student's *t*-test was used for obtaining reported *P*-values.

2.2.6 Seeding effects

Aliquots of preformed aggregates were added to freshly prepared holo SOD1 samples (10% (w/w)), and aggregation was monitored by light scattering as above. The aliquots contained either "early" or "late" seeds obtained at the end of the lag phase or the plateau phase, respectively. Cross-seeding experiments were performed by adding early seeds from different isoforms of SOD1 to fresh pWT solution (3 mg/mL).

2.2.7 Atomic force microscopy (AFM)

Aliquots of aggregation samples at various time points were diluted in MilliQ water to a suitable concentration for AFM imaging (~0.5 µg/mL) and then centrifuged (10,000 rpm, 6 min). Diluted unaggregated (control) and aggregated (pellet from the centrifuge tube) protein solutions were applied to freshly cleaved mica, then rinsed with MilliQ water, and air-dried overnight. Imaging was performed at room temperature using a PicoScan^{TM} atomic force microscope (Molecular Imaging) using the tapping mode. All images were acquired using a 225 µm silicon single-crystal cantilever (NCL type) with a typical tip radius of 10 nm and resonance frequency of ~170 kHz. A scanner with the maximum scan size of 6×6 µm^2 was used. Images were obtained at a resolution of 512×512 pixels on a scale of 1 µm × 1 µm.

To obtain the size of a protein particle, an image analysis program (Scion Image, Scion Corporation) was used. An individual particle was selected and its width and height were measured. To remove tip effects on the determination of the real width of objects probed by AFM, the measured widths were converted using the following equation (Fung *et al*, 2003):

$$W^{\bullet} = W - 2\sqrt{H(2R_c - H)}$$

Eq. 2.5

where W* is the actual width, W is the observed width, H is the observed height, and R_c is the radius of curvature of the tip (10 nm). The volume of the particle was calculated using

the converted width and measured height assuming the particle has a circular cylinder shape. The calculated volume was divided by the volume of the native dimer SOD1 (ellipsoidal dimensions of ~30 x 40 x 70 Å) (Parge, Hallewell & Tainer, 1992) in order to get the number of dimers within the particle. This approach assumes the association creates no significant volume change.

2.2.8 In-torch vaporization inductively coupled plasma atomic emission spectroscopy (ITV-ICP-AES)

Ultra high sensitivity ITV-ICP-AES was used to analyze the amounts of Cu, Zn and S in aggregated and unaggregated SOD1. The ICP-AES system with attached rhenium-cup ITV is described in detail elsewhere (Badiei & Karanassios, 1999). Calibration curves for Cu, Zn, and S were made using standard solutions (ICP-mass spectroscopy grade, SCP Science). Aggregates were prepared by centrifuging plateau phase samples (2000 g for 15 min). The pellets were washed using 1 mL of MilliQ water followed by centrifugation (2000 g for 15 min), 5 times, and then resuspended in MilliQ water for analysis. Each sample was measured in triplicate and the amounts of Cu, Zn, and S determined using the calibration curves. [S] was used to determine the concentration of the SOD1 polypeptide based on 2 S per polypeptide chain from the 2 cysteine residues. The values of [Cu]/ [Zn] in unaggregated soluble pWT, G85R, and G93V are 0.93 ± 0.10, 1.00 ± 0.14, and 1.22 ± 0.05, respectively.

2.2.9 Electrospray ionization-mass spectrometry (ESI-MS)

The molecular weight of SOD1 before and after aggregation was analyzed using a Micromass Q-TOF Ultima Global (Waters). Aggregate pellets were prepared as described for metal analysis (see Materials and Methods, section 2.2.8). Supernatants were prepared for analysis by exchanging the sample from HEPES buffer into MilliQ water by ultrafiltration (Nanosep 3K Omega, PALL Corporation) by 15 rounds of ~10-fold concentration (8700 g for 8 min) at 13°C. The prepared supernatants were diluted to a final concentration of 1 µM with 50/50 (v/v) methyl cyanide (MeCN)/H_2O containing 0.2 % (v/v) of formic acid (FA) prior to the measurements. The prepared pellets were dissolved in 20 µL of 50/50 (v/v) MeCN/H_2O containing 0.2 % (v/v) of FA prior to the measurements. Samples were infused by electrospray ionization, and measured in positive ion mode. The capillary voltage and cone voltage were 3 kV and 80 V, respectively. The signal was accumulated for at least for 1 min and the average of m/z data from the accumulated signal was reported. Prior to mass measurements, 1% of phosphoric acid solution in 50/50 of MeCN in water was used for m/z calibration.

2.2.10 Thioflavin T (ThT) fluorescence

6.8 µL of pWT aggregation sample prepared at either 8.7 mg/mL or 3.2 mg/mL were diluted to 1.00 or 0.36 mg/mL, respectively, in 0.17 mM ThT and 20 mM HEPES at various time points. Fluorescence emission spectra were obtained immediately (unless otherwise stated) using an excitation wavelength of 440 nm. The slit widths for excitation and emission

were 1 and 5 nm, respectively. Fluorescence spectra were obtained using a Fluorolog3-22 spectrofluorometer (Jobin Yvon-Spex, Instruments S.A., Inc.) at 25 °C.

2.2.11 Anilinonaphthalene sulphonic acid (ANS) fluorescence

A solution of 680 µM ANS was prepared by dissolving ANS in water and the concentration was confirmed by its absorption at 351 nm (the extinction coefficient = 6240 $M^{-1}cm^{-1}$ (Lai *et al*, 1996)). 3.1 µL of aggregation samples prepared with either 8.7 mg/mL or 3.2 mg /mL of pWT and 62.5 µL of the prepared ANS solution were mixed and then fluorescence emission spectra (400 – 600 nm) were obtained immediately (unless otherwise stated) using an excitation wavelength of 410 nm. The slit widths for excitation and emission were 2 and 4 nm, respectively. Fluorescence spectra were obtained using a Fluorolog3-22 spectrofluorometer (Jobin Yvon-Spex, Instruments S.A., Inc.) at 25 °C.

2.2.12 Competition enzyme linked immunosorbent assay (ELISA)

Competition ELISA assays for unaggregated (control) and aggregated pWT were conducted in parallel to ensure accurate comparison. Competing C-terminal peptide (see Fig.2.1b) was added to the plate (0.05 µg/well), incubated for 1 hour at RT, then the plate was washed a total of 5 times, 3 times using phosphate buffered saline (PBS, this solution contained 8 g of NaCl, 0.2 g of KCl, 1.44 g of Na_2HPO_4, and 0.24 g of KH_2PO_4 per liter, pH 7.4) containing 0.05 % (v/v) of Tween 20 (PBST) followed by 2 washes with PBS solution. Next, blocking solution (1% (w/v) BSA in PBS) was added to the plate, which was incubated

overnight at 4 °C. The plate was washed a total of 5 times, 2 washes using PBST followed by 3 washes using PBS solution. Meanwhile, a polyclonal antibody preparation from rabbit, SEDI antibody was diluted (1000 times) in blocking solution. Then, this was combined with either aggregated SOD1 from the plateau phase or with unaggregated SOD1, and incubated for 2 hours at RT with gentle shaking. The final concentration of SOD1 in the SEDI solution was 180 nM. Control solutions of SEDI solution with no added SOD1 were also prepared. These solutions were added to the plates (50 μL/well), incubated for 35 min at RT with no agitation, and then washed a total of 7 times, 5 washes using PBST followed by 2 washes using PBS solution. Horseradish peroxidase (HRP)-conjugated anti-rabbit IgG secondary antibody (Pierce) was diluted in blocking solution (1:2000) and then added to the plate, incubated for 80 minutes at RT, and the plate washed for a total of 7 times, 5 washes using PBST followed by 2 washes using PBS solution. For visualization, 100 μl/well of 2-2'-azino-di-(3-ethylbenzthiazoline sulfonic acid (ABTS) substrate (Pierce) was added, incubated for 30 minutes at RT, and read at 405 nm using a plate reader (Spectramax Plus384,Molecular Devices). For a given experiment, samples for SEDI with/without unaggregated pWT were prepared on one plate and samples for SEDI with/without aggregated pWT were prepared on the other plate. Each sample was prepared in 3 wells. Three independent SEDI binding experiments were conducted, and the average and standard deviation of the 3 experiments were obtained. The reading from the samples of SEDI with either unaggregated or aggregated pWT was normalized against the reading from the sample of SEDI without pWT from the same plate. The normalized values were reported.

2.3 Results

2.3.1 Aggregation is formed from the holo form of SOD1.

Aggregation from the holo form of SOD1 was followed using light scattering to measure particle formation in solution as a function of time. The experiments were conducted at close to physiological conditions of temperature (37 °C), pH (7.8) and protein concentration (100 – 1000 µM, 3-30 mg/mL) (Rakhit *et al*, 2004). Diverse ALS-associated mutations were studied: G85R, which disrupts metal binding (Cao *et al*, 2008); A4V, A4T, A4S, and I149T, in the dimer interface; and G93V, G93S, and G93D, at a mutational hotspot in a loop (Fig. 2.1). Proper metallation and folding of holo SOD1 preparations were confirmed by ICP-AES, DSC and pyrogallol activity assay prior to aggregation measurements (see Materials and Methods, section 2.2.1).

Remarkably, all of the SOD1s (A4T, A4S, I149T, G93D, G93V, and G85R) including pWT, exhibit a sigmoidal-like increase in light scattering intensity with time (Fig. 2.2). Previously, sigmoidal aggregation profiles were reported for A4V and G93A (Stathopulos, 2005). The aggregation time courses resemble those of many other disease-associated proteins (Morris *et al*, 2008). The observation of aggregation for pWT supports the hypothesis that SOD1 aggregation can also contribute to the pathology of sALS (Shibata, Asayama, Hirano & Kobayashi, 1996; Shibata *et al*, 1994).

62
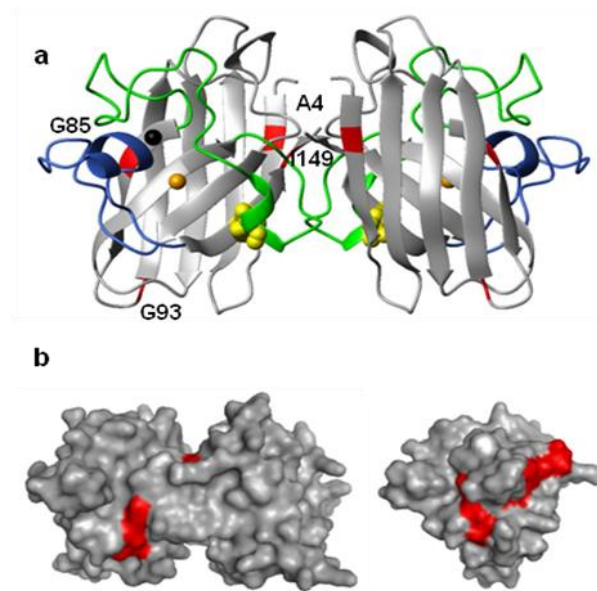
Figure 2.1 Structure of Cu/Zn SOD1

(a) Ribbon representation of dimeric holo pWT (Parge, Hallewell & Tainer, 1992) (pdb code

1SOS). Cu and Zn ions are shown as orange and black spheres, respectively. The

intrasubunit disulfide bond between cysteines 57 and 146 is shown in yellow space filling

representation. The two active site loops, electrostatic loop VII (residues 121-142) and loop

IV (residues 49-82), are colored blue and green, respectively. Loop IV is composed of three

regions: the dimer interface region (residues 49-54); the disulfide bond region (residues 55-

61); and the Zn binding region (residues 62-82) (Hornberg, Logan, Marklund & Oliveberg,

2007). Sites of fALS mutations characterized here are colored red and labeled. (b) The

epitope (residues 143-151, red) for the SEDI antibody is buried in the dimer form of SOD1

(left) and exposed in the monomer form (right). The dimer view is the same as in (a) but the

monomer is rotated to clearly show the epitope. The figure was made using Molmol (Koradi,

Billeter & Wuthrich, 1996) and Pymol for (a) and (b), respectively.
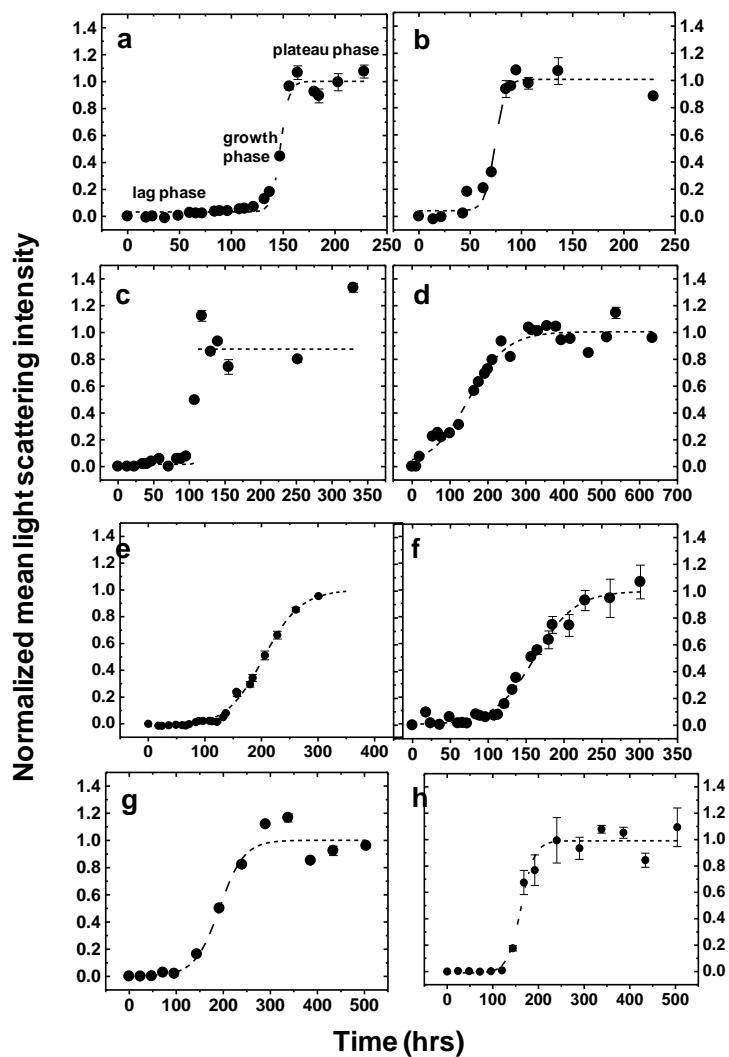
Figure 2.2 Representative sigmoidal aggregation profiles for holo SOD1s monitored by light scattering.

(a) pWT, (b) A4T, (c) A4S, (d) I149T, (e) G93D, (f) G93V, (g) G93S, and (h) G85R.

Dashed lines show the fit of the data to an empirical sigmoidal equation for aggregation, Eq.

64

2.1 (Nielsen *et al*, 2001) (see Materials and Methods, section 2.2.5). R^2 values from the fitting are 0.986, 0.844, 0.969, 0.990, 0.984, 0.994, 0.969, and 0.978 for (a) to (h), respectively. Plotted values (●) and error bars are the means and standard deviation for 3 light scattering measurements per sample at each time point (see Materials and Methods, section 2.2.3). Some error bars are smaller than the symbols.

2.3.1.1 Differences from previous studies of holo SOD1 aggregation

Previous studies generally have reported lack of aggregation for holo SOD1 (Banci *et al*, 2007b; Chattopadhyay *et al*, 2008), although recently WT and A4V in the pWT background were reported to aggregate (Oztug Durer *et al*, 2009) and there is also evidence for aggregation from holo SOD1 in other studies (Banci *et al*, 2005; Rumfeldt *et al*, 2006). The differences between some of the previous studies (Banci *et al*, 2007b; Chattopadhyay *et al*, 2008) and the results here may be due to various experimental factors. The previous studies monitored aggregation primarily using ThT binding, a probe of amyloid formation (LeVine, 1995). The aggregates from holo SOD1 reported here do not bind ThT, nor do they have other characteristics of amyloid (see Discussion, section 2.4.1). Light scattering used here is sensitive to the formation of any larger particles (Lomakin *et al*, 1999). An additional experimental difference is the increased number and/or longer time course of measurements here, enabling observation of aggregation from the holo state of SOD1 even though this is less favourable than aggregation from other states (Chattopadhyay *et al*, 2008; Furukawa *et al*, 2008; Oztug Durer *et al*, 2009; Shaw & Valentine, 2007; Stathopulos *et al*, 2003). When we incubated identical holo SOD1 samples in parallel, with one sample being measured as

usual and the other not, aggregation occurred more quickly for the regularly measured sample, suggesting that the process of sample measurements and mixing promotes aggregation (Fig. 2.3). This is consistent with other studies that show sample agitation can promote aggregation of SOD1 and other proteins (Chattopadhyay *et al*, 2008; Furukawa *et al*, 2008; Khurana *et al*, 2001; Oztug Durer *et al*, 2009; Souillac *et al*, 2003). In order to facilitate comparisons among mutant holo SOD1s, a consistent frequency of measurements was used for all samples (see Materials and Methods, section 2.2.2). In addition, the results obtained here are not inconsistent with numerous previous studies characterizing holo SOD1 reported by our group and others since, based on activity and aggregation restart experiments (see below*),* considering that the majority of SOD1 in solution (>80%) does not aggregate. Furthermore, this is similar to the extent of aggregation observed for other proteins (Huang *et al*, 2000; Morel *et al*, 2006; Piazza *et al*, 2006).
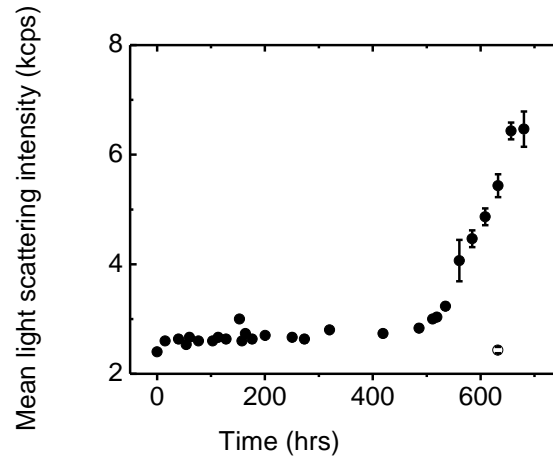
Figure 2.3 Sampling effect on aggregation of holo pWT

Aggregation profiles of pWT (10 mg/mL) were monitored by light scattering measurements. (●, ○) symbols represent light scattering intensity of the sample with and without daily measurements, respectively. The plotted values and error bars are the average light scattering intensity and s.d. from the 3 replicates of 10 measurements for 30 sec. The sampling effect on aggregation was observed in two other cases, where no aggregation was observed after over 2 weeks incubation.

2.3.1.2 Quality check of holo SOD1 aggregation

Aggregation is very sensitive to environmental factors (*e.g.,* agitation and head volume (Kiese *et al*, 2008; Sasahara *et al*, 2008; Sluzky *et al*, 1991)) as well as varying solution conditions (pH, ionic strength, and temperature (Glabe, 2008)). Therefore, great

caution is required for sample preparation, especially with protein concentration and filtering steps, which can cause the proteins to unfold or form oligomers. For aggregation, samples were filtered using a 20 nm cut off filter prior to sample incubation and initially did not contain detectable aggregates based on light scattering measurements. It should be noted that light scattering is extremely sensitive to the presence of larger species owing to the dependence of scattering intensity on the 6th power of the radius of the scattering species (Lomakin, Benedek & Teplow, 1999). For example, considering a hypothetical mixture containing only 5 and 50 nm diameter species in solution and the 50 nm diameter species account for only 0.1 % of the total proteins in solution by mass, 99% of the scattering intensity will come from this species. The initial light scattering measurements clearly show: (1) consistently low light scattering intensities at ~2 kcps (from a Brookhaven 90 plus particle sizer); and (2) a single exponential autocorrelation function for all samples, indicating that the solutions are monodisperse, *i.e.,* consist of a single species with hydrodynamic radius of ~5 nm as expected for a protein the size of the SOD1 native dimer (Wilkins *et al*, 1999) (Chapter 3 will discuss this in more detail). In contrast, samples that were not filtered showed shorter lag times consistent with a previous study from the Meiering laboratory (Stathopulos, 2005). It is important to note that some of the filtered SOD1 aggregation profiles show quite short or no appreciable lag times (Fig. 2.4), suggesting that some aggregates or seeds may sometimes be present initially and facilitate further aggregation. Fig. 2.4c shows the aggregation profile of a "pre-seeded" holo SOD1 sample, in which the sigmoidal fit using Eq. 2.1 (see Materials and Methods, section 2.2.5) does not give a reasonable Y_i value (the fitted value for Y_i is negative instead of the expected ~1.9

kcps). It is important to mention that the light scattering intensity is not noticeably higher at t=0h even in the case of Fig. 2.4c. 57 % of total aggregation experiments show similar case of pre-seeded aggregation profiles. Only profiles with good fits where a fitted value for Y_i is within 35 % variability of a measured Y_i, such as Fig. 2.4a were used for lag time comparison (Fig. 2.5) as well as log AB^2 and log B^2 comparison (see chapter 3).
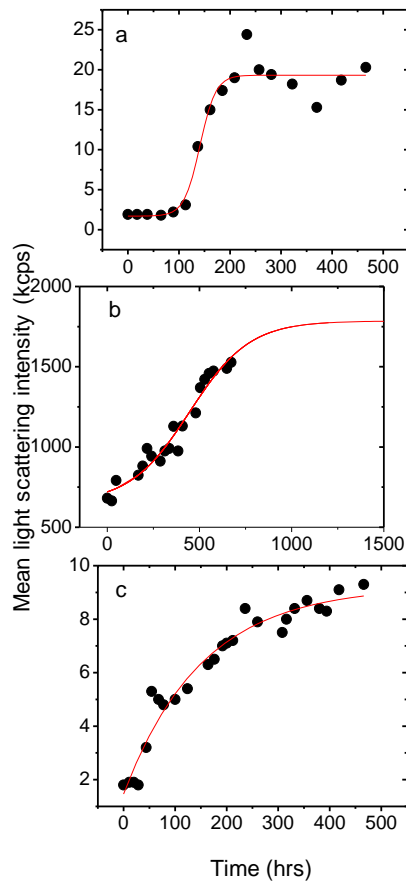
Figure 2.4 Examples of the various goodness about fits of aggregation time courses to the sigmoidal equation (Eq. 2.1)

(a-c) The plotted values are the average light scattering from the 3 replicates of 10 measurements for 30 sec (a and c) and 5 measurements for 10 sec. (b), and fits are shown as red lines (—). It is worth noting that the y-axis scales are different because the data were collected using different light scattering instruments (see Materials and Methods, section 2.2.2). The criterion for the goodness of the data fit is how well Y_i and Y_f in Eq. 2.1 agree with the measured values for the initial and the average plateau intensities, respectively. (a) The aggregation profile fits well to the sigmoidal equation (Eq. 2.1). (b) The fitting result of Y_f does not represent the average plateau reading. This is probably due to the premature end of data collection. (c) The fitted value for Y_i does not match the initial intensity. This is likely due to pre-seeding of the sample (*i.e.,* the presence of aggregates at t=0).

2.3.1.3 Aggregation is facilitated by dimer dissociation.

The aggregation time courses were fit to an empirical equation for a sigmoidal curve, and fitted parameters used to calculate lag times and apparent rate constants (Nielsen *et al*, 2001). An approximate comparison of aggregation for different SOD1 mutants was made by averaging fitted values obtained from multiple independent aggregation time courses, excluding time courses from samples that appeared to be "pre-seeded" (Fig. 2.4c). There are no clear trends in the aggregation time course parameters with respect to protein stability or ALS characteristics (data not shown). This is reasonable because aggregation can depend on various protein properties, including global and local instability and charge, in complex ways that are not well understood (Chiti & Dobson, 2009; Chiti *et al*, 2003a; Rodriguez *et al*,

2005; Shaw & Valentine, 2007). It is noteworthy that sALS had a similar disease duration to many fALS cases, typically ~3-5 years. Also, different mutant SOD1-fALS tend to have characteristic disease durations, for example the dimer interface mutant A4V has a particularly short duration of ~1 year (Wang, Johnson, Agar & Agar, 2008). Interestingly, the lag times for the dimer interface mutants tend to be shorter than for pWT and other mutants (Fig. 2.5), suggesting that aggregation from holo SOD1 involves dimer dissociation. This is further supported by the protein concentration dependence of aggregation and antibody binding experiments (see below).
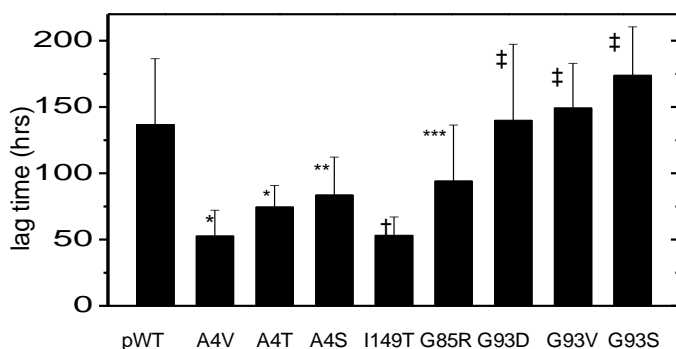
Figure 2.5 Aggregation lag times for holo SOD1s

The lag times were calculated using Eq. 2.1 (see Materials and Methods, section 2.2.5). The presented values are means ± s.d. for 17, 6, 4, 3, 1, 4, 7, 5, and 5 independent experiments for pWT, A4V, A4T, A4S, I149T, G85R, G93D, G93V and G93S, respectively. (†) indicates error estimate from the fitting program for this single experiment. Symbols indicate

71

statistical significance of each lag time value with respect to that of pWT (*, $P < 0.001$; **, $P < 0.065$; ***, $P < 0.05$; and ‡, $P > 0.1$), determined using the two tailed Student's t-test.

2.3.1.4 Aggregation involves changes in metal binding.

We further checked that aggregation occurs from the holo form of SOD1, and not from misfolded or mismetallated SOD1, by measuring specific activity during aggregation as well as conducting restart aggregation experiments. SOD1 activity absolutely requires Cu and is sensitive to protein mismetallation or misfolding (Valentine, Doucette & Zittin Potter, 2005). Thus, if samples initially contain some misfolded or mismetallated SOD1 with lower activity than the holo form, aggregation of the lower activity protein should cause the specific activity of the remaining unaggregated protein to increase with time. Fig. 2.6 illustrates that the specific activity instead *decreases* as aggregation proceeds. These decreases may be caused by altered metal binding and/or formation of soluble aggregates (see below).
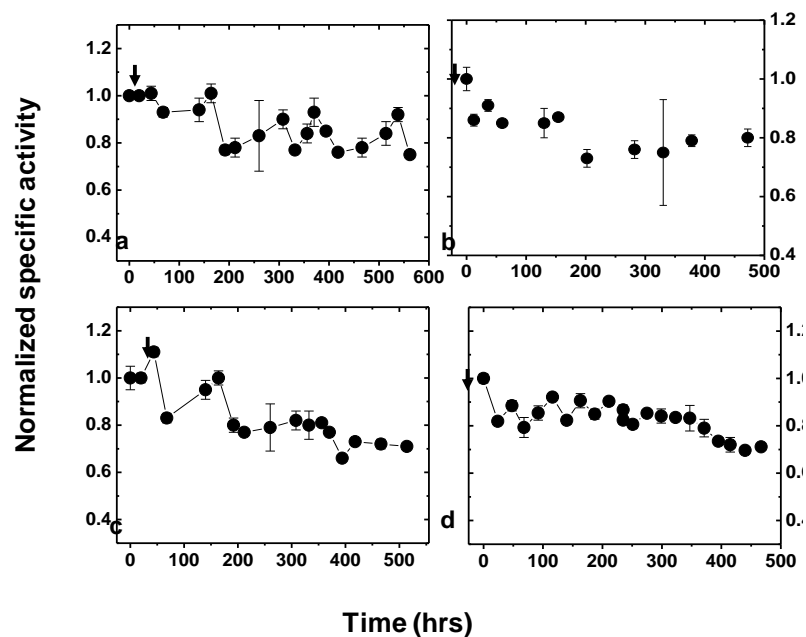
Figure 2.6 SOD1 specific activity decreases as a function of incubation time

(a) pWT, (b) I149T, (c) G85R and (d) G93V. Closed circles (●) represent the normalized ratio (see Materials and Methods, section 2.2.4). Ratios were calculated from the average values for 3-5 activity measurements, and then normalized to 1 at t=0 (see Materials and Methods, section 2.2.4). The vertical error bars are the s.d. from the replicate measurements. The arrows indicate the end of the lag phase from light scattering measurements conducted in parallel with activity measurements. Some error bars are smaller than the symbols.

Furthermore, if aggregation originates from a pre-existing pool of mismetallated or misfolded SOD1, no further aggregation should be observed if aggregates are removed after the plateau phase of the time course is reached. Instead, a previously published study from

73

the Meiering laboratory showed another sigmoidal aggregation time course of pWT, A4V, G85R, and G93V occurs even after removal of the aggregates (Stathopulos, 2005). This experiment was repeated with other mutants of SOD1, G85R and I149T, and showed the same results. Together these results strongly support that aggregation arises from the holo protein.

The metal content of aggregates was determined using ITV-ICP-AES. The data clearly show that aggregates contain bound metals, but the protein is not fully metallated (Table 2.1). Measurements of absorbance during aggregation time courses further support that changes in metal binding occur with time (details in chapter 3). Thus, aggregation arises from the holo protein but involves some, though not complete, loss of metals.

Table 2.1 SOD1 metal content is decreased in aggregates.

Protein	$[Cu]_{aggregate}/[Cu]_{native}$ [a]	$[Zn]_{aggregate}/[Zn]_{native}$ [b]
pWT	0.25 ± 0.03	0.44 ± 0.32
G85R	0.23 ± 0.08	0.11 ± 0.05
G93V	0.38 ± 0.06	0.47 ± 0.06

[a] Calculated as the ratio of $[Cu]_{aggregate}/[S]_{aggregate}$ to $[Cu]_{native}/[S]_{native}$ and [b] calculated from $[Zn]_{aggregate}/[S]_{aggregate}$ and $[Zn]_{native}/[S]_{native}$, where $_{aggregate}$ represents aggregates and $_{native}$ represents fresh unaggregated protein solution.
The values are means ± s.d. for 4 (pWT and G85R) and 2 (G93V) independent aggregation time courses, for which samples were analyzed at least in triplicate.

2.3.2 SOD1 in aggregates is not significantly oxidized.

Oxidative damage arising from aberrant Cu-mediated chemistry has been proposed to be a toxic function of mutant SOD1. In order to investigate whether this is involved in the observed aggregation from holo SOD1 samples, ESI-MS was performed to try to detect oxidative modifications: 13 samples including pWT, G85R and I149T from the plateau phase of aggregation, were analyzed. In general, no changes in mass are observed except for one sample (out of 13 analyzed by MS); the protein species with increased mass by 16 mass unit (+ 16 adduct) was observed (Fig. 2.7). The +16 adduct may be occurring from the oxidation of histidine residues (*e.g.,* 2 oxo-histidine) near the Cu binding site, as seen in a previous study where aggregation of holo wild-type SOD1 was induced by the addition of Cu and ascorbate (Rakhit *et al*, 2002; Uchida & Kawakishi, 1994). The results suggest that most aggregation occurs without Cu mediated aberrant chemistry and Cu mediate aberrant chemistry is not the primary toxic mechanism of disease since the +16 Da adduct was observed only once.
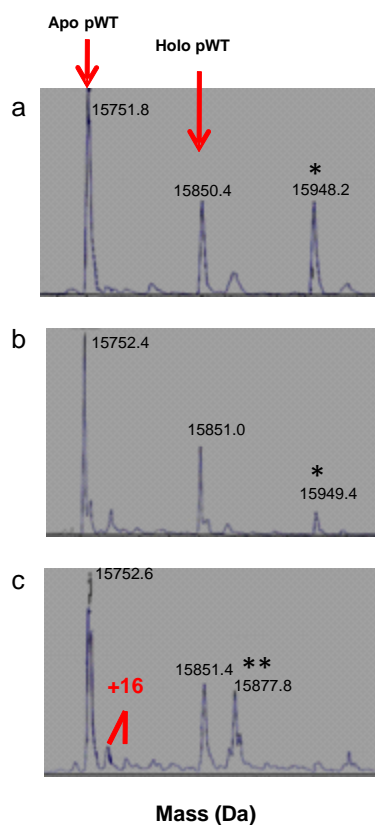
Figure 2.7 Mass spectrum of pWT before and after aggregation

Molecular mass of pWT before aggregation (a) and supernatants (b) and pellets (c) of pWT after reaching plateau was determined. Symbols (*, **) represent +96 adducts and +26 adducts, respectively. These adducts probably come from sulfate ion and sodium ions. The +98 adducts are frequently observed since ammonium sulfate is used for SOD1 purification (see Materials and Methods, section 2.2.1).

76

2.3.3 Holo SOD1 aggregation is less concentration dependent than typical aggregation.

In protein aggregation reactions, lag phases occur because the initial nucleation event is unfavorable, and this is followed by relatively favorable and rapid aggregation (Harper & Lansbury, 1997). For various disease-associated proteins, the lag phase has been found to depend on protein concentration, since the nucleation step requires association of protein subunits (Harper & Lansbury, 1997). The concentration dependence of aggregation was determined for both pWT and the fALS associated mutant, G93V (Fig. 2.8). For all samples, again a sigmoidal-like time course was observed. The lag phase for both proteins decreases with increasing protein concentration (Fig. 2.8), as expected for a protein association reaction, though the concentration dependence is quite moderate (Ferrone *et al*, 1980; Nielsen *et al*, 2001). One likely explanation is that SOD1 aggregation involves dissociation of the native dimer to monomers. Similarly, increased formation of native dimer relative to aggregation-prone monomer at increased protein concentration was found to slow aggregation of immunoglobulin light chain (Souillac *et al*, 2002) and a similar mechanism has been proposed for SOD1 (Khare, Caplow & Dokholyan, 2004). Thus, while increasing protein concentration can favour protein association reactions, it may also simultaneously disfavour aggregation by favouring competing association processes, such as formation of the native dimer for SOD1.
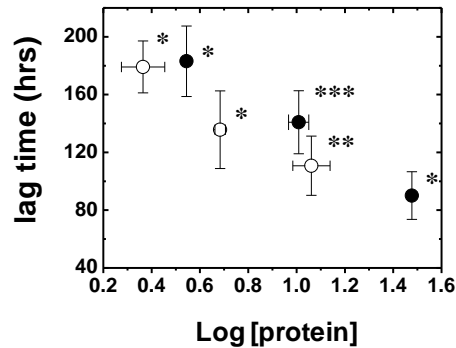
Figure 2.8 Concentration dependence of holo SOD1 aggregation

The concentration dependence of the lag phase for pWT (●) and G93V (○) is shown. (*), (**), and (***) represent averages of 2, 4, and 5 independent experiments, respectively. Plotted values are average lag phase and the vertical error bars are the s.d. from the independent measurements per sample.

2.3.4 Holo SOD1 aggregation is nucleation dependent.

2.3.4.1 Self-and cross- seeding diminish the lag phase of aggregation.

A hallmark of nucleated aggregation reactions is that the addition of preformed aggregates as seeds decreases or abolishes the lag phase (Chiti & Dobson, 2006; Harper & Lansbury, 1997). Seeding has a central role in many diseases, such as Alzheimer's (Harper & Lansbury, 1997) and prion diseases (Prusiner, 1998). Previously, aggregation of samples before and after filtering with a 20 nm cutoff filter showed different lag phases, in which filtering increased the lag phase, suggesting that the presence of some seeds in the initial samples promotes aggregation (Stathopulos, 2005). However, holo SOD1 nevertheless

remained capable of aggregating even when nuclei/aggregates (*i.e.,* formed during sample preparation) are removed by filtration. Seeding was examined further by adding aliquots of solutions that had been allowed to aggregate for different periods of time to fresh solutions of SOD1 (Fig. 2.9). SOD1 exhibits both self-seeding for a given protein (pWT and A4V, Fig. 2.9a-b), and cross-seeding between different variants (A4T, A4S and G93D with pWT, Fig. 2.9c-e). These findings are pertinent to understanding disease because SOD1-linked fALS is typically autosomal dominant, with patients having a single copy of the mutant gene as well as one copy of the wild type (Boillee, Vande Velde & Cleveland, 2006a), and it is not yet clear what roles the two forms of the protein may have in ALS (see Discussion, section 2.4.3).
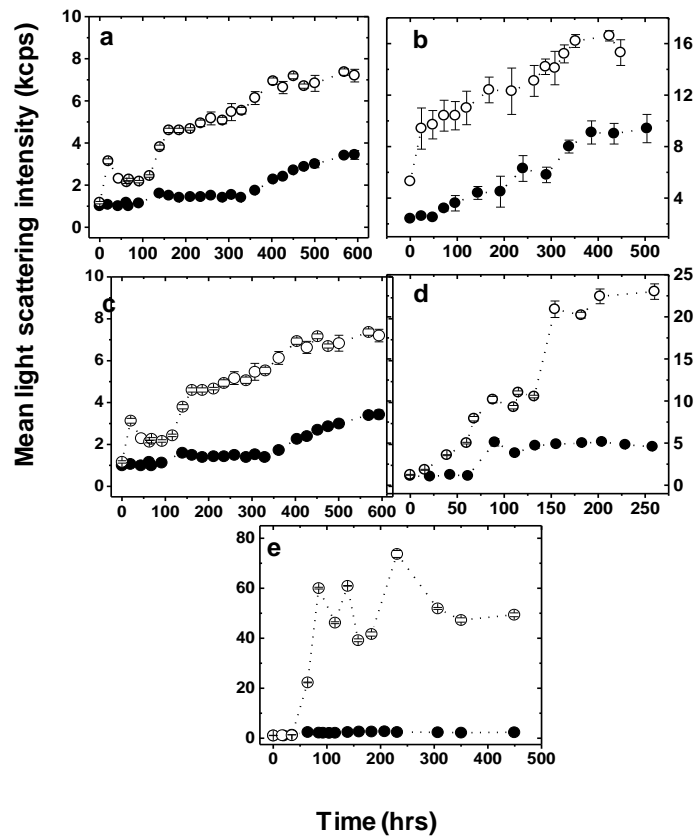
Figure 2.9 Concentration dependence of holo SOD1 aggregation

The effects of self-seeding on the lag phase for aggregation of (a) pWT and (b) A4V and cross-seeding on the lag phase for aggregation of pWT upon addition of 10% (w/w) early seeds of (c) A4S, (d) A4T, and (e) G93D, respectively, are shown. (a-e) Aggregation time courses for unseeded and 10% (w/w) early seeds of holo SOD1s are shown by (●) and (○), respectively. Plotted values are average light scattering intensity and the vertical error bars are the s.d. from the 3 replicate measurements per sample and each measurement was composed of 10 runs for 30 sec. Some error bars are smaller than the symbols. The lag phase of the aggregation time course for SOD1 with seeds is significantly shorter ($P < 0.001$

at 66.5 h in (a) and at 48 h in (b), and $P < 0.001$ at 140 h in (c), at 60 h in (d), and at 64 h in (e)) than for the control samples (unseeded).

2.3.4.2 Holo SOD1 undergoes heterogeneous nucleation.

Two major types of nucleation mechanisms have been reported for protein aggregation: primary and secondary nucleation. In homogeneous nucleation, only primary nuclei are formed, generating linear, unbranched aggregates (*e.g.,* polyglutamine aggregation associated with Huntington's disease) (Chen *et al*, 2002). In secondary nucleation, additional nucleation sites are formed; this may occur by formation of heterogeneous nucleation sites on the sides of fibrillar aggregates, or by fragmentation of fibrillar aggregates, generating new ends for further aggregate growth. Heterogeneous nucleation sites on the sides of fibres were originally described for hemoglobin in sickle cell anemia (Ferrone, Hofrichter, Sunshine & Eaton, 1980). Fragmentation has now also been reported for prion propagation (Collins *et al*, 2004) and β2-microglobulin amyloid formation (Xue *et al*, 2008). Secondary nucleation can be characterized by branched aggregate structures and more rapid aggregate growth compared to the formation of aggregates involving only primary nucleation (Ferrone, 1999). The time courses of SOD1 aggregation were fit to models for primary and secondary nucleation (Fig. 2.10) as per Ferrone *et al.* (Ferrone, 1999) (see Materials and Methods, section 2.2.5). The data for all the SOD1s are better fit by secondary nucleation.

81
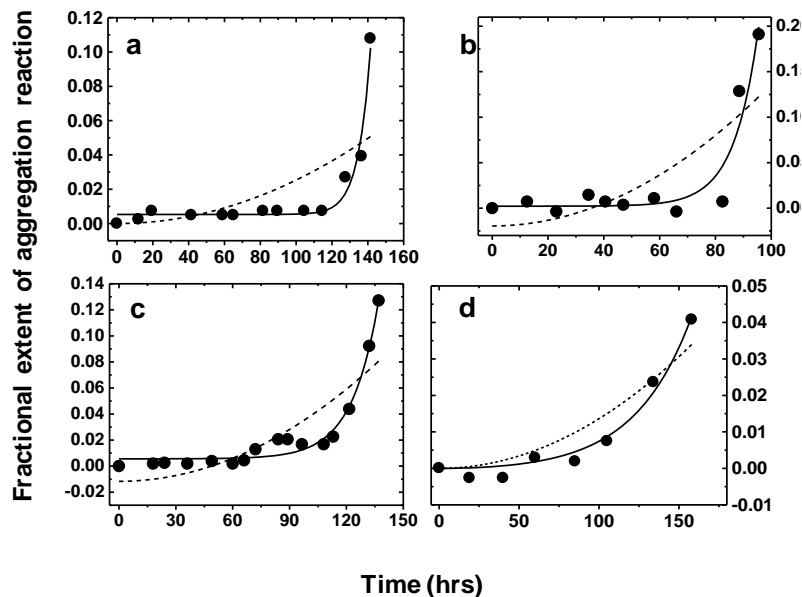
Figure 2.10 Holo SOD1 aggregation time course is indicative of secondary nucleation.
Data fitting to Eq. 2.3 and Eq. 2.4 (see Materials and Methods, section 2.2.5) was used to distinguish primary (- -) and secondary (—) nucleation mechanisms, respectively, for (a) pWT, (b) A4T, (c) G93V and (d) G93D. R^2 values for secondary nucleation fits for pWT, A4T, G93V and G93D are 0.972, 0.916, 0.975, and 0.984, respectively, and each of those is higher than the corresponding one for primary nucleation fitting. Therefore, the rapid increases in light scattering are better fit by a secondary nucleation process.

Further evidence for the occurrence of secondary nucleation was provided by analysis of aggregate structures by AFM. AFM images at different stages of aggregation are shown in Fig. 2.11 for pWT and the fALS associated mutant, G93V. The same types of species are

observed for both proteins. During the lag phase, the predominant species is the native dimer (Fig. 2.12), and some globular amorphous species are also present (Fig. 2.11, yellow arrows). These amorphous species resemble the toxic "oligomers" formed by many other disease-associated proteins (Glabe, 2008). There are also some elongated species that look like associated spherical species or protofibrils (Chiti & Dobson, 2006) (Fig. 2.11 cyan arrows). During the rapid growth phase, dimers are still the most abundant species (Fig. 2.12), but amorphous species increase in abundance and size (Fig. 2.11, red arrows). Some of these immature aggregates show signs of branching (Fig. 2.11, cyan arrows), which becomes more pronounced in the mature aggregates from the plateau phase (Fig. 2.11 green arrows). The branched aggregates may become smoother with time (Fig. 2.11 e and f). It is not clear from the available data whether the branched structures arise from the formation of heterogeneous nuclei on the sides of linear aggregates or from fragmentation; in either case, the branched or tangled fibrillar structures are indicative of the occurrence of secondary nucleation. Aggregates in ALS patients have been described as granules and tangled 15-20 nm granule-coated fibrils (Kato *et al*, 2001; Shibata *et al*, 1994). In addition, in mice models early aggregates are amorphous and later aggregates have similar fibrillar morphologies with these in ALS patients (Kato *et al*, 2001). Thus, the structural characteristics of the holo SOD1 aggregates reported here strongly resemble those observed in ALS.
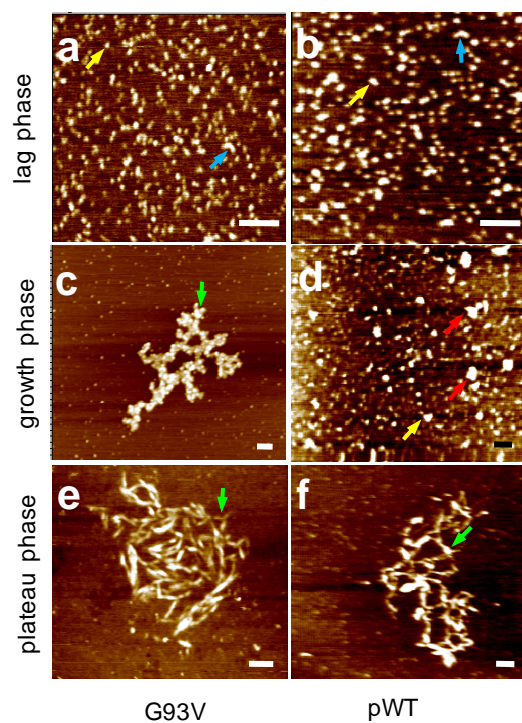
Figure 2.11 AFM structural analyses show holo SOD1s gives rise to soluble oligomers followed by larger amorphous and tangled fibrillar species.

Bars are 100 nm. The AFM images are for G93V (a, c, and e) and pWT (b, d, and f) during the lag phase (a) and (b), rapid growth (c) and (d), and plateau (e) and (f) phases. The yellow, cyan, red and green arrows point to oligomers, protofibrils, amorphous aggregates, and branched fibrils, respectively. The cyan arrows also indicate possible branch points on the fibrils, which may arise from heterogeneous nucleation. Samples were prepared by Y.M. Hwang, and AFM data acquired and analyzed by H. Yang and Y.M. Hwang, respectively.
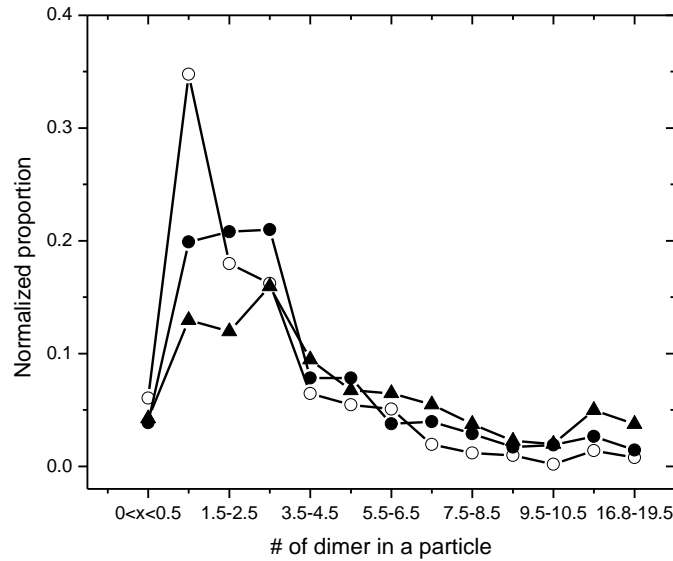
Figure 2.12 Quantitative analysis of AFM images shows a gradual decrease of dimer species and increase in larger species upon incubation.

The symbols represent particle distribution at t=0h (−○−), lag phase (−•−), and exponential phase (−▲−) of G93V holo aggregation. The aggregation samples correspond to G93V in previous Fig. 2.11.

2.3.5 Characterization of aggregate properties

Since aggregate formation is generally highly sensitive to experimental conditions (Glabe, 2008), it is important to check that aggregates generated *in vitro* have the same characteristics as aggregates observed in disease. Thus, the following sections characterize the aggregation with regards to tinctorial and antibody binding properties to determine the relevance of aggregates formed from holo SOD1 to these in ALS patients.

2.3.5.1 Tinctorial properties of aggregates formed from holo SOD1s

The AFM images in Fig. 2.11 show that aggregates formed from holo SOD1 do not exhibit the typical morphology of amyloid fibrils (*i.e.,* smooth and unbranched fibrils) but rather show tangled and granular coated fibrillar morphologies similar to those found in ALS patients and mice models (Kato *et al*, 2001; Shibata *et al*, 1994). To establish further whether holo SOD1 aggregates have other properties typical of amyloid, binding of ThT, which is commonly used to detect amyloid formation, was measured upon aggregation (Hawe *et al*, 2008; Munishkina & Fink, 2007). Fig. 2.13 shows that there is only a very small increase in ThT fluorescence upon aggregation (Fig. 2.13b) compared to that observed for other proteins that form amyloid (Munishkina & Fink, 2007). Congo red dye is another dye that is typically used for detecting amyloid. The absorption spectrum of the dye is red-shifted upon binding to amyloid. There was no change in Congo red absorption spectra upon binding to aggregates formed from pWT (P. Stathopolus and E.M. Meiering, unpublished data). Additionally, ANS is commonly used for detecting exposed hydrophobic patches. There is no significant increase in ANS fluorescence upon aggregation (Fig. 2.13c) or during aggregation (Fig. 2.13d), and a blue shift in the maximum wavelength of ANS emission was not detected, implying that there is no significant hydrophobic area exposed during aggregation. Together with AFM data (Fig. 2.11) and FTIR spectra (chapter 3), ThT, Congo red, and ANS dye binding data indicates that aggregates of holo SOD1s do not possess amyloid properties and do not require significant hydrophobic area exposed for aggregation.
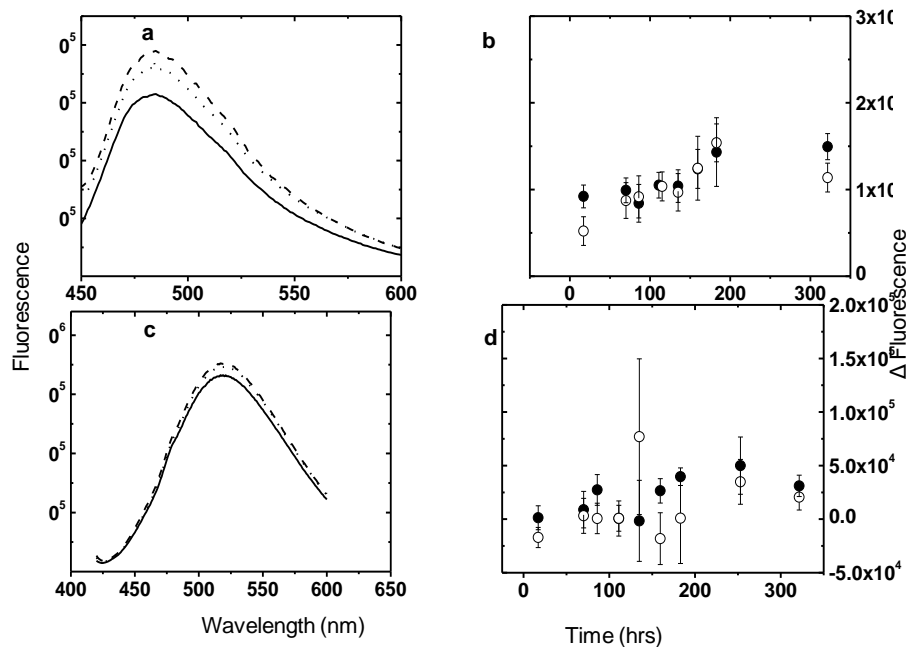
Figure 2.13 ThT and ANS binding by holo pWT aggregates

(a) ThT binding assay of holo pWT; the dye alone (—), the aggregates from 3 mg/mL ($\cdots$) and 8.7 mg/mL (---). (b) The intensity change at λ_{max} (relative to the dye alone) in the ThT fluorescence is plotted as a function of incubation time for 3 mg/mL ($\bullet$) and 8.7 mg/mL ($\circ$) samples. (c) ANS binding assay of holo SOD1s; the dye alone (—), with aggregates from 3 mg/mL ($\cdots$) and 8.7 mg/mL (---) solutions of pWT. (d) The intensity change at λ_{max} (relative to the dye alone) of the ANS fluorescence is plotted against the aggregation time of 3 mg/mL ($\bullet$) and 8.7 mg/mL ($\circ$) SOD1 samples. The aggregation samples (3 and 8.7 mg/mL) for both ThT and ANS dye binding experiments had reached plateaus based on light scattering measurements (321.5 hrs incubation at 37 °C). The samples were not separated between aggregates and supernatant. The presented spectra and values are the average of at least two

different measurements of aliquots taken from the same samples, and the error bars are the s.d of the repeated measurements. Each data point in b and d was calculated by subtracting the signal of the dye alone from the signal of the dye with the protein.

2.3.5.2 Aggregates formed from holo SOD1 are recognized by ALS-specific antibody.

Antibody binding experiments provide further evidence for the medical relevance of the holo SOD1 aggregates studied here. Recently, an antibody that is specific for SOD1 in ALS was developed (Rakhit *et al*, 2007). This antibody recognizes the SOD1 Exposed Dimer Interface (SEDI) by binding to a C-terminal peptide that is buried in the native dimer (Rakhit *et al*, 2007) (Fig. 2.1). SEDI antibody specifically recognizes aggregated SOD1 in post mortem fALS patients and in mice models before and after the onset of disease symptoms, but does not bind to native holo SOD1 (Rakhit *et al*, 2007). It should be noted that SEDI has not been found to detect SOD1 in sALS patients (Hsueh-Ning Liu *et al*, Published Online: 20 Mar 2009); however, this does not preclude a role for SOD1 aggregation in sALS (see Discussion, section 2.4.3). Competition ELISA experiments on purified unaggregated (control) and aggregated holo SOD1 show that SEDI binding increases upon aggregation (Fig. 2.14, $P < 0.05$). The recognition of the dimer interface in the aggregates supports the proposed interpretation of lag phase and protein concentration dependence data, which suggests that formation of aggregates involved dimer dissociation to expose the interface (Fig. 2.2, Fig.2.5, and Fig. 2.8). This striking finding is the first

demonstration of specific antibody binding to aggregates formed by purified SOD1 and in the disease.
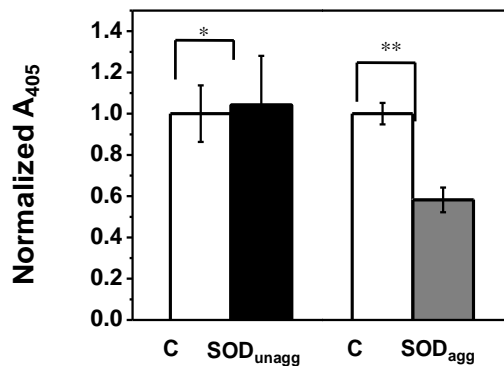
Figure 2.14 SEDI antibody specifically recognizes aggregates formed from holo SOD1.

Specific SEDI binding to aggregated (SOD$_{agg}$) or unaggregated (SOD$_{unagg}$) pWT was measured with competition of the C-terminal peptide epitope (see Materials and Methods, section 2.2.12). C represents the control of SEDI binding to the C-terminal peptide coated to the plate with SOD1 omitted. The increased binding of aggregates relative to control is significant (**, $P < 0.05$), but there is no difference for unaggregated protein relative to control (*, $P > 0.1$). The plotted values represent means $\pm$ s.d. for three independent aggregation experiments, for which sample measurements were made at least in duplicate.

2.4 Discussion

This chapter has demonstrated for the first time that under physiologically relevant conditions holo SOD1 forms, by a nucleation dependent process, aggregates having the same structural as well as dye and antibody binding characteristics as aggregates observed in ALS patients and mice models. Also, the aggregation appears to occur without significant levels of Cu-mediated aberrant chemistry. These results have extensive implications for understanding disease mechanisms in ALS and other protein misfolding disorders, which are a growing group of devastating and prevalent diseases.

2.4.1 Aggregation formed from holo SOD1 does not resemble amyloid.

Aggregation reactions are typically complex, with competing reactions that are highly sensitive to solution conditions (Jahn & Radford, 2008a) and hard to characterize owing to sample heterogeneity (Glabe, 2008) (this is also evident here in the mixture of structures seen by AFM, Fig. 2.9). Consequently, it can be difficult to compare and ascertain the relevance of different *in vitro* and *in vivo* studies. A common aggregate structure formed in many neurodegenerative and other diseases is known as amyloid (Chiti & Dobson, 2006), and there has been debate as to whether or not ALS is an amyloid disease. SOD1 has been shown to form amyloid under destabilizing conditions when subjected to sonication (Stathopulos *et al*, 2004), low pH (DiDonato *et al*, 2003), or agitation (Chattopadhyay *et al*, 2008; Furukawa *et al*, 2008; Oztug Durer *et al*, 2009). Furthermore, there is extensive evidence that all proteins can form amyloid under suitable, typically destabilizing, conditions (Chiti *et al*, 1999; Stefani

& Dobson, 2003). Aggregates found in ALS patients do not exhibit the classic properties of amyloid, such as green-gold Congo Red birefringence (Linke, 2009; Okamoto *et al*, 1991) or smooth unbranched fibrillar structures (Kato *et al*, 2001; Shibata *et al*, 1994).   The aggregates studied here have high *in vivo* relevance because they form under physiologically relevant conditions and, based on multiple criteria (structure and dye and antibody binding), their properties match those of aggregates formed in ALS.

2.4.2 SOD1 can aggregate by many pathways.

The mechanism of aggregation from holo SOD1 likely involves both loss of metals and dimer dissociation. Based on the high stability of holo SOD1 under the solution conditions used here, the population of the unfolded state for pWT and mutants will be extremely small (Rumfeldt *et al*, 2006), consistent with aggregation occurring from a state that is closer to the native state. Previously, holo SOD1 has been proposed to be incapable of forming aggregates owing to its high stability (Shaw & Valentine, 2007).   However, aggregation could be initiated *via* local structural fluctuations (Chiti & Dobson, 2009), which are not necessarily linked to global stability (Khare & Dokholyan, 2006).   Recent experimental data suggest that the metal binding characteristics of SOD1 give rise to frustration and misfolding (Nordlund *et al*, 2009). The activity and metal analysis data show that aggregation involves loss of some, but not all, metal (Fig. 2.6 and Table 2.1) and the lag phase (Fig. 2.2 and Fig. 2.5) and SEDI binding data (Fig. 2.14) suggest that dimer dissociation is occurring.

The experimental results herein support a mechanism similar to that proposed by Dokholyan and coworkers (Khare, Caplow & Dokholyan, 2004), modified to allow for additional partial as well as the originally proposed complete loss of metal:

Scheme 2.1
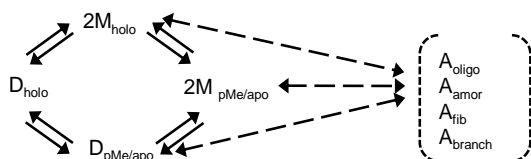
Multiple pathways for pathological SOD1 aggregation. D_{holo}, M_{holo}, $D_{pMe/apo}$, $M_{pMe/apo}$, A_{oligo}, A_{amor}, A_{fib}, and A_{branch} represent the holo dimer, holo monomer, partially metallated or apo dimer, partially metallated or apo monomer, soluble oligomers, amorphous aggregates, fibrillar aggregates and branched aggregates, respectively. The expanded mechanism of Dokholyan and coworkers (Khare, Caplow & Dokholyan, 2004) is shown in solid lines and are supported by the data herein. Fully metallated SOD1s may monomerize or lose metal by local fluctuation. Either step may promote the other as the next step. Dashed lines indicate additional possible aggregation pathways (which may include multiple steps) that are not excluded by the current data, and are supported by other findings from the literature. The various aggregated species included in dashed square brackets may interconvert.

There is considerable experimental support for Scheme 2.1 ((Khare, Caplow & Dokholyan, 2004) and references therein). Extensive additional data from the literature (Oztug Durer *et al*, 2009; Shaw & Valentine, 2007) (Banci *et al*, 2005; Banci *et al*, 2007b; Chattopadhyay *et al*, 2008; Stathopulos *et al*, 2003) can be included and rationalized by including additional pathways for aggregation of SOD1. Similarly, multiple pathways have also been proposed for amyloid formation (Chiti & Dobson, 2006; Jahn & Radford, 2008a). Also, a key and often overlooked point is that *all* SOD1 mutations studied to date destabilize the holo protein

(Hayward *et al*, 2002; Rumfeldt *et al*, 2006; Stathopulos *et al*, 2003), which is not consistently the case for the apo protein (Rodriguez *et al*, 2005). In addition, the dimer interface for holo SOD1 is only slightly stronger than for apo SOD1 (Hornberg, Logan, Marklund & Oliveberg, 2007; Rumfeldt *et al*, 2006; Vassall *et al*, 2006); assuming dimer dissociation is required for aggregation; this means that it is certainly feasible for holo SOD1 to aggregate. Furthermore, fALS-associated mutations of the holo form increase dynamics, causing complex changes that propagate throughout the structure, as shown by NMR and x-ray studies of G93A (Shipp *et al*, 2003), A4V (Hough *et al*, 2004a), I113T (Hough *et al*, 2004a), and S134N (Banci *et al*, 2005). Interestingly, the lag phase for G85R, which has weakened metal binding (Cao *et al*, 2008), is shorter than for pWT and G93 mutants (Fig. 2.3), suggesting that loss of metal may favor dimer dissociation and hence aggregation. This is reasonable because the Zn binding loop leads into the dimer interface (Fig. 2.1) (Hornberg, Logan, Marklund & Oliveberg, 2007). Conversely, the dimer interface mutants A4V, A4T and I113T have weakened Zn binding(Crow *et al*, 1997a). Computational studies on many mutants have shown complex coupling between the dimer interface and metal binding loops (Khare & Dokholyan, 2006). Thus, the proposed expanded aggregation mechanism accounts for our new data as well as extensive previous experimental and computational findings. Further support for loss of metals from holo SOD1 during aggregation is presented in Chapter 3.

The Zn binding loop and electrostatic loops (Fig. 2.1) may be involved in forming intermolecular interactions in SOD1 aggregates. Recently, as-isolated SOD1s that are partially metallated have been reported to exhibit structural and dynamic changes affecting

mainly the electrostatic and Zn binding loops (Molnar *et al*, 2009). Although many mutant SOD1s are wild-type-like and appear to be predominantly properly metallated *in vivo*, there is also evidence for incomplete metallation of numerous mutants in various *in vivo* systems (Borchelt *et al*, 1994; Goto *et al*, 2000; Hayward *et al*, 2002; Seetharaman *et al*, 2009; Valentine, Doucette & Zittin Potter, 2005). Common intermolecular interactions involving these loops and giving rise to branched assemblies have been identified in holo wild type and mutant SOD1 crystal structures (Hough *et al*, 2004a). Also, many variations involving these (and various other) loops have been noted in crystal structures of partially or fully metal depleted wild type and mutant SOD1s, very often with formation of fibrillar assemblies (Elam *et al*, 2003). Pertinent to the secondary nucleation observed here, the intermolecular interactions in the crystals may provide clues regarding possible heterogeneous nucleation sites on the sides of fibrils. The above considerations together with the results presented herein suggest that aggregation from the holo protein may play a critical role in disease.

2.4.3 Limited role for intermolecular disulfide bond formation in aggregation

Many previous studies have focussed on the role of intermolecular disulfide bonds in SOD1 aggregation. Recently, Borchelt and coworkers have shown that intermolecular disulfide bond formation is favoured only in the later stages of disease in mice and so it is likely a secondary effect (Karch *et al*, 2009). *In vitro* studies of oxidative aggregation of wild-type apo SOD1 have also reported evidence for non-covalent interactions (Banci *et al*, 2007b; Chattopadhyay *et al*, 2008; Furukawa *et al*, 2008; Oztug Durer *et al*, 2009). Our studies are most pertinent to understanding non-covalent association, since the free cysteines

are eliminated in pWT. This may be particularly important for the formation of pathogenic aggregates early in disease, and also contribute to ongoing toxic aggregation as the disease progresses.

2.4.4 Implications for disease

The observation of the same type of aggregation for pWT and mutant holo SOD1 suggests that the holo protein may play an important role in both forms of the disease. SOD1 is a particularly abundant protein (see Introduction, section 2.1.1), placing it at high risk for aggregation (Rakhit *et al*, 2004). Furthermore, motor neurons are particularly vulnerable to the toxic effects of protein aggregation (Boillee, Vande Velde & Cleveland, 2006a). There is extensive evidence that many forms of SOD1 may aggregate, consistent with the general mechanism proposed in Scheme 2.1. Aggregated SOD1 is generally found in fALS, but has only been reported for a subset of sALS cases (Hsueh-Ning Liu *et al*, Published Online: 20 Mar 2009; Shibata, Asayama, Hirano & Kobayashi, 1996; Shibata *et al*, 1994). This does not, however, rule out a role for SOD1 aggregation in additional sALS cases. Detection of SOD1 in aggregates, and indeed the types of protein inclusions observed in different cases of ALS, vary considerably (Kato, 2008). Also, SOD1 aggregates could be involved in early disease stages but do not accumulate to high levels in end-stage aggregates. Alternatively, SOD1 may be present in end-stage aggregates but may not be detected due to inaccessibility of SOD1 epitopes, for example due to ubiquitination (Kato *et al*, 2001; Okamoto *et al*, 1991). It is also possible that the structures of SOD1 aggregates in ALS vary, perhaps in specific ways associated with different mutations (Shaw & Valentine, 2007) and disease

characteristics such as duration or onset, analogous to varying disease and aggregate characteristics in different prion strains (Prusiner, 1998). Consistent with this, different mutant SOD1-mouse models have distinct phenotypes (Kato, 2008). Further studies are needed to determine the characteristics of aggregates formed by different forms of SOD1 (fALS mutations and metallation states) (Banci *et al*, 2005; Banci *et al*, 2007b; Elam *et al*, 2003; Khare, Caplow & Dokholyan, 2004; Oztug Durer *et al*, 2009; Rakhit *et al*, 2004; Stathopulos *et al*, 2003), and different disease characteristics and stages.

The seeding and secondary nucleation observed here also have important implications for understanding the disease characteristics of ALS. The autosomal dominant inheritance of SOD1-fALS means that just one copy of the mutant SOD1 gene causes disease, and patients also express wild-type SOD1 (Boillee, Vande Velde & Cleveland, 2006a). The cross-seeding of mutant and pWT show that the two forms can co-aggregate. This is consistent with results from cell culture fALS models where pWT and mutant SOD1 co-aggregate when co-expressed (Prudencio *et al*, 2009), and with fALS mice studies that found overexpression of pWT is required to convert A4V mice to a disease phenotype (Deng *et al*, 2006) and enhances the disease phenotype in other mutant SOD1 fALS mice models (Turner & Talbot, 2008). Combining different mutants with wild-type may have different aggregation (Fig. 2.7) and hence disease characteristics. Mutations could enhance initiation and/or propagation of aggregation and so favor disease. Also, seeding and the very rapid growth of aggregates due to secondary nucleation processes may be linked to the very rapid disease progression in ALS.

The aggregation observed here for holo SOD1 shares many characteristics with the aggregation of other disease-associated proteins, including occurrence of a lag phase (due to unfavorable nucleation, which can be overcome by seeding), formation of amorphous and fibrillar species, and very rapid aggregate growth due to secondary nucleation. These findings support the hypothesis that SOD1 aggregation has common toxic effects with protein aggregation in other diseases. The experimental system reported here represents a breakthrough for further elucidation of mechanistic details of SOD1 aggregation and co-aggregation, and further defining key commonalities with and difference from other diseases. It can also be used to determine the nature and consequences of possible inappropriate interactions between SOD1 aggregates and other cellular components, such as chaperones, protein degradation machinery and membranes (Boillee, Vande Velde & Cleveland, 2006a). Finally, it may ultimately be useful for developing new therapeutics, such as small molecules or antibodies, which have shown promising initial results (Ray *et al*, 2005; Urushitani, Ezzi & Julien, 2007). In summary, the current results provide new and potentially general insights into protein aggregation in disease and provide the basis for further studies to define aggregation mechanisms, identify inappropriate interactions, and develop urgently needed therapeutic strategies against toxic protein aggregation.

Chapter 3

The role of metal loss in aggregation from holo SOD1

3.1 Introduction

Protein aggregation is a subject that has been extensively investigated in the field of biochemistry. This is partially because protein aggregation has been implicated in the pathology of many different human diseases. Importantly, aggregation can sometimes occur naturally with protein function (Chiti & Dobson, 2006; Ross & Poirier, 2004). For example, polymerization of the muscle protein, actin controls the mobility and shape of the cells (Carlier & Pantaloni, 1997; Condeelis, 1993). Thus, understanding aggregation is important not only in disease but also in natural protein function. Pioneering work in understanding aggregation mechanisms using kinetic and thermodynamic approaches was reported by Oosawa and coworkers in 1959, who developed an aggregation model (Oosawa *et al*, 1959). This classical model has been used extensively over the years by other researchers. Based on Oosawa and coworkers' work, various related models and model systems have been developed, such as hemoglobin polymerization (Bishop & Ferrone, 1984) and prion protein self-replication (Griffith, 1967). In general, however, aggregation is not yet well understood due to the complexity of aggregating systems.

A general overview of aggregation is given in Fig 3.1, which is simplified from the scheme proposed by Roberts (Roberts, 2007). It is important to keep in mind that this simple depiction is an attempt to describe protein aggregation, but aggregation reactions are much

98

more complicated than depicted in Fig. 3.1. In particular, aggregation *in vivo* is far more complex due to the many possible modulating effects in the cellular environment, including crowding effects (Munishkina *et al*, 2004) and/or interactions of various cellular components such as chaperones, protein degradation machinery, and membranes (Bellotti & Chiti, 2008). Fig. 3.1 illustrates three stages pertinent to aggregation: pre-stage, stage I, and stage II. Stage I is the reversible association of two or more reactive units, which was first introduced by Oosawa and coworkers (Oosawa, 1975; Oosawa *et al*, 1959). Their reactive unit was the folded monomer of actin and therefore they did not consider a pre-stage in their work. These early studies considered aggregation as a simple association reaction and usually monomers were the addition unit (Bishop & Ferrone, 1984; Ferrone, 1999; Oosawa, 1975). Later, protein unfolding pathways (corresponding to the pre-stage in Fig. 3.1) were added to aggregation mechanisms as many experimental results supported the importance of additional monomer unfolding events proceeding the aggregation process (Andrews & Roberts, 2007; Arnaudov & de Vries, 2007; Kelly, 1998). Thus, competition between re-folding and aggregation can add additional complexity (Arnaudov & de Vries, 2007; Hamada *et al*, 2009; Wiseman *et al*, 2005). In addition, many different types of unfolding intermediates have been proposed as the reactive units in the aggregation of different proteins. A partially unfolded monomer is likely to act as the reactive unit in most aggregating systems, for example, for monomeric proteins such as lysozyme (Booth *et al*, 1997) or β2-microglobulin (Chiti *et al*, 2001), and for multimeric proteins such as TTR (Wiseman, Powers & Kelly, 2005) and β-lactoglobulin (Hamada *et al*, 2009). Generally, multimeric proteins are proposed to dissociate before aggregating. It is important to note that

99

the same protein can form different aggregate structures (*i.e.,* having different morphology) due to different experimental conditions that result in the formation of different reactive units (Khurana *et al*, 2001).

Stages I and II are separated by the formation of nuclei, the least stable species in aggregation pathway and, therefore, the least populated species (Fig. 3.1) (Ferrone, 1999). Historically, nucleation-dependent aggregation was first introduced by Oosawa and Asakura (Oosawa, 1975) as primary (homogeneous) nucleation, whereby reactive units associate at the end of oligomers to form primary nuclei during a thermodynamically unfavorable process, generating linear, unbranched aggregates (*e.g.,* polyglutamine aggregation associated with Huntington's disease) (Chen *et al*, 2002). Ferrone *et al*. later introduced the secondary nucleation mechanism, whereby reactive units add to a secondary nucleus site *via* heterogeneous nucleation (sides of an existing aggregate) or fragmentation generating new ends for further aggregation growth. Aggregates formed by secondary nucleation are characterized by branched structure and rapid aggregate growth preceeding an exponential phase (Ferrone, 1999) (this is described in more detail in section 2.3.6). After nucleation, thermodynamically favored additions (*i.e.,* irreversible additions) occur during Stage II. One can also include additional interactions between aggregates in stage II, such as cross-linking and lateral associations of various fibrillar aggregated species (Roberts, 2007).

a

Native multimer

Partially unfolded monomer

Reactive unit

Nucleus

Mature fiibrils

Native monomer

Pre-Stage

Stage I

Stage II

b

ΔG (kcal/mol)

i or j = Critical nucleus

Aggregate size
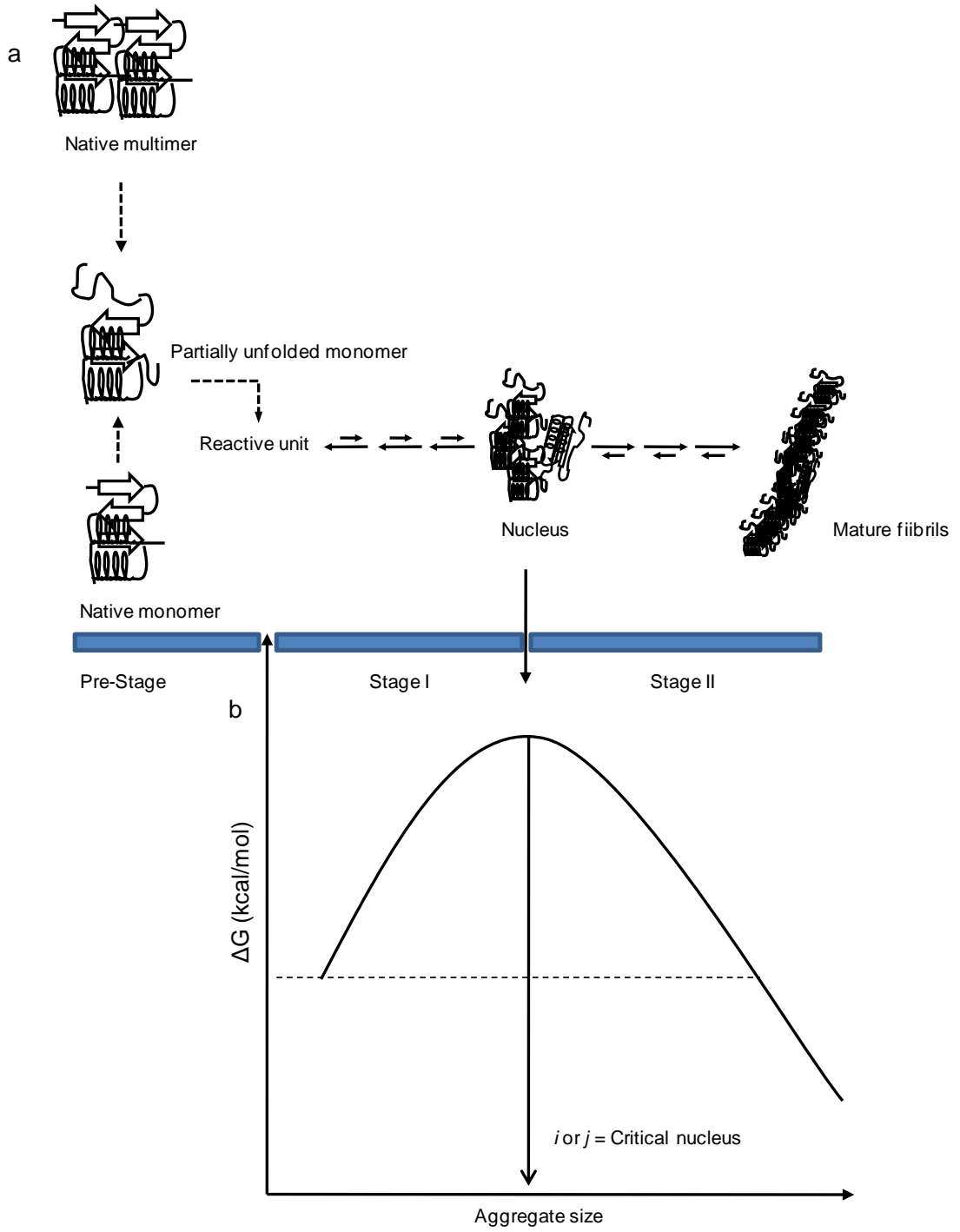
Figure 3.1 General scheme for protein aggregation

This figure was modified from Roberts *et al* (Lowry, Rosebrough, Farr & Randall, 1951). (a) Pre-stage represents a protein unfolding event which results in the formation of reactive units. Partially unfolded monomers have been proposed as reactive units, or to be closely related to the reactive unit. Alternative pathways for formation of the reactive unit from a native multimer or monomer are illustrated here. Stage I is the energetically unfavourable step of reversible association of reactive units to form a nucleus, and stage II is the subsequent favourable stage of irreversible addition of reactive units to form a fibrillar aggregate structure. (b) Relative energy diagram for reactive units, nucleus, and mature fibrils.

3.1.1 Theoretical aspects of protein aggregation

This section describes the differential equations for the kinetics of aggregation including both homogeneous and heterogeneous nucleation. The rate equations for the formation of aggregates and the disappearance of native proteins are formulated using the classical model proposed by Oosawa and coworkers (Oosawa, 1975) with the addition of heterogeneous nucleation introduced by Ferrone and coworkers (Bishop & Ferrone, 1984; Ferrone *et al*, 1985). The equations from Eq.3.1 to Eq. 3.10 are based on Oosawa's model, which is based on primary nucleation, followed by inclusion of equations for heterogeneous nucleation. The heterogeneous nucleation model of Ferrone and coworkers has been used extensively to study the polymerization of deoxygenated hemoglobin S involved in the

pathophysiology of sickle cell disease (Bishop & Ferrone, 1984; Ferrone, Hofrichter & Eaton, 1985). This model has also been applied to other systems, including β-lactoglobulin (Arnaudov & de Vries, 2007) and polyglutamine aggregation (Chen *et al*, 2002) and is also applied here to demonstrate the heterogeneous nucleation dependence of aggregation from holo SOD1s (see Results, section 2.3.6).

According to Oosawa's model, the first association step in protein aggregation is represented as:

$$A + A \rightleftharpoons A_2 \qquad K_2 = \frac{[A_2]}{[A]^2} \qquad \qquad \text{Eq. 3.1}$$
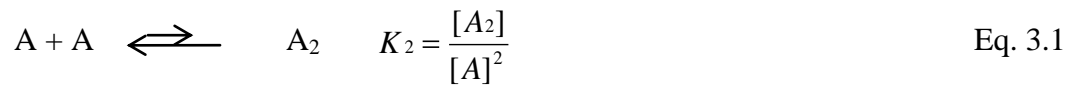
where A is the monomer, A_2 is the dimer, and K_2 is the equilibrium constant for association. Prior to formation of the nucleus, association reactions are reversible and dissociation is favored (the length of the arrows represent the relative size of the corresponding rate constants). The concentration of A_2 can be expressed using K_2 as:

$$[A_2] = K_2[A]^2 \qquad \qquad \text{Eq. 3.2}$$

The next association and equilibrium constant are shown in the same manner as Eq. 3.1:

$$A_2 + A \rightleftharpoons A_3 \qquad K_3 = \frac{[A_3]}{[A_2][A]} = \frac{[A_3]}{K_2[A]^3}, \qquad \qquad \text{Eq. 3.3}$$

103
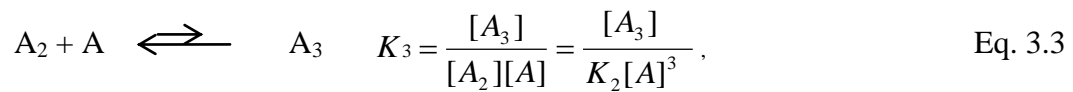
where $[A_2]$ is replaced using Eq. 3.2. Therefore, the concentration of A_x (for any given x-mer) can be expressed in terms of K_x:

$$[A_x] = K_2 K_3 \cdots K_x [A]^x$$

Eq. 3.4

We define *i*-mers (the associated species containing *i* units of A) as the homogeneous nucleus, which is the least stable species in the reaction. Additionally, the rate constant for formation of A_i from $A + A_{i-1}$-mer and the reverse dissociation reaction are taken to be equal (Ferrone, 1999). The equilibrium constant, K_i and the concentration of A_i, are given by:

$$A_{i-1} + A \rightleftharpoons A_i \qquad K_i = \frac{[A_i]}{[A_{i-1}][A]} = \frac{[A_i]}{K_2 K_3 .... K_{i-1}[A]^i},$$

$$[A_i] = K_2 K_3 ...... K_i [A]^i = K^* [A]^i$$

Eq. 3.5

where $K^* = K_2 K_3 \cdots K_{i-1}$. The rate equations for *i*-mers (nucleation) and (*i*+1)-mers can then be expressed in terms of individual association and dissociation rate constants as:

$$\frac{d[A_i]}{dt} = k_{+i}[A_{i-1}][A] - k_{-i}[A_i] + k_{-(i+1)}[A_{i+1}] - k_{+(i+1)}[A_i][A]$$

Eq. 3.6

$$\frac{d[A_{i+1}]}{dt} = k_{+(i+1)}[A_i][A] - k_{-(i+1)}[A_{i+1}] + k_{-(i+2)}[A_{i+2}] - k_{+(i+2)}[A_{i+2}][A]$$

Eq. 3.7

Assuming that the total concentration of aggregates formed by primary nucleation (C_{P1}, where P1 represents aggregates formed by primary nucleation) is the sum of the concentrations of all species of size ($i+1$) or larger and setting the rate constant for addition and dissociation of the monomer during the formation of the primary nucleus in stage 1 and the aggregates (P1) in stage II to be (k_+) and (k_-), respectively, then the rate of aggregate formation is given by:

$$\frac{d[C_{P1}]}{dt} = \frac{d}{dt} \sum_{x=i+1}^{\infty} C_x = k_+[A_i][A] - k_-[A_{i+1}]$$

Eq. 3.8

where C_x is the concentration of aggregates at a given size. Note the last two terms in any given rate equation are cancelled out by the first two terms in the rate equation of the next larger aggregate (*i.e.,* with one more monomer added). Eq. 3.8 can be simplified using the assumption $k_+[A] \gg k_-[A_{i+1}]$:

$$\frac{d[C_{P1}]}{dt} = k_+[A_i][A]$$

Eq. 3.9

If [A_i] is replaced using Eq. 3.5, then the Eq. 3.9 becomes:

$$\frac{d[C_{P1}]}{dt} = k_+ K^*[A]^{i+1}$$

Eq. 3.10

This is the general equation for growth of aggregates formed by a primary nucleation process with subsequent addition of monomer, A.

Now, let us consider heterogeneous nucleation as per Ferrone *et al.* (Bishop & Ferrone, 1984; Ferrone, Hofrichter & Eaton, 1985) in addition to primary nucleation (Fig. 3.2).
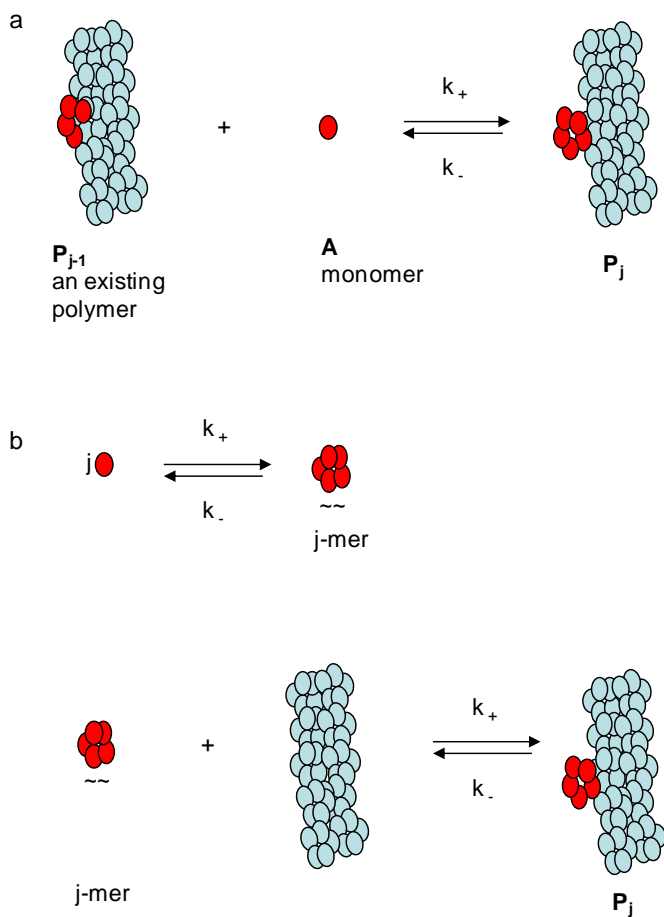
Figure 3.2 Formation of heterogeneous nucleus, Pj

(a) P_j is formed by the association of a monomer to the existing polymer, P_{j-1}. (b) The formation of P_j is treated as an equilibrium process with two hypothetical steps (*top* and *bottom*): (1) the formation of *j*-mers first in the solution; and (2) the attachment of the *j*-mer onto the surface of an existing polymer.

The first association of a monomer (A) onto the surface of an existing polymer (P_1) can be written as:

$$P_1 + A \rightleftharpoons P_2 \qquad K_2 = \frac{[P_2]}{[P_1][A]}$$

Eq. 3.11
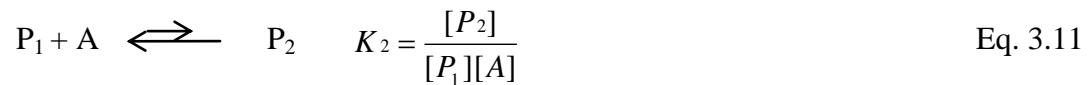
Using a similar model and derivation as for homogeneous nucleation but with *j* (instead of *i*) monomers forming the heterogeneous nucleus (instead of homogeneous, for details see Appendix A), the rate equation of aggregate formation is given by:

$$\frac{dC_{P2}}{dt} = k_+[P_j][A]$$

Eq. 3.12

where C_{P2} is the total concentration of aggregates (P2, any species of size (P_{j+1}) or larger) formed *via* heterogeneous nucleation, P_j is a heterogeneous nucleus, k_+ is the rate constant for addition of monomer, A, to form homogeneous and heterogeneous nuclei and aggregates (P1

and P2). Therefore, the total aggregation from both primary and heterogeneous nucleation is given by:

$$\frac{d[C_P]}{dt} = k_+ K^* [A]^{i+1} + k_+ [P_j][A]$$

Eq. 3.13

where P is the sum of P1 and P2, and C_P is the total concentration of aggregates. It is convenient to treat $[P_j]$ as an equilibrium process taking place in two hypothetical steps: (1) the formation of free j-mer in solution, (2) the attachment of this j-mer onto the surface of an aggregate (Fig. 3.2). In order to express $[P_j]$ in terms of initial protein concentration $[A_0]$, the Langmuir isotherm derivation is considered for the equilibrium of heterogeneous nucleation. Then, $[P_j]$ can be expressed as (see Appendix B and C for details):

$$[P_j] = [P_{jt}]K_j C_j = \theta(A_0 - A)\overline{K_j}[C_j] = \theta(A_0 - A)\overline{K_j}\tilde{K}_j[A]^j$$

Eq. 3.14

where $[P_{jt}]$ is the total concentration of available sites for attaching a solution phase j-mer, $\overline{K_J}$ is the equilibrium constant for attaching a solution phase j-mer to the polymer surface, C_j is the concentration of solution phase j-mer, A_0 is the initial total monomer concentration of the protein, $\bar{\theta}$ is a scaling factor that determines the number of available nucleation sites per polymerized monomer, and $\tilde{K}_j$ is the equilibrium constant for formation of a j-mer in solution from j monomers. Therefore, the change in concentration of aggregates with time can be obtained by combining Eq. 3.13 and 3.14 as:

$$\frac{d[C_P]}{dt} = k_+ K^*[A]^{i+1} + k_+[P_j][A] = k_+ K^*[A]^{i+1} + k_+ \overline{\theta}(A_0 - A)\overline{K_j}\,\tilde{K}_j[A]^{j+1}$$

`Eq.3.15

This is the general equation for growth of aggregates formed by homogeneous and heterogeneous nucleation processes with subsequent addition of monomers.

The rate equation for loss of the native protein from solution into the homogeneous aggregate is given by:

$$\frac{-d[A]}{dt} = \frac{d}{dt}(\sum_{x=i+1}^{\infty} x[A_x]) \cong (k_+A - k_-)C_p$$

Eq. 3.16

where the details are described in Appendix D.

Since the differential rate equations (Eq. 3.15 and 3.16) become more complicated due to the addition of heterogeneous nucleation, the equations cannot be integrated analytically. Ferrone *et al*. (Bishop & Ferrone, 1984; Ferrone, Hofrichter & Eaton, 1985) solved this problem by linearizing the rate equations as Taylor series and then truncating the series to first-order terms. This method produces a simplified set of equations that can be integrated and applied to the initial 10-15% of aggregation reactions (Bishop & Ferrone, 1984; Ferrone, Hofrichter & Eaton, 1985). As a result, the concentration of protein that is incorporated into aggregates ($\Delta = A_0$-A_{free}, where A_0 is the initial (non-aggregated) protein

concentration and A_{free} is the concentration of non-aggregated protein at a given time and can be written as:

$$\Delta = \frac{a_0}{a_1}(\cosh(a_1 b_0)^{1/2} t - 1)$$
<div align="right">Eq. 3.17\</div>

where $a_0 = k_- K_i [A_0]^{i+1}$, $a_1 = (i+1)k_+ K_i [A_0]^i + k_+ \bar{\theta} \overline{K}_J \widetilde{K}[A_0]^{i+1}$, and $b_0 = k_+([A_0] - [A_s])$. Eq. 3.17 actually corresponds to Eq. 2.4, (*i.e.,* fractional completion $= |A|$ {cosh($|Bt|$)-1}). However, the parameters A and B in Eq. 2.4 are expressed in kinetic and thermodynamic terms relating to the aggregation model. Fitting of aggregation data to Eq. 3.17 /2.4 provides insight into the mechanism, as described in Chapter 2. The formalism of Oosawa and Ferrone allows for interpretation in terms of kinetics and thermodynamic terms.

Additional insight into the aggregation mechanism can be obtained by considering, AB^2 and B^2 since AB^2 is composed of the terms related to only primary nucleation and information related to heterogeneous nucleation can be deduced from the combination of AB^2 and B^2 (Bishop & Ferrone, 1984; Ferrone, Hofrichter & Eaton, 1985).

$$AB^2 = a_0 b_0 = K_+^2([A_0] - [A_s])K_i A_0^{i+1}$$
<div align="right">Eq. 3.18</div>

$$B^2 = a_1 b_0 = k_+([A_0] - [A_s])\{(i+1)K_i[A_0]^i + \bar{\theta}\overline{K}_J \widetilde{K}_J[A_0]^{j+1}\}$$
<div align="right">Eq. 3.19</div>

where A_s is soluble protein concentration at equilibrium. Equations 3.18 and 3.19 can be used to gain further insight into the aggregation mechanism for holoSOD1 as a log-log plot of AB^2 *versus* A_0 can provide information about the size of the nuclei since the slope of the plot is (i+1).

3.1.2 Methods to characterize aggregation

A variety of techniques has been used for characterization of aggregation processes involving the partially unfolded reactive unit and the oligomers that form prior to fibril formation. These include sodium dodecyl sulfate polyacrylamide gel electrophoresis (SDS-PAGE), light scattering (LS), Fourier transform infrared (FTIR) spectroscopy, atomic force microscopy (AFM), CD spectroscopy, analytical ultracentrifugation (AUC) (Liu *et al*, 2006), and intrinsic and extrinsic fluorescence (Alcaraz & Donaire, 2004) (reviewed in (Frieden, 2007; Morris *et al*, 2009; S.E., 2006)). In the current work, the mechanism of holo SOD1 aggregation is further investigated using LS, FTIR, CD, ultraviolet (UV), and fluorescence spectroscopy. The application of optical spectroscopies involves well established qualitative analyses. The following section describes the background theory for quantitative analysis of dynamic light scattering (DLS) since DLS was used as a tool to analyze aggregation profiles.

3.1.2.1 Dynamic Light Scattering (DLS)

In contrast to static light scattering (SLS) which collects scattered light from particles, DLS measures changes in light scattering over time since the intensity of light scattering

from particles in a solution fluctuates due to Brownian motion. The time-dependent

fluctuation depends on how fast the particles move. The rapid change of the light scattering

intensity is commonly analyzed using autocorrelation functions. The following processes are

used to accomplish the autocorrelation analysis: first, the deviation of scattered intensity (Δi

(t)) at time t is defined from the intensity (i (t)) at time t and the average intensity i as:

$$\Delta i\ (t) = i\ (t) - i \qquad\qquad \text{Eq. 3.20}$$

Then, the autocorrelation function is defined using a fixed τ as:

$$G(\tau) = \overline{\Delta i\ (t) \bullet \Delta i\ (t + \tau)} \qquad\qquad \text{Eq. 3.21}$$

where $\Delta i\ (t + \tau)$ is the deviation of scattered intensity at some later time ($t + \tau$) and the bar

means to average the product over t, using a fixed interval τ. When τ is very small, both

terms used in Eq. 3.21 will have the same sign, whereas when τ is large, the value of $\Delta i\ (t) \bullet$

$\Delta i\ (t + \tau)$ will be negative as often as positive, having a higher chance to be zero (Fig. 3.3)

(van Holde Kensal E., Johnson W. Curtis & Shing, 1998).
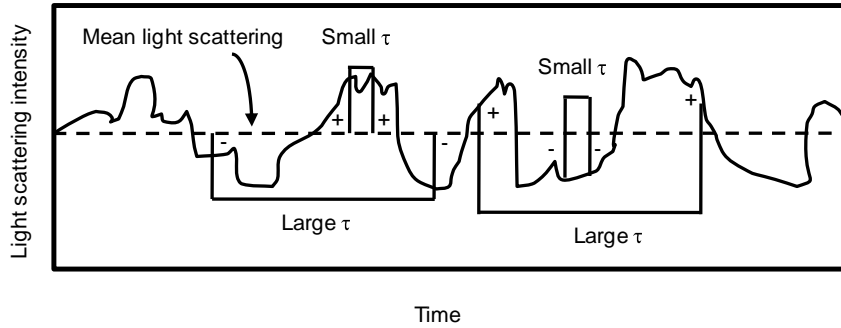
Figure 3.3 Autocorrelation of two different cases with large and small τ

For large τ, the chance that the average of $\Delta i\ (t) \bullet \Delta i\ (t + \tau)$ over time, t in Eq. 3.21 becomes

zero is high, whereas for small τ, $\Delta\ i(t)$ and $\Delta\ i(t + \tau)$ in Eq. 3.21 usually have the same sign.

Thus, the quantity of $G(\tau)$ decays exponentially with τ according to:

$$G(\tau) = exp(-Dq^2\tau)$$

Eq. 3.22

where D is the diffusion coefficient of solution, and q is the scattering vector. The scattering

vector is given by:

$$q = \left(\frac{4\pi n}{\lambda_0}\right)\sin\left(\frac{\theta}{2}\right)$$

Eq. 3.23

where n is the refractive index of solution, λ_0 is the wavelength of the incident light, and θ is the scattering angle. Using the diffusion coefficient, the hydrodynamic radius of particles can be determined from the Stokes-Einstein relationship with the assumption that the particles are hard spheres (Jachimska *et al*, 2008; van Holde Kensal E., Johnson W. Curtis & Shing, 1998):

$$R_h = \frac{kT}{6\pi\eta D} \qquad\qquad \text{Eq. 3.24}$$

where k is Boltzmann's constant, T is temperature in Kelvin and η is the solvent viscosity at T. When the distribution of particle sizes is narrow and monodisperse, the average radius can be determined by the well known method of cumulants analysis (Koppel, 1972). However, when the particle distribution is polydisperse, as can occur during protein aggregation, cumulants analysis is no longer applicable. In this case, Eq. 3.22 must be integrated over all possible sizes and corresponding diffusion coefficients using the CONTIN method (Provencher, 1982).

Although DLS has been developed as a tool for monitoring aggregation time courses (Nicolai & Durand, 2007), it still has weak points for applications with protein aggregation. For example, the hydrodynamic radius of the particles estimated using Eq. 3.24 is based on the assumption that the particles are hard spheres. Often, proteins form aggregates with fibrillar shapes, which cannot be analyzed as described above. There is, however, an

empirical equation available to convert the calculated diameter to fibril length (Lomakin *et al*, 1996).

3.1.3 Chapter Overview

The results presented in this chapter show that dimer dissociation and metal loss play important roles in the aggregation that arises from the native, holo form of SOD1, with or without fALS associated mutations, under physiologically relevant solution conditions (37 °C and pH 7.8). Moreover, various structural probes (intrinsic fluorescence, CD, and UV spectroscopies) provide evidence for two aggregation pathways that differ with respect to dimer dissociation and metal loss. Thus, this chapter provides additional experimental evidence for the aggregation mechanism proposed in chapter 2 (Scheme 2.1) and further supports the hypothesis that the most stable form of SOD1 can play an important role in pathological aggregation of ALS.

3.1.4 Other contributions

This work includes data obtained by various people, which is acknowledged in the following text. I was involved in obtaining all of the data described in this chapter unless otherwise stated. I would like to thank: Kristin Dimmick, who assisted in collecting aggregation data including light scattering measurements; and Ming Sze Tong, an MSc student who also assisted in collecting aggregation profiles of holo A4S and holo A4T.

Metal analysis for confirming Cu/Cu SOD1 was done at the ALS laboratory Group in Waterloo using inductively coupled plasma- mass spectrometry (ICP-MS).

3.2 Materials and Methods

3.2.1 Expression and purification of pWT and mutant SOD1

The SOD1 proteins were prepared as described in section 2.2.1.

3.2.2 Preparation of apo from holo SOD1

Extensive dialysis was used for preparation of apo SOD1 from holo SOD1. A dialysis bag (3000 Da cutoff, cellulose membrane. Spectrum Laboratories, Inc.) was regenerated by soaking it into water for 3 times (20 min per each time) prior to being used. Holo proteins were dialyzed first against 50 mM sodium acetate, 100 mM ethylenediaminetetraacetic acid (EDTA), pH 3.8 at 4 °C (at least 3 exchanges of 4 L, 8 hrs per each time). Then, the protein is dialyzed against 50 mM sodium acetate with 100 mM NaCl, pH 3.8 at 4 °C (at least 3 exchanges of 4 L, 8 hrs per each time). Lastly, the proteins were dialyzed against milliQ water at 4 °C (at least 3 exchanges of 4 L, 8 hrs per each time). The apo proteins were concentrated using an Amicon untrafiltration device (YM3 amion untrafiltration membrane, Millipore Ltd.). Protein concentration was determined using the Lowy assay (Lowry, Rosebrough, Farr & Randall, 1951) and aliquoted into various volumes. Then the proteins were kept at -80 °C.

3.2.3 Preparation of Cu/E and E/Zn SOD1

To identify whether holo SOD1 loses metals during aggregation by taking UV measurements, Cu/E and E/Zn SOD1 (E represents empty) were prepared as following the procedures in a previous study (Beem *et al*, 1974). Apo pWT was diluted to 0.45 mg/mL in Milli Q water, and then 1 eq. (per monomer) of $CuCl_2$ or $ZnCl_2$ (*i.e.,* 5.6 μL of 5mM of $CuCl_2$ or $ZnCl_2$) was added. (Note that at the end of the apo SOD1 preparation, the pH of the solution is 3.8; hence an additional acidification step was not needed (Beem, Rich & Rajagopalan, 1974)). Since the metal reconstitution is time-dependent (Beem, Rich & Rajagopalan, 1974), the mixtures were incubated overnight at room temperature. Cu/Cu SOD1 was prepared using a bench-top fermentor by adding excess Cu ions and the metal contents in the proteins was identified using a ELAN9000 (Perkin Elmer) following the procedure of EPA200.8.

3.2.4 Static and dynamic light scattering (SLS and DLS)

Static and dynamic light scattering were measured simultaneously, using a 90Plus particle sizer (Brookhaven Instruments, Inc.) or a Zetasizer Nano-SZ (Malvern). Comparable results were obtained with both instruments. The autocorrelation functions measured for the protein samples are an average of 10 (5) consecutive measurements for 30 sec (10 sec) with the 90Plus (Nano-SZ) instrument. The hydrodynamic diameter was calculated from the autocorrelation function using cumulants or CONTIN analysis, using the software supplied by the instrument manufacturers.

3.2.5 Attenuated total reflectance (ATR)- FTIR spectroscopy

FTIR spectra of SOD1s were collected using a Tensor 27 FTIR spectrometer (Bruker Optics) at room temperature (RT). A mercury-cadmium-telluride (MCT) detector was used because it can be used for a broad spectral range (400 to 4000 cm^{-1}) and was operated at a liquid N_2 cooled temperature. The IR spectrometer was purged extensively by N_2 gas prior to and during IR measurements to minimize interference of CO_2 and H_2O signals. Protein samples contained 20 mM HEPES at pH 7.8, and 3 mg/mL protein. A volume of 30 μL of the protein samples was placed onto the ATR sample holder. For each spectrum, 254 scans were collected in single beam mode with 4 cm^{-1} resolution. Buffer spectra were collected under identical conditions. Only the spectra that met the criterion of effective water subtraction (flat baseline between 1700 – 2000 cm^{-1}) were used for further analysis. The reported spectra of SOD1 were not subjected to any further manipulation, but the reported first derivative spectra (Fig. 3.15) were smoothed using Origin 7.5 by a second order Savitzky-Golay derivative with 11 point smoothing to decrease noise (Bromba & Ziegler, 1981). The ATR sample holder was cleaned between sample measurements by first adding SDS solution (1% (w/v) SDS in MilliQ water) and then incubating for 5 min, then the SDS solution was pipetted for several times to remove proteins that were adhered onto the ATR sample holder. MilliQ water replaced the SDS solution by pipetting, and this step was repeated until no more foam was created by pipetting. The holder was then dried using a Q-tip, according to recommendations from the instrument manufacturer. The secondary

structure of the proteins was analyzed by pattern recognition algorithms using the QUANT2 analysis tool supplied by the manufacturer.

3.2.6 Temperature Ramp of ATR-FTIR spectroscopy

The FTIR spectra were collected as a function of temperature using the same method described in 3.2.5, except that the number of scans was reduced to 100 scans. Background spectra of 20 mM HEPES, pH 7.8, were obtained first as a function of temperature, and then the spectra of protein samples (3 mg/mL in 20mm HEPES, at pH 7.8) were obtained at the same temperatures as the background spectra. 30 µL of the protein solution was placed onto the ATR sample holder and a Teflon O-ring was used to prevent evaporation. The reported IR spectra of protein samples were analyzed after subtracting from the background spectra at each temperature. For the temperature ramp, IR spectra were obtained every 5 °C between 30 °C and 60 °C (program 1), every 2 °C between 60 °C and 66 °C (program 2), every 1 °C between 66°C and 80°C (program 3), and 2 °C between 80 °C and 90 °C (program 4) respectively. Program 1, 2, 3, and 4 used 30 sec, 60 sec, 30 sec, and 60 sec for equilibration time after reaching the desired temperature, respectively. Temperature was controlled using a Thermo HAAKDC 30 water bath (Haake). The difference spectra relative to the spectra obtained at 35 °C were performed from the simple calculation; the spectra at higher temperature (90, 80, 75, 70, 60, 50, and 40 °C) minus the spectra at 35 °C.

3.2.7 Holo SOD1 aggregation monitored by optical spectroscopic methods

The samples for holo SOD1 aggregation experiments were prepared as described in section 2.2.2. Aliquots were removed at various time points of incubation for various spectroscopic measurements including fluorescence, CD and UV spectroscopy (see below). At various time points, 54 µL of the aggregation solution was diluted in 1 mL MilliQ water (*i.e.,* final concentration is 0.54 mg/mL SOD1 in 1.08 mM HEPES). The diluted protein was centrifuged (14000 g, 10 min) using an eppendorf centrifuge), and then 700 µL of supernatant was removed for fluorescence, CD, and UV spectroscopic measurements. If the pellet (the bottom 300 µL) was used for analysis, then it is stated. After the measurements were obtained, the protein concentration was measured using the Lowry assay (Lowry, Rosebrough, Farr & Randall, 1951) for normalization of various data. For unaggregated protein samples as a control (fluorescence and CD measurements), the proteins (0.54 mg/mL) were prepared in 1.08 mM HEPES, pH 7.8 after being freshly thawed from −80 °C freezer.

3.2.7.1 Intrinsic fluorescence spectroscopy

Unaggregated and aggregated protein samples were prepared as previously described (see Materials Methods, section 3.2.7). The supernatant of holo SOD1 aggregation samples at various time points was placed into a cuvette to measure fluorescence using a Fluorolog3-22 (Instrument SA, Edison, NJ) at 25°C. The samples were excited at 280 nm and emission was scanned between 300 – 400 nm. Excitation and emission slit widths are 1 and 2 nm, respectively. To facilitate accurate measurement of wavelength maxima and intensity, the

raw spectra were smoothed using Origin 7.5 by a second order Savitzky-Golay derivative with 11 point smoothing (Bromba & Ziegler, 1981).

3.2.7.2 CD spectroscopy

Unaggregated and aggregated protein samples were prepared as previously described (see Materials Methods, section 3.2.7). CD spectra for SOD1s were collected using a J715 CD spectrometer (Jasco, Inc.) with a 1.0 mm path-length quartz cuvette at 25 °C. The parameters: 1 nm for resolution, 2.0 nm for bandwidth, and 50 nm/min for speed, were used.

3.2.7.3 UV spectroscopy

UV measurements were made during aggregation time courses using a Cary 300 UV spectrometer (Varian, Inc.) with a 1 cm pathlength quartz cuvette at RT. 400 μL of the prepared protein samples (see Materials Methods, section 3.2.7) were placed in the cuvette and UV spectra were obtained between 230 – 400 nm spectral range. Prior to protein sample measurements, the buffer (20 mM HEPES, pH 7.8) was scanned and this was subtracted from the sample spectrum. In particular, the UV slope between 255 – 270 nm, calculated as: $(A_{270} - A_{255})/15$, was used as a measure of metal loss during aggregation.

3.2.8 Metal analysis

Metal analysis was carried out as described in section 2.2.8.

3.3 Results

3.3.1 Common aggregation kinetics for pWT and fALS-associated mutant SOD1s

The sigmoidal aggregation time courses of pWT and fALS-associated mutants of SOD1 that were obtained using SLS are shown in chapter 2 (see Results, section 2.3.1). Additional information on the size distribution of the aggregates can be obtained using DLS measurements. Fig. 3.4-3.7 show the aggregation profiles, autocorrelation functions and size distributions for holo SOD1 samples at different time points during aggregation time courses.
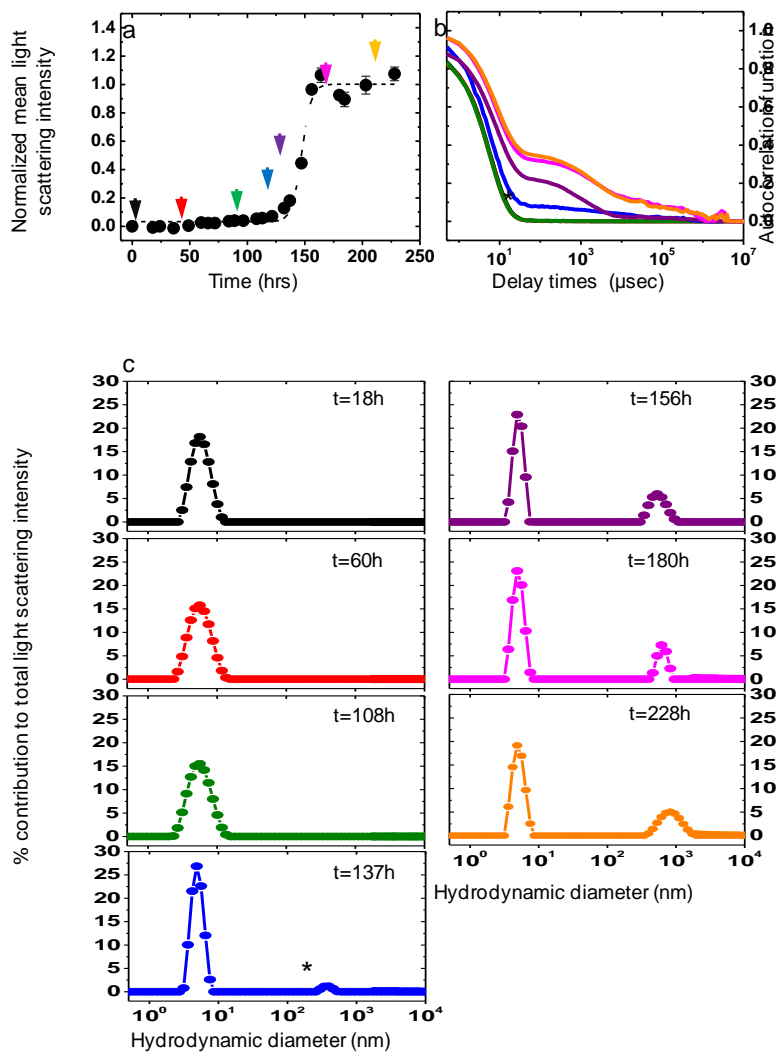
Figure 3.4 Evolution of pWT aggregation

(a) A representative sigmoidal aggregation profile for pWT. The colored arrows indicate time at 18 h, 60 h, 108 h, 137 h, 156 h, 180 h, and 228 h. The color code for the arrows matches that in (b and c) (*i.e.,* from earlier to later; the color is black, red, green, blue, purple, magenta, and orange). The broken line in (a) shows the fit of the data to the empirical equation (Eq. 2.1). The plotted values and the associated error bars are normalized mean light scattering and s.d. from the 3 replicates of 5 measurements for 10 sec. (b) Time

evolution of autocorrelation function during the aggregation shown in (a). (c) The size

distributions (hydrodynamic diameter, nm) during the aggregation shown in (a). In (b and c),

(*) indicates the second species at t = 137 h.
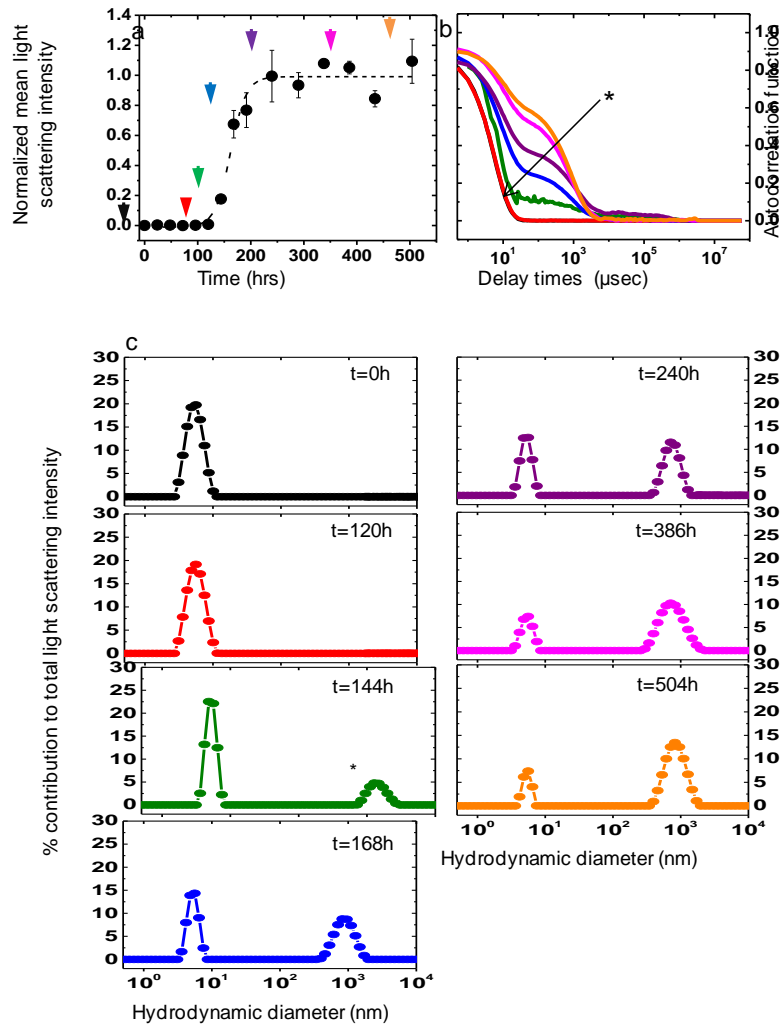
Figure 3.5 Evolution of G85R aggregation

(a) A representative sigmoidal aggregation profile for G85R. The arrows indicate time at 0 h, 120 h, 144 h, 168 h, 240 h, 386 h, and 504 h. The same color code as in Figure 3.4 is used. The broken line in (a) shows the fit of the data to the empirical equation (Eq. 2.1). The plotted values and the associated error bars are normalized mean light scattering and s.d. from 3 replicates of 5 measurements for 10 sec. (b) Time evolution of autocorrelation function during the aggregation of (a). (c) The size (hydrodynamic diameter, nm) change during the aggregation of (a). In (b and c), (*) indicates the second species at t = 144 h.
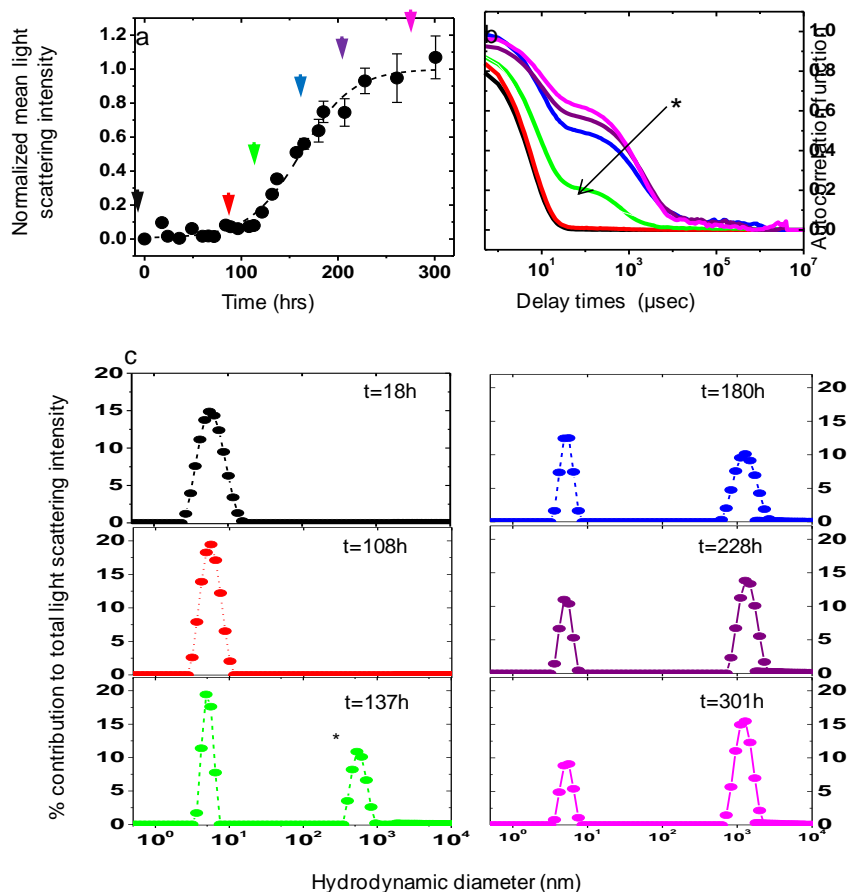
Figure 3.6 Evolution of G93V aggregation

(a) A representative sigmoidal aggregation profile for G93V. The arrows indicate time at 18 h, 108 h, 137 h, 180 h, 228 h, and 301. The same color code as in Fig. 3.4 is used. The broken line in (a) shows the fit of the data to the empirical equation (Eq. 2.1). The plotted values and the associated error bars are normalized mean light scattering and s.d. from 3 replicates of 5 measurements for 10 sec. (b) Time evolution of autocorrelation function during the aggregation of (a). (c) The size (hydrodynamic diameter, nm) change during the aggregation of (a). In (b and c), (*) indicates the second species at t = 137 h.
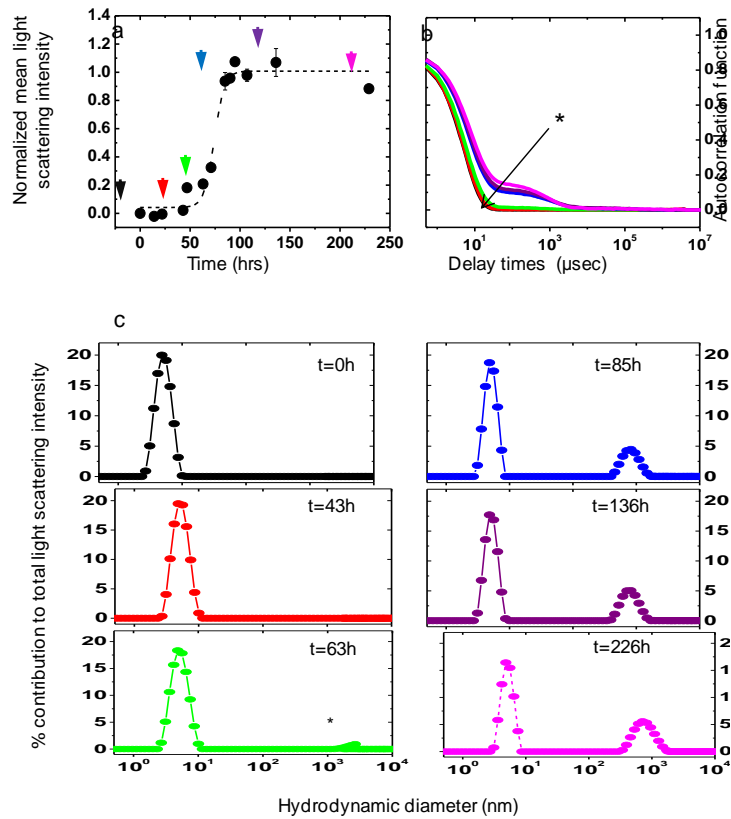
Figure 3.7 Evolution of A4T aggregation

(a) A representative sigmoidal aggregation profile for G93V. The arrows indicate time at 0 h, 43 h, 63 h, 85 h, 136 h, and 226 h. The same color code as in Fig. 3.4 is used. The broken line in (a) shows the fit of the data to the empirical equation (Eq. 2.1). The plotted values and the associated error bars are normalized mean light scattering and s.d. from 3 replicates of 5 measurements for 10 sec. (b) Time evolution of autocorrelation function during the aggregation of (a). (c) The size (hydrodynamic diameter, nm) change during the aggregation of (a). In (b and c), (*) indicates the second species at t = 63 h.

The experimental conditions for aggregation were the same as in chapter 2 (see Materials and Methods, section 2.2.2): holo SODls (generally 10 mg/mL in 20mM HEPES, at pH 7.8) were incubated at 37 °C. At t=0 h (or t=18h), the autocorrelation functions for all the samples show a single decay, indicating that the solutions are monodisperse (*i.e.,* consist of a single species). DLS is extremely sensitive for the detection of larger species relative to smaller species, because the intensity of scattered light is proportional to the sixth power of the radius (Lomakin, Benedek & Teplow, 1999). By deconvolution of single-phase correlation functions using the method of cumulants (Koppel, 1972), the hydrodynamic diameters of the species were determined to be 5.38 ± 0.10 nm, 5.32 ± 0.13 nm, 5.44 ± 0.11 nm and 4.93 ± 0.06 nm for pWT, G85R, G93V, and A4T, respectively. These measured diameters agree with the calculated size of the holo SOD1 dimer using Eq. 3.24 with the assumption that the viscosity of the protein solution is the same as that of water at 37 °C. Furthermore, the measured diameter is in agreement with other published hydrodynamic diameters of smiliar MW proteins by DLS: β lactoglobulin (36.8 kDa, 6.27 nm (de la Torre *et al*, 2000), tetramer of insulin (23.2 kDa, 5.0 nm); and hexamer of insulin (34.8 kDa, 5.9 nm) (Kadima *et al*, 1993) . It is interesting to note that A4T, a dimer interface mutant, has a smaller hydrodynamic diameter compared to the others ($P < 0.0003$ for A4V compared with pWT). If the smaller diameter for A4T is due to its higher population of monomers, it supports the finding in chapter 2; aggregation of A4T has a shorter lag phase than pWT and G93 mutants and the proposed reason for this observation is that dimer dissociation is required for aggregation (see Fig. 2.2, 2.5, and 2.14).

DLS has been used for detecting soluble oligomers or protofibrils that are formed during aggregation of various proteins (Kumar *et al*, 2007; Plakoutsi *et al*, 2005; Walsh *et al*, 1997). Interestingly, it is clear that there are no detectable oligomers during the lag phase from the size distributions and the single-phase correlation function during this phase of holo SOD1 aggregation. However, AFM reveals the presence of oligomers during the lag phase (see Results, section 2.3.6). It is important to note that the practical limitation on the accurate analysis of particle sizes using DLS can be as high as 1 order to magnitude (Lomakin, Benedek & Teplow, 1999). In order to be well resolved by DLS, the diameters of two different species should generally differ by 10 fold (Lomakin, Benedek & Teplow, 1999). Thus, for a mixture of SOD1 dimers ($\sim$ 5 nm in diameter), monomers, small oligomers ($<$ 50 nm in diameter), the diffusion coefficient and hence diameter determined by DLS will represent an average of the species. Therefore, an increase in the polydispersity about the average diameter during lag phase is compatible with the presence of small oligomers (data not shown).

From the beginning of the growth phase and onwards, the autocorrelation functions contain a shoulder (multi-phase) and the size distribution profiles show a peak around 1000 nm (*i.e.,* aggregates appear in the size distributions of the samples) (asterisk Fig. 3.4-3.7). Interestingly, the major time components for each decay (*i.e.,* the first decay occurs between 10 $\sim$ 100 µsec and the second decay occurs between 100 $\sim$ 10000 µsec) is similar for all the multi-phase correlation functions. This suggests that the particle sizes of the protein are not changing very much with incubation time. Moreover, since different mutants of SOD1s show the consistent time for each decay relative to pWT, this suggests that aggregate size

formed by all the different SOD1s is relatively consistent. All holo SOD1s studied, which includes pWT and three fALS associated mutants; G85R, G93D, and A4T shown in Fig. 3.4-3.7, as well as A4S, I149T, G93A, G93V, and G93S (data not shown) also show similar aggregation time course described above.

3.3.2 Aggregation kinetics monitored using intrinsic fluorescence

Fluorescence spectroscopy has become one of the most useful biophysical techniques for studying protein folding, kinetics, and assembly (D'Auria *et al*, 2000; Eftink, 2000; Hawe, Sutter & Jiskoot, 2008; Munishkina & Fink, 2007). These applications utilize the intrinsic fluorescence of aromatic amino acids: Trp, Tyr and Phe. In particular, the amino acid, Trp has the strongest fluorescence amongst the three aromatic amino acids and its fluorescence intensity and maximum wavelength (λ_{max}) are more sensitive to its microenvironment. Thus, Trp fluorescence is the most widely used in protein science (van Holde Kensal E., Johnson W. Curtis & Shing, 1998). Intrinsic fluorescence has also been used to elucidate many different types of protein aggregations (Dusa *et al*, 2006; Polymeropoulos *et al*, 1997). Typically, a blue shift of the spectral maximum wavelength occurs when the fluorophore of interest becomes more solvent inaccessible owing to aggregation. For example, an α-synuclein mutant (Y39W) in Parkinson's disease showed a λ_{max} blue shift, from 355 to 346 nm, and an increase in intensity during oligomerization, implying that Y39 participates in aggregation (Polymeropoulos *et al*, 1997).

The maximum wavelength (λ_{max}) in fluorescence emission spectra was monitored during aggregation in order to detect changes in the environmental polarity near the Trp (Fig. 3.8a). SOD1 only has one Trp at residue 32, which is located near the dimer interface and partially solvent exposed. In Fig. 3.8a, the λ_{max} of the emission spectra remains constant during aggregation of pWT, G93D, G93V, and I149T, which indicates that Trp-32 is not buried in the aggregates. The fluorescence of the insoluble fraction of the aggregated samples (separated *via* centrifugation, see Materials and Methods, section 3.2.7) was also measured and a significant blue shift did not appear.

In addition, the intensity of fluorescence at λ_{max} is plotted as a function of time along with the corresponding aggregation profile monitored by light scattering to obtain further information on the relationship between aggregate formation and changes in Trp environment (Fig. 3.8 b-e). Both pWT and fALS associated mutants; G93D, G93V, I149T and G85R (data not shown) exhibit a decrease in fluorescence intensity with time; however, the mutants show a greater decrease than pWT. There is no clear correlation between the light scattering and the signal change in fluorescence. The fluorescence intensity begins to decrease during the lag phase. It is worth noting that the Trp fluorescence was used previously to monitor denaturation (unfolding) of holo SOD1s by guanidinium chloride (GdmCl) and a cooperative increase in fluorescence signal was observed upon denaturation (Rumfeldt *et al*, 2006). Interestingly, prior to denaturation, the fluorescence signal decreases between 0 and 1 M GdmCl. Thus, the intensity decrease in Trp fluorescence, without significant change in λ_{max} of the emission spectrum, observed during holo SOD1s aggregation is most probably due to a subtle change in the microenvironment near the Trp

residue rather than significant unfolding (*i.e*., a change that is akin to the 0 to 1 M GdmCl partial unfolding process) (Hermann *et al*, 1997; Rumfeldt *et al*, 2006).
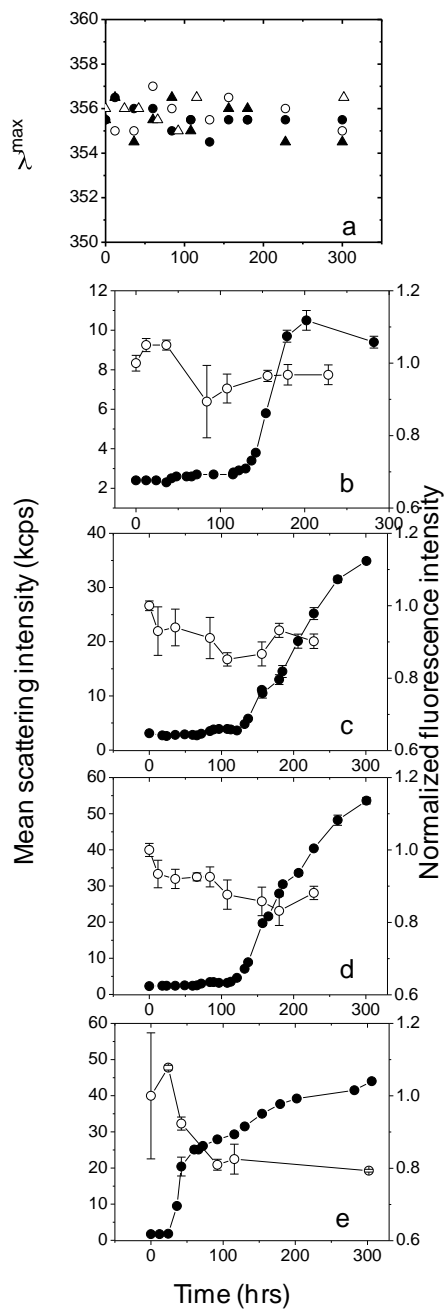
Figure 3.8 The time courses of aggregation monitored in parallel by light scattering and fluorescence emission

132

(a) The λ_{max} of the fluorescence emission spectrum of the Trp residue, for the supernatants for pWT (●), G93D (○), G93V (▲) and I149T (△) is plotted with time. (b-e) The aggregation profile of pWT (b), G93D (c), G93V (d), and I149T (e) was monitored using the fluorescence intensity at λ_{max} (○) and light scattering aggregation profiles (●). The supernatant (see Material and Methods, section 3.2.7) from the various time points was used for fluorescence measurements. (b-e) After the fluorescence measurements, the protein concentration was obtained using the Lowry assay (Lowry, Rosebrough, Farr & Randall, 1951) and the fluorescence spectrum was normalized. The presented values and the associated error bar for fluorescence are the average and s.d. of at least two measurements. The values for light scattering are the average of three measurements at a given time point and each of these 3 measurements is an average of 10 measurements for 30 sec. The error bars are the s.d. of the three measurements.

3.3.3 Aggregation kinetics monitored using CD spectropolarimetry

The aggregation of holo SOD1s was also monitored using CD spectropolarimetry. A typical CD spectrum for an α helical protein contains negative bands at about 222 and 208 nm, whereas β proteins show a negative band at about 215 nm (van Holde Kensal E., Johnson W. Curtis & Shing, 1998). The CD spectrum for holo SOD1 shows a broad negative band in the 225 – 200 nm range (Fig. 3.9), which is consistent with a previous study of SOD1 and typical for β proteins (Mei *et al*, 1992; van Holde Kensal E., Johnson W. Curtis & Shing, 1998). Fig. 3.9 shows the CD spectra for holo and apo pWT as well as holo G85R,

prior to aggregation. The spectra of the apo and holo form of pWT can be distinguished by differences in intensity at 209 and 230 nm (Fig. 3.9), consistent with results reported previously for holo and apo SOD1 (Rumfeldt *et al*, 2006). It is worth noting that although there are some differences in the spectra of the three proteins, the estimated secondary structure are similar among all samples. In other words, α helical structures in holo pWT, holo G85R and apo pWT are all 5 % and β structures in holo pWT, holo G85R and apo pWT are 40, 39, and 40 %, respectively. These estimates were derived from the atomic structures (1SOS for holo pWT (Parge, Hallewell & Tainer, 1992), 1HL4 for apo pWT (Strange *et al*, 2003) and 3CQP for holo G85R (Cao *et al*, 2008)) using the approach described by Kabsch and Sander (Kabsch & Sander, 1983)). Interestingly, holo G85R shows higher (less negative) intensity at 209 nm compared to holo pWT but almost the same intensity as holo pWT at 230nm. As holo proteins were carefully checked for full metallation, using specific activity and DSC measurements, the altered spectrum of holo G85R is likely due to structural changes in the metal binding site (especially, Zn binding site owing to location of the mutation (Cao *et al*, 2008)), but not necessarily different metal content.
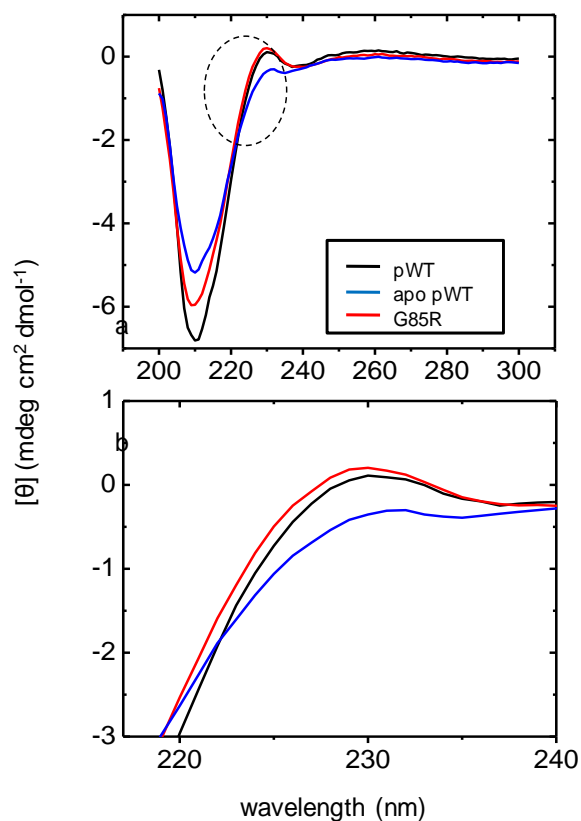
Figure 3.9 The CD spectra of holo pWT, apo pWT, and holo G85R, a metal binding mutant

The region of the circle in (a) is expanded in (b). The color code used in (b) is same as in (a).

In holo SOD1 aggregation experiments, the total change of $[\theta]$ at 209 nm upon aggregation is 0.69, 0.57, and 0.61 mdegcm^{2}dmol^{-1} for pWT, G93D, and G93V, respectively, whereas apo pWT shows 1.63 mdeg·cm^{2}dmol^{-1} difference at 209 nm relative to holo pWT (Fig. 3.9 and 3.10). The change upon aggregation is less than the difference between the holo and apo form of pWT. The small change in CD spectra upon aggregation is consistent

with the FTIR results (see below, Fig. 3.15), indicating that there is no substantial change in secondary structure upon aggregation.

CD has been used as a tool to detect conformational changes in many different aggregating systems (Ahmad *et al*, 2005; Booth *et al*, 1997; Kumar, Mohanty & Udgaonkar, 2007; Lai, Colon & Kelly, 1996; Pedersen *et al*, 2004; Plakoutsi *et al*, 2005; Souillac, Uversky & Fink, 2003). The conformational changes occurring during holo SOD1 aggregation were monitored using CD spectropolarimetry in parallel with light scattering. Fig. 3.10 and 3.11 show the changes of mean residue ellipticity ($[\theta]_{209}$ and $[\theta]_{230}$, respectively) for the CD spectra and the corresponding light scattering signals for aggregation profiles of pWT, G93D and G93V. Fig. 3.10 and 3.11 show that the band at 209 nm becomes less negative and the shoulder at 230 nm becomes less positive upon aggregation. It is suggested the spectra obtained during aggregation become more like that of apo SOD1, implying that the holo protein loses metals.
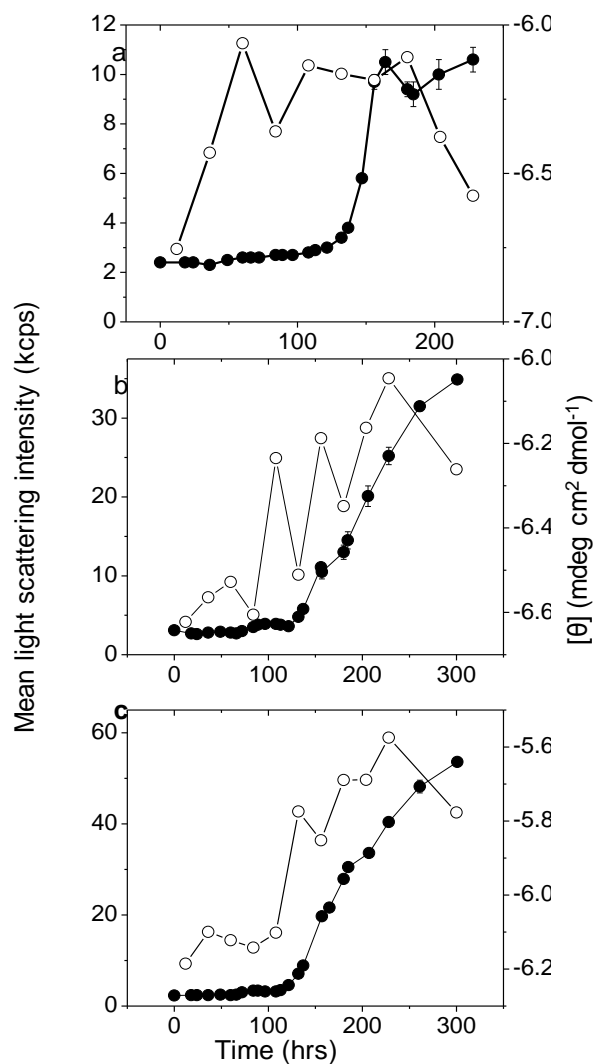
Figure 3.10 The time courses of aggregation monitored by light scattering and CD spectra

The aggregation of pWT (a), G93D (b), and G93V (c) was monitored using light scattering (●) and CD spectra ([θ]$_{209,}$ (○)) in parallel. The supernatant (see Materials and Methods, section 3.2.7) from the various time points was used for CD measurements. The values for light scattering are the average of 3 measurements, each measurement was composed of 10 measurements for 30 min, and the error bars are the s.d. of the three measurements.
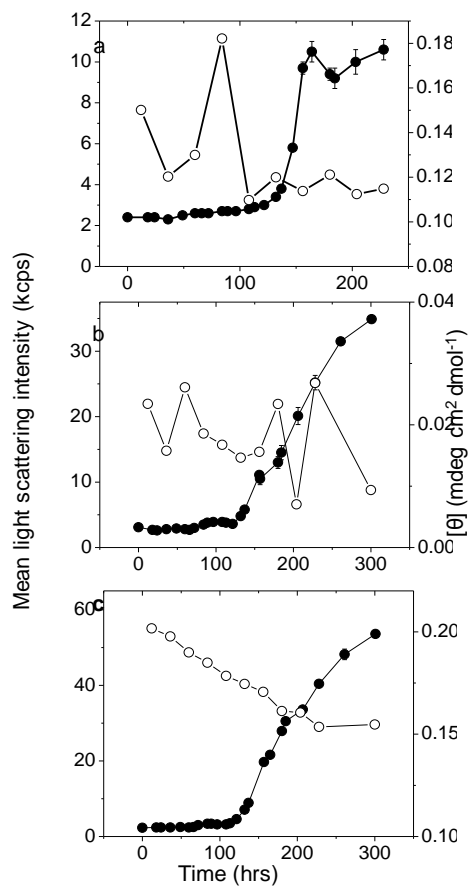
Figure 3.11 The time course of aggregation monitored by light scattering and CD spectra

The aggregation of pWT (a), G93D (b), and G93V (c) was monitored using light scattering (●) and CD spectra ($[\theta]_{230}$, (○)) in parallel. The supernatant (see Materials and Methods, section 3.2.7) from the various time points was used for CD measurements. The values for light scattering are the average of 3 measurements, each measurement was composed of 10 measurements for 30 min, and the error bars are the s.d. of the three measurements.

138

3.3.4 Aggregation kinetics monitored using UV spectroscopy

The UV and visible spectra of SOD1 were commonly used during the 1970s - 1990s for different metal reconstitution studies (Beem, Rich & Rajagopalan, 1974; Mailer *et al*, 1989). Here, the characteristic UV spectra of the various metallated states of SOD1 are used to investigate the role of the metals in holo SOD1 aggregation.

Proteins have characteristic UV spectra in the wavelength region of 250 - 300 nm mainly due to three amino acids: Phe (245 – 270 nm); Try (265 – 285 nm); and Trp (265 – 295) (Lucas *et al*, 2006). The maximum absorbance for proteins in this spectral range is typically ~280 nm; however SOD1s have distinct UV spectra with a shoulder at 288 nm and distinctive Phe absorption regions (Fig. 3.12a) (Mailer, Addetia & Livesey, 1989). The major chromophores for SOD1 are four Phe residues and one Trp residue per monomer (*i.e.,* there is no Tyr). Three of the Phe residues are comparatively close to the Cu binding site while the Trp is quite distant from the Cu binding site (Mailer, Addetia & Livesey, 1989). Consequently, different Cu metallation in SOD1 affects the UV spectra of the protein in Phe absorption regions (250 - 265 nm). The current study uses the slope between 255 – 270 nm (calculated as: $(A_{270} - A_{255})$ /15) to obtain information about the Cu composition in the protein. Fig. 3.12a demonstrates the different UV spectra of SOD1 in different metallation states. The Cu/E (E represents empty) protein has almost the same but slightly less positive slope (0.00006) compared to that of the holo protein (0.00033). On the other hand, the E/Zn protein has a more positive slope (0.00053) than that of the holo protein, which can be explained by the absence of Cu ions. Moreover, Cu/Cu SOD1 has a negative slope (-

0.00065). These results are in agreement with previous studies (Beem, Rich & Rajagopalan, 1974; Mailer, Addetia & Livesey, 1989).

By applying the method described above, mechanistic information regarding metal loss can be obtained by monitoring the slope change in the UV spectra of SODs during holo aggregation time courses. In Fig. 3.12b-d, the change in 255 – 270 nm slope during aggregation is plotted with the corresponding light scattering profile. In particular, during the exponential phase, an increase of slope in the 255 – 270 nm regions is observed, implying that holo SOD1 loses Cu generally during this phase. This observation is consistent with a decrease in specific activity during exponential phase (Fig. 2.6), since Cu ions are absolutely required for activity.
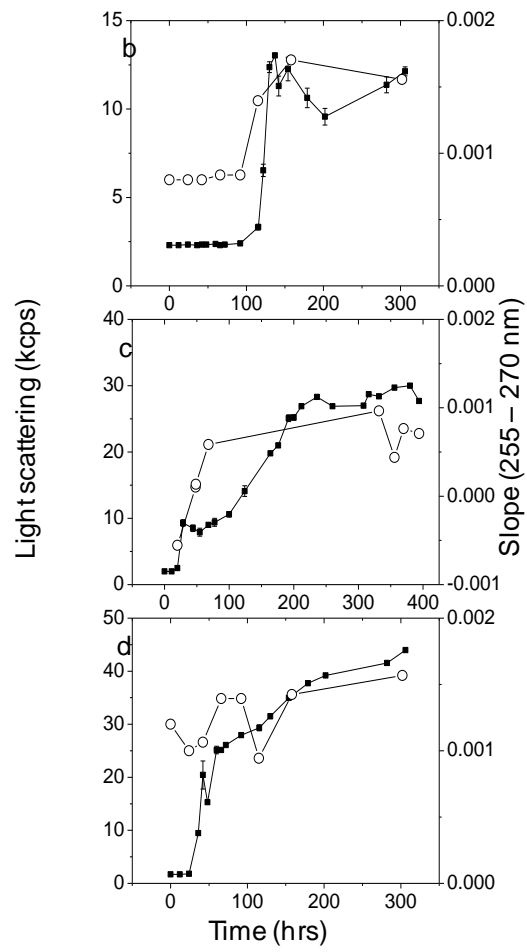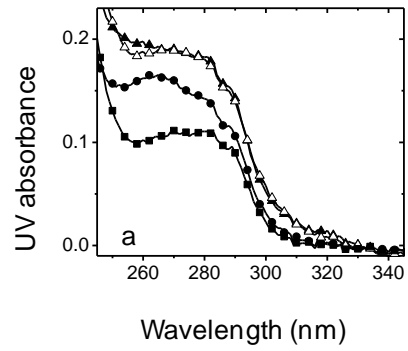
Figure 3.12 Time courses of holo SOD1 aggregation monitored by UV absorption and light scattering

(a) The UV absorption spectra of holo Cu/Zn (─●─), Cu/Cu (─▲─), Cu/E (─△─), and E/Zn (─■─) of pWT were obtained. The UV spectra of the supernatant (see Materials and Methods, section 3.2.7) for pWT (b), G85R (c), and I149T (d) at various time points during aggregation were obtained. The slope between 255 – 270 nm was calculated and is plotted (○) along with the corresponding light scattering profile (●). The reported light scattering values and associated error bars are the average and s.d. from 3 measurements of 10 replicates for 30 sec.

3.3.5 Two distinct aggregation profiles

Holo SOD1 aggregation shows time courses with variable lag phase, final intensities, and durations even after excluding the "pre-seeded" profiles (see chapter 2) (Fig. 3.13). The variable aggregation profiles were observed even with the same mutant with protein samples that were produced from the same batch of protein preparation, implying that environmental factors play an important role in aggregation. Furthermore, two samples produced at the same time from the same batch of protein sometimes gave quite different aggregation profiles, suggesting that random nucleation events affect the aggregation time course. Interestingly, two distinct patterns in the aggregation profiles were observed: aggregation with low light scattering intensity at the plateau phase and shorter duration; and aggregation with higher light scattering intensity at the plateau phase and longer duration (Fig. 3.13). This observation is not specific for a given mutant (*i.e.,* given mutant form of holo SOD1 can

exhibit both patterns). Furthermore, these two different patterns of aggregation time course

can be related to different metal loss during aggregation (see below).
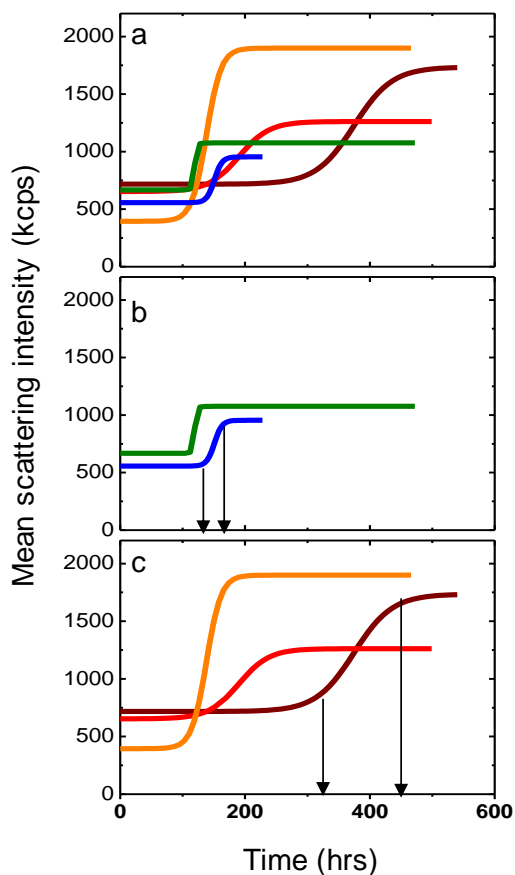
Figure 3.13 Variable aggregation profiles

(a) 5 different aggregation profiles for 10 mg/mL pWT show different lag phases, plateau

intensity and duration. The 5 different aggregation profiles are divided into two groups in (b)

and (c). (b) When aggregation has a shorter duration, then the total light scattering increase

is less than the other case (c). (c) When aggregation has a longer duration, then the plateau is

higher than the other (b). The plots are the fits for 5 different aggregation profiles. The

arrows illustrate the duration of aggregation by pointing to the end of lag phase and the beginning of the plateau.

3.3.6 Different metal loss during aggregation

Chapter 2 shows that decrease in specific activity (see Results, section 2.3.2) and the metal content in aggregates is less than that in unaggregated holo SOD1 (see Results, section 2.3.3), indicating that holo SOD1s lose metals during aggregation. Additionally, CD and UV experimental data (see Results, section 3.3.3 and 3.3.4, respectively) and thermal unfolding using ATR-FTIR (see below) suggest metal loss during aggregation, as well. The previous section (see Results, section 3.3.5) shows the two different patterns of aggregation profiles that were obtained using light scattering. This section proposes that these two aggregation profiles may be related to different ratio of metals (Cu/Zn) in the aggregates (Fig. 3.14). The aggregation profiles with short duration and low light scattering intensity (*i.e.,* the case of Fig.3.13b) appear to be associated with aggregates that contain more Cu ions than Zn ions, implying that the protein loses more Zn ions during aggregation. On the other hand, the aggregation profiles with longer duration and higher light scattering intensity (*i.e.,* the case of Fig. 3.13c) are associated with aggregates that contain more Zn ions than Cu ions, implying that the protein loses more Cu ions during aggregation. This trend is further demonstrated by plotting metal composition of the aggregates (as measured by ITV-ICP-AES, see Materials and Methods, section 2.2.8) *versus* final light scattering intensity (Fig. 3.14e) and duration (Fig. 3.14f). It is worth noting that relative metal amounts to the total protein amounts in

aggregates was not achieved using ITV-ICP-AES method since the baseline for carbon detection was not stable to estimate quantitatively.

A possible interpretation of the different consequences for loss of more Zn relative to Cu and vice versa on aggregation can be based on the roles of these metals in protein structure and activity. Since the Zn ion is known to be more important for maintaining SOD1 structure (Potter *et al*, 2007; Sun *et al*, 1997), it is reasonable that the former pattern of aggregation has a shorter duration (*i.e.,* when the holo protein loses Zn ions, the protein will have more unstructured regions, which can promote aggregation). Another consequence of Zn loss is that the Cu ions remaining in the partially structured protein may cause oxidative damage, which further promotes aggregation (see section 1.3.1). On the other hand, if the protein retains the Zn ions, it will be more structured, which may lengthen the duration of aggregation.
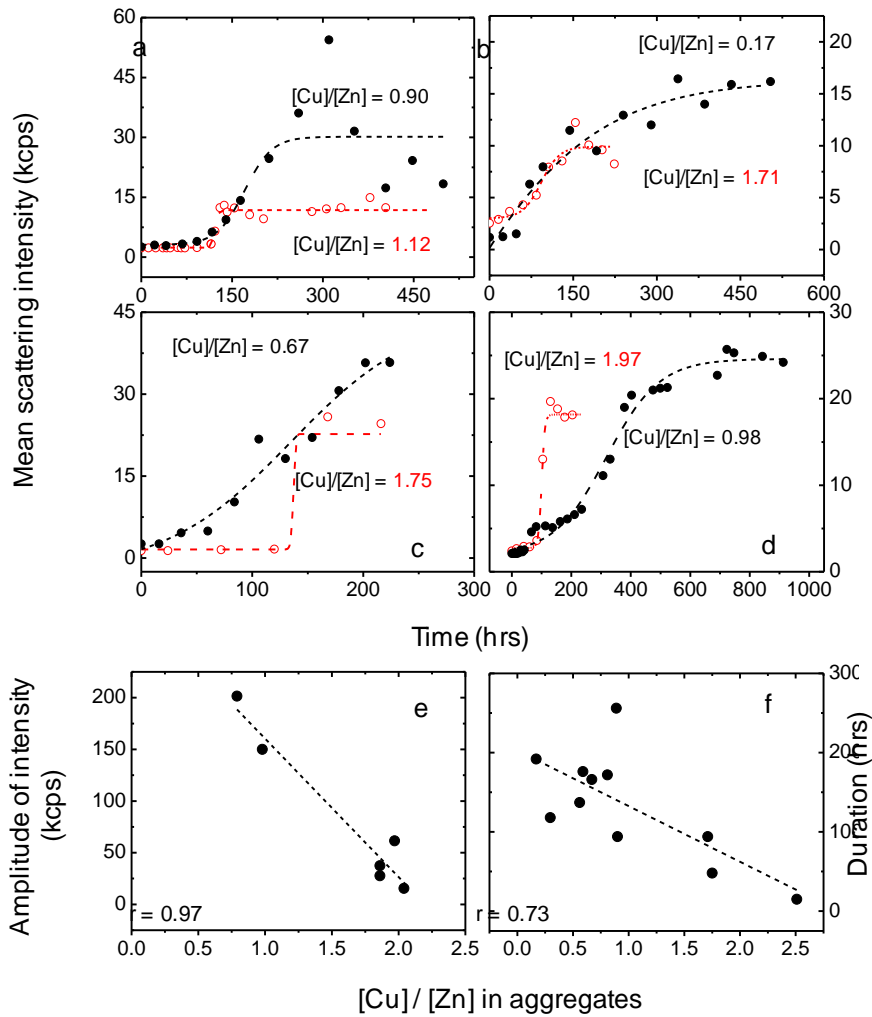
Figure 3.14 Relationship of aggregation profiles to metal loss

A mutant of holo SOD1 can lose either Cu or Zn more than the other metal, which affects the

aggregation profiles of (a) pWT, (b) A4V (c) G93V, and (d) G85R. The aggregation profiles

with a higher intensity plateau and a longer duration tend to be associated with aggregates

with lower Cu/Zn ratios, (*i.e.,* relatively less Cu (●)), whereas the aggregation profiles with

lower intensity plateaus and shorter durations tend to be associated with aggregates with

higher Cu/Zn ratios, (*i.e.,* relatively more Cu (○)). The dotted lines are the fits of the data to Eq. 2.1. The Cu/Zn ratio measured for the aggregates is plotted versus amplitude of intensity in G85R aggregation (e) and duration from aggregation profiles using pWT and different mutants of holo SOD1s (f). The metal analysis was performed as described in Materials and Methods, section 3.2.8. (e and f) the fits were performed in Origin 7.5 and the reported r values were from the fitting.

3.3.7 Characterization of the aggregates formed from holo SOD1s

3.3.7.1 Structure analysis using ATR-FTIR

Generally, the shape and location of the amide I band in an FTIR spectrum are used to predict the predominant secondary structure of the protein (Dong *et al*, 1995) (Bhattacharjee *et al*, 2005; Chiumiento *et al*, 2006; Dong, Huang & Caughey, 1995; Dupeyrat *et al*, 2004; Elliott & Ambrose, 1950; Jahn *et al*, 2008; Leone *et al*, 1998; Lo & Rahman, 1996; Meersman *et al*, 2002) (Jackson & Mantsch, 1995). In the following experiments, the amide I band was also used to analyze structural changes upon aggregation of holo SOD1s. Fig. 3.15 shows the FTIR and first derivative spectra between 1750 and 1300 cm^{-1} of both unaggregated and aggregated pWT in 20 mM HEPES at pH 7.8. Shoulders for peaks in the FTIR spectrum were identified using first derivative spectra (Fig. 3.15b). The spectra of unaggregated SOD1s were very reproducible, whereas the spectra of aggregated SOD1s showed slight, but not significant, variability between independent experiments. The spectrum of unaggregated pWT, shown in Fig. 3.15a is in good agreement

with previous studies (Chiumiento *et al*, 2006; Dong, Huang & Caughey, 1995; Lo & Rahman, 1996). The maxima for the amide I, II, and III bands of unaggregated pWT are at 1640, 1540, and 1390 cm^{-1}, respectively. The amide I and II bands include shoulders at 1680 and 1619 cm^{-1}, and 1522 cm^{-1}, respectively. The secondary structure analyses for the unaggregated pWT FTIR spectra were performed as proposed by Jackson *et al.* (Jackson & Mantsch, 1995) (see below). The most prominent amide I band at 1640 cm^{-1} can be assigned to disordered structures, while the shoulder at 1619 cm^{-1} can be assigned to β-sheet structures (Jackson & Mantsch, 1995). The other shoulder at 1680 cm^{-1} is also assigned to β-sheet structures, based on the assignments of Bhattacharjee and coworkers (Bhattacharjee *et al*, 2005) and Dong and coworkers (Dong, Huang & Caughey, 1995). The assignments are consistent with previous IR studies of other proteins (Chiumiento *et al*, 2006; Dong, Huang & Caughey, 1995; Lo & Rahman, 1996). From a comparison the FTIR spectrum of unaggregated pWT to that of aggregated pWT, no significant changes of secondary structure occur upon aggregation.
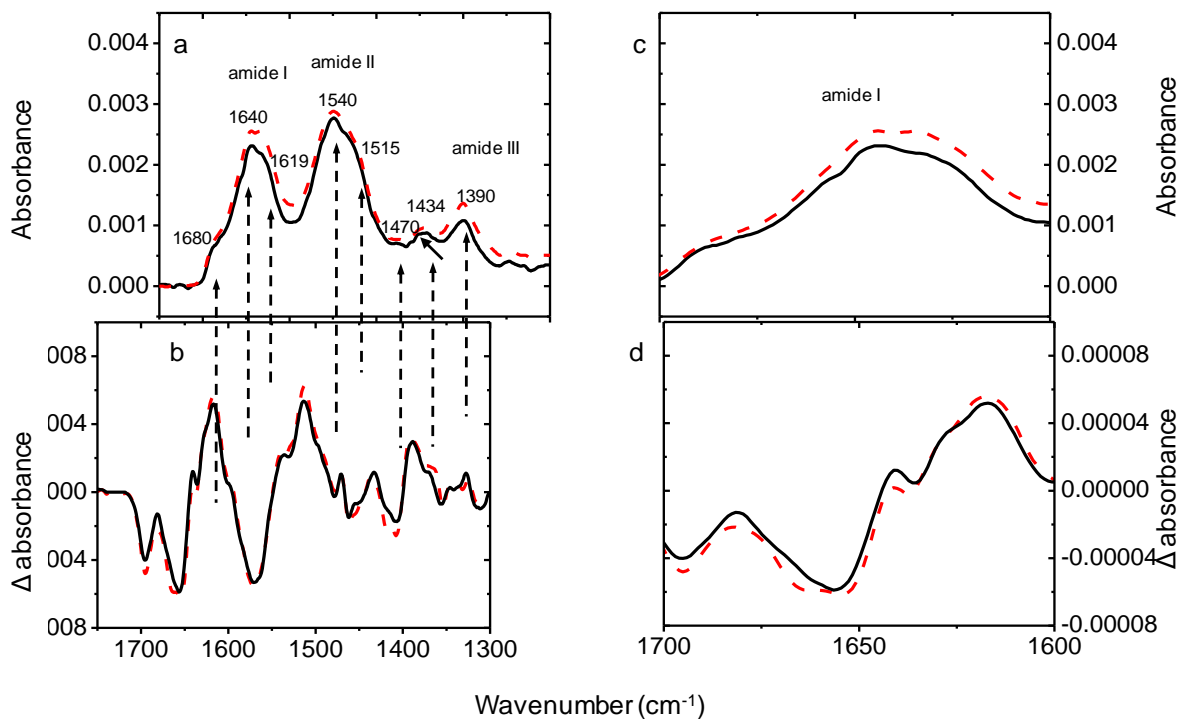
Figure 3.15 FTIR spectra comparison for pWT before and after aggregation

The aggregated sample was taken from the plateau phase. The FTIR spectra (a) and the first derivative spectra (b) of unaggregated (—) and aggregated (- - -) pWT are shown in the amide I, II and III regions. The arrows in the first derivative spectra (b) point to the corresponding shoulders in the FTIR spectra (a). Amide I band in (a and b) are expanded in and shown in(c and d), respectively.

Furthermore, the quantitative estimate of secondary structure was obtained using QUANT2, a tool provided by the manufacturer and the results (Table 3.1) agree with the X-ray crystal structure reported for pWT. Table 3.1 confirms that there is no significant

difference ($P > 0.5$) in secondary structure estimations between aggregated and unaggregated SOD1s. Assuming that SOD1 dimer dissociation and partial metal loss (see Discussion, 2.4.1) initiate aggregation of holo SOD1, one can expect that the aggregating species will undergo dramatic structural changes. However, since dimer dissociation and partial metal loss can be accomplished by two external loops, loop IV and the electrostatic loop, it is possible that the protein retain much of their α and β structure. Also, it is possible that the difference in secondary structure before and after aggregation is below the detection limit of ATR-FTIR since the aggregates correspond to a small percentage of the total protein.

Table 3.1 Secondary structure analyses of SOD1 by FTIR

	secondary structure		
	α helix	β sheet	
pWT [a]	5	40	
pWT$_{unagg}$ [b]	3.47 ± 0.42	45.56 ± 1.55	
pWT$_{agg}$ [c]	3.13 ± 0.83	46.87 ± 1.56	$P > 0.5$
A4T$_{agg}$ [b]	4.63 ± 1.12	45.91 ± 0.32	$P > 0.5$
pWT$_{seeded}$ [c]	3.96 ± 3.14	45.90 ± 1.67	$P > 0.5$

[a] The values are from the RCSB PDB website (www.rcsb.org/pdb) using pdb code 1SOS (Parge, Hallewell & Tainer, 1992) and the secondary structure analysis by pattern recognition process (Kabsch & Sander, 1983).

[b] For pWT$_{unagg}$, the values are means ± s.d. from the same batch of the protein as for aggregation and the three different measurements at different days. The s.d. of A4T$_{agg}$ was calculated from the three measurements from one aggregation experiment.

[c] The values are means ± s.d. from 2 (for pWT$_{agg}$), and 5 (for pWT$_{seeded}$) independent aggregation experiments, for which samples was analyzed at least in duplicate.

P values indicate statistical significance of the estimation of secondary structures with respect to that of pWT$_{unagg}$.

Additionally, FTIR studies have been used to identify structural differences between native β-sheet proteins and cross β-sheets in amyloid fibrils ((Zandomeneghi *et al*, 2004) and references therein). Typically, amyloid fibrils show a lower amide I band wavenumber compared to the native β-sheet structure. For example, the amide I band of the native form of TTR is 1630 cm^{-1}, whereas the amyloid form has the amide I band at 1615 cm^{-1}. Amyloid formation also causes a downshift in the amide I band in the case of prion propagation in prion disease (Jones & Surewicz, 2005), polyglutamine aggregation in Huntington's disease (Thakur *et al*, 2009), and β2 microglobulin in dialysis related amyloidosis (Jahn, Tennent & Radford, 2008). Currently, it is widely accepted that the band at 1620 cm^{-1} represents amyloid, although the amide I band downshift varies between proteins (Zandomeneghi, Krebs, McCammon & Fandrich, 2004). To support this notion, FTIR microspectroscopy and ATR-FTIR identify amyloids from Alzheimer's patients with the band at 1620 cm^{-1} (Choo *et al*, 1996; Jahn, Tennent & Radford, 2008). Fig. 3.15 (a and b) shows no significant difference between the spectra from aggregated and unaggregated pWT and the band at 1620 cm^{-1} did not appear in the aggregated SOD1s. This supports the hypothesis that holo SOD1 aggregates do not possess the classical properties of amyloid fibrils (see Discussion, section 2.4.1).

3.3.7.2 Thermal unfolding of the aggregates using ATR-FTIR

The structural changes of unaggregated and aggregated pWT during thermal unfolding were investigated by ATR-FTIR spectra at different temperatures in the range of 35-90 °C. Overall, the shape of the spectra at various temperatures remains similar. Fig.

3.16 (a and b) illustrates the differences between the unaggregated and the aggregated pWT during thermal unfolding using difference FTIR spectra, which were calculated as the spectrum for a given temperature *minus* the spectrum obtained at 35 °C. As temperature increases, the intensity at 1663, 1644, 1536, and 1392 cm^{-1} increases in the difference FTIR spectra of both unaggregated and aggregated pWT. The increasing absorbance at 1644 cm^{-1} reflects increased amounts of unstructured regions upon thermal unfolding (Jackson & Mantsch, 1995). The difference spectrum of unaggregated pWT shows very little change between 35 and 75 °C but dramatic changes in the range of 80-90 °C, consistent with a cooperative change in secondary structure upon thermal unfolding. These changes are roughly as expected for holo pWT, which has a melting temperature in solution of ~92°C (Stathopulos, 2005). In contrast, Fig. 3.16b shows that the spectrum of aggregated pWT begins to change at 66 °C, implying some species in the aggregated sample are more vulnerable to thermal unfolding. Fig. 3.16c shows the change in the band height at 1644 cm^{-1} with increasing temperature. Since the melting temperature for apo pWT is ~60 °C (Stathopulos *et al*, 2006), and part-metallated SOD1s have melting temperatures between those of holo and apo (Rodriguez *et al*, 2002), the species in the aggregated sample are probably not apo, but most likely are part- or mis- metallated or aggregated (Potter *et al*, 2007). Although the overall secondary structure of this species remains very similar to native SOD1, the FTIR results are consistent with the CD (Fig. 3.10) and UV (Fig. 3.12) data as well as activity and metal analysis data (see chapter 2); all indicate holo SOD1s lose metals and/or alter metal binding sites during aggregation.
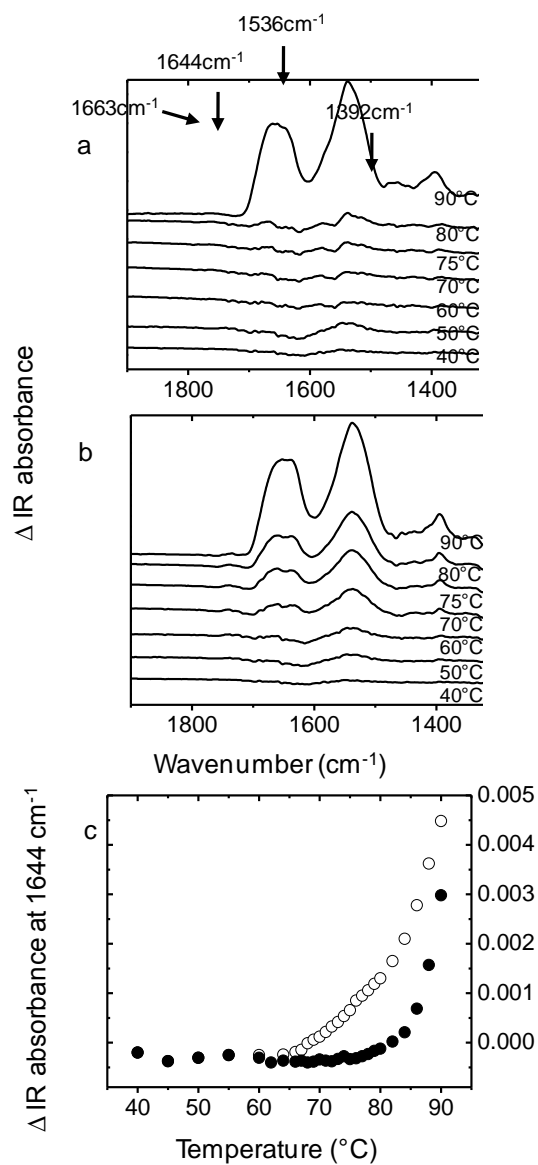
Figure 3.16 Thermal unfolding of unaggregated and aggregated pWT monitored by ATR FTIR

The ATR-FTIR difference spectra of unaggregated pWT (a) and aggregated pWT (b) were obtained from the simple calculation; the spectra at higher temperature (90, 80, 75, 70, 60, 50, and 40 °C. from *top* to *bottom*) minus the spectra at 35 °C. The ATR FTIR spectra of the

proteins were obtained as described in 3.2.8. The signals at 1663 cm^{-1}, 1644 cm^{-1}, 1536 cm^{-1}, and 1392 cm^{-1} show the most change during thermal unfolding. The aggregated pWT was obtained from the plateau phase. (c) The change of the band height at 1644 cm^{-1} illustrates a loss of structure above 80 °C for the unaggregated pWT (●) and above 66 °C for aggregated pWT (○).

3.3.7.3 AB^2 and B^2 comparison between the various mutants of holo SOD1

Log-log plots of AB^2 *versus* A_0 and B^2 *versus* A_0 were made for pWT and 9 fALS associated mutants: the dimer interface mutants, A4V, A4T, A4T and I149T; three G93 mutants, G93D, V, and S; and the metal-binding mutant, G85R. All data were obtained at the same protein concentration (*i.e.,* 10 mg/mL), allowing for a comparison of the AB^2 and B^2 values among the proteins. The time courses of all SOD1 aggregation were fit to models for heterogeneous nucleation (Eq. 2.4) and the fitted parameters (*A* and *B* from Eq. 2.4) used to calculate AB^2 and B^2 (Ferrone, 1999). Fig. 3.17 shows that the values of log (AB^2) for pWT and fALS-associated mutants are not significantly different ($P > 0.1$), except for A4V and A4T ($P = 0.017$ and 0.073, respectively, compared to pWT). The high tendency of A4V and A4T to monomerize may contribute to its large log (AB^2) value ((Stathopulos, 2005) and Vassall, K.V. and Meiering, E.M. unpublished data for dimer dissociation constant of apo SOD1s). In detail, assuming that pWT and fALS-associated mutants form the same sized primary nuclei (*i*) and share the same values of A_s, then pWT and all the mutants, except for A4V and A4T, have similar k_+ and K_i values. On the other hand, A4V and A4T would have

154

a larger value for k_+ and K_i, in that the association rate of reactive unit onto aggregates and the equilibrium constant of primary nucleation are larger than the other proteins.

The log B^2 values for pWT and the fALS-associated mutants are compared in Fig. 3.17b. The dimer interface mutants, A4T, A4S and I149T, and the metal binding mutant, G85R, have higher values for B^2, suggesting that dimer dissociation and metal loss may play an important role to promote heterogeneous nucleation. In particular cases of A4S, I149T and G85R, it can be deduced that the values for $\bar{\theta}\overline{K}_J\widetilde{K}_J$ should be larger than the other proteins since k_+, K_i, A_s and i could be the same as these of pWT and three G93 mutants of SOD1 (see above). Thus, larger AB^2 values of A4V and A4T and larger B^2 values of A4T/S, I149T and G85R support the lag phase comparison results (Fig. 2.5), where the dimer interface mutants (A4V/T/S and I149T) and G85R tend to have shorter lag phases than the G93 mutants and pWT.
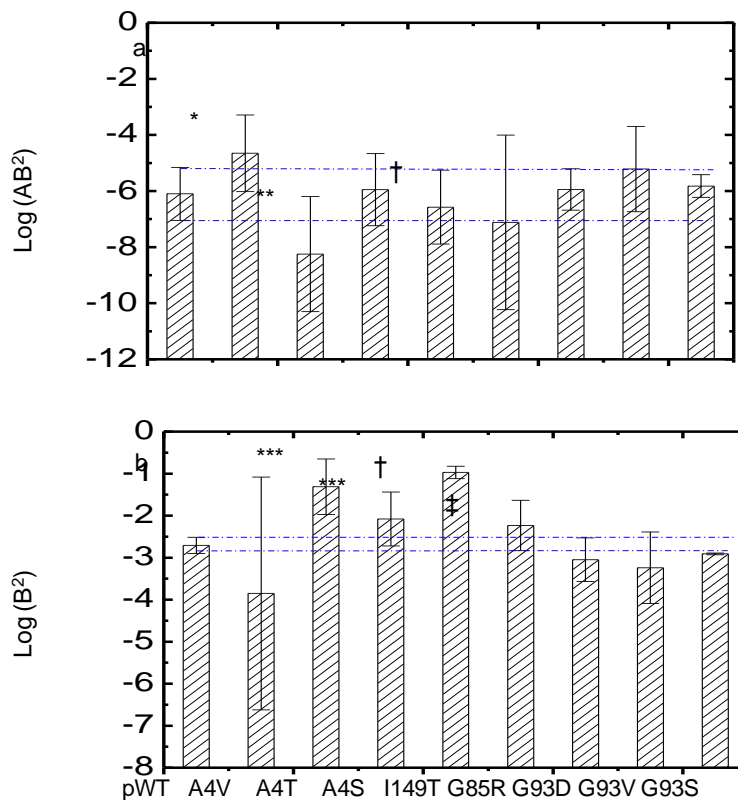
Figure 3.17 Comparison of log (AB^2) and log (B^2) for pWT and the fALS associated mutant SOD1s

The presented values are mean ± s.d. for 14, 5, 5, 3, 4, 3, 3, and 3 independent experiments at 10 mg/mL for pWT, A4V, A4T, A4S, G85R, G93D, G93V, and G93S, respectively. In a, (* and **) indicates statistically significant difference for the log (AB^2) value for A4V and A4T with respect to pWT ($P = 0.017$ and 0.073). (†) indicates error estimate from the fitting parameters for this single measurement. In the case of G93S in (b), the error bar is too small to be seen on the plot. In b, (***) and (‡) indicate statistically significant difference of log (B^2) values for A4T, A4S, and G85R with respect to that of pWT (***, $P < 0.06$ and ‡, $P = 0.1$). (a and b) For the remaining data, there is no significant difference between the values

for mutants and pWT ($P > 0.1$). The dotted lines represent the area of s.d. for log (AB^2) and log (B^2) for pWT in order to easy to compare with other mutants.

3.4 Discussion

3.4.1 A4V aggregate property

The lag phase in aggregation occurs because the initial nucleation event is thermodynamically unfavorable (Fig. 3.1) (Harper & Lansbury, 1997). Aggregation profiles obtained from different mutants of SOD1 are fitted better to the double nucleation mechanism (Fig. 2.10). The double nucleation mechanism consists of a combination of homogeneous and heterogeneous nucleation. In other words, homogeneous nucleation initiates polymerization, followed by heterogeneous nucleation on the surface of existing ones (Ferrone, Hofrichter & Eaton, 1985). It is worth thinking further about the implication of AB^2 and B^2 values of A4V in disease. A4V shares a similar B^2 value with pWT and G93D, V, and S ($P > 0.1$), although A4V is a dimer interface mutant. However, A4V has higher AB^2 values than the other mutants, suggesting that A4V forms primary nuclei faster but heterogeneous nuclei slowly. This suggests that there is a higher population of aggregates without branches (before participating in heterogeneous nucleation). This may be why A4V has a particularly short disease duration of ~1 year (Wang, Johnson, Agar & Agar, 2008), since the soluble oligomers have been found to be more cytotoxic than mature fibrils (Ross & Poirier, 2004).

157

3.4.2 Aggregation mechanism

There is increasing evidence suggesting that partially folded intermediates are involved in protein aggregation (Arnaudov & de Vries, 2007; Booth *et al*, 1997; Chiti *et al*, 2001; Fandrich *et al*, 2003a; Khurana *et al*, 2001; Lai, Colon & Kelly, 1996). For example, several α-helical proteins have been shown to undergo significant conformational changes to predominantly β-structures, before forming amyloid; these include lysozyme (α + β protein) (Fandrich *et al*, 2003a) and apo-myoglobin (α-protein) (Yamasaki, Li, Johnson & Huntington, 2008). However, some proteins form aggregates under physiological conditions without significant structure changes but *via* thermal fluctuations; these include serpins (Chiti & Dobson, 2009), TTR, and β2-microglobulin (see more examples in (Chiti & Dobson, 2009)). Similarly, the holo SOD1s can form aggregates under physiologically relevant conditions (37 °C and pH 7.8) without significant structural change, which is supported by observation: no λ_{max} change of fluorescence spectra; and no significant CD and FTIR spectra change during aggregation (Fig. 3.8, 3.10 and 3.11). This finding suggests that the aggregates retain most of their native structure and/or extremely small amounts of aggregates are formed from holo SOD1s. The former is possible if dimer dissociation and loss of metals disrupt mainly two loops (loop IV and loop VII) but the main structure of the protein, 8-β sheets, remains intact. The latter is consistent with visible observation. Nevertheless, it is important to determine how the aggregation process is initiated with regards to dimer dissociation and metal loss. Here, detailed analyses of kinetics of aggregation monitored using different structural probes provide some insights into the molecular basis of

158

aggregation. The following section separately discusses into the lag phase and the exponential phase and discusses the findings with regard to the aggregation mechanism.

3.4.2.1 Early events during lag phase

In order to elucidate the underlying aggregation mechanism during the lag phase, several key observations were considered. First, the intrinsic fluorescence decreases during the aggregation and the absence of a lag phase in the observed kinetics of the intrinsic fluorescence suggest that the change in microenvironment near Trp-32 occurs almost spontaneously during the lag phase (Fig. 3.8). Since aggregation profiles monitored using light scattering have at least 50 hrs lag phase, the change in microenvironments near Trp-32 must be related to the very early aggregation (Fig. 3.8). The λ_{max} of the emission spectra does not blue-shift during aggregation, which suggests the Trp-32 does not become buried (Fig. 3.8). Taken together, the decrease in the intrinsic fluorescence implies that the dimer interface is disrupted, which probably lead to dimer dissociation. The decrease in the intrinsic fluorescence can be caused by the quenching effect of the intramolecular disulfide bond formed between C57 and C146 or solvents. For the former, when the dimer interface becomes more flexible, the disulfide loop (residues C57-C146) can interfere with fluorescence of Trp-32 since both are located near the dimer interface. For the latter, Trp-32 becomes partially exposed when the dimer interface becomes more flexible and, therefore, solvents can quench the Trp fluorescence (Qiu *et al*). It is not clear from the available data whether the decrease in intrinsic fluorescence arises from the former reason or the latter; in either case, the results indicate that the dimer interface is disrupted during the lag phase.

159

The various kinetics of the holo protein aggregation monitored using CD and UV spectroscopy suggest multiple pathways of aggregation are possible during the lag phase. There is an interesting observation of aggregation profiles; Fig. 3.10a and 3.12b, which are different analyses on the same aggregation of pWT (*i.e.,* the same samples were subjected to two different experiments, CD and UV as well as light scattering measurements). In Fig. 3.12b, the UV slope (255 – 270 nm) remains constant during the lag phase, which suggests either no metal composition change or Zn loss. It is probably due to the latter reason because the increase in $[\theta]_{209}$ (Fig. 3.10a) indicates a conformational change in the protein similarly to apo SOD1. The disrupted dimer interface can affect loop IV, since loop IV encompasses three different regions: the dimer interface region (residues 49-54); the disulfide bond region (residues 55-61); and the Zn binding region (residues 62-82) (Hornberg, Logan, Marklund & Oliveberg, 2007). Thus, the disrupted dimer interface and loop IV can promote Zn loss during the lag phase. This coupled interaction between dimer interface and metal binding loops is supported by a recent study on the molecular dynamics of SOD1 (Khare & Dokholyan, 2006). In addition, Zn has lower affinity to SOD1 than Cu, implying that SOD1 may be more prone to lose Zn ions (Crow *et al*, 1997b). Moreover, a previous study on holo SOD1 unfolding kinetics indicated preferential Zn loss during unfolding (Rumfeldt *et al*, 2009). It is important to mention that when holo SOD1 loses Zn ions, the protein contains Cu ion in the partially structured protein, which can cause oxidative damage, which promote aggregation, as well. This sequential events can be one of many aggregation pathways. From the limited data available, it seems likely that there are more than one universal

aggregation pathways, which may be related to different duration, final intensity and metal amounts in the aggregates (Fig. 3.13 and 3.14) (see below).

3.4.2.2 Cu loss during exponential phase

The exponential phase begins with the appearance of a second peak in the hydrodynamic diameter distribution, corresponding to the size of the aggregates (~ 1000 nm), and a shoulder in the autocorrelation function (Fig. 3.4 – 3.7). Since protein association is thermodynamically favored during the exponential phase, the rapid growth in aggregation profiles is observed during this phase. The details of aggregation mechanism during the exponential phase are discussed below.

From the lag phase and onwards, the intrinsic fluorescence of Trp-32 decreases continuously without a change of λ_{max} in the emission spectra (Fig. 3.8), which indicates that the microenvironments near Trp-32 change continuously due to aggregation but the residue does not become buried. A decrease in the UV slope (from 255 – 270 nm) is detected during the exponential phase regardless of different pathways observed from the lag phases, which indicates that the proteins lose Cu ions during the exponential phase (Fig. 3.12). Importantly, the decrease in the specific activity (Fig. 2.6) during the exponential phase supports the loss of Cu in this phase, as well. In summary, during the exponential phase, the dimer interface is continuously disrupted and Cu loss is the key event during this time.

3.4.2.3 Multiple routes for the holo SOD1 aggregation

The experimental results in this chapter further support the proposed aggregation mechanism from holo SOD1 in chapter 2 in terms of the involvement of both metal loss and dimer dissociation (Scheme 2.1). In addition to a lag phase comparison among mutants of SOD1 and SEDI binding data in chapter 2 (Fig 2.2, 2.5 and 2.14), SOD1 aggregation monitored using the intrinsic fluorescence and the AB^2 and B^2 comparison with various mutants of SOD1 (Fig. 3.8 and 3.18, respectively) indicate that dimer interface disruption and the dimer dissociation occur during holo aggregation. In addition to specific activity and metal analysis in chapter 2 (Fig 2.6 and Table 2.1), CD data, UV slope (255 – 270 nm) change data, the B^2 comparison and the thermal unfolding of the aggregates (Fig. 3.10, 3.11, 3.12 and 3.16) indicate that aggregation from holo SOD1 involves metal loss.

In order to ascertain the underlying kinetic scheme to explain all the observation: (1) the two different aggregation profiles including two distinct patterns for duration in the exponential phase and final intensity in plateau (Fig. 3.13); (2) Cu loss in the exponential phase indicated from UV data (Fig. 3.12); and (3) metal contents in final aggregates (Fig. 3.14), Scheme 3.1 is proposed. The model shown in Scheme 3.1 is the simplest version in which a dimeric species dissociates in the lag phase. In one model, the protein species proceeds to have a shorter duration and a lower plateau, and produces aggregates containing more Cu ions. On the other hand, the dimer is dissociated and this species proceeds to have a longer duration and a higher plateau. The final aggregates are with more Zn ions. In both cases, the proteins lose Cu ions during the exponential phase. Other studies have observed similar effects with metal loss on the aggregation profiles of SOD1, in which E/Zn shows a

162

longer duration and higher plateau, whereas Cu/E of SOD1 shows a shorter duration and lower plateau (Chattopadhyay *et al*, 2008). It seems likely that the various kinetics observed during the lag phase might be related to the different aggregation profiles (Scheme 3.1). The particular aggregation mechanism described above (see Discussion, section 3.4.2.1) suggested that Zn loss during the lag phase and interestingly the final intensity of light scattering was relatively low, implying the final aggregates have less Zn than Cu ions. From the limited data, it can be speculated that specific metal loss during the lag phase affects the entire aggregation. More data should be collected for making any conclusion.

Scheme 3.1
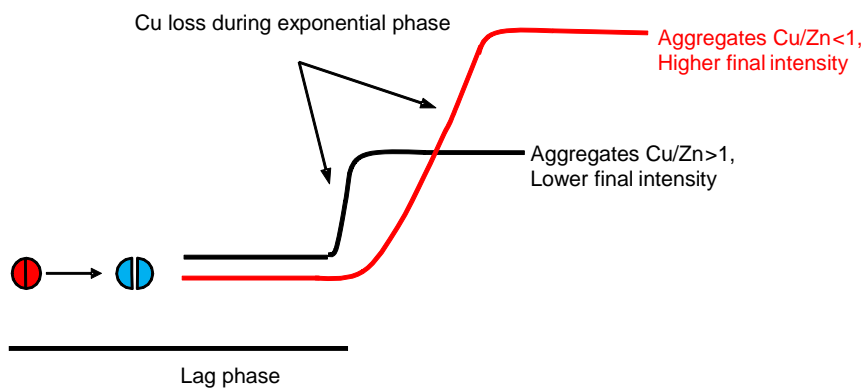
Multi-pathway of holo SOD1 aggregation. Red circle and blue half circle represent dimer SOD1 and monomer SOD1. The black line and red line represent two different aggregation pathways with regard to metal loss as well as duration and final intensity. In both pathways, proteins lose Cu during exponential phase.

3.4.3 Disease implications

The experimental system presented herein proposes mechanistic details of SOD1 aggregation for the first time with regard to metal loss, in that holo SOD1s can lose more of either metal (Cu or Zn). How this mechanism is actually related to *in vivo* is not clear to date since there are no experimental results of metal contents in aggregates from ALS patients (Hayward *et al*, 2002). However, it is interesting that fALS patients with the H46R mutation, a Cu binding mutant having only Zn cofactor in the protein, have the longest disease duration, which is consistent with the proposed mechanism. A large number of fALS-associated SOD1 mutants, regardless of location, have shown decreased metal affinity (Hayward *et al*, 2002) or dimer interaction (Stathopulos, 2005). Since metal binding and dimer interface are coupled (Hornberg, Logan, Marklund & Oliveberg, 2007), one can affect the other. Thus, the proposed multi-pathway aggregation could explain how unrelated mutations in SOD1 cause the same fALS pathology. Furthermore, despite its stable structure, fully metallated pWT also follows the same mechanism of aggregation as the fALS associated mutants (monomerization and metal loss) and this may be the link between fALS and sALS as supporting the hypothesis of common disease mechanism of fALS and sALS (Boillee, Vande Velde & Cleveland, 2006a).

The aggregation mechanism observed here for holo SOD1 shares a characteristic with those of other disease-associated proteins, namely the dissociation of multimeric proteins. This has been implicated in many other diseases as a critical step (Foss *et al*, 2005). For example, in TTR linked familial amyloidosis, it is found that mutants of the tetrameric protein, TTR, promote amyloidosis when enhancing dissociation of the native tetramer (Foss,

164

Wiseman & Kelly, 2005). Similarly, this chapter also proposed that dimer interface disruption is an early event in aggregation. Also, the holo SOD1 aggregation has unique properties. Unlikely to other protein aggregation processes that are related to amyloidosis, subtle changes can induce aggregation as seen by the agitation effect, implying that small a local pH change or subtle abnormal interactions with membranes in cells can initiate undesired interactions to disrupt the dimer interface and/or loop IV or electrostatic loop (loop VII). Also, since aggregation does not require significant structural changes from the native structure, proteasomes and/or chaperones can miss these species, which can initiate aggregation, especially, in old age. This might be why ALS is a late onset disease. Furthermore, if the cell defense mechanisms fail to remove initial aggregates, then successive aggregation is much easier due to the seeding effect, which may be related to the fast disease progression in ALS. In summary, the current results provide new and potentially general insights into SOD1 aggregation and therefore, ALS. The system can be used for a model system for ALS to develop urgently needed therapeutic strategies against toxic protein aggregation. To do this, several key elements such as the metal content of patient aggregates, how the different aggregation pathways are related to the disease, how the different intermediates interact with proteosomes and/or chaperons and which intermediates are more toxic need to be determined.

Chapter 4

Sonication, and its damaging mechanisms on proteins

4.1 Introduction

Sound is a travelling wave that is transmitted through a medium and sound beyond the human hearing threshold is termed ultrasound (Timothy J. Mason & Peters, 2002). Typical frequencies of ultrasound are between 20 kHz and 1 MHz (Joseph *et al*, 2009). The action of applying ultrasound, known as sonication, has been used in a wide variety of processes in chemistry laboratories and industries. The effect of sonication is induced not by interaction of sound waves with molecules in solution, but by the process of cavitation: the formation, growth and implosive collapse of microbubbles in solution (Suslick, 1990). More specifically, cavitational collapse generates enormous local temperatures (roughly 5000 °C) and pressures (approximately 500 atm) and an extraordinary heating and cooling rate (10^9 K/s). Cavitational bubbles are formed when the inter-molecular distance exceeds the critical distance necessary to hold the liquid intact due to the negative pressure of an expansion wave (rarefaction) (Suslick, 1990; Timothy J. Mason & Peters, 2002).

The effects of sonication are divided into physical and chemical effects from cavitation. The physical effects of cavitation are shock waves and microstreaming from frequent creation and collapse of microbubbles. These two effects combined are called shear stress. Chemical effects of cavitation involve the formation of highly reactive intermediates

166

such as hydroxyl radicals and hydrogen peroxide which are formed inside bubbles (Suslick, 1990; Timothy J. Mason & Peters, 2002). There are many factors that influence cavitation, including frequency of ultrasound, solvent conditions (*e.g.,* viscosity and vapor pressure), and external factors (*e.g.,* temperature and pressure). For example, it is harder to create cavitation at higher frequencies because the time to produce cavitation during rarefaction is too short, which is why higher frequencies are used for medical application of sonication (Timothy J. Mason & Peters, 2002).

Sonication has been used in various fields including: biotechnology, food industries, medical fields, and chemistry laboratories. For example for biotechnology applications, sonication assists in biofuel production with effectively mixing natural oils and methanol (Rokhina *et al*, 2009). Additionally, sonication is used for biosensor preparation, in which sonication enhances immobilization of enzymes onto spectroscopic grade graphite (Rokhina, Lens & Virkutyte, 2009). These applications make use of the shock wave properties of sonication. In the food industry, sonication has been utilized for a wide variety of applications from grading beef to sterilization. In the case of sterilization, sonication is combined with other preservation methods such as high pressure or heat (Butz & Tauscher, 2002; Piyasena *et al*, 2003). For medical applications, ultrasound imaging and dental descaling are common; however, ultrasound with microbubble contrast agents has been under recent investigation for drug delivery and imaging purposes (Ferrara *et al*, 2007). In addition, sonication is being investigated for diagnosing the presence of extremely low levels of prion infectious agents. In this case, minute amounts of the infectious prion are amplified by cycles of sonication. This procedure is called protein misfolding cyclic amplification

(PMCA) (Saborio *et al*, 2001). Lastly, sonication is used in chemistry laboratories as part of preparative procedures. For example, the degassing of buffer for chromatography can be done by sonication (Timothy J. Mason & Peters, 2002). Although sonication has been considered as a useful tool for many different fields, the potential damage to biological materials (*e.g.,* proteins) caused by sonication has received little attention (Stathopulos *et al*, 2004). Since proteins maintain their native structures mainly by weak non-covalent interactions such as hydrogen bonds and hydrophobic interaction, the effects of sonication (local heating, sheer stress, and free radical reaction) can affect protein native structure. Moreover, since the functions of proteins are dependent on correct folding, a loss of function can occur when undesired cavitation occurs and alters protein structure during the application of sonication. Stathopulos *et al.* have found that sonication of proteins can cause amyloid-like aggregation (Stathopulos *et al*, 2004). This finding has significant implications because amyloid has been implicated in the pathogenesis of many different human diseases (Dobson, 2001a). Furthermore, since amyloid aggregates can act as seeds to promote further amyloid formation (Harper & Lansbury, 1997), the use of sonication for food and medical processes should be reconsidered due to the potential undesirable consequences of amyloid formation.

4.1.1 Chapter overview

The experiments described in this chapter characterize protein damage induced by sonication with a set of structurally diverse proteins. The damage includes: aggregation and amyloid formation, protein unfolding, and free radical-mediated modification. Thioflavin T

(ThT), a dye commonly used for detecting amyloid, trypsin digestion, mass spectroscopy (MS), and SDS-PAGE were used for detecting protein damage. Additionally, this chapter shows protein damage induced by sonication can be reduced by altering the experimental conditions to use low temperatures and addition of the free radical scavenger, glutathione (GSH). The characterization of sonication-induced protein damage and its mechanism provide valuable information on the effects of sonication on proteins in solution and these findings have implications for medicine, industry and basic research laboratories as sonication is a possible cause of the aggregates that resemble amyloid.

4.1.2 Acknowledgments

I would like to thank a former student in our lab, Peter Stathopulos who initially showed me how to use sonication for the study of proteins.

4.2 Materials and Methods

4.2.1 Materials

ThT, horse heart myoglobin, hen egg white lysozyme, trypsin and β-lactoglobulin were purchased from Sigma (Sigma Chemical Co.). HEPES, SDS and BSA were obtained from Bioshop (Bioshop Canada Inc.). Recombinant SOD1 was prepared as described in section 2.2.1, and recombinant hisactophilin was obtained from a previous colleague in our lab, Joe Meissner. Briefly, recombinant hisactophilin was expressed in *E. coli* and purified

using affinity and size exclusion chromatography (Hammond *et al*, 1998). Ultrapure water deionized using a Milli-Q system (Millipore) was used throughout.

4.2.2 Sonication

Protein samples were prepared at 3 mg/mL in 20 mM HEPES, pH 7.8, and were filtered using a 20 nm cutoff filter (Anatop 10, Whatman Ltd.). Sonication was performed using a W 225 probe sonicator (Heat Systems, Ultrasonics, Inc.) at room temperature (RT, unless otherwise stated) and the tip of the sonicator was fixed at the 100 µL level in a sample container to prevent foam formation. If the protein solution was turned into a complete foam during sonication, the sample was not further analyzed. Sonication was conducted with a sample volume of 500 µL. Prior to sonication, the tip was cleaned with sandpaper and then dried by ethanol. Solutions were sonicated for either 20 cycles or 40 cycles, in which each cycle was composed of 5 pulses of 1 s followed by a 1 min incubation period (Fig.4.1). For all sonication experiments, the frequency used was 20 kHz and the power output was set to 30 W.

For sonication of heterogeneous samples, each protein in solution was prepared at 1.5mg/mL and the remaining procedures for sonication were the same as described above. Moreover, when evaluating the effect of temperature on sonication, sonication was conducted at different temperatures such as RT, approximate temperature 4.5 °C in an ice bath, and 40 °C in a water bath. The temperatures during sonication (except for RT) were controlled by a water bath (VWR) during sonication. Temperature change was measured

using a thermocouple (Temperature controller, Barnat), in which voltage was converted to temperature using a standard curve created prior to experiments. The standard curve was generated using a temperature controlled water bath (VWR).
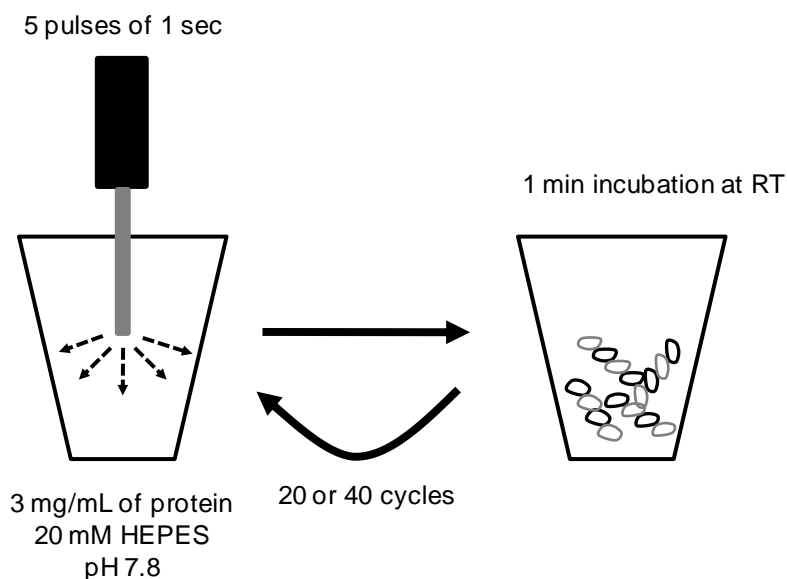
Figure 4.1 Cyclic protein sonication

Filtered protein solutions were sonicated for 5 pulses of 1 sec (20 kHz, 30W) and the protein solution was subsequently incubated at RT for 1 min. The procedure was typically repeated 20 or 40 times. For experiments monitoring temperature effects on sonication, the procedure was performed in an ice bath (approximate temperature 4.5 °C) or in a water bath (40 °C).

4.2.3 Light scattering measurements

For the cycle dependence of lysozyme aggregation, light scattering was measured for the estimation of aggregation. Two protein samples (2 x 500 µL) were prepared for sonication. One was sonicated for a different number of cycles (as described in section 4.2.2). Immediately after sonication, without dilution, static light scattering was measured using a Zetasizer Nano ZS (Malvern). For the control, the other sample was used and light scattering was measured in the same way as the sonicated sample.

4.2.4 ThT enhancement

Protein samples (3 mg/mL in 20 mM HEPES, pH 7.8) were diluted to 1 mg/mL in 75µM ThT, 20 mM HEPES (pH 7.8). Fluorescence emission spectra were acquired immediately using a Fluorolog3-22 spectrofluorometer (Jobin Yvon-Spex, Instruments S.A. Inc.). The excitation wavelength was 440 nm and the emission data was collected between 445 – 600 nm. The slit widths for excitation and emission were 1 and 5 nm, respectively. The reported spectra of protein samples are the result of the ThT spectrum of the protein subtracted from the spectrum for corresponding samples with no ThT. For example, ThT spectrum for sonicated BSA was subtracted from the spectrum of the sonicated BSA without ThT.

4.2.5 Denaturing gel electrophoresis

Sonicated samples were spun down (13000 g for 4 min) and pipetted to obtain well mixed samples (aggregates and soluble fraction). 20 µL of sonicated samples were mixed with the same volume of gel loading buffer, consisting of 1.25 mL of stacking gel buffer (see below), 1.95 mL of 10 % SDS solution, 1.0 mL of glycerol, 0.2 mL of bromophenol blue, and 0.1 mL of H_2O made for a total of 5 mL. The mixed solution was then boiled for 10 min and subjected to gel electrophoresis. The reducing agent, β-mercaptoethanol was used (4 % v/v, final concentration in loading buffer) during the characterization of higher molecular weight species. SDS-PAGE was performed as described by Laemmli (Laemmli, 1970). Briefly, gels were prepared with 6 % (w/v) acrylamide in the stacking gel buffer and 15 % (w/v) acrylamide in the separating gel buffer. The separating gel was made from: 3.75 mL of 40 % (w/v) polyacrylamide solution, 3.55 mL of MilliQ water, 2.25 mL of 1.5 M Tris buffer (pH 8.8), 100 µL of 10 % (w/v) SDS, 100 µL of 10 % (w/v) ammonium persulfate (APS) and 5 µL of N, N, N', N'-tetramethylethylenediamine (TEMED). The stacking gel was made from: 0.75 mL of 40 % (w/v) polyacrylamide, 2.575 mL of MilliQ water, 0.625 mL of 1 M Tris buffer (pH 8.8), 50 µL of 10 % (w/v) SDS, 50 µL of 10 % (w/v) ammonium persulfate (APS) and 5 µL of N, N, N', N'-tetramethylethylenediamine (TEMED). Running buffer contained 14.4 g of glycine and 1g of NaSDS dissolved in 25 mM Tris buffer, pH 8.8 to final volume of 1L. Gels were run at 150 V (constant voltage). Gels were stained using Coomassie Blue and destained using 40% (v/v) methanol and 7% (v/v) acetic acid in water.

4.2.6 Trypsin digestion

For evaluating the cycle dependence of aggregation, the samples with different numbers of sonication cycles were subjected to trypsin digestion. Trypsin was prepared in MilliQ water (1.5 mg/mL).   Sonicated protein samples (3 mg/mL) were vortexed and 25 µL of protein samples before and after sonication were mixed with 5 µL of the trypsin solution to give a trypsin: protein ratio (w/w) of 1: 10. The mixture was then incubated for 12 min at RT for digestion, after which 30 µL of gel loading buffer for SDS-PAGE was added and the sample immediately boiled in order to stop the digestion reaction.

For different ratios of trypsin digestion, different concentrations of trypsin (1.5, 0.6, 0.3, and 0.15 mg/mL), were prepared by diluting a stock solution (6 mg/mL in MilliQ water). 25 µL of protein samples (before and after sonication) were obtained after vortexing and then mixed with 5 µL of the various concentrations of trypsin in order to make the following trypsin: protein ratios (w/w): 1: 2.5, 1: 10, 1: 25, 1: 50 and 1: 100. The rest of the procedures were the same as described above. Typically, SDS-PAGE was conducted directly after boiling the samples.

4.2.7 Mass Spectrometry (MS)

Sonicated samples were centrifuged (13000 g for 5 min) in order to obtain soluble species. Protein samples were diluted to 1 µM in 50/50 of MeCN in water containing 0.2 % (v/v) FA. Each sample was incubated for 1.5 min and then applied to electrospray ionization using a Micromass Q-TOF Ultima Global (Waters). The capillary voltage and cone voltage

were 3 kV and 80 V, respectively. The signal was accumulated for at least for 1 min and the average of m/z data from the accumulated signal was reported. Prior to mass measurements, a 1 % phosphoric acid solution in 50/50 of MeCN in water was used for m/z calibration.

4.2.8 Effect of glutathione (GSH) on protein sonication

Stock GSH solution (50 mM) was prepared fresh for each experiment by dissolving glutathione in degassed MilliQ water. Prior to sonication, 10.2 µL of the stock GSH solution was added to each protein solution (500 µL of 3 mg/mL protein in 20 mM HEPES, pH 7.8, prepared as described above) to give final concentrations of 1 mM GSH and 2.94 mg/mL protein. The mixed solution was subjected to sonication for 20 cycles as described in section 4.2.2. Following sonication, the ThT fluorescence enhancement of the samples was measured as described in section 4.2.4.

4.3 Results

The experimental conditions used herein for sonication were similar to those in the previous work of the Meiering lab (Stathopulos *et al*, 2004), which were initially based on conditions developed by Saborio *et al.* for PMCA (Saborio, Permanne & Soto, 2001) (see Materials and Methods, section 4.2.2). One modification from earlier experiments was that the position of the sonicator tip was fixed at the 100 µL level in order to minimize foam formation, which can contribute to additional protein unfolding. When the position of the sonicator tip was varied during sonication, samples occasionally turned completely into

foam. Such samples were not further analyzed. In order to correlate protein damage caused by sonication with characteristic protein properties, proteins with varying physicochemical properties were selected for study. These include: BSA, myoglobin, lysozyme, β-lactoglobulin, hisactophilin, and holo SOD1 (Fig. 4.2 and Table 4.1). All proteins are monomeric except for holo SOD1 and β-lactoglobulin which are dimeric. The protein structures range from mainly α helical (myoglobin and BSA), to mixed α helical and β sheet (lysozyme and β-lactoglobulin), and mainly β sheet (hisactophilin and holo SOD1). Free radicals commonly target Cys residues (Stadtman & Levine, 2003), hence the cysteine content of the proteins was also chosen to vary, from zero (myoglobin) to 17 (BSA) (Fig. 4.2 and Table 4.1). Melting temperatures, total number of amino acid residues and the numbers of Arg and Lys residues, which is important information for trypsin digestion (see below) are also listed in Table 4.1. The following sections describe sonication-induced protein damage and how this process is affected by temperature and the free radical scavenger, GSH.

177
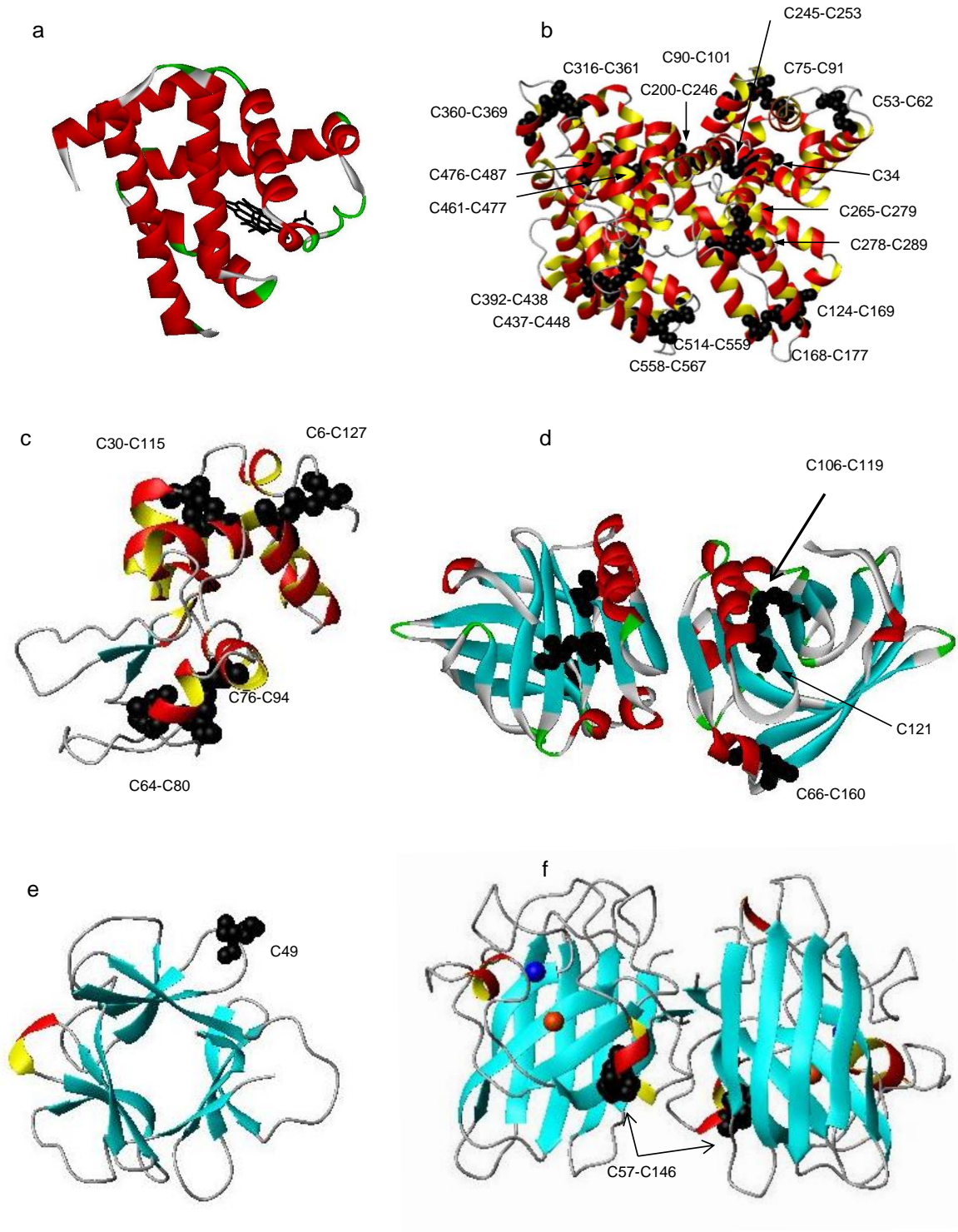
Figure 4.2 Structure of myoglobin, human serum albumin, lysozyme, β-lactoglobulin, hisactophilin, and holo SOD1

Ribbon and helical structure represent monomeric myoglobin (a), monomeric human serum albumin (b), monomeric lysozyme (c), dimeric β-lactoglobulin (d), monomeric hisactophilin (e) and dimeric holo SOD1 (f). The pdb codes for the proteins are 1WLA for myoglobin, 1AO6 for human serum albumin (as the structure of BSA has not been reported), 1E8L for lysozyme, 2AKQ for β-lactoglobulin, 1HCE for hisactophilin, and 1SOS for holo SOD1. In (a), the bound heme is shown as black sticks and in (f) Cu and Zn ions are colored orange and blue, respectively. Cys residues are shown in black with space filling representation and residue numbers indicated within the figure. If the cysteine residue is involved in intermolecular disulfide bonding, this is also indicated by a dash notation (for example, C57-C146). (a and d) were made using ViewerLite 5.0 and (b, c, e, and f) were made using MolMol (Koradi, Billeter & Wuthrich, 1996).

Table 4.1 Biochemical data for the proteins subjected to sonication

Protein	Molecular weight (kDa)[a]	Number of disulfide bonds [b]	Number of free thiols [b]	Number of Lys residues[b]	Number of Arg residues[b]	Number of total residues[b]	Native secondary structure[b]		Melting temperature[e] (°C)
							α (%)	β (%)	
Myoglobin	17.0	0	0	19	2	153	73	n.a[c]	76.7
BSA	66.4	17	1	59	23	581	48.7	0[d]	59.0
Lysozyme	14.6	4	0	6	10	129	34	3	61.5
β-lactoglobulin	36.8	4	2	28	6	324	15	40	69.1
Holo SOD1 [f]	31.8	2	0	22	8	306	5	40	92.0
Hisactophilin	13.7	0	1	9	1	118	2	52	61.7

[a] Molecular weight is for the native proteins, which are all monomers except for β-lactoglobulin and holo SOD1.

[b] Number of disulfide bonds, free thiols, Lys residues, Arg residues, total amino acid residues and native secondary structure (Kabsch & Sander, 1983) are from the RCSB PDB website (www.rcsb.org/pdb), except for BSA (Brown, 1976).

[c] not available

[d] Percent secondary structure is from the work of Oberg *et al.* (Oberg & Uversky, 2001).

[e] References for melting temperature: Kelly *et al.*(Kelly & Holladay, 1990) for myoglobin at pH 9.87; Arakawa *et al.* (Arakawa & Kita, 2000) for BSA at pH 7.2; Wray *et al.* (Wray *et al*, 2000) for lysozyme at pH 7.4; Fessas, *et al.* (Fessas *et al*, 2001) for β-lactoglobulin at pH 6.8; Stathopulos (Stathopulos, 2005) for holo SOD1 pH 7.8; and Liu *et al.* (Liu *et al*, 2001) for hisactophilin at pH 6.25.

[f] A well established pseudo wild type (pWT) background was used for holo SOD1, in which the free cysteines at positions 6 and 111 are mutated to alanine and serine, respectively. The pWT has very similar structure, dynamics, stability and activity to wild-type SOD1 (Lepock, Frey & Hallewell, 1990; Parge *et al*, 1986).

4.3.1 Cycle dependence of aggregation

The formation of aggregates due to sonication was investigated as a function of the number of sonication cycles and characterized using static light scattering, trypsin digestion, and ThT fluorescence enhancement. Fig. 4.3 shows that light scattering intensity of lysozyme increases linearly with sonication cycles. A similar linear relation was reported previously by Stathopulos *et al.* (Stathopulos *et al*, 2004) using BSA. The previous work reported that the distribution of particle sizes measured by dynamic light scattering (DLS) did not change significantly above 5 sonication cycles (Stathopulos *et al*, 2004). Thus, the observed light scattering results suggest that the number of aggregates induced by sonication is proportional to the number of sonication cycles.

To further investigate the dependence of aggregation on the number of sonication cycles, lysozyme after sonication was subjected to trypsin digestion (Fig. 4.3b). Trypsin cleaves at two positively charged amino acids: Lys and Arg. One can expect that if sonication causes the protein to unfold in some way, then sensitivity to protease digestion should increase. When lysozyme was sonicated for greater than 5 cycles (Fig. 4.3b lane 3-7), it became more sensitive to digested by trypsin, resulting in an additional band slightly above the main band in the SDS PAGE gel (Fig. 4.3b, arrow). In contrast, unsonicated lysozyme shows no intensity of this digested band (Fig. 4.3b lane2). When trypsin cleaves at a site between the two Cys residues to form a disulfide bond (Fig. 4.3c), the protein can nevertheless remain intact but run more slowly on the gel due to a more expanded structure. Lysozyme contains 6 Lys residues, 10 Arg residues and 4 intramolecular disulfide bonds (Table 4.1) and 5 Lys residues, 8 Arg residues are located between the two Cys residues to

form a disulfide bond. The intensity of the digested protein band (Fig. 4.3b, arrow) is not dependent on sonication cycle (*i.e.,* the band intensity does not change significantly above 5 sonication cycles). Overall, it can be concluded that sonication destabilizes lysozyme so that it becomes more sensitive to trypsin digestion.

a

b

c
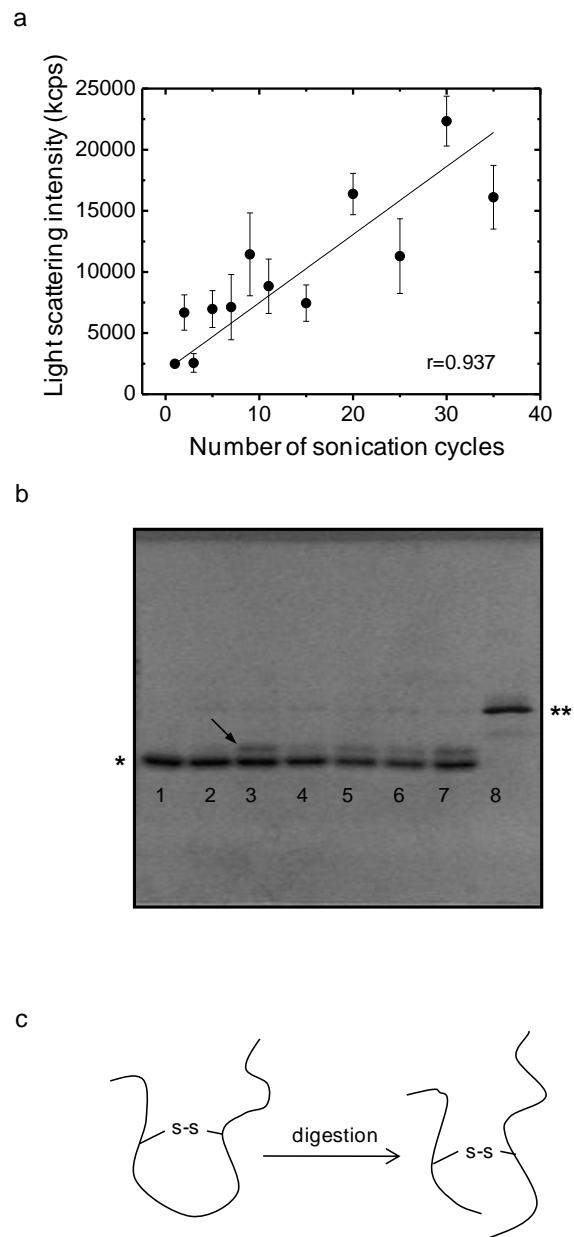
Figure 4.3 Cycle-dependence of aggregation

(a) Light scattering intensity of sonicated lysozyme solution is plotted against the number of

sonication cycles. The data were fit to a straight line obtained using Origin 7.5 and showed a

strong correlation (r = 0.937). (b) Trypsin digestion of unsonicated and sonicated lysozyme.

The number of cycles of sonication is 0 (lane 1, lane 2, and lane 8), 5 (lane 3), 15 (lane 4), 25 (lane 5), 30 (lane 6) and 35 (lane 7). Samples in lanes 2-7 were digested at 1:10 ratio of trypsin: lysozyme. Symbols (*, **) represent lysozyme without trypsin digestion and trypsin by itself, respectively. (c) Scheme of lysozyme digestion by trypsin. If trypsin cleaves lysozyme between two residues that form a disulfide bond, then the molecular weight of the protein is not changed but the species is expanded and so runs slower on the gel (indicated by the arrow in (b)) and is located just above the undigested species shown in lane 1.

4.3.2 Amyloid formation upon sonication

ThT is a fluorescent dye that is commonly used for the detection of amyloid (Lindgren *et al*, 2005). Typically, when ThT binds to amyloid species, its fluorescence is enhanced and λ_{max} of the spectrum is shifted from 440 to 482 nm. Sonication has been shown previously to induce the amyloid formation of numerous proteins, including BSA, myoglobin, lysozyme, hisactophilin, holo SOD1, β2-microglobulin and TTR (Misumi *et al*, 2008; Ohhashi *et al*, 2005; Stathopulos *et al*, 2004). Since the experimental criteria used here is different from the previous works (see Materials and Methods, section 4.2.2) (Stathopulos *et al*, 2004), it was necessary to confirm amyloid formation by ThT fluorescence herein (Fig. 4.4). Under more restricted experimental conditions (*i.e.*, by ensuring no foam formation), sonication also promotes amyloid formation. Fig. 4.4 and Table 4.2 compare the enhancement of ThT fluorescence for various proteins at two different sonication cycles (20 and 40 cycles). The intensity of ThT fluorescence tends to be less than that observed in the previous work of Stathopulos *et al.* (Stathopulos *et al*, 2004), which is not surprising since in

183

the current experiments, samples were discarded when the sonicated solutions completely foamed. The ThT data supports the finding that increasing sonication cycles results in increased formation of amyloid aggregates, although the degree of amyloid formation varies among the examined proteins. It is worth noting that the heme cofactor in myoglobin has significant absorbance at 410 nm, resulting in an underestimation of ThT fluorescence enhancement (Stathopulos *et al*, 2004) (Marden *et al*, 1986; Neves-Petersen *et al*, 2007). However, myoglobin did demonstrate non-physiological dimer formation on a gel (see below) as well as a significant increase in light scattering upon sonication (269 fold), indicating that it produces significant amounts of aggregates when subjected to sonication.
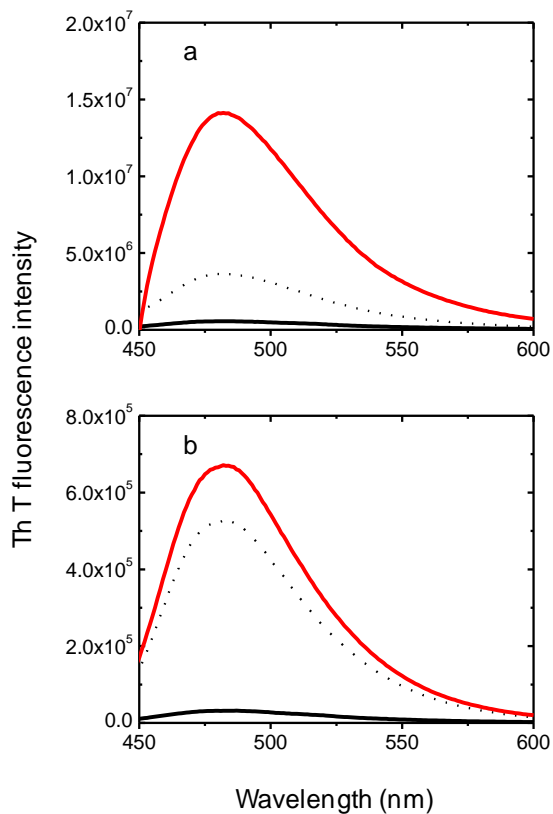
Figure 4.4 ThT fluorescence enhancement of sonicated BSA with 20 and 40 cycles

ThT fluorescence emission spectra are shown for solutions with no added protein (—), BSA

at 1 mg/mL before sonication (····), or 1 mg/mL sonicated BSA (—), for 40 cycles (a) and 20

cycles (b).

Table 4.2 Summary of ThT fluorescence enhancement for proteins subjected to 20 and 40 sonication cycles

Protein	# of cycle	Th T Increase (fold) [a]	2º Structure (native state) [b]	# S-S/-SH (native state) [b]
BSA	20	1.3	α	17/1
Myoglobin	20	1.0	α	0/0
β-lactoglobulin	20	1.2	αβ	2/1
Lysozyme	20	1.4	αβ	4/0
Hisactophilin	20	2.8	β	1/0
BSA	40	3.9	α	17/1
β- lactoglobulin	40	2.0	αβ	4/2
Holo SOD1[c]	40	8.0	β	2/0

[a] The fold increase in ThT fluorescence is obtained from the ratio of the of ThT intensities at λ_{max} between native protein and the sonicated protein, after subtraction of the background fluorescence of the corresponding protein solution without ThT.

[b] The native secondary structure (Kabsch & Sander, 1983), number of disulfide bonds and free thiols were obtained from the RCSB PDB website (www.rcsb.org/pdb), except for BSA (Brown, 1976).

[c] A well established pWT background was used for holo SOD1, in which the free cysteines at positions 6 and 111 are mutated to alanine and serine, respectively. The pWT has very similar structure, dynamics, stability and activity to wild-type SOD1 (Lepock, Frey & Hallewell, 1990; Parge *et al*, 1986).

4.3.3 Non-physiological dimer species and fragments formation upon sonication

To further investigate the properties and the amount of the aggregates formed by sonication and the possible occurrence of fragmentation, light scattering and denaturing gel electrophoresis (SDS-PAGE) were used. Additionally, the nature of high molecular weight species was investigated using β-mercaptoethanol on an SDS PAGE gel (Fig. 4.5), which can reduce intermolecular disulfide linkages. Fig. 4.5a demonstrates that all three proteins, myoglobin, lysozyme, and β-lactoglobulin, exhibit non-physiological dimers on the gel under non-reducing conditions after 40 cycles of sonication (see lanes 1-3). Also, the dimer formation of β-lactoglobulin was also detected using MS (see below). However, Fig. 4,5b shows that only myoglobin forms a non-physiological dimer under non-reducing condition after 20 cycles of sonication (see lanes 1-3). The latter is additional experimental evidence supporting the notion that aggregation from sonication is cycle dependent. Also, it is concluded that sonication-induced aggregates are mainly formed *via* hydrophobic interaction since the size of the aggregates was > 100 nm by DLS (Stathopulos *et al*, 2004), which is larger than that of dimers of the proteins. Fig. 4.5 (a and b) demonstrates that most dimers disappear upon addition of β-mercaptomethanol (compare lanes 1-3 and lanes 4-6), suggesting that dimerization occurs *via* Cys residue cross-links. The observed dimer formation is probably caused by free radicals due to cavitation, since free radicals commonly target Cys residues (Stadtman & Levine, 2003). Formation of intermolecular disulfide bonds can be another mechanism of expanding aggregation, as well, as seen previously in β-

lactoglobulin fibrils under thermal unfolding conditions (Prabakaran & Damodaran, 1997) (see Discussion for details) and amyloid formation of metal free SOD1 (Banci *et al*, 2007b). However, decreases in intensity of non-physiological dimer formation of myoglobin by addition of the reducing reagent should be understood as experimental errors such as contamination of Cys containing proteins since myoglobin does not contain any Cys residues (Fig. 4.5b). Nevertheless, the low intensity of the band corresponding to the dimer of myoglobin resulting from being unaffected by the reducing agent is still observed in Fig 4.5a (see lane 5), implying that this dimer is formed *via* non-Cys residue cross linking. Myoglobin dimerization has been reported, in which the highly reactive oxygen species, hydrogen peroxide can mediate non-physiological dimerization *via* linkage of Tyr residues, Tyr 103 and Tyr 151 (Tew & Demontellano, 1988). It is possible that the observed myoglobin dimers may be formed by the same mechanism since cavitation can produce hydrogen peroxide (Timothy J. Mason & Peters, 2002). The non-physiological dimer species formed after 40 cycles of sonication also appears to contain protein fragments, which become apparent upon the addition of the reducing agent as broad and weak bands below the main bands (Fig. 4.5 a, lanes 4-6). In other words, fragments are attached to other protein species *via* intermolecular disulfide bonding. However, protein fragments were not detected by MS (see below), suggesting that the presence of fragments upon sonication should be minimal, if at all. Sonication induces protein modifications such as non-physiological dimerization and fragmentation, *via* free radical reactions involving cysteines and other residues.

188
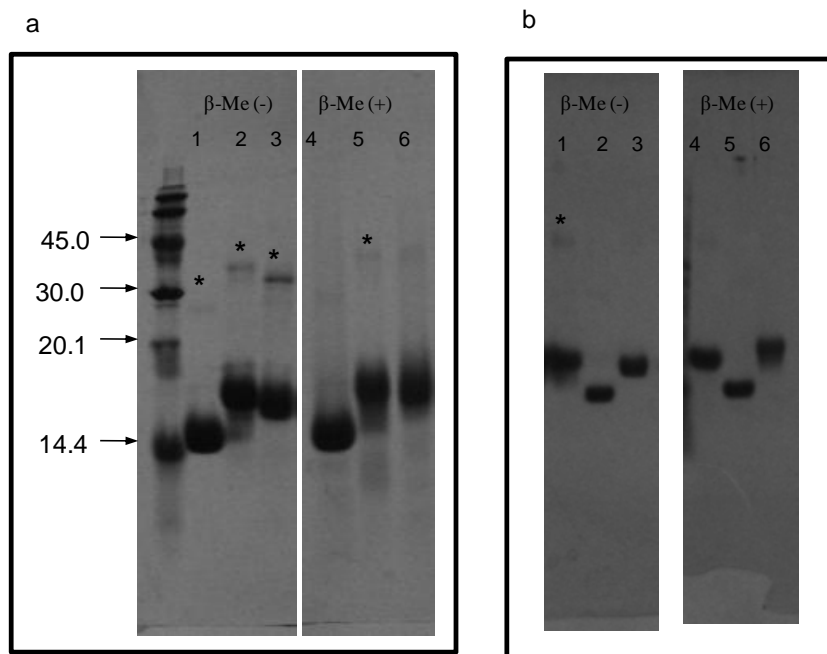
Figure 4.5 Higher molecular species and fragments from sonicated proteins shown by denaturing gel electrophoresis

Samples in panel (a) and (b) were subjected to 40 and 20 sonication cycles, respectively. In both panels, lanes 1-3 do not contain 4 % (v/v) β-mercaptoethanol and lanes 4-6 do contain 4 % (v/v) β-mercaptoethanol. The protein samples are as follows: lysozyme (lane 1(a) and lane 2 (b)), myoglobin (lane 2 (a) and lane 1 (b)) and β-lactoglobulin (lanes 3 (a and b)). Two pieces of each gel (a and b) were originally from one gel, but for ease of comparison of the effect of the reducing agent on dimer species, sections of the gel involved in this analysis have been cut out and placed beside each other. Non-physiological dimer species are indicated by an asterisk symbol (*). Molecular weight markers are shown at the left side of the gel.

189

4.3.4 Protein unfolding upon sonication

4.3.4.1 Mass spectroscopy (MS)

Previously, Stathopulos *et al.* reported that > 90 % of the protein remained in solution after sonication (Stathopulos *et al*, 2004). Also, the bulk of sonicated proteins in solution are not significantly modified since differential scanning calorimetry thermograms of sonicated protein solutions and unsonicated solutions are not considerably different (Jessica Rumfeldt, Jimes R. Lepock and E.M. Meiering, unpublished data). Thus, it is important to characterize properties of protein remaining in solution after sonication. The increased sensitivity of sonicated proteins to trypsin digestion suggests that sonication induces protein unfolding (Fig. 4.3). Partially unfolded proteins are known to be particularly prone to aggregate (Booth *et al*, 1997; Chiti *et al*, 2001; Hamada *et al*, 2009; Wiseman, Powers & Kelly, 2005). Therefore, protein unfolding induced by sonication was further investigated using ESI-MS since unfolded proteins can accommodate higher net charges than native proteins in ESI-MS (Chowdhury *et al*, 1990). This gives complementary information to denaturing SDS-PAGE, which cannot distinguish the native form of a protein from unmodified unfolded forms under non-reducing conditions. Fig. 4.6 shows that sonication of holo SOD1 for 40 cycles gives rise to a second m/z envelope at lower m/z ratios; regardless of incubation temperature (the effect of temperature is discussed in section 4.3.8). The envelope of higher m/z peaks corresponds to protein with lower net charge (mainly "9+" charged, Fig. 4.6a) indicates a more folded protein state. Additionally, the observed charge state (9+) agrees with the expected charge state of a folded protein with 18 kDa MW (Heck & Van Den Heuvel, 2004). With sonicated SOD1, the envelope of lower m/z peaks corresponds to proteins with higher

190

net charge (mainly "11+" charged, Fig. 4.6 b-d), which indicates that the protein is more

unfolded. This finding implies that the sonication destabilizes SOD1 to unfold compared to

the unsonicated protein SOD1. In the case of SOD1 the different m/z peaks correspond to

species with the calculated monomer holo SOD1 MW (15879 Da); however, it should not be

precluded that small mass changes, such as chemical modifications due to random free

radical reactions may be occurring, since there is uncertainty in the calculated MW.
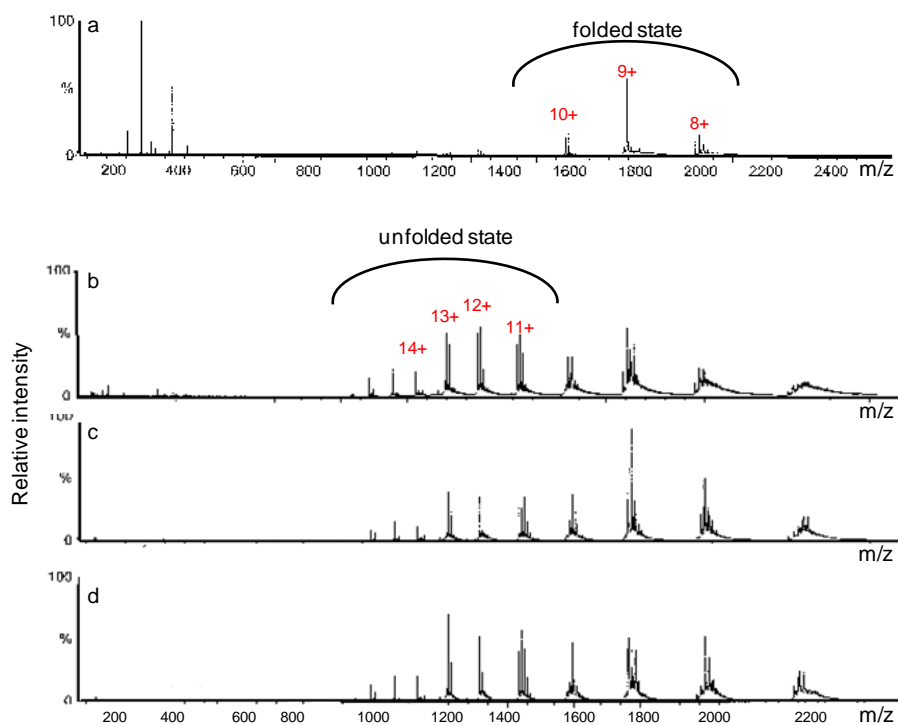
Figure 4.6 MS m/z spectra of unsonicated and sonicated holo SOD1

m/z spectra are shown for holo SOD1 before sonication (a) and sonicated (40 cycles) at 4.5

°C (b), RT (c), and 40 °C (d). All the samples were treated in the same way (see Materials

and Methods, section 4.2.7). The charge state for the corresponding peak is given as the

number above the peak. A charge state and the m/z peak are related as: *i.e.,* for +9 of SOD1 (15879 Da): m/z = (15879+9)/9 = 1765.

When 40 cycles of sonication were performed on β-lactoglobulin, an additional set of peaks corresponding to the dimeric form of the protein are observed (Fig. 4.7), consistent with the results obtained by SDS-PAGE (Fig. 4.5). Only the soluble species in the supernatant of sonicated samples was analyzed by MS. Thus, the soluble fraction contains considerable amounts of damaged proteins, non-physiological dimer species, which contribute to formation of amyloid aggregates *via* hydrophobic interaction and/or intermolecular disulfide bonds (Fig. 4.5).

The MS spectra were also inspected for evidence of fragmented species since Fig. 4.5 indicates the possibility of the presence of fragments induced by sonication, but these were not detected implying that there are not substantial populations of fragments.
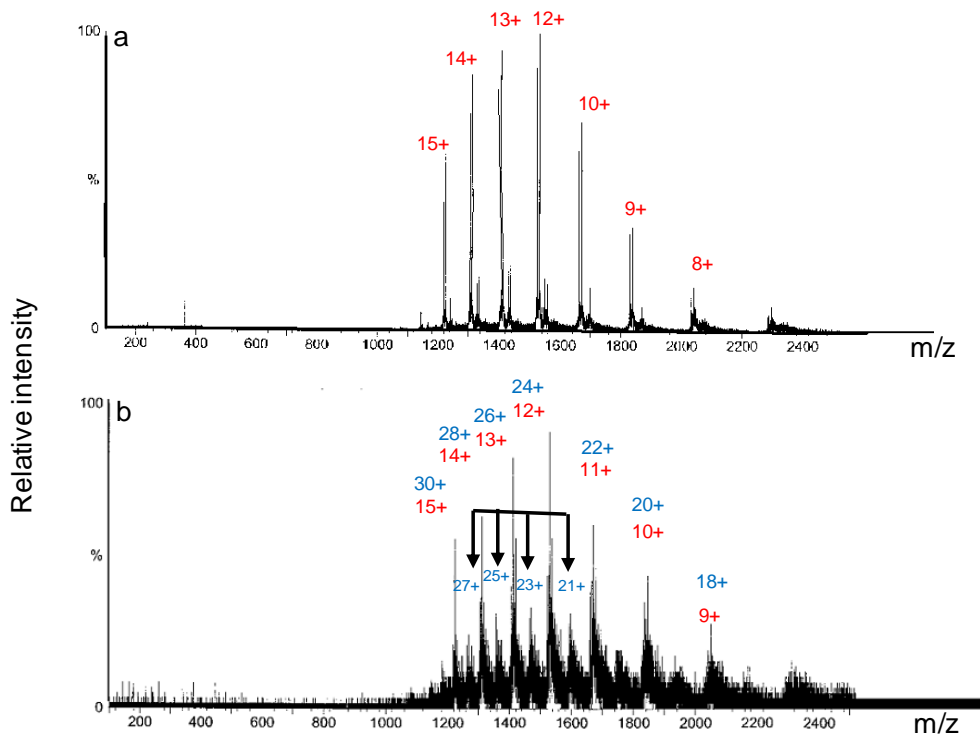
Figure 4.7 MS m/z spectra of unsonicated and sonicated β-lactoglobulin

m/z spectra are shown for β-lactoglobulin solution before sonication (a) and sonicated (40 cycles) at RT (b). All the samples were treated in the same way (see Materials and Methods section 4.2.7). The arrows indicate peaks corresponding to a dimer of β-lactoglobulin. The charge state for the corresponding peak is given as the number above the peak, in which red and blue numbers represent a charge state assuming that the β-lactoglobulin remains monomeric and dimeric, respectively. For example, a charge state and the m/z peak are related as: *i.e.,* for +12 of monomeric β-lactoglobulin (18365 Da): m/z = (18364+12)/12 = 1531 and for +23 of dimeric β-lactoglobulin (36730 Da): m/z = (36730+23)/23 = 1598.

193

4.3.4.2 Trypsin digestion

Fig. 4.5b demonstrates that no detectable change upon 20 cycles of sonication of lysozyme, β-lactoglobulin and myoglobin, although ThT fluorescence enhancement results indicate that 20 cycles of sonication can also induce amyloid formation (Table 4.2). Trypsin digestion was conducted with protein samples sonicated for 20 cycles without separation of aggregates to further detect protein unfolding induced by sonication. Samples were sonicated and then digested by different amount of trypsin. For trypsin digestion, the band of trypsin in SDS PAGE decreases as the trypsin to protein ratio decreases. The intensity for the main band (corresponding to native protein) for lysozyme and hisactophilin does not change significantly upon addition of trypsin, whereas the main band for BSA decreases in intensity as the amount of trypsin is increased. This may be explained by the relatively higher number of Arg and Lys residues in BSA (Table 4.1). Thus, a decrease in the total amount of stained BSA at higher trypsin to protein ratio (see the lanes 3, 4, 5, and 6 in Fig. 4.8b) is likely due to extensive degradation to short peptides which may not be well fixed in the gel and/or stained by Coomassie Blue. From the comparison of digestion patterns before and after sonication, the main difference between the sonicated samples and the unsonicated control for lysozyme, BSA, and hisactophilin (Fig. 4.8 a - c) is a decrease in intensity of the main protein bands, suggesting that sonication destabilizes the proteins so that they become more sensitive to trypsin digestion (compare lanes 3 and 4 in Fig. 4. 8a-c). Some non physiological hisactophilin dimers may show resistance to trypsin under the experimental condition. However, larger molecular weight species of hisactophilin (→ in Fig. 4.8c) are all

194

digested.   Additionally, lysozyme shows the formation of the slower migrating species having same MW indicated by the arrow in Fig. 4.8a, which is also seen in Fig. 4.3, likely resulting from a cleavage of the protein backbone by the attack of free radicals.   To summarize these results, although 20 cycles of sonication does not result in the formation of substantial quantities of high molecular weight species except for hisactophilin, protein unfolding and backbone cleavage does occur.
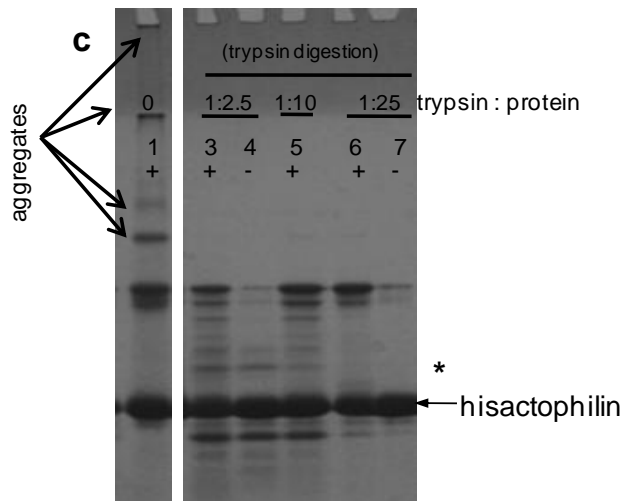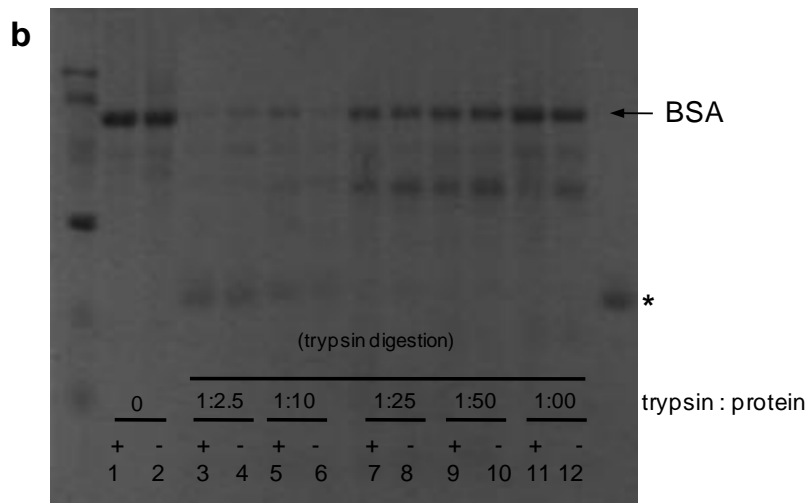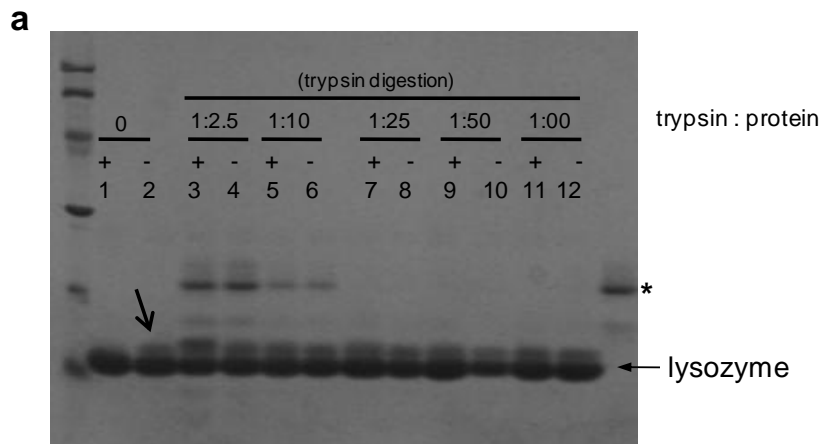
Figure 4.8 Trypsin digestion of lysozyme, BSA, and hisactophilin subjected to 20 cycles of sonication at RT

Sonication increases sensitivity to digestion by trypsin for (a) lysozyme, (b) BSA, and (c) hisactophilin. Gel electrophoresis was conducted without a reducing agent. The numbers and (+ and -) symbols on the SDS-PAGE gels represent sonicated and unsonicated protein, respectively. The ratio represents trypsin: protein (w/w). Thus, "0" indicates no trypsin digestion. The location of trypsin on the gel is indicated by asterisk symbols. The arrow ($\rightarrow$) in (a) indicates the protein species that results from a cleavage of the lysozyme backbone by the attack of free radicals. The arrow ($\rightarrow$) in (c) represents a high molecular weight species of hisactophilin that resulted from sonication. Molecular weight markers are shown at the left of the gels, corresponding to 96.0, 66.0, 45.0, 30.0, 20.1, and 14.4 kDa from top to bottom.

4.3.5 Additional aggregate formation upon further incubation of sonicated samples

Since trypsin digestion and MS experiments suggest that sonication results in the formation of various levels of unfolded species, the process by which unfolded proteins may contribute to further protein damage was investigated. This was studied using BSA samples which were sonicated and then incubated at RT and monitored for changes in ThT fluorescence. Fig.4.9 shows clearly that ThT fluorescence increases upon further incubation, suggesting amyloid formation continues after sonication. This suggests that destabilized

197

forms of the protein will continue to aggregate and/or the aggregates formed by sonication can also recruit soluble protein (seeding), as was shown in the previous study (Stathopulos *et al*, 2004).
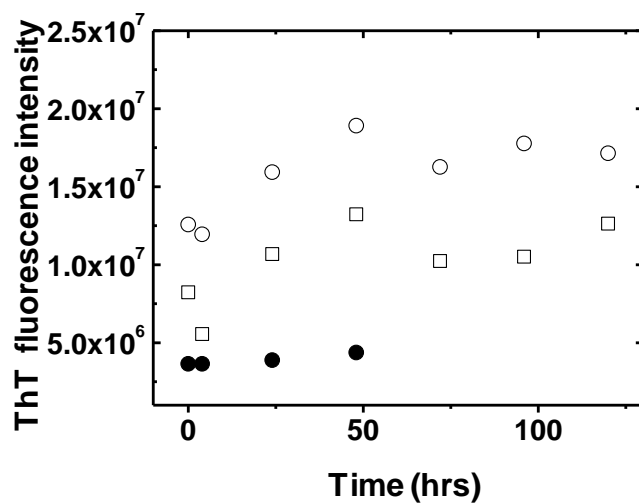
Figure 4.9 Post-sonication amyloid formation by BSA

ThT fluorescence enhancement is shown upon incubation of BSA solution (1 mg/mL) that has not been sonicated (●), and that has been sonicated at RT for 40 cycles (○) and sonicated at 4.5 °C for 40 cycles (□).

4.3.6 Effect of temperature on aggregation induced by sonication

Local heating is one of the mechanisms by which sonication can damage proteins (Timothy J. Mason & Peters, 2002); thus, the effect of temperature on sonication-induced aggregation was investigated. The temperature in solution was determined by measuring the thermocouple voltage and determining the corresponding temperatures using a calibration curve (see Materials and Methods, section 4.2.2). A calibration curve was generated for the temperature range, $1 - 80$ °C (Fig. 4.11a). The temperature is linearly related to the measured voltage over the experimental temperature range. The temperature of sonicated samples was determined by measuring the voltage immediately after 5 pulses of the sonication and at the end of the 1 minute incubation period by immersing the thermocouple in the sonicated solutions (Fig.4.1). The sonication procedure was conducted at different incubation temperatures, such as 4.5 °C (ice bath), RT, and 40 °C (water bath) (see Materials and Methods, section 4.2.2). For experiments at 40°C, the Eppendorf tube was immersed in a water bath throughout the sonication procedure and for experiments at 4 °C, the Eppendorf tube was immersed in an ice bath. Fig. 4.11b shows temperature change during 40 cycles of sonication at RT, in which the solution temperature reaches 65 °C after 11 cycles of sonication and plateaus. This high temperature is significant because it is in the range where many proteins are thermally unfolded (Table 4.1). The pattern for the change in temperature is very similar for the other incubation conditions; however, the absolute temperature difference between post-cycle and pre-cycle (ΔT) varies. Table 4.3 summarizes the

differences and clearly indicates that temperature is regulated better when immersed in water or an ice bath, instead of at ambient temperature.

Table 4.3 Summary of temperature change during sonication at different incubation temperatures

Incubation Temp (°C)	Pre-cycle Temp (°C)	Post-cycle Temp (°C)	ΔT
4.5	10.5	30.0	19.5
RT	53.5	65.5	12.0
40	47.0	62.7	15.7

$$b = -0.043 + 0.042a$$
$$r = 0.997$$

after 5 pulses of sonication (pre-cycle)

after 1 min incubation (post-cycle)

ΔT
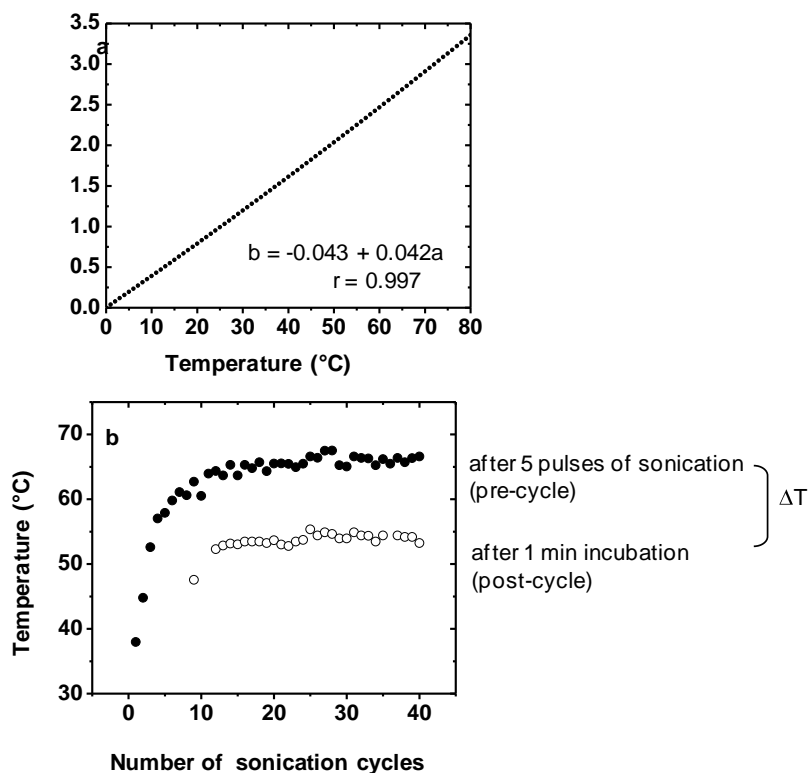
Figure 4.10 Temperature changes during sonication at RT

(a) A calibration curve that was obtained using a thermocouple. The presented values are data points and data were fit to a straight line using linear regression (Origin 7.5); however the fitting line is not shown since the line is coincident with the data points. (b) The temperature of sonicated solutions is shown immediately after 5 pulses of sonication and at the end of the following 1 minute incubation (*i.e.,* just before the next 5 sonication pulses) (Fig.4.1). Measured voltages were converted to temperature using the standard curve in (a).

The extent of aggregate formation was also monitored using ThT fluorescence. Fig. 4.11 shows that incubating protein samples of BSA, hisactophilin, β-lactoglobulin, and lysozyme in an ice bath, with approximate temperature of 4.5 °C, during sonication markedly decreases aggregate formation as measured by ThT compared to higher temperature (RT). There is still a small increase in ThT fluorescence for BSA and hisactophilin, but not for β-lactoglobulin and lysozyme. However, Fig. 4.9 indicates that the sonicated BSA solution in an ice bath shows additional increases in ThT upon further incubation after sonication.
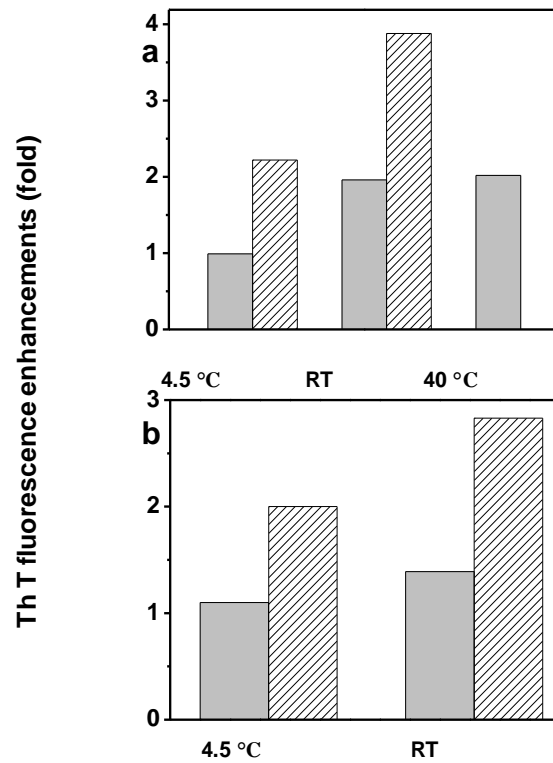
Figure 4.11 Effect of temperature on aggregate formation caused by sonication

(a) ThT fluorescence enhancement after 40 sonication cycles for β-lactoglobulin (▨) and

BSA (▨). (b) ThT fluorescence enhancement after 20 sonication cycles for lysozyme (▨) and

hisactophilin (▨).

4.3.7 GSH effects on amyloid formation

Free radical mediated oxidation of free amino acids and amino acid residues in proteins has been studied and these modifications are recognized as a form of protein damage (Stadtman & Levine, 2003). The involvement of free radicals in protein damage upon sonication was investigated further here using the free radical scavenger, GSH, a tripeptide antioxidant. GSH plays an important role in guarding against ROS in living cells by acting as an electron donor to reduce ROS (Hayes & McLellan, 1999). After reduction, GSH is oxidized to form GSSG (Owens & Belcher, 1965). As a strong free radical scavenger, GSH was therefore added to the protein samples, BSA, hisactophilin and β-lactoglobulin, prior to sonication in order to examine the involvement of free radicals in protein aggregation. Fig. 4.12 shows that amyloid formation, as monitored by increased ThT fluorescence for BSA, β-lactoglobulin, and hisactophilin, is completely inhibited by the presence of 1 mM GSH during sonication. This is clear evidence that free radicals from cavitation are significantly responsible for aggregate formation resultant from sonication.
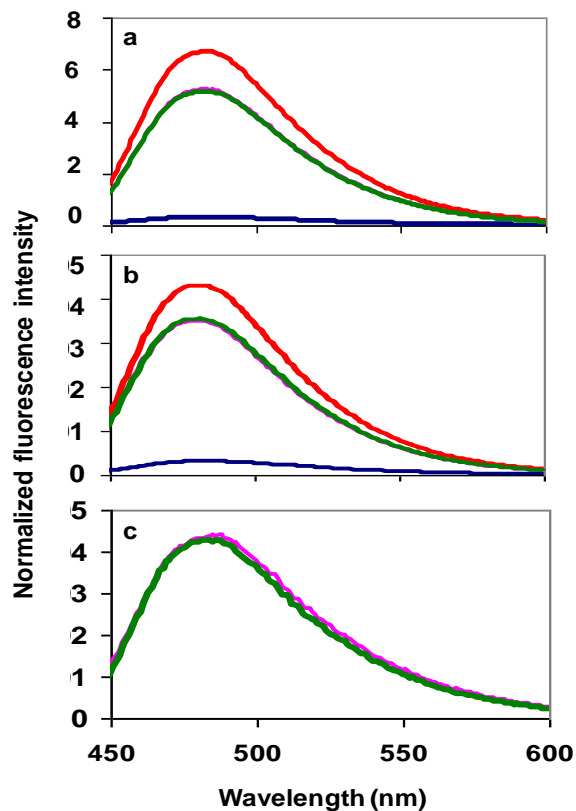
Figure 4.12 Effect of GSH on sonication-induced aggregate formation for BSA, β-lactoglobulin, and hisactophilin

(a) Fluorescence intensity of ThT alone (—), ThT with unsonicated BSA (—), ThT with BSA sonicated for 20 cycles at RT (—) and ThT with BSA and GSH mixture sonicated for 20 cycles at RT (—). (b) Fluorescence intensity of ThT alone (—), ThT with unsonicated β-lactoglobulin (—), ThT with β-lactoglobulin sonicated for 20 cycles at RT (—) and ThT with β-lactoglobulin and GSH mixture sonicated for 20 cycles at RT (—). (c) Fluorescence

intensity of ThT with unsonicated hisactophilin (—), and ThT with hisactophilin and GSH

mixture sonicated for 20 cycles at RT (—).

4.3.8 Sonication of mixed protein solutions

When sonication is used for food processing, for example for mayonnaise preparation

and meat processing, different proteins exist together during sonication. In order to

investigate the possible effects of these processes and the way two different proteins behave

was studied when they are sonicated together. Lysozyme was chosen as a primary protein

since Fig. 4.8 shows evidence for substantial modification (cleaved backbone polypeptide

chain) induced by sonication, which may promote interaction with another protein. Fig. 4.13

shows that when lysozyme is sonicated for 20 cycles with myoglobin and BSA, there is no

formation of heterodimeric protein species *i.e.,* lysozyme linked to myoglobin or to BSA.
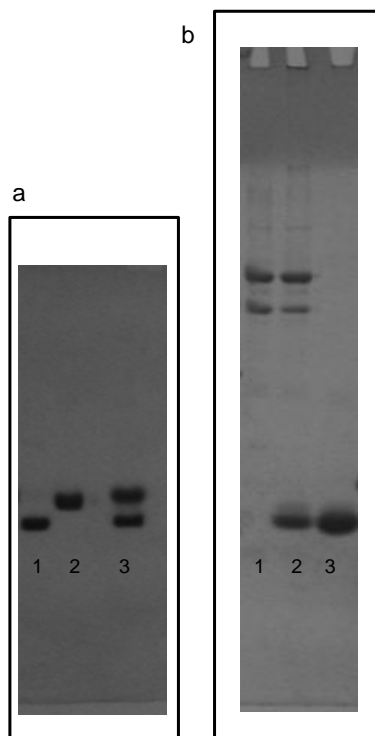
Figure 4.13 Sonication of mixed protein solutions

Lysozyme and myoglobin (a), lysozyme and BSA (b) were sonicated for 20 cycles at RT and then analyzed by SDS-PAGE. In (a), bands are observed for lysozyme and myoglobin before sonication (lanes 1 and 2, respectively), and sonicated lysozyme with myoglobin (lane 3). In (b), the samples are BSA before sonication (lane 1), sonicated lysozyme with BSA (lane 2), and lysozyme before sonication (lane 3).

4.4 Discussion

The use of sonication has received increased attention over the last decade for enhancement of various processes in a range of different fields including biotechnology,

medical application and food industry. On the other hand, possible damage induced by sonication had been received less attention. Stathopulos *et al.* (2004) studied the effects of sonication on proteins for the first time systematically and reported that sonication of proteins can cause formation of amyloid-like aggregates (Stathopulos *et al*, 2004). The results presented in this chapter can advance the findings of Stathopulos *et al.* (Stathopulos *et al*, 2004), in that sonication of proteins results in amyloid formation, free radical mediated modifications, including non-physiological dimer formation, fragmentation, and chain cleavage, and protein unfolding.

4.4.1 Sonication induces amyloid-like aggregates.

Previously, sonication has been shown to induce the amyloid formation of BSA, myoglobin, lysozyme, hisactophilin, holo SOD1, β2-microglobulin and TTR (Misumi *et al*, 2008; Ohhashi, Kihara, Naiki & Goto, 2005; Stathopulos *et al*, 2004). For current work, a more controlled sonication procedure was used to investigate if sonication is a sole effect on amyloid formation and the result confirms that sonication of structurally diverse proteins, BSA, myoglobin, lysozyme, hisactophilin, holo SOD1 and β-lactoglobulin, cause amyloid formation (Fig. 4.4 and Table 4.2). Additional evidence of amyloid formation upon protein sonication was provided including aggregate morphology, increase in β components in secondary structure, dye binding assays using amyloid specific dyes, ThT and Congo Red, and seeding effects (Stathopulos *et al*, 2004). It is important to note that Stathopulos *et al.* observed a mixture of morphologies for aggregates by TEM, some of which are clearly amyloid-like smooth fibrillar structures, but others are amorphous (Stathopulos *et al*, 2004).

Observation of amorphous aggregates implies another possible toxic mechanism of sonication as such aggregates are more related to toxic species than mature aggregates (Chiti & Dobson, 2006). Interestingly, none of the proteins used in current work are associated with amyloidosis, except for lysozyme; two mutants of lysozyme are known to be amyloid precursors that are implicated in the pathogenesis of non-neuropathic amylodosis (Pepys *et al*, 1993; Zalin *et al*, 1991). This is consistent with the observation that any protein is able to form amyloid *in vitro* under destabilizing conditions (Chiti *et al*, 2003b). Remarkably, the α helical proteins, BSA and myoglobin can also form amyloid by sonication, such that the α helical structure in the proteins are converted to β structure upon sonication. Together, these findings confirm that sonication can promote amyloid-like aggregates of various proteins, unrelated to amyloid disease and having diverse sequences as well as structures.

This chapter shows ways of decrease initial amyloid formation, in that the use of more controlled sonication procedure, less cycles of sonication (Table 4.2), lower incubation temperature (Fig. 4.11), and GSH addition (Fig. 4.12) can decrease amyloid formation. However, post-sonication amyloid formation is an issue of using sonication, which can be promoted by unfolded proteins by sonication and/or initial aggregates (seeding) (Fig. 4.9). Partially unfolded proteins are considered to be responsible for many different protein aggregation processes (Booth *et al*, 1997; Chiti *et al*, 2001; Hamada *et al*, 2009; Wiseman, Powers & Kelly, 2005). Thus, extreme sample conditions (*e.g.,* increased temperature, extreme pH, and addition of chemicals to induce oxidizing condition) have frequently been associated with protein aggregation. For example, myoglobin and lysozyme can form aggregates at high temperature (Fandrich *et al*, 2003b; Morozova-Roche *et al*, 2000) and

208

SOD1 can form aggregates in Cu medicated oxidizing solution conditions (Rakhit *et al*, 2004) and in low pH (Stathopulos *et al*, 2003). In fact, MS data and trypsin digestion pattern of sonicated proteins provide evidence that there are proteins unfolded even if there is no sonochemical modifications observed. Therefore, sonication enhances formation of unfolded protein species that may more readily unfold and the protein species are responsible for post-sonication aggregation. Thus, addition of stabilizing agents to help refolding after sonication can be considerate to prevent post-sonication amyloid formation.

4.4.2 Free radical effects on protein damages upon sonication

The experimental results herein support the notion that free radical mediated reaction can cause protein modifications upon sonication. Free radicals can be produced during sonication due to hydrolysis of water molecules by extremely high temperature and high pressure that are created by cavitation. Sonochemistry is the field making use of free radicals from cavitation (Timothy J. Mason & Peters, 2002). However, reactions involving free radicals are known to cause diverse chemical modifications on proteins. These include peptide bond cleavage, site-specific metal-catalyzed oxidation, oxidation of aromatic amino acid and methionine, and protein-protein cross-linking using tyrosine and cysteine (Stadtman & Levine, 2003). Thus, it is conclusive that non-physiological dimer formations of myoglobin and β-lactoglobulin, fragmentation of myoglobin, lysozyme and β-lactoglobulin (Fig. 4.5 and Fig. 4.7), and chain cleavage of lysozyme (Fig. 4.3) are mediated by free radical reactions. In particular, non-physiological dimer formation occurs *via* cysteine and tyrosine cross-linking. A previous study showed that non-native disulfide bond formation during

thermal unfolding of β-lactoglobulin can lead to polymerization of the protein. During heating, the native dimer was first dissociated, and then partial unfolding monomer exposes the free thiol group (Cys 121) to solvents (Prabakaran & Damodaran, 1997). The thiol group in a monomer of β-lactoglobulin started to form intermolecular disulfide bonds (Prabakaran & Damodaran, 1997). Thus, if sheer stress, local heating, and/or free radical reactions can dissociate dimer of β-lactoglobulin and unfold the monomers, then the free thiols (Cys 121) can be exposed and then form intermolecular disulfide bonds. However, it is not precluded that free radical can attack the solvent exposed intramolecular disulfide bond (C66-C160), resulting in thiyl radicals, which can form intermolecular disulfide bond with a thiyl radical on another monomer. Myoglobin has been shown to facilitate two Tyr residues, Tyr 103 and Tyr 151 for non-physiological dimer formation (Tew & Demontellano, 1988). Typically, solvent exposed Tyr 151 is a primary target by free radicals (Tew & Demontellano, 1988). Thus, it is possible that the observed non-physiological dimer of myoglobin upon sonication is formed by these two Tyr residues (Tyr 103 and Tyr 151). Moreover, backbone cleaved lysozyme (Fig. 4.8) and fragments of proteins (Fig. 4.5) are more evidence of protein damage induced by free radicals from sonication (Stadtman & Levine, 2003). However, currently available data cannot provide site specific information of chain cleavage and fragmentation of the proteins. Importantly, such modifications can promote amyloid formation *via* newly exposed hydrophobic interaction and/or cross-linking (Rakhit *et al*, 2004; Rakhit *et al*, 2002).

4.4.3 Possible sonication mechanism of protein damage

Cavitation generated by sonication is mainly responsible for protein damage. When microbubbles collapse, sheer stress from shock waves and microstreaming is induced as well as free radicals, extremely high temperatures and pressure (Timothy J. Mason & Peters, 2002). The net effects are sufficiently powerful to alter protein structure. For example, as seen in Table 4. 3, sonication at RT and 40 °C can increase solution temperatures up to 65.5 °C, which can induce protein unfolded, for instance, lysozyme with a T_m of 61.5 °C. Therefore, local heating by sonication can damage protein, since high temperature itself can induce amyloid formation (Fandrich *et al*, 2003b; Morozova-Roche *et al*, 2000). Sonication at a 4.5 °C can increase the temperature of a solution only up to 30 °C (Table 4.3) and decrease in amyloid formation is observed (Fig. 4.11). The sheer effect has been recognized as the main mechanism of breaking existing aggregates (Chatani *et al*, 2009). Breaking existing aggregates can induce further aggregation indirectly by generating seeds (Saborio, Permanne & Soto, 2001). Importantly, addition of free radical scavenger can inhibit amyloid formation almost completely (Fig. 4.12). Therefore, free radicals appear to play an important role for the induction of amyloid formation. However, it is not clear whether the free radical scavenger can completely prevent protein unfolding, which can be induced by sheer stress and local heating without free radical reactions. Nevertheless, at least adding a free radical scavenger can inhibit initial aggregation. Taken together, high temperature, sheer stress, and free radical reactions all affect initial amyloid formation induced by sonication.

The results presented here show that protein damage induced by sonication varies among the examined proteins, however, there is some correlation. By comparison of ThT

fluorescence enhancement among different proteins (Table 4.2), β components in a native structure play an important role with amyloid formation, in that the most ThT enhancements by sonication are observed by β-structure rich proteins, holo SOD1 (40 cycles) and hisactophilin (20 cycles) regardless of melting temperature of proteins. Also, the number of Cys residues contributes to protein damage by sonication, since BSA forms significant amounts of aggregates although the protein contains all α-helical structure but BSA has 17 disulfide bonds and 1 free Cys residue. This is probably because free radicals target Cys residues, resulting in promoting amyloid formation.

4.4.4 Potential risks of sonication

Although sonication is commonly used in various fields, there has been very little investigation of the detailed effects of sonication at the molecular level on proteins with the exception of a few studies (Krishnamurthy *et al*, 2000; Ohhashi, Kihara, Naiki & Goto, 2005; Stathopulos *et al*, 2004). The observations reported here including amyloid formation, protein unfolding, post-sonication amyloid formation, and free radical mediated modification provide important new data concerning the effects of sonication on proteins. The findings further support that caution is warranted when applying sonication to food and the human body (Stathopulos *et al*, 2004) even though prion aggregate is the only amyloid form that is known to be infectious to date, the relation between sonication for any medical purpose and amyloidosis has not been reported, and sonication equipment for diagnostic imaging is not designed for cavitation. In particular, ultrasound contrast agents have been developed

212

whereby gas or fluorinated compounds are encapsulated in sonicated spheres of serum. These agents have applications for imaging blood flow (Ferrara, Pollard & Borden, 2007). It is possible that formation of amyloid may occur during generation of the contrast agents, but not be detected, and perhaps subsequently grow by seeding effect in blood. Therefore, further examination of the influence of sonication on protein in the living body with respect to protein aggregation and/or amyloid formation is warranted. The findings provide useful information to prevent amyloid formation directly and indirectly such as addition of free radical scavenger agents, decrease incubation temperature, use minimum cycles of sonication, and addition of stabilizing agents after sonication. In summary, experimental results reported here advance further understanding of sonication and controlling the damaging effects of sonication on proteins.

Chapter 5
Summary and future work

5.1 Key findings of this thesis

5.1.1 Aggregation from holo SOD1

Pathological aggregates formed from the native, holo state of SOD1, with or without ALS-associated mutations, under physiologically relevant solution conditions (37 °C and pH 7.8) were characterized in chapter 2 and chapter 3 using light scattering techniques. In particular, the free-thiol free form of holo SOD1 (pWT, C6A and C111S) was used as a reference state (control) to avoid formation of non-physiological intermolecular disulfide bonds during aggregation, which has been shown to be a secondary effect in the progression of ALS (Karch *et al*, 2009). The aggregation profiles of pWT as well as ALS-related mutant SOD1s in this background showed a sigmoidal profile having a lag phase, an exponential phase, and a plateau phase, implying that the aggregation is nucleation dependent (Fig. 2.2). Lag phase comparison showed that dimer interface mutants and metal binding mutants tend to have shorter lag phases than pWT (Fig. 2.5). Moreover, ALS associated mutants of SOD1 did not aggregate more readily than pWT, which may explain that why 90% of ALS cases are sALS and sALS have similar onset and duration of the disease with some of fALS cases. Mechanistic details of aggregation (dimer dissociation and partial metal loss, scheme 2.1) were elucidated, based on experimental results including the observed lag times for different holo SOD1s (Fig. 2.5), the moderate protein concentration dependence of lag time (Fig. 2.8),

214

binding of the dimer interface-specific antibody, SEDI, to the aggregates (Fig. 2.14), decreases in specific activity during aggregation time courses (Fig. 2.6), and metal analysis of aggregates (Table 2.1). In addition, seeding and cross seeding was found to decrease the lag phase for aggregation analogous to what has been observed for aggregation of other proteins associated with misfolding diseases (Harper & Lansbury, 1997; Prusiner, 1998). The data fitting using the hyperbolic cosine function as well as AFM images indicates that heterogeneous nucleation is the underlying mechanism for holo aggregation (Fig.2.10 and 2.11). This may explain the relatively quick disease progression of ALS. AFM revealed a range of aggregate morphologies, including oligomers, protofibrils, amorphous aggregates and fibrillar aggregates. Also, it appears that Cu mediated aberrant chemistry is not an important factor in promoting the aggregation (Fig. 2.7). Most importantly, the data in chapter 2 show that the aggregates have common structural, tinctorial (distinct from amyloid, Fig. 2.13) as well as immunological characteristics as aggregates formed in ALS patients (Fig. 2.14), supporting that the observed aggregation is medically relevant.

Chapter 3 provided further experimental evidence for the findings in chapter 2 that dimer dissociation and/or metal loss promote aggregation from holo SOD1s. Various structural probes (intrinsic fluorescence, CD, UV absorbance and FTIR) were used in this chapter. Aggregation profiles monitored using intrinsic fluorescence suggest that there is no major change in the environment of the single solvent exposed Trp residue during aggregation (Fig. 3.8). CD and UV absorbance measurements at various time points during holo SOD1 aggregation revealed multiple pathways of aggregation (Fig. 3.10, 3.11, and 3.12). In particular, the UV measurements suggest that the proteins lose Cu during the

exponential phase. In addition, the proposed heterogeneous nucleation described in chapter 2 was investigated further by comparing log (AB^2) and log (B^2) among different mutants of SOD1 (see Eq. 3.17 and 3.18). The comparison indicated that dimer interface mutants and metal binding mutants have bigger log (AB^2) and log (B^2) values, implying that dimer dissociation and metal loss are required for the nucleation events. Unlike aggregation of other proteins whose structure changes significantly upon aggregation (Booth *et al*, 1997; Fandrich *et al*, 2003a; Padrick & Miranker, 2002; Ruschak & Miranker, 2007), FTIR measurements of plateau phase SOD1 aggregates (Fig. 3.15) show no significant structural change (*i.e.,* the aggregation does not occur from unfolded protein). Similar aggregation for other proteins from a native-like state is increasingly being recognized (Chiti & Dobson, 2009; Yamasaki, Li, Johnson & Huntington, 2008). However, the comparison of FTIR-monitored thermal unfolding of aggregated and control samples revealed destabilization of the aggregated sample, likely due to altered metal binding (Fig. 3.16). Based on the combined intrinsic fluorescence, CD, and UV experimental results (Fig. 3.8, 3.10, 3.11 and 3.12) as well as metal analysis of final aggregates, analysis of aggregation profiles in terms of duration, and final light scattering intensity (Fig. 3.14) two different aggregation pathways was propsed (Scheme 3.1). In one pathway, the aggregation profiles exhibit shorter durations, lower final intensities, and aggregates with more Cu ions than Zn ions. The other aggregation pathways exhibit longer durations, higher final intensities, and aggregates with more Zn ions than Cu ions. However, the trigger(s) that direct the aggregation to different metal loss needs to be investigated.

Due to the high stability of the holo form of SOD1s, it has been thought to be incompatible with aggregation (Shaw & Valentine, 2007). Also, previous *in vitro* aggregation studies have failed to report aggregation from holo SOD1s (Banci *et al*, 2007b; Chattopadhyay *et al*, 2008). The results presented here can be considered to be different from the previous studies; however, various experimental factors are found to be reasons for the different observation of aggregation (see Results, section 2.3.1.1). Nevertheless, there is some evidence of aggregation from the holo state found in the NMR study (Banci *et al*, 2005) and other studies (Oztug Durer *et al*, 2009; Rumfeldt *et al*, 2006). More interestingly, many previous studies have shown that loss of metals, either Cu or Zn ions, can promote aggregation by various pathways (DiDonato *et al*, 2003; Estevez *et al*, 1999; Rakhit *et al*, 2002; Roberts *et al*, 2007). Taken together, the results obtained here are consistent with previous studies. Furthermore, specific antibody binding to aggregates formed by purified SOD1 and in the disease (see Results, section 2.3.5) was demonstrated for the first time, suggesting the aggregation from holo SOD1 is closely related to disease mechanism(s) of ALS.

5.1.2 Sonication-induced aggregation

Chapter 4 described damage induced by sonication of structurally diverse proteins. The experimental conditions were changed relative to previous studies in the Meiering lab (Stathopulos *et al*, 2004) in order to minimize denaturation caused by foaming (see Materials and Methods Section 4.2.1). This chapter showed that sonication of proteins can induce

amyloid formation, which was detected by enhancement of ThT fluorescence (Fig. 4.4 and Table 4.2). The ThT fluorescence enhancement upon sonication, *i.e.,* amyloid formation, decreased when sonication was performed at lower temperature (4.5 °C, Fig. 4.11) and with addition of free radical scavenger (GSH, Fig. 4.12). These results suggest that local heating, sheer stress and free radicals created by cavitation are the main cause of damage due to sonication. The involvement of free radical-induced damage was further indicated by observation of free radical-mediated modification (non-physiological dimerization, fragmentation, and backbone cleavage) and protein unfolding detected by MS, SDS-PAGE and trypsin digestion (Fig. 4.5, 4.6, 4.7, and 4.8). The observation of additional aggregate formation after sonication indicates that the initial aggregates and/or unfolded proteins formed during sonication may promote further amyloid formation (Fig. 4.9). Thus, addition of stabilizing agents after sonication may be useful to prevent post-sonication amyloid formation. Proteins having a higher proportion of native β structure and/or more free thiols (or disulfide bonds) are more vulnerable to sonication-induced damage.

Although use of sonication has been received great attention, very little is known about sonication and sonication-induced protein damage. Here, chapter 3 extends previous studies from the Meiering laboratory (Stathopulos *et al*, 2004), with aim of better characterization of the mechanism of sonication-induced aggregation and effects on different proteins. The experimental results in this chapter can provide reasons why caution should be taken when using sonication, in particular for medical and food industrial applications, and strategies of preventing sonication-induced protein damages should be developed.

5.2 Medical implications

The aggregation studies in chapter 2 and 3 have shown that aggregation is formed from holo SOD1s, is facilitated by dimer dissociation and involves changes in metal bindings. These findings provide possible strategies to prevent the aggregation, and, therefore, the disease. First, the holo form of SOD1 is newly recognized in this thesis to be important species in the disease progression. Thus a possible strategy is to stabilize the holo state of the protein. For example, finding small molecules to stabilize the SOD1 dimer and/or two metal binding loops would be one of possibilities. A previous study found 15 drug-like molecules out 1.5 million molecules from commercial databases to inhibit *in vitro* aggregation of partially metallated SODls by stabilizing the dimer of SOD1 (Ray, Nowak, Brown & Lansbury, 2005). Unfortunately, there are no subsequent studies; however, these findings can provide possible compounds to try into the aggregation system.

Aggregates formed from holo SOD1s possess very similar properties from those observed in the patients such as morphologies and tinctorial and antibody binding characteristics (see Discussion, section 2.4.1). This implies that the aggregation system developed in chapter 2 and 3 has a great potential for a model system to better understand disease mechanism(s) of ALS. Readily available potential toxic species can be used for antibody development(s). Previously, an immunization using purified anti-human mutant SOD1 antibody showed promising initial results with alleviating disease symptoms and prolonging the life span of G93A SOD1 mice. If finding the toxic species from the system is successful, the outcome would be more promising. However, caution should be followed when considering an immunotherapy for ALS patients. When immunotherapy was applied

to Alzheimer's disease patients, the side effect, T-lymphocyte meningoencephalitis, was reported (Nicoll *et al*, 2003), although vaccination with amyloid-β results in clearance of amyloid plaques in patients and the mice models (Bard *et al*, 2000; Morgan *et al*, 2000; Nicoll *et al*, 2003; Schenk *et al*, 1999).

Although the studies of aggregation formed from the holo state provide significant potential and different avenues for ALS research and/or general aggregation fields, aggregation parameters (*e.g.,* lag phase or final plateau intensity) obtained from the experimental results herein did not clearly correlate to disease characteristics (*e.g.,* disease onset and/or duration). It seems likely that many different states of SOD1s (with regard to metallation and/or intramolecular disulfide bond formation) can be involved in progression of ALS and these states of SODls have different effect on different hSOD1 mutants associated with fALS. Thus, further research with more mutants and/or different metallation of SOD1s will advance understanding of SOD1 aggregation in ALS.

5.3 Future directions

5.3.1 Aggregation from holo SOD1

There are a number of avenue for future research that are important to pursue in order to better understand aggregation arising from holo SOD1. An initial objective is to find more direct evidence to support or disprove the proposed aggregation mechanisms involving various modes of metal loss (Scheme 3.1). First, aggregation can be investigated with partially metallated states, more mutants, for example for ones that alter metal binding or the

dimer interface, more disease associated mutants and non-disease associated mutants. In particular, metal binding site mutants (*e.g.,* the Zn ligand mutation, H80R, and the copper ligand mutation, H46R) could be used to analyze effects of altering different metal binding. For example, if the proposed aggregation mechanisms (Scheme 3.1) are correct, H46R aggregation should exhibit long duration and high final intensity as a consequence of loss of Cu binding. In the proposed aggregation mechanism, the electrostatic loop and the Zn binding loop play important roles in dimer dissociation and metal loss. Additional studies with structure-specific antibodies (such as SEDI) could be very valuable. For example, it would be interesting to analyze antibody binding throughout the aggregation time course.

Investigating aggregation from the holo state of SOD1 in reduced conditions would be another reasonable experiment since the cytosol is a reducing environment. All the experiments described in chapter 2 and 3 were performed on pWT, free-free cysteines (C6A/C111S). Thus, a comparison of the aggregation behavior of wild type to that of pWT would provide useful information of a role for intermolecular disulfide bonds. Comparing the *in vivo* results (*i.e.,* formation of intermolecular disulfide bonds is the secondary effect on disease process) would be useful as well. Another avenue for investigation is the effect of solution agitation, and whether mechanical stress and/or air/water interface modulate aggregation.

Since the SOD1 can exist in various forms that differ in metallation as well as disulfide status (reduced or oxidized, cross-seeding of different aggregates formed from different SOD1 species can provide useful information for understanding complexity in ALS. Some of these studies are ongoing in the Meiering lab. In addition, experiments assessing

the toxicity of the different species formed during aggregation (*e.g..,* from the lag phase or exponential phase) can provide insight into the roles of different species in initiating or propagating disease. From these findings, urgently needed therapeutic strategies for ALS can be developed to target the critical species to inhibit or reverse protein aggregation.

5.3.2 Sonication

Future experiments on sonication- induced protein damage could be aimed at determining details of sonication-induced damage mechanism between free radical mediated reactions, shear stress and local heating as well as additional ways to inhibit damage. Sonication of proteins under different solution conditions such as different pH, ionic strength and/or adducts can provide more information on the mechanism of the sonication effect. In addition, seeding experiments using the aggregates formed by sonication and soluble proteins may have significant consequences on the use of ultrasound in medicine and industry. It would also be very important to test the toxicity of sonication-induced aggregates, as well.

Appendix A

Heterogeneous nucleation

This is a sample Appendix. Insert additional appendices with the "Start New Appendix" command.

Some of initial sequential addition; monomers attach on the surface of an existing aggregate for the heterogeneous nucleation, can be written in the group of chemical reaction and formulas:

$$P_1 + A \rightleftharpoons P_2 \qquad K_2 = \frac{[P_2]}{[P_1][A]}, \quad [P_2] = K_2[P_1][A]$$

$$P_2 + A \rightleftharpoons P_3 \qquad K_3 = \frac{[P_3]}{[P_2][A]} = \frac{[P_3]}{K_2[P_1][A]^2}, \quad [P_3] = K_2 K_3 [P_1][A]^2$$

$$P_3 + A \rightleftharpoons P_4 \qquad K_4 = \frac{[P_4]}{[P_3][A\}} = \frac{[P_4]}{K_2 K_3 [P_1][A]^3}, \quad [P_4] = K_2 K_3 K_4 [A]^3$$
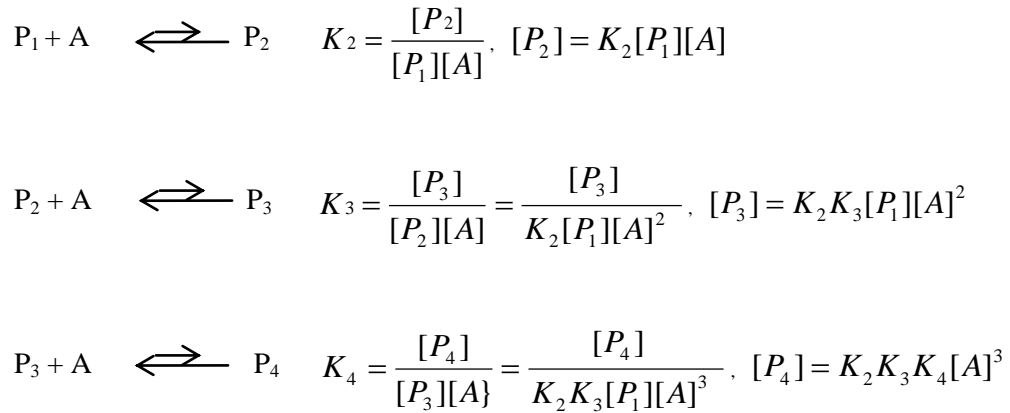
<div align="right">Eq. A1</div>

where P_x ($x > j$, j is the size of heterogeneous nucleation) A and K_x represent an existing aggregate with association of x-mers on its surface, the monomer and the equilibrium constant of the formation of P_x, respectively. Before the nucleation, the reaction is reversible and, therefore, favored to dissociation (*i.e.,* the length of the arrows represent relative size in the rate constants.). Now, let us assume that *j*-mer (the association of (*j*-1) numbers of A) is the heterogeneous nucleation. Therefore, the chemical reaction, K_j and the concentration of P_j can be written as:

$$P_{j-1} + A \rightleftharpoons P_j \qquad K_j = \frac{[P_j]}{[P_{j-1}][A]} = \frac{[P_j]}{K_2 K_3 .... K_{j-1}[P_1][A]^{j-1}},$$

$$[P_j] = K_2 K_3 ..... K_j [P_1][A]^{j-1}$$
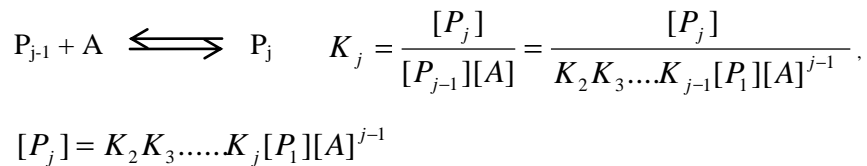
<div align="right">Eq.A2</div>

The rate equations of P_j and P_{j+1} are given, respectively by:

<div align="center">223</div>

$$\frac{d[P_j]}{dt} = k_{+j}[P_{j-1}][A] - k_{-j}[P_j] + k_{-(j+1)}[P_{j+1}] - k_{+(j+1)}[P_j][A]$$

Eq. A3

$$\frac{d[P_{j+1}]}{dt} = k_{+(j+1)}[P_j][A] - k_{-(j+1)}[P_{j+1}] + k_{-(j+2)}[P_{j+2}] - k_{+(j+2)}[P_{j+1}][A]$$

Eq. A4

If we define a heterogeneous polymer (C_{P2}) as any species of size (j+1) or larger with the assumption that the rate constant of additions and dissociations of monomers during the formation of aggregates are same as (k_+) and (k_-), respectively, then the rate of aggregate formation is expressed as:

$$\frac{dC_{P2}}{dt} = k_+[P_j][A] - k_-[P_{j+1}]$$

Eq. A5

The Eq. 3.8 is simplified with assumption; $k_+[A] \gg k_-[A_{i+1}]$, as:

$$\frac{dC_{P2}}{dt} = k_+[P_j][A]$$

Eq. A6

Appendix B
Heterogeneous nucleation 2

The two hypothetical-equilibrium processes are considered as the alternative pathway of formation of P_j: (1) the formation of free j-mer in solution; (2) the attachment of this *j*-mer onto the surface of an aggregate. Fig. 3.2 illustrates the first step in the chemical reaction:

$$jA \rightleftharpoons C_j \qquad\qquad \text{Eq. B1}$$

where A and C_j represent the monomer and j-mer in solution phase, respectively. The equilibrium constant ($\tilde{K}_j$) for the reaction is expressed as:

$$\tilde{K}_j = \frac{[C_j]}{[A]^j} \qquad\qquad \text{Eq. B2}$$

Using the concept of the Langmuir isotherm-derivation (see Appendix C), θ can be shown as:

$$\theta = \frac{[P_j]}{[P_{jt}]} = \frac{\overline{K_j}[C_j]}{(1+\overline{K_j}[C_j])} \cong \overline{K_j}[C_j] \qquad\qquad \text{Eq. B3}$$

where θ is a scale factor that determines the member of available nucleation sites per a polymerized monomer, $[P_{jt}]$ is the total concentration of available sites for attaching a solution phase *j*-mer, and $\overline{K_J}$ is the equilibrium constant for attaching a solution phase *j*-mer to the polymer surface. Also the last term is simplified with assumption; $1 >> \overline{K_j}[C_j]$. Therefore, $[P_j]$ can be rewritten using Eq. B3 as:

$$[P_j] = [P_{jt}]\overline{K_j}C_j = \overline{\vartheta}(A_0 - A)\overline{K_j}[C_j]$$

<div align="right">Eq. B4</div>

where $\bar{\theta}$ is a scaling factor that determines the number of available nucleation sites per polymerized monomer and A_0 and A are the protein concentration initially and during aggregation, respectively.

Thus, Eq. B4 can be rewritten using Eq. B2 as:

$$[P_j] = [P_{jt}]\overline{K_j}C_j = \theta(A_0 - A)\overline{K_j}[C_j] = \theta(A_0 - A)\overline{K_j}\tilde{K_j}[A]^j$$

<div align="right">Eq. B5</div>

which is the same as Eq. 3.14.

Appendix C

Langmuir isotherm derivation from equilibrium consideration

V-*   +   G(g) $\Longleftrightarrow$ V-G
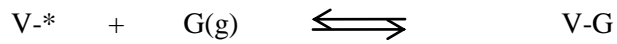
Where, V-* represents vacant surface site and G(g) represents gas. The equilibrium of chemical reaction above can be written as:

$$K = \frac{[V-G]}{[V-^*][G]}$$

Eq.C1

However, using the new term, (θ, the surface coverage), defining another equilibrium constant b is possible, as given below:

$$b = \frac{\theta}{(1-\theta)P}$$

$$\theta = \frac{bP}{1+bP}$$

Eq.C2

where [V-G] is replaced by (θ) because it is proportional to the surface coverage of adsorbed molecules, [V-*] is replaced by (1-θ) because it is proportional to the number of vacant sites, and [G] is proportional to the pressure of gas, P.

Appendix D
Eq. 3.16 simplification

The rate equation for the disappearance of the native proteins from the solution phase into aggregation can be written in the form as:

$$\frac{-d[A]}{dt} = \frac{d}{dt}(\sum_{x=i+1}^{\infty} x[A_x])$$

$$= \sum_{x=i+1}^{\infty} x\frac{d}{dt}[A_x]$$

$$= \sum_{x=i+1}^{\infty} (i+1)\frac{d}{dt}[A_x] + \sum_{x=i+1}^{\infty} (x-(i+1))\frac{d}{dt}[A_x]$$

$$= (i+1)\sum_{x=i+1}^{\infty} \frac{d}{dt}[A_x] + \sum_{x=i+1}^{\infty} (x-(i+1))(k_+ AA_{x-1} - k_- A_x + k_- A_{x+1} - k_+ AA_x)$$

$$= (i+1)C_p + \sum_{x=i+1}^{\infty} (x-(i+1))\{k_+ A(A_{x-1} - A_x) - k_-(A_x - A_{x+1})\}$$

$$= (i+1)C_p + \sum_{x=i+1}^{\infty} (x-(i+1))\{k_+ A(A_{x-1} - A_x)\} - \sum_{x=i+1}^{\infty} (x-(i+1))k_-(A_x - A_{x+1})$$

$$= (i+1)C_p + k_+ AC_p - k_- C_p$$

Eq.D1

Eq. D1 is simplified and is given by:

$$\frac{-d[A]}{dt} = \frac{d}{dt}(\sum_{x=i+1}^{\infty} x[A_x]) = (i+1)C_p + k_+ AC_p - k_- C_p \cong (k_+ A - k_-)C_p$$

Eq.D2

Bibliography

Abe K, Pan LH, Watanabe M, Kato T & Itoyama Y (1995) Induction of Nitrotyrosine-Like Immunoreactivity in the Lower Motor-Neuron of Amyotrophic-Lateral-Sclerosis. *Neurosci Lett* **199:** 152-154

Ahmad A, Uversky VN, Hong D & Fink AL (2005) Early events in the fibrillation of monomeric insulin. *J Biol Chem* **280:** 42669-42675

Alcaraz LA & Donaire A (2004) Unfolding process of rusticyanin: evidence of protein aggregation. *Eur J Biochem* **271:** 4284-4292

Andrews JM & Roberts CJ (2007) A Lumry-Eyring nucleated polymerization model of protein aggregation kinetics: 1. Aggregation with pre-equilibrated unfolding. *J Phys Chem B* **111:** 7897-7913

Andrus PK, Fleck TJ, Gurney ME & Hall ED (1998) Protein oxidative damage in a transgenic mouse model of familial amyotrophic lateral sclerosis. *Journal of Neurochemistry* **71:** 2041-2048

Anfinsen CB (1973) Principles That Govern Folding of Protein Chains. *Science* **181:** 223-230

Antonyuk S, Elam JS, Hough MA, Strange RW, Doucette PA, Rodriguez JA, Hayward LJ, Valentine JS, Hart PJ & Hasnain SS (2005) Structural consequences of the familial amyotrophic lateral sclerosis SOD1 mutant His46Arg. *Protein Sci* **14:** 1201-1213

Arakawa T & Kita Y (2000) Stabilizing effects of caprylate and acetyltryptophanate on heat-induced aggregation of bovine serum albumin. *Biochim Biophys Acta-Protein Struct Molec Enzym* **1479:** 32-36

Arnaudov LN & de Vries R (2007) Theoretical modeling of the kinetics of fibrilar aggregation of bovine beta-lactoglobulin at pH 2. *J Chem Phys* **126:** 145106

Badiei HR & Karanassios V (1999) Direct elemental analysis of lead in micro-samples of human fingernails by rhenium-cup in-torch vaporization-inductively coupled plasma atomic emission spectrometry (ITV-ICP-AES). *J Anal At Spectrom* **14:** 603-605

Banci L, Bertini I, Boca M, Girotto S, Martinelli M, Valentine JS & Vieru M (2008) SOD1 and amyotrophic lateral sclerosis: mutations and oligomerization. *PLoS ONE* **3:** e1677

Banci L, Bertini I, Cramaro F, Del Conte R & Viezzoli MS (2002) The solution structure of reduced dimeric copper zinc superoxide dismutase - The structural effects of dimerization. *European Journal of Biochemistry* **269:** 1905-1915

Banci L, Bertini I, Cramaro F, Del Conte R & Viezzoli MS (2003) Solution structure of Apo Cu,Zn superoxide dismutase: role of metal ions in protein folding. *Biochemistry* **42:** 9543-9553

Banci L, Bertini I, D'Amelio N, Gaggelli E, Libralesso E, Matecko I, Turano P & Valentine JS (2005) Fully metallated S134N Cu,Zn-superoxide dismutase displays abnormal mobility and intermolecular contacts in solution. *J Biol Chem* **280:** 35815-35821

Banci L, Bertini I, D'Amelio N, Libralesso E, Turano P & Valentine JS (2007a) Metalation of the amyotrophic lateral sclerosis mutant glycine 37 to arginine superoxide dismutase (SOD1) apoprotein restores its structural and dynamical properties in solution to those of metalated wild-type SOD1. *Biochemistry* **46:** 9953-9962

Banci L, Bertini I, Durazo A, Girotto S, Gralla EB, Martinelli M, Valentine JS, Vieru M & Whitelegge JP (2007b) Metal-free superoxide dismutase forms soluble oligomers under physiological conditions: a possible general mechanism for familial ALS. *Proc Natl Acad Sci U S A* **104:** 11263-11267

Bard F, Cannon C, Barbour R, Burke RL, Games D, Grajeda H, Guido T, Hu K, Huang J, Johnson-Wood K, Khan K, Kholodenko D, Lee M, Lieberburg I, Motter R, Nguyen M, Soriano F, Vasquez N, Weiss K, Welch B, Seubert P, Schenk D & Yednock T (2000) Peripherally administered antibodies against amyloid beta-peptide enter the central nervous system and reduce pathology in a mouse model of Alzheimer disease. *Nat Med* **6:** 916-919

Barondeau DP, Kassmann CJ, Bruns CK, Tainer JA & Getzoff ED (2004) Nickel superoxide dismutase structure and mechanism. *Biochemistry* **43:** 8038-8047

Basso M, Massignan T, Samengo G, Cheroni C, De Biasi S, Salmona M, Bendotti C & Bonetto V (2006) Insoluble mutant SOD1 is partly oligoubiquitinated in amyotrophic lateral sclerosis mice. *J Biol Chem* **281:** 33325-33335

Battistoni A (2003) Role of prokaryotic Cu,Zn superoxide dismutase in pathogenesis. *Biochemical Society Transactions* **31:** 1326-1329

Beckman JS (1996) Oxidative damage and tyrosine nitration from peroxynitrite. *Chem Res Toxicol* **9:** 836-844

Beckman JS, Carson M, Smith CD & Koppenol WH (1993) Als, Sod and Peroxynitrite. *Nature* **364:** 584-584

Beckman JS, Ischiropoulos H, Zhu L, Vanderwoerd M, Smith C, Chen J, Harrison J, Martin JC & Tsai M (1992) Kinetics of Superoxide Dismutase-Catalyzed and Iron-Catalyzed Nitration of Phenolics by Peroxynitrite. *Arch Biochem Biophys* **298:** 438-445

Beem KM, Rich WE & Rajagopalan KV (1974) Total reconstitution of copper-zinc superoxide dismutase. *J Biol Chem* **249:** 7298-7305

Bellotti V & Chiti F (2008) Amyloidogenesis in its biological environment: challenging a fundamental issue in protein misfolding diseases. *Curr Opin Struct Biol* **18:** 771-779

Bhattacharjee C, Saha S, Biswas A, Kundu M, Ghosh L & Das KP (2005) Structural changes of beta-lactoglobulin during thermal unfolding and refolding--an FT-IR and circular dichroism study. *Protein J* **24:** 27-35

Bishop MF & Ferrone FA (1984) Kinetics of nucleation-controlled polymerization. A perturbation treatment for use with a secondary pathway. *Biophys J* **46:** 631-644

Boillee S, Vande Velde C & Cleveland DW (2006a) ALS: a disease of motor neurons and their nonneuronal neighbors. *Neuron* **52:** 39-59

Boillee S, Yamanaka K, Lobsiger CS, Copeland NG, Jenkins NA, Kassiotis G, Kollias G & Cleveland DW (2006b) Onset and progression in inherited ALS determined by motor neurons and microglia. *Science* **312:** 1389-1392

Booth DR, Sunde M, Bellotti V, Robinson CV, Hutchinson WL, Fraser PE, Hawkins PN, Dobson CM, Radford SE, Blake CC & Pepys MB (1997) Instability, unfolding and aggregation of human lysozyme variants underlying amyloid fibrillogenesis. *Nature* **385:** 787-793

Borchelt DR, Lee MK, Slunt HS, Guarnieri M, Xu ZS, Wong PC, Brown RH, Jr., Price DL, Sisodia SS & Cleveland DW (1994) Superoxide dismutase 1 with mutations linked to familial amyotrophic lateral sclerosis possesses significant activity. *Proc Natl Acad Sci U S A* **91:** 8292-8296

Boston-Howes W, Gibb SL, Williams EO, Pasinelli P, Brown RH & Trotti D (2006) Caspase-3 cleaves and inactivates the glutamate transporter EAAT2. *J Biol Chem* **281:** 14076-14084

Bromba MUA & Ziegler H (1981) APPLICATION HINTS FOR SAVITZKY-GOLAY DIGITAL SMOOTHING FILTERS. *Analytical Chemistry* **53:** 1583-1586

Brown JR (1976) Structural origins of mammalian albumin. *Fed Proc* **35:** 2141-2144

Bruijn LI, Beal MF, Becher MW, Schulz JB, Wong PC, Price DL & Cleveland DW (1997a) Elevated free nitrotyrosine levels, but not protein-bound nitrotyrosine or hydroxyl radicals, throughout amyotrophic lateral sclerosis (ALS)-like disease implicate tyrosine nitration as an aberrant in vivo property of one familial ALS-linked superoxide dismutase 1 mutant. *Proc Natl Acad Sci U S A* **94:** 7606-7611

Bruijn LI, Becher MW, Lee MK, Anderson KL, Jenkins NA, Copeland NG, Sisodia SS, Rothstein JD, Borchelt DR, Price DL & Cleveland DW (1997b) ALS-linked SOD1 mutant G85R mediates damage to astrocytes and promotes rapidly progressive disease with SOD1-containing inclusions. *Neuron* **18:** 327-338

Bruijn LI, Houseweart MK, Kato S, Anderson KL, Anderson SD, Ohama E, Reaume AG, Scott RW & Cleveland DW (1998) Aggregation and motor neuron toxicity of an ALS-linked SOD1 mutant independent from wild-type SOD1. *Science* **281:** 1851-1854

Bruijn LI, Miller TM & Cleveland DW (2004) Unraveling the mechanisms involved in motor neuron degeneration in ALS. *Annual Review of Neuroscience* **27:** 723-749

Bryngelson JD, Onuchic JN, Socci ND & Wolynes PG (1995) Funnels, Pathways, and the Energy Landscape of Protein-Folding - a Synthesis. *Proteins* **21:** 167-195

Butz P & Tauscher B (2002) Emerging technologies: chemical aspects. *Food Res Int* **35:** 279-284

Cao X, Antonyuk SV, Seetharaman SV, Whitson LJ, Taylor AB, Holloway SP, Strange RW, Doucette PA, Valentine JS, Tiwari A, Hayward LJ, Padua S, Cohlberg JA, Hasnain SS & Hart PJ (2008) Structures of the G85R variant of SOD1 in familial amyotrophic lateral sclerosis. *J Biol Chem* **283:** 16169-16177

Carlier MF & Pantaloni D (1997) Control of actin dynamics in cell motility. *J Mol Biol* **269:** 459-467

Carroll MC, Girouard JB, Ulloa JL, Subramaniam JR, Wong PC, Valentine JS & Culotta VC (2004) Mechanisms for activating Cu- and Zn-containing superoxide dismutase in the absence of the CCS Cu chaperone. *Proc Natl Acad Sci U S A* **101:** 5964-5969

Casareno RLB, Waggoner D & Gitlin JD (1998) The copper chaperone CCS directly interacts with copper/zinc superoxide dismutase. *J Biol Chem* **273:** 23625-23628

Charcot JM & Joffoary A (1869) Deaux cas d'atrophie musculaire progressive avec lesions de la grise et des faisceaux
antrerolateraux de la moelle epiniere. *Arch Physiol* **2:** 629-760

Chatani E, Lee YH, Yagi H, Yoshimura Y, Naiki H & Goto Y (2009) Ultrasonication-dependent production and breakdown lead to minimum-sized amyloid fibrils. *Proc Natl Acad Sci U S A* **106:** 11119-11124

Chattopadhyay M, Durazo A, Sohn SH, Strong CD, Gralla EB, Whitelegge JP & Valentine JS (2008) Initiation and elongation in fibrillation of ALS-linked superoxide dismutase. *Proc Natl Acad Sci U S A* **105:** 18663-18668

Chen S, Berthelier V, Hamilton JB, O'Nuallain B & Wetzel R (2002) Amyloid-like features of polyglutamine aggregates and their assembly kinetics. *Biochemistry* **41:** 7391-7399

Chiti F, De Lorenzi E, Grossi S, Mangione P, Giorgetti S, Caccialanza G, Dobson CM, Merlini G, Ramponi G & Bellotti V (2001) A partially structured species of beta 2-microglobulin is significantly populated under physiological conditions and involved in fibrillogenesis. *J Biol Chem* **276:** 46714-46721

Chiti F & Dobson CM (2006) Protein misfolding, functional amyloid, and human disease. *Annu Rev Biochem* **75:** 333-366

Chiti F & Dobson CM (2009) Amyloid formation by globular proteins under native conditions. *Nat Chem Biol* **5:** 15-22

Chiti F, Stefani M, Taddei N, Ramponi G & Dobson CM (2003a) Rationalization of the effects of mutations on peptide and protein aggregation rates. *Nature* **424:** 805-808

Chiti F, Stefani M, Taddei N, Ramponi G & Dobson CM (2003b) Rationalization of the effects of mutations on peptide and protein aggregation rates. *Nature* **424:** 805-808

Chiti F, Webster P, Taddei N, Clark A, Stefani M, Ramponi G & Dobson CM (1999) Designing conditions for in vitro formation of amyloid protofilaments and fibrils. *Proc Natl Acad Sci U S A* **96:** 3590-3594

Chiu AY, Zhai P, Dal Canto MC, Peters TM, Kwon YW, Prattis SM & Gurney ME (1995) Age-dependent penetrance of disease in a transgenic mouse model of familial amyotrophic lateral sclerosis. *Mol Cell Neurosci* **6:** 349-362

Chiumiento A, Dominguez A, Lamponi S, Villalonga R & Barbucci R (2006) Anti-inflammatory properties of superoxide dismutase modified with carboxymetil-cellulose polymer and hydrogel. *J Mater Sci Mater Med* **17:** 427-435

Choo LP, Wetzel DL, Halliday WC, Jackson M, LeVine SM & Mantsch HH (1996) In situ characterization of beta-amyloid in Alzheimer's diseased tissue by synchrotron Fourier transform infrared microspectroscopy. *Biophys J* **71:** 1672-1679

Chou SM, Wang HS & Komai K (1996) Colocalization of NOS and SOD1 in neurofilament accumulation within motor neurons of amyotrophic lateral sclerosis: An immunohistochemical study. *J Chem Neuroanat* **10:** 249-258

Chowdhury SK, Katta V & Chait VT (1990) Probing conformational changes in proteins by mass spectrometry. *Journal of the American Chemical Society* **112:** 9012-9013

Clement AM, Nguyen MD, Roberts EA, Garcia ML, Boillee S, Rule M, McMahon AP, Doucette W, Siwek D, Ferrante RJ, Brown RH, Jr., Julien JP, Goldstein LS & Cleveland DW (2003) Wild-type nonneuronal cells extend survival of SOD1 mutant motor neurons in ALS mice. *Science* **302:** 113-117

Collins SR, Douglass A, Vale RD & Weissman JS (2004) Mechanism of prion propagation: amyloid growth occurs by monomer addition. *PLoS Biol* **2:** e321

Condeelis J (1993) Life at the leading edge: the formation of cell protrusions. *Annu Rev Cell Biol* **9:** 411-444

Crow JP, Sampson JB, Zhuang Y, Thompson JA & Beckman JS (1997a) Decreased zinc affinity of amyotrophic lateral sclerosis-associated superoxide dismutase mutants leads to enhanced catalysis of tyrosine nitration by peroxynitrite. *J Neurochem* **69:** 1936-1944

Crow JP, Sampson JB, Zhuang YX, Thompson JA & Beckman JS (1997b) Decreased zinc affinity of amyotrophic lateral sclerosis-associated superoxide dismutase mutants leads to enhanced catalysis of tyrosine nitration by peroxynitrite. *Journal of Neurochemistry* **69:** 1936-1944

Culotta VC, Klomp LWJ, Strain J, Casareno RLB, Krems B & Gitlin JD (1997) The copper chaperone for superoxide dismutase. *J Biol Chem* **272:** 23469-23472

D'Auria S, Rossi M, Gryczynshi Ignacy & Lakowicz JR (2000) *Fluorescence of Extreme Thermophilic Proteins* Vol. 6, New York: Plenum Publishers.

Dalcanto MC & Gurney ME (1994) Development of Central-Nervous-System Pathology in a Murine Transgenic Model of Human Amyotrophic-Lateral-Sclerosis. *Am J Pathol* **145:** 1271-1279

de la Torre JG, Huertas ML & Carrasco B (2000) Calculation of hydrodynamic properties of globular proteins from their atomic-level structure. *Biophysical Journal* **78:** 719-730

Deng HX, Shi Y, Furukawa Y, Zhai H, Fu R, Liu E, Gorrie GH, Khan MS, Hung WY, Bigio EH, Lukas T, Dal Canto MC, O'Halloran TV & Siddique T (2006) Conversion to the amyotrophic lateral sclerosis phenotype is associated with intermolecular linked insoluble aggregates of SOD1 in mitochondria. *Proc Natl Acad Sci U S A* **103:** 7142-7147

DiDonato M, Craig L, Huff ME, Thayer MM, Cardoso RM, Kassmann CJ, Lo TP, Bruns CK, Powers ET, Kelly JW, Getzoff ED & Tainer JA (2003) ALS mutants of human superoxide dismutase form fibrous aggregates via framework destabilization. *J Mol Biol* **332:** 601-615

Dobson CM (2001a) The structural basis of protein folding and its links with human disease. *Philos Trans R Soc Lond B Biol Sci* **356:** 133-145

Dobson CM (2001b) The structural basis of protein folding and its links with human disease. *Philos Trans R Soc Lond Ser B-Biol Sci* **356:** 133-145

Dong A, Huang P & Caughey WS (1995) Redox-dependent changes in beta-sheet and loop structures of Cu,Zn superoxide dismutase in solution observed by infrared spectroscopy. *Arch Biochem Biophys* **320:** 59-64

Dupeyrat F, Vidaud C, Lorphelin A & Berthomieu C (2004) Long distance charge redistribution upon Cu,Zn-superoxide dismutase reduction: significance for dismutase function. *J Biol Chem* **279:** 48091-48101

Dusa A, Kaylor J, Edridge S, Bodner N, Hong DP & Fink AL (2006) Characterization of oligomers during alpha-synuclein aggregation using intrinsic tryptophan fluorescence. *Biochemistry* **45:** 2752-2760

Eftink MR (2000) *Intrinsic Fluorescence of Proteins*, Vol. 6: Protein Fluorescence, New York: Kluwer Academic/Plenum Publishers.

Elam JS, Taylor AB, Strange R, Antonyuk S, Doucette PA, Rodriguez JA, Hasnain SS, Hayward LJ, Valentine JS, Yeates TO & Hart PJ (2003) Amyloid-like filaments and water-filled nanotubes formed by SOD1 mutant proteins linked to familial ALS. *Nat Struct Biol* **10:** 461-467

Elliott A & Ambrose EJ (1950) Structure of synthetic polypeptides. *Nature* **165:** 921-922

Estevez AG, Crow JP, Sampson JB, Reiter C, Zhuang YX, Richardson GJ, Tarpey MM, Barbeito L & Beckman JS (1999) Induction of nitric oxide-dependent apoptosis in motor neurons by zinc-deficient superoxide dismutase. *Science* **286:** 2498-2500

Fandrich M, Forge V, Buder K, Kittler M, Dobson CM & Diekmann S (2003a) Myoglobin forms amyloid fibrils by association of unfolded polypeptide segments. *Proc Natl Acad Sci U S A* **100:** 15463-15468

Fandrich M, Forge V, Buder K, Kittler M, Dobson CM & Diekmann S (2003b) Myoglobin forms amyloid fibrils by association of unfolded polypeptide segments. *Proc Natl Acad Sci U S A* **100:** 15463-15468

Farr SB, Dari R & Touati D (1986) Oxygen-Dependent Mutagenesis in Escherichia-Coli Lacking Superoxide-Dismutase. *Proceedings of the National Academy of Sciences of the United States of America* **83:** 8268-8272

Ferrante RJ, Shinobu LA, Schulz JB, Matthews RT, Thomas CE, Kowall NW, Gurney ME & Beal MF (1997) Increased 3-nitrotyrosine and oxidative damage in mice with a human copper/zinc superoxide dismutase mutation. *Annals of Neurology* **42:** 326-334

Ferrara K, Pollard R & Borden M (2007) Ultrasound microbubble contrast agents: Fundamentals and application to gene and drug delivery. *Annu Rev Biomed Eng* **9:** 415-447

Ferrone F (1999) Analysis of protein aggregation kinetics. *Methods Enzymol* **309:** 256-274

Ferrone FA, Hofrichter J & Eaton WA (1985) Kinetics of sickle hemoglobin polymerization. II. A double nucleation mechanism. *J Mol Biol* **183:** 611-631

Ferrone FA, Hofrichter J, Sunshine HR & Eaton WA (1980) Kinetic studies on photolysis-induced gelation of sickle cell hemoglobin suggest a new mechanism. *Biophys J* **32:** 361-380

Fessas D, Iametti S, Schiraldi A & Bonomi F (2001) Thermal unfolding of monomeric and dimeric beta-lactoglobulins. *European Journal of Biochemistry* **268:** 5439-5448

Forman HJ & Fridovic.I (1973) Stability of Bovine Superoxide Dismutase - Effects of Metals. *J Biol Chem* **248:** 2645-2649

Foss TR, Wiseman RL & Kelly JW (2005) The pathway by which the tetrameric protein transthyretin dissociates. *Biochemistry* **44:** 15525-15533

Fridovic.I (1974) Evidence for Symbiotic Origin of Mitochondria. *Life Sciences* **14:** 819-826

Fridovich I (1975) Superoxide Dismutases. *Annual Review of Biochemistry* **44:** 147-159

Fridovich I (1986) Biological Effects of the Superoxide Radical. *Arch Biochem Biophys* **247:** 1-11

Frieden C (2007) Protein aggregation processes: In search of the mechanism. *Protein Sci* **16:** 2334-2344

Fung SY, Keyes C, Duhamel J & Chen P (2003) Concentration effect on the aggregation of a self-assembling oligopeptide. *Biophysical Journal* **85:** 537-548

Furukawa Y, Kaneko K, Yamanaka K, O'Halloran TV & Nukina N (2008) Complete loss of post-translational modifications triggers fibrillar aggregation of SOD1 in the familial form of amyotrophic lateral sclerosis. *J Biol Chem* **283:** 24167-24176

Furukawa Y, Torres AS & O'Halloran TV (2004) Oxygen-induced maturation of SOD1: a key role for disulfide formation by the copper chaperone CCS. *Embo J* **23:** 2872-2881

Getzoff ED, Cabelli DE, Fisher CL, Parge HE, Viezzoli MS, Banci L & Hallewell RA (1992a) Faster Superoxide-Dismutase Mutants Designed by Enhancing Electrostatic Guidance. *Nature* **358:** 347-351

Getzoff ED, Cabelli DE, Fisher CL, Parge HE, Viezzoli MS, Banci L & Hallewell RA (1992b) Faster superoxide dismutase mutants designed by enhancing electrostatic guidance. *Nature* **358:** 347-351

Getzoff ED, Tainer JA & Olson AJ (1986) Recognition and Interactions Controlling the Assemblies of Beta-Barrel Domains. *Biophysical Journal* **49:** 191-206

Getzoff ED, Tainer JA, Stempien MM, Bell GI & Hallewell RA (1989) Evolution of Cuzn Superoxide-Dismutase and the Greek Key Beta-Barrel Structural Motif. *Proteins* **5:** 322-336

Getzoff ED, Tainer JA, Weiner PK, Kollman PA, Richardson JS & Richardson DC (1983) Electrostatic Recognition between Superoxide and Copper, Zinc Superoxide-Dismutase. *Nature* **306:** 287-290

Glabe CG (2008) Structural classification of toxic amyloid oligomers. *J Biol Chem* **283:** 29639-29643

Gong YH, Parsadanian AS, Andreeva A, Snider WD & Elliott JL (2000) Restricted expression of G86R Cu/Zn superoxide dismutase in astrocytes results in astrocytosis but does not cause motoneuron degeneration. *J Neurosci* **20:** 660-665

Goto JJ, Zhu H, Sanchez RJ, Nersissian A, Gralla EB, Valentine JS & Cabelli DE (2000) Loss of in vitro metal ion binding specificity in mutant copper-zinc superoxide dismutases associated with familial amyotrophic lateral sclerosis. *J Biol Chem* **275:** 1007-1014

Grace SC (1990) Phylogenetic Distribution of Superoxide-Dismutase Supports an Endosymbiotic Origin for Chloroplasts and Mitochondria. *Life Sciences* **47:** 1875-1886

Griffith JS (1967) Self-replication and scrapie. *Nature* **215:** 1043-1044

Gurney ME (1997) The use of transgenic mouse models of amyotrophic lateral sclerosis in preclinical drug studies. *J Neurol Sci* **152 Suppl 1:** S67-73

Hall LT, Sanchez RJ, Holloway SP, Zhu HN, Stine JE, Lyons TJ, Demeler B, Schirf V, Hansen JC, Nersissian AM, Valentine JS & Hart PJ (2000) X-ray crystallographic and analytical ultracentrifugation analyses of truncated and full-length yeast copper chaperones for SOD (LYS7): A dimer-dimer model of LYS7-SOD association and copper delivery. *Biochemistry* **39:** 3611-3623

Hamada D, Tanaka T, Tartaglia GG, Pawar A, Vendruscolo M, Kawamura M, Tamura A, Tanaka N & Dobson CM (2009) Competition between folding, native-state dimerisation and amyloid aggregation in beta-lactoglobulin. *J Mol Biol* **386:** 878-890

Hammond MS, Houliston RS & Meiering EM (1998) Two-dimensional 1H and 15N NMR titration studies of hisactophilin. *Biochem Cell Biol* **76:** 294-301

Harper JD & Lansbury PT, Jr. (1997) Models of amyloid seeding in Alzheimer's disease and scrapie: mechanistic truths and physiological consequences of the time-dependent solubility of amyloid proteins. *Annu Rev Biochem* **66:** 385-407

Hart PJ, Liu H, Pellegrini M, Nersissian AM, Gralla EB, Valentine JS & Eisenberg D (1998) Subunit asymmetry in the three-dimensional structure of a human CuZnSOD mutant found in familial amyotrophic lateral sclerosis. *Protein Sci* **7:** 545-555

Hawe A, Sutter M & Jiskoot W (2008) Extrinsic fluorescent dyes as tools for protein characterization. *Pharm Res* **25:** 1487-1499

Hayes JD & McLellan LI (1999) Glutathione and glutathione-dependent enzymes represent a Co-ordinately regulated defence against oxidative stress. *Free Radic Res* **31:** 273-300

Hayward LJ, Rodriguez JA, Kim JW, Tiwari A, Goto JJ, Cabelli DE, Valentine JS & Brown RH (2002) Decreased metallation and activity in subsets of mutant superoxide dismutases associated with familial amyotrophic lateral sclerosis. *J Biol Chem* **277:** 15923-15931

Heck AJ & Van Den Heuvel RH (2004) Investigation of intact protein complexes by mass spectrometry. *Mass Spectrom Rev* **23:** 368-389

Hermann A, Laws WR & Harpel PC (1997) Oxidation of apolipoprotein(a) inhibits kringle-associated lysine binding: the loss of intrinsic protein fluorescence suggests a role for tryptophan residues in the lysine binding site. *Protein Sci* **6:** 2324-2335

Higgins CMJ, Jung CW & Xu ZS (2003) ALS-associated mutant SOD1G93A causes mitochondrial vacuolation by expansion of the intermembrane space and by involvement of SOD1 aggregation and peroxisomes. *Bmc Neuroscience* **4**

Hinault MP, Ben-Zvi A & Goloubinoff P (2006) Chaperones and proteases - Cellular fold-controlling factors of proteins in Neurodegenerative diseases and aging. *Journal of Molecular Neuroscience* **30:** 249-265

Hirano A, Donnenfeld H, Sasaki S & Nakano I (1984) Fine-Structural Observations of Neurofilamentous Changes in Amyotrophic Lateral Sclerosis. *J Neuropathol Exp Neurol* **43:** 461-470

Hodgson EK & Fridovich I (1975) Interaction of Bovine Erythrocyte Superoxide-Dismutase with Hydrogen-Peroxide - Inactivation of Enzyme. *Biochemistry* **14:** 5294-5299

Holtzman DM (2008) Alzheimer's disease: Moving towards a vaccine. *Nature* **454:** 418-420

Hornberg A, Logan DT, Marklund SL & Oliveberg M (2007) The coupling between disulphide status, metallation and dimer interface strength in Cu/Zn superoxide dismutase. *J Mol Biol* **365:** 333-342

Hough MA, Grossmann JG, Antonyuk SV, Strange RW, Doucette PA, Rodriguez JA, Whitson LJ, Hart PJ, Hayward LJ, Valentine JS & Hasnain SS (2004a) Dimer destabilization in superoxide dismutase may result in disease-causing properties: structures of motor neuron disease mutants. *Proc Natl Acad Sci U S A* **101:** 5976-5981

Hough MA, Grossmann JG, Antonyuk SV, Strange RW, Doucette PA, Rodriguez JA, Whitson LJ, Hart PJ, Hayward LJ, Valentine JS & Hasnain SS (2004b) Dimer destabilization in superoxide dismutase may result in disease-causing properties: Structures of motor neuron disease mutants. *Proc Natl Acad Sci U S A* **101:** 5976-5981

Hsueh-Ning Liu, Teresa Sanelli, Patrick Horne, Erik P. Pioro M, Michael J. Strong, Ekaterina Rogaeva, Juan Bilbao, Lorne Zinman & Robertson J (Published Online: 20 Mar 2009) Lack of evidence of monomer/misfolded SOD1 in sporadic ALS. *Annals of Neurology*

Huang TH, Yang DS, Plaskos NP, Go S, Yip CM, Fraser PE & Chakrabartty A (2000) Structural studies of soluble oligomers of the Alzheimer beta-amyloid peptide. *J Mol Biol* **297:** 73-87

Huie RE & Padmaja S (1993) The Reaction of No with Superoxide. *Free Radic Res Commun* **18:** 195-199

Ince PG, Tomkins J, Slade JY, Thatcher NM & Shaw PJ (1998) Amyotrophic lateral sclerosis associated with genetic abnormalities in the gene encoding Cu/Zn superoxide dismutase: Molecular pathology of five new cases, and comparison with previous reports and 73 sporadic cases of ALS. *Journal of Neuropathology and Experimental Neurology* **57:** 895-904

Jachimska B, Wasilewska M & Adamczyk Z (2008) Characterization of globular protein solutions by dynamic light scattering, electrophoretic mobility, and viscosity measurements. *Langmuir* **24:** 6866-6872

Jackson M & Mantsch HH (1995) The use and misuse of FTIR spectroscopy in the determination of protein structure. *Crit Rev Biochem Mol Biol* **30:** 95-120

Jahn TR & Radford SE (2008a) Folding versus aggregation: polypeptide conformations on competing pathways. *Arch Biochem Biophys* **469:** 100-117

Jahn TR & Radford SE (2008b) Folding versus aggregation: Polypeptide conformations on competing pathways. *Arch Biochem Biophys* **469:** 100-117

Jahn TR, Tennent GA & Radford SE (2008) A common beta-sheet architecture underlies in vitro and in vivo beta2-microglobulin amyloid fibrils. *J Biol Chem* **283:** 17279-17286

Johnston JA, Dalton MJ, Gurney ME & Kopito RR (2000) Formation of high molecular weight complexes of mutant Cu, Zn-superoxide dismutase in a mouse model for familial amyotrophic lateral sclerosis. *Proc Natl Acad Sci U S A* **97:** 12571-12576

Jones EM & Surewicz WK (2005) Fibril conformation as the basis of species- and strain-dependent seeding specificity of mammalian prion amyloids. *Cell* **121:** 63-72

Joseph CG, Li Puma G, Bono A & Krishnaiah D (2009) Sonophotocatalysis in advanced oxidation process: a short review. *Ultrason Sonochem* **16:** 583-589

Kabsch W & Sander C (1983) Dictionary of Protein Secondary Structure - Pattern-Recognition of Hydrogen-Bonded and Geometrical Features. *Biopolymers* **22:** 2577-2637

Kadima W, Ogendal L, Bauer R, Kaarsholm N, Brodersen K, Hansen JF & Porting P (1993) The influence of ionic strength and pH on the aggregation properties of zinc-free insulin studied by static and dynamic laser light scattering. *Biopolymers* **33:** 1643-1657

Karch CM, Prudencio M, Winkler DD, Hart PJ & Borchelt DR (2009) Role of mutant SOD1 disulfide oxidation and aggregation in the pathogenesis of familial ALS. *Proc Natl Acad Sci U S A*

Karplus M (1997) The Levinthal paradox: yesterday and today. *Folding & Design* **2:** S69-S75

Kato S (2008) Amyotrophic lateral sclerosis models and human neuropathology: similarities and differences. *Acta Neuropathol* **115:** 97-114

Kato S, Hayashi H, Nakashima K, Nanba E, Kato M, Hirano A, Nakano I, Asayama K & Ohama E (1997) Pathological characterization of astrocytic hyaline inclusions in familial amyotrophic lateral sclerosis. *Am J Pathol* **151:** 611-620

Kato S, Horiuchi S, Liu J, Cleveland DW, Shibata N, Nakashima K, Nagai R, Hirano A, Takikawa M, Kato M, Nakano I & Ohama E (2000) Advanced glycation endproduct-modified superoxide dismutase-1 (SOD1)-positive inclusions are common to familial amyotrophic lateral sclerosis patients with SOD1 gene mutations and transgenic mice expressing human SOD1 with a G85R mutation. *Acta Neuropathol* **100:** 490-505

Kato S, Horiuchi S, Nakashima K, Hirano A, Shibata N, Nakano I, Saito M, Kato M, Asayama K & Ohama E (1999) Astrocytic hyaline inclusions contain advanced glycation endproducts in familial amyotrophic lateral sclerosis with superoxide dismutase 1 gene mutation: immunohistochemical and immunoelectron microscopical analyses. *Acta Neuropathol* **97:** 260-266

Kato S, Nakashima K, Horiuchi S, Nagai R, Cleveland DW, Liu J, Hirano A, Takikawa M, Kato M, Nakano I, Sakoda S, Asayama K & Ohama E (2001) Formation of advanced glycation end-product-modified superoxide dismutase-1 (SOD1) is one of the mechanisms responsible for inclusions common to familial amyotrophic lateral sclerosis patients with SOD1 gene mutation, and transgenic mice expressing human SOD1 gene mutation. *Neuropathology* **21:** 67-81

Kato S, Shimoda M, Watanabe Y, Nakashima K, Takahashi K & Ohama E (1996) Familiar amyotrophic lateral sclerosis with a two base pair deletion in superoxide dismutase 1 gene: Multisystem degeneration with intracytoplasmic hyaline inclusions in astrocytes. *Journal of Neuropathology and Experimental Neurology* **55:** 1089-1101

Kayed R, Head E, Thompson JL, McIntire TM, Milton SC, Cotman CW & Glabe CG (2003) Common structure of soluble amyloid oligomers implies common mechanism of pathogenesis. *Science* **300:** 486-489

Kelly JW (1998) The alternative conformations of amyloidogenic proteins and their multi-step assembly pathways. *Curr Opin Struct Biol* **8:** 101-106

Kelly L & Holladay LA (1990) A comparative study of the unfolding thermodynamics of vertebrate metmyoglobins. *Biochemistry* **29:** 5062-5069

Khare SD, Caplow M & Dokholyan NV (2004) The rate and equilibrium constants for a multistep reaction sequence for the aggregation of superoxide dismutase in amyotrophic lateral sclerosis. *Proc Natl Acad Sci U S A* **101:** 15094-15099

Khare SD & Dokholyan NV (2006) Common dynamical signatures of familial amyotrophic lateral sclerosis-associated structurally diverse Cu, Zn superoxide dismutase mutants. *Proc Natl Acad Sci U S A* **103:** 3147-3152

Khurana R, Gillespie JR, Talapatra A, Minert LJ, Ionescu-Zanetti C, Millett I & Fink AL (2001) Partially folded intermediates as critical precursors of light chain amyloid fibrils and amorphous aggregates. *Biochemistry* **40:** 3525-3535

Kiese S, Papppenberger A, Friess W & Mahler HC (2008) Shaken, not stirred: Mechanical stress testing of an IgG1 antibody. *Journal of Pharmaceutical Sciences* **97:** 4347-4366

Klug D, Fridovic.I & Rabani J (1972) Direct Demonstration of Catalytic Action of Superoxide Dismutase through Use of Pulse Radiolysis. *J Biol Chem* **247:** 4839-&

Kong JM & Xu ZS (1998) Massive mitochondrial degeneration in motor neurons triggers the onset of amyotrophic lateral sclerosis in mice expressing a mutant SOD1. *J Neurosci* **18:** 3241-3250

Koppel DE (1972) Analysis of Macromolecular Polydispersity in Intensity Correlation Spectroscopy - Method of Cumulants. *J Chem Phys* **57:** 4814-&

Koradi R, Billeter M & Wuthrich K (1996) MOLMOL: a program for display and analysis of macromolecular structures. *J Mol Graph* **14:** 51-55, 29-32

Krishnamurthy R, Lumpkin JA & Sridhar R (2000) Inactivation of lysozyme by sonication under conditions relevant to microencapsulation. *International Journal of Pharmaceutics* **205:** 23-34

Kristiansen M, Deriziotis P, Dimcheff DE, Jackson GS, Ovaa H, Naumann H, Clarke AR, van Leeuwen FW, Menendez-Benito V, Dantuma NP, Portis JL, Collinge J & Tabrizi SJ (2007) Disease-associated prion protein oligomers inhibit the 26S proteasome. *Mol Cell* **26:** 175-188

Kumar S, Mohanty SK & Udgaonkar JB (2007) Mechanism of formation of amyloid protofibrils of barstar from soluble oligomers: evidence for multiple steps and lateral association coupled to conformational conversion. *J Mol Biol* **367:** 1186-1204

Kuo YM, Emmerling MR, VigoPelfrey C, Kasunic TC, Kirkpatrick JB, Murdoch GH, Ball MJ & Roher AE (1996) Water-soluble A beta (N-40, N-42) oligomers in normal and Alzheimer disease brains. *J Biol Chem* **271:** 4077-4081

Kurahashi T, Miyazaki A, Suwan S & Isobe M (2001) Extensive investigations on oxidized amino acid residues in H2O2-treated Cu,Zn-SOD protein with LC-ESI-Q-TOF-MS, MS/MS for the determination of the copper-binding site. *Journal of the American Chemical Society* **123:** 9268-9278

Kurobe N, Suzuki F, Okajima K & Kato K (1990) Sensitive enzyme immunoassay for human Cu/Zn superoxide dismutase. *Clin Chim Acta* **187:** 11-20

Laemmli UK (1970) Cleavage of Structural Proteins During Assembly of Head of Bacteriophage-T4. *Nature* **227:** 680-&

Lai Z, Colon W & Kelly JW (1996) The acid-mediated denaturation pathway of transthyretin yields a conformational intermediate that can self-assemble into amyloid. *Biochemistry* **35:** 6470-6482

Lamb AL, Wernimont AK, Pufahl RA, Culotta VC, O'Halloran TV & Rosenzweig AC (1999) Crystal structure of the copper chaperone for superoxide dismutase. *Nat Struct Biol* **6:** 724-729

Lenaz G (1998) Role of mitochondria in oxidative stress and ageing. *Biochim Biophys Acta-Bioenerg* **1366:** 53-67

Leone M, Cupane A, Militello V, Stroppolo ME & Desideri A (1998) Fourier transform infrared analysis of the interaction of azide with the active site of oxidized and reduced bovine Cu,Zn superoxide dismutase. *Biochemistry* **37:** 4459-4464

Lepock JR, Frey HE & Hallewell RA (1990) Contribution of conformational stability and reversibility of unfolding to the increased thermostability of human and bovine superoxide dismutase mutated at free cysteines. *J Biol Chem* **265:** 21612-21618

LeVine I, H. (1995) Thioflavine T interaction with amyloid β-sheet structures *Amyloid* **2:** 1-6

Li MW, Ona VO, Guegan C, Chen MH, Jackson-Lewis V, Andrews LJ, Olszewski AJ, Stieg PE, Lee JP, Przedborski S & Friedlander RM (2000) Functional role of caspase-1 and caspase-3 in an ALS transgenic mouse model. *Science* **288:** 335-339

Lindberg MJ, Normark J, Holmgren A & Oliveberg M (2004) Folding of human superoxide dismutase: disulfide reduction prevents dimerization and produces marginally stable monomers. *Proc Natl Acad Sci U S A* **101:** 15893-15898

Lindberg MJ, Tibell L & Oliveberg M (2002) Common denominator of Cu/Zn superoxide dismutase mutants associated with amyotrophic lateral sclerosis: decreased stability of the apo state. *Proc Natl Acad Sci U S A* **99:** 16607-16612

Lindgren M, Sorgjerd K & Hammarstrom P (2005) Detection and characterization of aggregates, prefibrillar amyloidogenic oligomers, and protofibrils using fluorescence spectroscopy. *Biophys J* **88:** 4200-4212

Linke RP (2009) Improved classification of various amyloid diseases using validated antibodies and Congo red fluorescence. Immunohistochemical typing of 662 patients. *Archives of Pathology and Laboratory Medicine*

Lino MM, Schneider C & Caroni P (2002) Accumulation of SOD1 mutants in postnatal motoneurons does not cause motoneuron pathology or motoneuron disease. *J Neurosci* **22:** 4825-4832

Liu CS, Chu D, Wideman RD, Houliston RS, Wong HJ & Meiering EM (2001) Thermodynamics of denaturation of hisactophilin, a beta-trefoil protein. *Biochemistry* **40:** 3817-3827

Liu J, Andya JD & Shire SJ (2006) A critical review of analytical ultracentrifugation and field flow fractionation methods for measuring protein aggregation. *Aaps J* **8:** E580-589

Liu RG, Althaus JS, Ellerbrock BR, Becker DA & Gurney ME (1998) Enhanced oxygen radical production in a transgenic mouse model of familial amyotrophic lateral sclerosis. *Annals of Neurology* **44:** 763-770

Lo YL & Rahman YE (1996) Interaction between superoxide dismutase and dipalmitoylphosphotidylglycerol bilayers: a fourier transform infrared (FT-IR) spectroscopic study. *Pharm Res* **13:** 265-271

Lomakin A, Benedek GB & Teplow DB (1999) Monitoring protein assembly using quasielastic light scattering spectroscopy. *Methods Enzymol* **309:** 429-459

Lomakin A, Chung DS, Benedek GB, Kirschner DA & Teplow DB (1996) On the nucleation and growth of amyloid beta-protein fibrils: detection of nuclei and quantitation of rate constants. *Proc Natl Acad Sci U S A* **93:** 1125-1129

Lowry OH, Rosebrough NJ, Farr AL & Randall RJ (1951) Protein measurement with the Folin phenol reagent. *J Biol Chem* **193:** 265-275

Lucas LH, Ersoy BA, Kueltzo LA, Joshi SB, Brandau DT, Thyagarajapuram N, Peek LJ & Middaugh CR (2006) Probing protein structure and dynamics by second-derivative ultraviolet absorption analysis of cation-{pi} interactions. *Protein Sci* **15:** 2228-2243

Lyons TJ, Gralla EB & Valentine JS (1999) Biological chemistry of copper-zinc superoxide dismutase and its link to amyotrophic lateral sclerosis. In *Metal Ions in Biological Systems, Vol 36* Vol. 36, pp 125-177. New York: Marcel Dekker

Lyons TJ, Nersissian A, Goto JJ, Zhu H, Gralla EB & Valentine JS (1998) Metal ion reconstitution studies of yeast copper-zinc superoxide dismutase: the "phantom" subunit and the possible role of Lys7p. *J Biol Inorg Chem* **3:** 650-662

Mailer K, Addetia R & Livesey DL (1989) UV spectroscopic studies of human erythrocyte superoxide dismutase. *J Inorg Biochem* **37:** 151-161

Malinowski DP & Fridovich I (1979) Subunit Association and Side-Chain Reactivities of Bovine Erythrocyte Superoxide-Dismutase in Denaturing Solvents. *Biochemistry* **18:** 5055-5060

Marden MC, Hoa GHB & Stetzkowskimarden F (1986) HEME PROTEIN FLUORESCENCE VERSUS PRESSURE. *Biophysical Journal* **49:** 619-627

Marklund S & Marklund G (1974) Involvement of the superoxide anion radical in the autoxidation of pyrogallol and a convenient assay for superoxide dismutase. *Eur J Biochem* **47:** 469-474

Meersman F, Smeller L & Heremans K (2002) Comparative Fourier transform infrared spectroscopy study of cold-, pressure-, and heat-induced unfolding and aggregation of myoglobin. *Biophys J* **82:** 2635-2644

Mei G, Rosato N, Silva N, Jr., Rusch R, Gratton E, Savini I & Finazzi-Agro A (1992) Denaturation of human Cu/Zn superoxide dismutase by guanidine hydrochloride: a dynamic fluorescence study. *Biochemistry* **31:** 7224-7230

Meiering EM (2008) The threat of instability: neurodegeneration predicted by protein destabilization and aggregation propensity. *PLoS Biol* **6:** e193

Miller AF (2004) Superoxide dismutases: active sites that save, but a protein that kills. *Curr Opin Chem Biol* **8:** 162-168

Misumi Y, Ueda M, Fujimori H, Shinriki S, Meng W, Kim J, Saito S, Obayashi K, Uchino M & Ando Y (2008) Transthyretin forms amyloid fibrils at physiological pH with ultrasonication. *Amyloid* **15:** 234-239

Molnar KS, Karabacak NM, Johnson JL, Wang Q, Tiwari A, Hayward LJ, Coales SJ, Hamuro Y & Agar JN (2009) A common property of amyotrophic lateral sclerosis-associated variants: destabilization of the copper/zinc superoxide dismutase electrostatic loop. *J Biol Chem* **284:** 30965-30973

Morel B, Casares S & Conejero-Lara F (2006) A single mutation induces amyloid aggregation in the alpha-spectrin SH3 domain: Analysis of the early stages of fibril formation. *Journal of Molecular Biology* **356:** 453-468

Morgan D, Diamond DM, Gottschall PE, Ugen KE, Dickey C, Hardy J, Duff K, Jantzen P, DiCarlo G, Wilcock D, Connor K, Hatcher J, Hope C, Gordon M & Arendash GW (2000) A beta peptide vaccination prevents memory loss in an animal model of Alzheimer's disease. *Nature* **408:** 982-985

Morozova-Roche LA, Zurdo J, Spencer A, Noppe W, Receveur V, Archer DB, Joniau M & Dobson CM (2000) Amyloid fibril formation and seeding by wild-type human lysozyme and its disease-related mutational variants. *J Struct Biol* **130:** 339-351

Morris AM, Watzky MA, Agar JN & Finke RG (2008) Fitting neurological protein aggregation kinetic data via a 2-step, minimal/"Ockham's razor" model: the Finke-Watzky mechanism of nucleation followed by autocatalytic surface growth. *Biochemistry* **47:** 2413-2427

Morris AM, Watzky MA & Finke RG (2009) Protein aggregation kinetics, mechanism, and curve-fitting: a review of the literature. *Biochim Biophys Acta* **1794:** 375-397

Munishkina LA, Cooper EM, Uversky VN & Fink AL (2004) The effect of macromolecular crowding on protein aggregation and amyloid fibril formation. *J Mol Recognit* **17:** 456-464

Munishkina LA & Fink AL (2007) Fluorescence as a method to reveal structures and membrane-interactions of amyloidogenic proteins. *Biochim Biophys Acta* **1768:** 1862-1885

Natvig DO, Imlay K, Touati D & Hallewell RA (1987) Human Copper-Zinc Superoxide-Dismutase Complements Superoxide Dismutase-Deficient Escherichia-Coli Mutants. *J Biol Chem* **262:** 14697-14701

Nelson R, Sawaya MR, Balbirnie M, Madsen AO, Riekel C, Grothe R & Eisenberg D (2005) Structure of the cross-beta spine of amyloid-like fibrils. *Nature* **435:** 773-778

Neves-Petersen MT, Klitgaard S, Carvalho ASL, Petersen SB, de Barros MRA & Melo EPE (2007) Photophysics and photochemistry of horseradish peroxidase A2 upon ultraviolet illumination. *Biophysical Journal* **92:** 2016-2027

Nicolai T & Durand D (2007) Protein aggregation and gel formation studied with scattering methods and computer simulations. *Curr Opin Colloid Interface Sci* **12:** 23-28

Nicoll JA, Wilkinson D, Holmes C, Steart P, Markham H & Weller RO (2003) Neuropathology of human Alzheimer disease after immunization with amyloid-beta peptide: a case report. *Nat Med* **9:** 448-452

Nielsen L, Khurana R, Coats A, Frokjaer S, Brange J, Vyas S, Uversky VN & Fink AL (2001) Effect of environmental factors on the kinetics of insulin fibril formation: elucidation of the molecular mechanism. *Biochemistry* **40:** 6036-6046

Niwa J, Ishigaki S, Hishikawa N, Yamamoto M, Doyu M, Murata S, Tanaka K, Taniguchi N & Sobue G (2002) Dorfin ubiquitylates mutant SOD1 and prevents mutant SOD1-mediated neurotoxicity. *J Biol Chem* **277:** 36793-36798

Nordlund A, Leinartaite L, Saraboji K, Aisenbrey C, Grobner G, Zetterstrom P, Danielsson J, Logan DT & Oliveberg M (2009) Functional features cause misfolding of the ALS-provoking enzyme SOD1. *Proc Natl Acad Sci U S A* **106:** 9667-9672

O'Halloran TV & Culotta VC (2000) Metallochaperones, an intracellular shuttle service for metal ions. *J Biol Chem* **275:** 25057-25060

Oberg KA & Uversky VN (2001) Secondary structure of the homologous proteins, alpha-fetoprotein and serum albumin, from their circular dichroism and infrared spectra. *Protein and Peptide Letters* **8:** 297-302

Ohhashi Y, Kihara M, Naiki H & Goto Y (2005) Ultrasonication-induced amyloid fibril formation of beta2-microglobulin. *J Biol Chem* **280:** 32843-32848

Okamoto K, Hirai S, Yamazaki T, Sun XY & Nakazato Y (1991) New ubiquitin-positive intraneuronal inclusions in the extra-motor cortices in patients with amyotrophic lateral sclerosis. *Neurosci Lett* **129:** 233-236

Oosawa F,
Asakura, S. (1975) *Thermodynamics of the Polymerization of Protein*
 New york: Academic Press.

Oosawa F, Asakura S, Hotta K, Imai N & Ooi T (1959) G-F Transformation of Actin as a Fibrous Condensation. *Journal of Polymer Science* **37:** 323-336

Owens CWI & Belcher RV (1965) A Colorimetric Micro-Method for Determination of Glutathione. *Biochemical Journal* **94:** 705-&

Oztug Durer ZA, Cohlberg JA, Dinh P, Padua S, Ehrenclou K, Downes S, Tan JK, Nakano Y, Bowman CJ, Hoskins JL, Kwon C, Mason AZ, Rodriguez JA, Doucette PA, Shaw BF & Selverstone Valentine J (2009) Loss of metal ions, disulfide reduction and mutations related to familial ALS promote formation of amyloid-like aggregates from superoxide dismutase. *PLoS ONE* **4:** e5004

Padrick SB & Miranker AD (2002) Islet amyloid: phase partitioning and secondary nucleation are central to the mechanism of fibrillogenesis. *Biochemistry* **41:** 4694-4703

Pardo CA, Xu Z, Borchelt DR, Price DL, Sisodia SS & Cleveland DW (1995) Superoxide dismutase is an abundant component in cell bodies, dendrites, and axons of motor neurons and in a subset of other neurons. *Proc Natl Acad Sci U S A* **92:** 954-958

Parge HE, Getzoff ED, Scandella CS, Hallewell RA & Tainer JA (1986) Crystallographic Characterization of Recombinant Human Cuzn Superoxide-Dismutase. *J Biol Chem* **261:** 6215-6218

Parge HE, Hallewell RA & Tainer JA (1992) Atomic structures of wild-type and thermostable mutant recombinant human Cu,Zn superoxide dismutase. *Proc Natl Acad Sci U S A* **89:** 6109-6113

Pedersen JS, Christensen G & Otzen DE (2004) Modulation of S6 fibrillation by unfolding rates and gatekeeper residues. *J Mol Biol* **341:** 575-588

Pepys MB, Hawkins PN, Booth DR, Vigushin DM, Tennent GA, Soutar AK, Totty N, Nguyen O, Blake CCF, Terry CJ, Feest TG, Zalin AM & Hsuan JJ (1993) Human Lysozyme Gene-Mutations Cause Hereditary Systemic Amyloidosis. *Nature* **362:** 553-557

Piazza R, Pierno M, Iacopini S, Mangione P, Esposito G & Bellotti V (2006) Micro-heterogeneity and aggregation in beta2-microglobulin solutions: effects of temperature, pH, and conformational variant addition. *Eur Biophys J* **35:** 439-445

Piyasena P, Mohareb E & McKellar RC (2003) Inactivation of microbes using ultrasound: a review. *Int J Food Microbiol* **87:** 207-216

Plakoutsi G, Bemporad F, Calamai M, Taddei N, Dobson CM & Chiti F (2005) Evidence for a mechanism of amyloid formation involving molecular reorganisation within native-like precursor aggregates. *J Mol Biol* **351:** 910-922

Polymeropoulos MH, Lavedan C, Leroy E, Ide SE, Dehejia A, Dutra A, Pike B, Root H, Rubenstein J, Boyer R, Stenroos ES, Chandrasekharappa S, Athanassiadou A, Papapetropoulos T, Johnson WG, Lazzarini AM, Duvoisin RC, Di Iorio G, Golbe LI & Nussbaum RL (1997) Mutation in the alpha-synuclein gene identified in families with Parkinson's disease. *Science* **276:** 2045-2047

Potter SZ, Zhu HN, Shaw BF, Rodriguez JA, Doucette PA, Sohn SH, Durazo A, Faull KF, Gralla EB, Nersissian AM & Valentine JS (2007) Binding of a single zinc ion to one subunit of copper-zinc superoxide dismutase apoprotein substantially influences the structure and stability of the entire homodimeric protein. *Journal of the American Chemical Society* **129:** 4575-4583

Prabakaran S & Damodaran S (1997) Thermal unfolding of beta-lactoglobulin: Characterization of initial unfolding events responsible for heat-induced aggregation. *J Agric Food Chem* **45:** 4303-4308

Provencher SW (1982) Contin - a General-Purpose Constrained Regularization Program for Inverting Noisy Linear Algebraic and Integral-Equations. *Comput Phys Commun* **27:** 229-242

Prudencio M, Durazo A, Whitelegge JP & Borchelt DR (2009) Modulation of mutant superoxide dismutase 1 aggregation by co-expression of wild-type enzyme. *J Neurochem* **108:** 1009-1018

Prusiner SB (1998) Prions. *Proc Natl Acad Sci U S A* **95:** 13363-13383

Puget K & Michelso.Am (1974) Isolation of a New Copper - Containing Superoxide-Dismutase Bacteriocuprein. *Biochemical and Biophysical Research Communications* **58:** 830-838

Qiu WH, Li TP, Zhang LY, Yang Y, Kao YT, Wang LJ & Zhong DP Ultrafast quenching of tryptophan fluorescence in proteins: Interresidue and intrahelical electron transfer, Vol. 350, pp 154-164.

Rae TD, Schmidt PJ, Pufahl RA, Culotta VC & O'Halloran TV (1999) Undetectable intracellular free copper: The requirement of a copper chaperone for superoxide dismutase. *Science* **284:** 805-808

Rakhit R, Crow JP, Lepock JR, Kondejewski LH, Cashman NR & Chakrabartty A (2004) Monomeric Cu,Zn-superoxide dismutase is a common misfolding intermediate in the oxidation models of sporadic and familial amyotrophic lateral sclerosis. *J Biol Chem* **279:** 15499-15504

Rakhit R, Cunningham P, Furtos-Matei A, Dahan S, Qi XF, Crow JP, Cashman NR, Kondejewski LH & Chakrabartty A (2002) Oxidation-induced misfolding and aggregation of superoxide dismutase and its implications for amyotrophic lateral sclerosis. *J Biol Chem* **277:** 47551-47556

Rakhit R, Robertson J, Vande Velde C, Horne P, Ruth DM, Griffin J, Cleveland DW, Cashman NR & Chakrabartty A (2007) An immunological epitope selective for pathological monomer-misfolded SOD1 in ALS. *Nat Med* **13:** 754-759

Ray SS, Nowak RJ, Brown RH, Jr. & Lansbury PT, Jr. (2005) Small-molecule-mediated stabilization of familial amyotrophic lateral sclerosis-linked superoxide dismutase mutants against unfolding and aggregation. *Proc Natl Acad Sci U S A* **102:** 3639-3644

Reaume AG, Elliott JL, Hoffman EK, Kowall NW, Ferrante RJ, Siwek DF, Wilcox HM, Flood DG, Beal MF, Brown RH, Jr., Scott RW & Snider WD (1996) Motor neurons in Cu/Zn superoxide dismutase-deficient mice develop normally but exhibit enhanced cell death after axonal injury. *Nat Genet* **13:** 43-47

Rhee SG, Yang KS, Kang SW, Woo HA & Chang TS (2005) Controlled elimination of intracellular H2O2: Regulation of peroxiredoxin, catalase, and glutathione peroxidase via post-translational modification. *Antioxid Redox Signal* **7:** 619-626

Ro LS, Lai SL, Chen CM & Chen ST (2003) Deleted 4977-bp mitochondrial DNA mutation is associated with sporadic amyotrophic lateral sclerosis: A hospital-based case-control study. *Muscle & Nerve* **28:** 737-743

Roberts BR, Tainer JA, Getzoff ED, Malencik DA, Anderson SR, Bomben VC, Meyers KR, Karplus PA & Beckman JS (2007) Structural characterization of zinc-deficient human superoxide dismutase and implications for ALS. *J Mol Biol* **373:** 877-890

Roberts CJ (2007) Non-native protein aggregation kinetics. *Biotechnol Bioeng* **98:** 927-938

Rodriguez JA, Shaw BF, Durazo A, Sohn SH, Doucette PA, Nersissian AM, Faull KF, Eggers DK, Tiwari A, Hayward LJ & Valentine JS (2005) Destabilization of apoprotein is insufficient to explain Cu,Zn-superoxide dismutase-linked ALS pathogenesis. *Proc Natl Acad Sci U S A* **102:** 10516-10521

Rodriguez JA, Valentine JS, Eggers DK, Roe JA, Tiwari A, Brown RH, Jr. & Hayward LJ (2002) Familial amyotrophic lateral sclerosis-associated mutations decrease the thermal stability of distinctly metallated species of human copper/zinc superoxide dismutase. *J Biol Chem* **277:** 15932-15937

Rokhina EV, Lens P & Virkutyte J (2009) Low-frequency ultrasound in biotechnology: state of the art. *Trends Biotechnol* **27:** 298-306

Rosen DR (1993) Mutations in Cu/Zn superoxide dismutase gene are associated with familial amyotrophic lateral sclerosis. *Nature* **364:** 362

Ross CA & Poirier MA (2004) Protein aggregation and neurodegenerative disease. *Nat Med* **10 Suppl:** S10-17

Rumfeldt JA, Lepock JR & Meiering EM (2009) Unfolding and folding kinetics of amyotrophic lateral sclerosis-associated mutant Cu,Zn superoxide dismutases. *J Mol Biol* **385:** 278-298

Rumfeldt JA, Stathopulos PB, Chakrabarrty A, Lepock JR & Meiering EM (2006) Mechanism and thermodynamics of guanidinium chloride-induced denaturation of ALS-associated mutant Cu,Zn superoxide dismutases. *J Mol Biol* **355:** 106-123

Ruschak AM & Miranker AD (2007) Fiber-dependent amyloid formation as catalysis of an existing reaction pathway. *Proc Natl Acad Sci U S A* **104:** 12341-12346

S.E. B (2006) Methods for measuring protein aggregation. *Curr Anal Chem* **2:** 157-170

Saborio GP, Permanne B & Soto C (2001) Sensitive detection of pathological prion protein by cyclic amplification of protein misfolding. *Nature* **411:** 810-813

Sandelin E, Nordlund A, Andersen PM, Marklund SSL & Oliveberg M (2007) Amyotrophic lateral sclerosis-associated copper/zinc superoxide dismutase mutations preferentially reduce the repulsive charge of the proteins. *J Biol Chem* **282:** 21230-21236

Sasahara K, Yagi H, Sakai M, Naiki H & Goto Y (2008) Amyloid nucleation triggered by agitation of beta2-microglobulin under acidic and neutral pH conditions. *Biochemistry* **47:** 2650-2660

Schenk D, Barbour R, Dunn W, Gordon G, Grajeda H, Guido T, Hu K, Huang J, Johnson-Wood K, Khan K, Kholodenko D, Lee M, Liao Z, Lieberburg I, Motter R, Mutter L, Soriano F, Shopp G, Vasquez N, Vandevert C, Walker S, Wogulis M, Yednock T, Games D & Seubert P (1999) Immunization with amyloid-beta attenuates Alzheimer-disease-like pathology in the PDAPP mouse. *Nature* **400:** 173-177

Schmidt PJ, Rae TD, Pufahl RA, Hamma T, Strain J, O'Halloran TV & Culotta VC (1999a) Multiple protein domains contribute to the action of the copper chaperone for superoxide dismutase. *J Biol Chem* **274:** 23719-23725

Schmidt PJ, Ramos-Gomez M & Culotta VC (1999b) A gain of superoxide dismutase (SOD) activity obtained with CCS, the copper metallochaperone for SOD1. *J Biol Chem* **274:** 36952-36956

Seetharaman SV, Prudencio M, Karch C, Holloway SP, Borchelt DR & Hart PJ (2009) Immature copper-zinc superoxide dismutase and familial amyotrophic lateral sclerosis. *Exp Biol Med (Maywood)* **234:** 1140-1154

Senoo Y, Katoh K, Nakai Y, Hashimoto Y, Bando K & Teramoto S (1988) Activity and Stability of Recombinant Human Superoxide-Dismutase in Buffer Solutions and Hypothermic Perfusates. *Acta Med Okayama* **42:** 169-174

Shaw BF, Lelie HL, Durazo A, Nersissian AM, Xu G, Chan PK, Gralla EB, Tiwari A, Hayward LJ, Borchelt DR, Valentine JS & Whitelegge JP (2008) Detergent-insoluble aggregates associated with amyotrophic lateral sclerosis in transgenic mice contain primarily full-length, unmodified superoxide dismutase-1. *J Biol Chem* **283:** 8340-8350

Shaw BF & Valentine JS (2007) How do ALS-associated mutations in superoxide dismutase 1 promote aggregation of the protein? *Trends Biochem Sci* **32:** 78-85

Shaw PJ, Chinnery RM & Ince PG (1994) [3H]D-aspartate binding sites in the normal human spinal cord and changes in motor neuron disease: a quantitative autoradiographic study. *Brain Res* **655:** 195-201

Shibata N, Asayama K, Hirano A & Kobayashi M (1996) Immunohistochemical study on superoxide dismutases in spinal cords from autopsied patients with amyotrophic lateral sclerosis. *Dev Neurosci* **18:** 492-498

Shibata N, Hirano A, Kobayashi M, Sasaki S, Kato T, Matsumoto S, Shiozawa Z, Komori T, Ikemoto A, Umahara T & Asayama K (1994) Cu/Zn superoxide dismutase-like immunoreactivity in Lewy body-like inclusions of sporadic amyotrophic lateral sclerosis. *Neurosci Lett* **179:** 149-152

Shipp EL, Cantini F, Bertini I, Valentine JS & Banci L (2003) Dynamic properties of the G93A mutant of copper-zinc superoxide dismutase as detected by NMR spectroscopy: implications for the pathology of familial amyotrophic lateral sclerosis. *Biochemistry* **42:** 1890-1899

Siklos L, Engelhardt J, Harati Y, Smith RG, Joo F & Appel SH (1996) Ultrastructural evidence for altered calcium in motor nerve terminals in amyotrophic lateral sclerosis. *Annals of Neurology* **39:** 203-216

Simpson EP, Yen AA & Appel SH (2003) Oxidative Stress: a common denominator in the pathogenesis of amyotrophic lateral sclerosis. *Current Opinion in Rheumatology* **15:** 730-736

Sluzky V, Tamada JA, Klibanov AM & Langer R (1991) Kinetics of insulin aggregation in aqueous solutions upon agitation in the presence of hydrophobic surfaces. *Proc Natl Acad Sci U S A* **88:** 9377-9381

Son M, Fathallah-Shaykh HM & Elliott JL (2001) Survival in a transgenic model of FALS is independent of iNOS expression. *Annals of Neurology* **50:** 273-273

Souillac PO, Uversky VN & Fink AL (2003) Structural transformations of oligomeric intermediates in the fibrillation of the immunoglobulin light chain LEN. *Biochemistry* **42:** 8094-8104

Souillac PO, Uversky VN, Millett IS, Khurana R, Doniach S & Fink AL (2002) Elucidation of the molecular mechanism during the early events in immunoglobulin light chain amyloid fibrillation. Evidence for an off-pathway oligomer at acidic pH. *J Biol Chem* **277:** 12666-12679

Sparrer HE, Santoso A, Szoka FC, Jr. & Weissman JS (2000) Evidence for the prion hypothesis: induction of the yeast [PSI+] factor by in vitro- converted Sup35 protein. *Science* **289:** 595-599

Stadtman ER & Levine RL (2003) Free radical-mediated oxidation of free amino acids and amino acid residues in proteins. *Amino Acids* **25:** 207-218

Stathopulos P (2005) Stability and Aggregation of Amytrophic Lateral Sclerosis-Associated Mutant Copper, Zinc Superoxide Dismutases. Ph.D Thesis, Chemistry, University of Waterloo, Waterloo

Stathopulos PB, Rumfeldt JA, Scholz GA, Irani RA, Frey HE, Hallewell RA, Lepock JR & Meiering EM (2003) Cu/Zn superoxide dismutase mutants associated with amyotrophic lateral sclerosis show enhanced formation of aggregates in vitro. *Proc Natl Acad Sci U S A* **100:** 7021-7026

Stathopulos PB, Rumfeldt JAO, Karbassi F, Siddall CA, Lepock JR & Meiering EM (2006) Calorimetric analysis of thermodynamic stability and aggregation for apo and holo amyotrophic lateral sclerosisassociated Gly-93 mutants of superoxide dismutase. *J Biol Chem* **281:** 6184-6193

Stathopulos PB, Scholz GA, Hwang YM, Rumfeldt JA, Lepock JR & Meiering EM (2004) Sonication of proteins causes formation of aggregates that resemble amyloid. *Protein Sci* **13:** 3017-3027

Steele JC & McGeer PL (2008) The ALS/PDC syndrome of Guam and the cycad hypothesis. *Neurology* **70:** 1984-1990

Stefani M & Dobson CM (2003) Protein aggregation and aggregate toxicity: new insights into protein folding, misfolding diseases and biological evolution. *J Mol Med* **81:** 678-699

Strange RW, Antonyuk S, Hough MA, Doucette PA, Rodriguez JA, Hart PJ, Hayward LJ, Valentine JS & Hasnain SS (2003) The structure of holo and metal-deficient wild-type human Cu, Zn superoxide dismutase and its relevance to familial amyotrophic lateral sclerosis. *Journal of Molecular Biology* **328:** 877-891

Strong MJ, Sopper MM, Crow JP, Strong WL & Beckman JS (1998) Nitration of the low molecular weight neurofilament is equivalent in sporadic amyotrophic lateral sclerosis and control cervical spinal cord. *Biochem Biophys Res Commun* **248:** 157-164

Sturtz LA, Diekert K, Jensen LT, Lill R & Culotta VC (2001) A fraction of yeast Cu,Zn-superoxide dismutase and its metallochaperone, CCS, localize to the intermembrane space of mitochondria. A physiological role for SOD1 in guarding against mitochondrial oxidative damage. *J Biol Chem* **276:** 38084-38089

Subramaniam JR, Lyons WE, Liu J, Bartnikas TB, Rothstein J, Price DL, Cleveland DW, Gitlin JD & Wong PC (2002) Mutant SOD1 causes motor neuron disease independent of copper chaperone-mediated copper loading. *Nat Neurosci* **5:** 301-307

Sun WY, Fang JL, Cheng M, Xia PY & Tang WX (1997) Secondary structure dependent on metal ions of copper, zinc superoxide dismutase investigated by Fourier transform IR spectroscopy. *Biopolymers* **42:** 297-303

Sunde M, Serpell LC, Bartlam M, Fraser PE, Pepys MB & Blake CCF (1997) Common core structure of amyloid fibrils by synchrotron X-ray diffraction. *Journal of Molecular Biology* **273:** 729-739

Suslick KS (1990) Sonochemistry. *Science* **247:** 1439-1445

Sutedja NA, Veldink JH, Fischer K, Kromhout H, Wokke JHJ, Huisman MHB, Heederik DJJ & Van den Berg LH (2007) Lifetime occupation, education, smoking, and risk of ALS. *Neurology* **69:** 1508-1514

Tainer JA, Getzoff ED, Beem KM, Richardson JS & Richardson DC (1982) Determination and analysis of the 2 A-structure of copper, zinc superoxide dismutase. *J Mol Biol* **160:** 181-217

Tan SY & Pepys MB (1994) Amyloidosis. *Histopathology* **25:** 403-414

Tew D & Demontellano PRO (1988) The Myoglobin Protein Radical - Coupling of Tyr-103 to Tyr-151 in the H2o2-Mediated Cross-Linking of Sperm Whale Myoglobin. *J Biol Chem* **263:** 17880-17886

Thakur AK, Jayaraman M, Mishra R, Thakur M, Chellgren VM, Byeon IJ, Anjum DH, Kodali R, Creamer TP, Conway JF, Gronenborn AM & Wetzel R (2009) Polyglutamine disruption of the huntingtin exon 1 N terminus triggers a complex aggregation mechanism. *Nat Struct Mol Biol* **16:** 380-389

Thomas PJ, Qu BH & Pedersen PL (1995) Defective Protein-Folding as a Basis of Human-Disease. *Trends BiochemSci* **20:** 456-459

Timothy J. Mason & Peters D (2002) *Practical Sonochemistry*, 2 edn. Chichester: Horwood Publishing Limited.

Turner BJ, Atkin JD, Farg MA, Zang DW, Rembach A, Lopes EC, Patch JD, Hill AF & Cheema SS (2005) Impaired extracellular secretion of mutant superoxide dismutase 1 associates with neurotoxicity in familial amyotrophic lateral sclerosis. *J Neurosci* **25:** 108-117

Turner BJ & Talbot K (2008) Transgenics, toxicity and therapeutics in rodent models of mutant SOD1-mediated familial ALS. *Prog Neurobiol* **85:** 94-134

Uchida K & Kawakishi S (1994) Identification of Oxidized Histidine Generated at the Active-Site of Cu,Zn-Superoxide Dismutase Exposed to H2o2 - Selective Generation of 2-Oxo-Histidine at the Histidine-118. *J Biol Chem* **269:** 2405-2410

Urushitani M, Ezzi SA & Julien JP (2007) Therapeutic effects of immunization with mutant superoxide dismutase in mice models of amyotrophic lateral sclerosis. *Proc Natl Acad Sci U S A* **104:** 2495-2500

Urushitani M, Sik A, Sakurai T, Nukina N, Takahashi R & Julien JP (2006) Chromogranin-mediated secretion of mutant superoxide dismutase proteins linked to amyotrophic lateral sclerosis. *Nat Neurosci* **9:** 108-118

Valentine JS, Doucette PA & Zittin Potter S (2005) Copper-zinc superoxide dismutase and amyotrophic lateral sclerosis. *Annu Rev Biochem* **74:** 563-593

Valtschanoff JG, Weinberg RJ & Rustioni A (1992) Nadph Diaphorase in the Spinal-Cord of Rats. *J Comp Neurol* **321:** 209-222

Van Den Bosch L & Robberecht W (2008) Crosstalk between astrocytes and motor neurons: what is the message? *Exp Neurol* **211:** 1-6

Van Den Bosch L, Van Damme P, Bogaert E & Robberecht W (2006) The role of excitotoxicity in the pathogenesis of amyotrophic lateral sclerosis. *Biochim Biophys Acta* **1762:** 1068-1082

van Holde Kensal E., Johnson W. Curtis & Shing HP (1998) *Principles of Physical Biochemistry*.

Vassall KA, Stathopulos PB, Rumfeldt JA, Lepock JR & Meiering EM (2006) Equilibrium thermodynamic analysis of amyotrophic lateral sclerosis-associated mutant apo Cu,Zn superoxide dismutases. *Biochemistry* **45:** 7366-7379

Velde CV, Miller TM, Cashman NR & Cleveland DW (2008) Selective assoction of misfolded ALS-linked mutant SOD1 with the cytoplasmic face of mitochondria. *Proceedings of the National Academy of Sciences of the United States of America* **105:** 4022-4027

Walsh DM, Lomakin A, Benedek GB, Condron MM & Teplow DB (1997) Amyloid beta-protein fibrillogenesis. Detection of a protofibrillar intermediate. *J Biol Chem* **272:** 22364-22372

Wang J, Slunt H, Gonzales V, Fromholt D, Coonfield M, Copeland NG, Jenkins NA & Borchelt DR (2003) Copper-binding-site-null SOD1 causes ALS in transgenic mice: aggregates of non-native SOD1 delineate a common feature. *Hum Mol Genet* **12:** 2753-2764

Wang Q, Johnson JL, Agar NY & Agar JN (2008) Protein aggregation and protein instability govern familial amyotrophic lateral sclerosis patient survival. *PLoS Biol* **6:** e170

Watanabe M, Dykes-Hoberg M, Culotta VC, Price DL, Wong PC & Rothstein JD (2001) Histological evidence of protein aggregation in mutant SOD1 transgenic mice and in amyotrophic lateral sclerosis neural tissues. *Neurobiol Dis* **8:** 933-941

WiedauPazos M, Goto JJ, Rabizadeh S, Gralla EB, Roe JA, Lee MK, Valentine JS & Bredesen DE (1996) Altered reactivity of superoxide dismutase in farmilial amyotrophic lateral sclerosis. *Science* **271:** 515-518

Wiedemann FR, Winkler K, Kuznetsov AV, Bartels C, Vielhaber S, Feistner H & Kunz WS (1998) Impairment of mitochondrial function in skeletal muscle of patients with amyotrophic lateral sclerosis. *J Neurol Sci* **156:** 65-72

Wijesekera LC & Leigh PN (2009) Amyotrophic lateral sclerosis. *Orphanet J Rare Dis* **4:** 3

Wilkins DK, Grimshaw SB, Receveur V, Dobson CM, Jones JA & Smith LJ (1999) Hydrodynamic radii of native and denatured proteins measured by pulse field gradient NMR techniques. *Biochemistry* **38:** 16424-16431

Williamson TL & Cleveland DW (1999) Slowing of axonal transport is a very early event in the toxicity of ALS-linked SOD1 mutants to motor neurons. *Nat Neurosci* **2:** 50-56

Wiseman RL, Powers ET & Kelly JW (2005) Partitioning conformational intermediates between competing refolding and aggregation pathways: insights into transthyretin amyloid disease. *Biochemistry* **44:** 16612-16623

Wong PC, Pardo CA, Borchelt DR, Lee MK, Copeland NG, Jenkins NA, Sisodia SS, Cleveland DW & Price DL (1995a) An Adverse Property of a Familial Als-Linked Sod1 Mutation Causes Motor-Neuron Disease Characterized by Vacuolar Degeneration of Mitochondria. *Neuron* **14:** 1105-1116

Wong PC, Pardo CA, Borchelt DR, Lee MK, Copeland NG, Jenkins NA, Sisodia SS, Cleveland DW & Price DL (1995b) An adverse property of a familial ALS-linked SOD1 mutation causes motor neuron disease characterized by vacuolar degeneration of mitochondria. *Neuron* **14:** 1105-1116

Worms PA (2001) The epidemiology of motor neuron diseases: a review of recent studies. *J Neurol Sci* **191:** 3-9

Wray JW, Abaase WA, Ostheimer GJ, Zhang XJ & Matthews BW (2000) Use of a non-rigid region in T4 lysozyme to design an adaptable metal-binding site. *Protein Engineering* **13:** 313-321

Wu YG, Li YF, Liu HL & Wu WT (1995) Induction of Nitric-Oxide Synthase and Motoneuron Death in Newborn and Early Postnatal Rats Following Spinal Root Avulsion. *Neurosci Lett* **194:** 109-112

Xue WF, Homans SW & Radford SE (2008) Systematic analysis of nucleation-dependent polymerization reveals new insights into the mechanism of amyloid self-assembly. *Proc Natl Acad Sci U S A* **105:** 8926-8931

Yamasaki M, Li W, Johnson DJ & Huntington JA (2008) Crystal structure of a stable dimer reveals the molecular basis of serpin polymerization. *Nature* **455:** 1255-1258

Youn HD, Youn H, Lee JW, Yim YI, Lee JK, Hah YC & Kang SO (1996) Unique isozymes of superoxide dismutase in Streptomyces griseus. *Arch Biochem Biophys* **334:** 341-348

Zalin AM, Jones S, Fitch NJS & Ramsden DB (1991) Familial Nephropathic Nonneuropathic Amyloidosis - Clinical-Features, Immunohistochemistry and Chemistry. *Q J Med* **81:** 945-956

Zandomeneghi G, Krebs MR, McCammon MG & Fandrich M (2004) FTIR reveals structural differences between native beta-sheet proteins and amyloid fibrils. *Protein Sci* **13:** 3314-3321

Zelko IN, Mariani TJ & Folz RJ (2002) Superoxide dismutase multigene family: A comparison of the CuZn-SOD (SOD1), Mn-SOD (SOD2), and EC-SOD (SOD3) gene structures, evolution, and expression. *Free Radical Biology and Medicine* **33:** 337-349

Zhang NY, Tang Z & Liu CW (2008) alpha-Synuclein protofibrils inhibit 26 S proteasome-mediated protein degradation: understanding the cytotoxicity of protein protofibrils in neurodegenerative disease pathogenesis. *J Biol Chem* **283:** 20288-20298